Development of a narrow bandwidth, tuneable RF and microwave trapped ion sensor

Harry Machin Bostock

Submitted for the degree of Doctor of Philosophy
University of Sussex, Brighton, United Kingdom. September 2019

Declaration

I hereby declare that this thesis has not been and will not be submitted in whole or in part to another University for the award of any other degree.

Signature:

Harry Machin Bostock

Dedication

This thesis is dedicated to my father, Roger Bostock, who passed away due to Alzheimers disease during my PhD studies. Thank you dad for always believing in me and being a source of never ending support. Even in death I know you'll always be with me spurring me to happiness and success.

- Your boy.

Acknowledgements

I first want to thank my loving family, for helping me during a very trying four years. This includes my mum, Caroline, who has always supported me and encouraged me even in the darkest times. I would like to thank my two sisters, Jane and Caz, with their wonderful families, who always brightened my day whenever I could spare the time to see them. I'd like to thank my girlfriend, Seyoung, for always keeping a smile on my face every day and encouraging me to be the best I can be.

Professor Winfried Hensinger has been a great inspiration for me, and inspired me to continue my career in academia. Dr. Sebastian Weidt has been a great supervisor, providing support to further the quantum sensing project. I would also like to thank my former team sensor members, Dr. Altaf Nizamani, for being a superb team leader and Dr. Ethan Potter. In the last year of my PhD, I worked very closely with Dr. Tomas Navickas who provided invaluable expertise to the experiment. My two undergraduate students Ronnie Parker and Toby Hawkins contributed good work to the project. Ian and Harry both worked with me and provided invaluable feedback with regards to the ion-coil idea. Dr. Simon Webster who was incredibly helpful in developing the ARTIQ software and hardware. Andrea for helping me understand the underlying theory of the project in my first year.

I'd like to thank my fellow group members from the rest of IQT both current and former: Nick for the supportive and infrequent tea breaks and not getting too angry with me about being noisy; Jesús for the long discussions about just about anything and the afternoon Doctor who sessions; Zak for all the many, many songs sung to me over the office; Raph for putting up with Zak; David for tolerating my pestering about your ever-changing laser system; Mitch for always lending an ear for advice at any time; Reuben for providing sage advice and giving me good chips; Fan; Eamon; Pedro; Mark; Alex and David Murgia.

Abstract

Quantum sensors are a new upcoming technology that offers to push the limits of how we can detect incredibly small signals in the DC and low RF regimes using magnetometers such as super-conducting quantum interference device (SQUID); N-V centres in Diamond, atomic vapour cells and atomic traps. All these technologies are currently being heavily invested in to push the boundaries of magnetometry for commercial applications. The quantum sensor I have been working to develop is set apart in several different aspects: unlike other quantum sensors it is very sensitive at the high RF and even 12.6 GHz microwave radiation; it has the ability to be rapidly tuned to different frequencies; due to the microwave decoupling technique we employ, the sensor is not sensitive to fluctuations in the DC field and therefore does not require bulky shielding or a laboratory environment to function. To this end I have built a demonstrator system capable of sensing RF and microwave fields and have measured the sensitivity of this device in both of these regimes. There has also been work on developing a portable version of the demonstrator and this work is ongoing within the group.

Contents

1 Introduction

RF sensors have existed for over a century in the form of simple classical antenna systems to send Morse code over long distances [1]. Microwave detection was not developed until just before the Second World War, half a century later due to the difficulties with detecting the shorter wavelength [2]. After another century of intensive development, classical RF and microwave sensors are used almost everywhere in modern life, from the minute microwave receivers in mobile phones to the RF antennas used for telecommunications. The number of applications in these fields is limitless hence the huge investment in these classical detectors, which has led to sensitivities below -100 dBm. Within the last couple of decades many quantum magnetometers have been developed, which have surpassed their classical peers in many fields (more details in my literature review in section 1.1). So far these quantum sensors have been confined to the DC and low RF (sub-kHz) frequency space, with their sensitivity quickly dropping off with increased frequency. The trapped-ytterbium RF and microwave sensor offers a novel sensing technique, which allows for $pT/\sqrt{Hz}$ level sensitivities with the possibility of going down to sub $fT/\sqrt{Hz}$ sensitivities using advanced techniques (see section 5).

The general principle of sensing with trapped-ions is quite similar to using trapped-ions for quantum computing applications [23]. A flux of neutral ytterbium-171 atoms is produced by an atomic oven, which is directed at a microfabricated chip trap. Once the atoms are over the trapping area of the chip, they are ionised by a 399 nm laser beam producing $^{171}Yb^{+}$. These ions are then trapped by a combination of electric DC potentials and RF rails to produce a rotating pseudo-potential known as a Paul trap. Once trapped they must be cooled using an off-resonant 369 nm beam, so that the ion can be put into its ground state for coherent manipulation and to ensure the ion does not overheat and leave the trap. Once the ion has been trapped, sensing can begin. One can sense in principle by tuning the sensor by applying a varied DC field to a particular frequency we wish to sense before preparing the ion in a particular quantum state and then allowing the field we wish to sense to drive the ion from the prepared state to a dressed state that we have prepared using microwaves. After a set amount of time we can find which state the system has collapsed to by applying a 369 nm laser so if the state collapsed to one level then you will see 369 nm fluorescence and if it collapsed to the other state then you will not observe fluorescence. We can repeat this experiment a number of times using the same exposure time to produce a probability of the state being in one state or the other after an amount of exposure time. If we repeat this experiment with different exposure times then we can produce a sine wave of the exposure time versus the state probability. The frequency of this sine wave is called the Rabi frequency and it is directly proportional to the intensity of the RF waves driving the transition. Much of this work was carried out by, Dr. Ethan Potter [39], whose work was based heavily on former group member, Joe Randall [63]. More details on how this is done and how exactly we measure the sensitivity of our sensor is detailed in section 2.

The majority of my project has been committed to demonstrating this technology with an on-table experiment we called the 'demonstrator device'. This was built from scratch at the beginning of my PhD to a fully realised RF and microwave sensing apparatus, by the end of my PhD. This design and assembly work was done in collaboration with my fellow PhD student Dr. Ethan Potter and post-doctoral fellow Dr. Altaf Nizamani. This work involved: designing a vacuum chamber that could accommodate our chip and connecting printed circuit board (PCB) apparatus; finding the best charge-coupled device (CCD) camera for initial trapping and trap calibration as well as a photo-multiplier tube (PMT) for conducting coherent experiments; designing optics and assembling optics that would allow us to examine the trapping area and maximise fidelity of our experiments by collecting the highest number of photons possible from a given fluorescence event; designing and ordering a 100-pin electrical DC feedthrough as well as designing custom ultra-high vacuum (UHV) compatible cabling for connecting them to the chip; ordering and assembling laser optics to fibre-couple the 369 nm, 399 nm and 935 nm lasers onto our optics table, then combine the lasers and focus them onto the trap; designing and assembling the Helmholtz coils around the system as well as a DC current supply to modulate the provided DC field; a 16-channel DC supply directly controllable via a LabVIEW interface on a desktop computer for the internal DC potentials; RF and microwave sources as well as an RF coil and microwave horn near the chip for coherent manipulation of the internal state of the Yb ions; RF source and resonator for RF potential applied to the trap to provide a trapping potential for the ions; finding and ordering an field-programmable gate array (FPGA) and assembling the electronics around it into a control box to manipulate RF and microwave pulses with nano-second response times; programme all the experiments in Python to be run on the FPGA as a sequence of pulses to manipulate the ion into a prepared state then experiment and finally readout from the PMT. More details on these aspects of the experimental set-up can be found in section 3.

In the last year in collaboration with my colleague, Ethan Potter, we succeeded in demonstrating RF sensing and for the first time for a trapped-ion quantum sensor measured exact microwave sensitivity. To this end, since initially trapping $^{174}Yb^{+}$, we subsequently trapped $^{171}Yb^{+}$, which is used for coherent experiments, because of its more desirable energy state manifold for RF and microwave sensing. Once we applied a DC field over the ion and lifted the degeneracy of the $m_s = \pm 1$, states then we can begin to calculate what the energy splitting is of the various relevant RF and microwave states used for sensing before further coherent experiments. To maximise the sensitivity of our sensing experiments, we had to ascertain exactly how long we would have to conduct our experiments. To find this time, we have to find the coherence time (T_2 time) of the ion. A Ramsey experiment was conducted on the ion to determine the coherence time, where a $\pi/2$ pulse is applied to the ion to place it in a 50/50 superposition state, then giving it a delay of a certain amount of time then applying a second $\pi/2$ but with a phase change from the first pulse. Then detection is carried out to find the state and this experiment is repeated multiple times to give a probability. Then we repeated these experiments while sweeping the phase difference of the second pulse. Once we swept the parameter space of 0 to 2π phase and plotted the probability this gave us a sine wave. This process was then repeated again, but with different delay times and as the delays get longer then the probability tends towards 0.5. By measuring how quickly the fringes of the sine waves decreased we could find the accurate coherence time of our experiment. With this information we could go about conducting Rabi experiments with delay time being roughly half the coherence time measured from the Ramsey experiments. Once enough measurements had been made we plotted these points and drew a best fit line of the data, then compared how closely the data points correlate with the best fit line to give an average uncertainty for this line. This uncertainty gives us our sensitivity. We did all these measurements for both RF and microwave sensing and achieved: $125 \pm 26\ pT/\sqrt{Hz}$ for RF measurements and $102 \pm 11\ pT/\sqrt{Hz}$ for microwaves. Further details can be found in section 4. It should be noted that all the data analysis and resulting plots that are presented in this thesis were produced by Dr. Ethan Potter, while I produced the Python code shown in the appendix A that ran the experiments that produced the data.

I will detail future experiments that I believe would be worth pursuing in future in section 5.4. This includes an innovative new method for detecting RF magnetic fields using a pickup coil or antenna to collect RF from a large area then feed the resulting current into the vacuum system and to a small coil around the chip to deliver the concentrated RF to the ion to enhance sensitivity. According to my calculations, this should result in a 10000 fold increase in power around 10 MHz. It would be relatively straightforward to implement this design into the system to demonstrate this amplification effect. I would also like to demonstrate the Qdyne technique [24], which is an experimental technique used on two-level quantum systems, such as ours to extend the coherence time artificially by stringing different measurements together with precise timing allowing us to make extremely long measurements capable of reducing the bandwidth of the sensor to the μHz regime. This opens up many new possible applications for far field sensing to compete with RF antennas and RADAR. Also we already have prepared newly fabricated chips designed by Dr. Altaf Nizamani, which should allow us to trap many ions on the chip simultaneously and hence increase our sensitivity and minimum detection time required for an experiment.

My ultimate goal for this project is to miniaturise the technology shown in the demonstrator device and produce a viable quantum sensor that could be carried into the field and conduct RF and microwave measurements on demand. To this end, during my PhD, myself and my colleagues have undertaken work on how exactly this could be done. These technologies include: the miniaturised laser system with accompanying optics; small control board capable of producing precise DC, RF and microwave potentials as well as controlling the pulse sequences for the experiment and provide a user interface; smaller optics tube and PMT/CCD detection device to be able to fit inside our shoebox-sized design; The vacuum system which should be small enough to fit in your palm but contain a 100 DC electrical feedthrough, RF and microwave feedthrough's, laser and optical access for detection and readout. This will be covered in detail in section 6.

I will go over the myriad of possible applications we have investigated over my PhD in section 7. These applications offer to revolutionise how RF and microwaves are detected as this regime is currently dominated by classical sensors using pick-up coils and amplifiers. These applications include: explosive and narcotic detection; microwave airport scanners; drone detection and pipeline detection.

In the conclusion in section 8 of this thesis I will summarise what I have built and achieved during my PhD and how it will have an impact on the literature and even the commercial space in the future. I will examine my results and show how they demonstrate, for the first time, the sensitivity of detecting microwaves using trapped-ions and how they are more sensitive in this regime than in any other quantum sensor on the market at the moment of writing. I will also discuss how I feel the project should be taken in future and what impact it could have.

1.1 State-of-the-art Quantum Magnetometry and RF Sensing

Currently there are many different quantum sensors, either in development or that have reached the market place such as SQUIDs [31], which are being used in medical scanners and devices for measuring the magnetic properties of materials [12]. These sensors are pushing the boundaries of what is possible for DC and RF sensing contributing to the fields of: medical imaging, geomagnetics, non-destructive materials evaluation, scanning probe microscopy and electrical measurements. I will now summarise the various quantum sensors being researched currently, I have used an unpublished report written by myself and my group collaborators, Dr. Ethan Potter and Dr. Altaf Nizamani, to write the below section.

For direct comparison between the different quantum sensors I have decided on the quantity $\delta B_{min}/\sqrt{Hz}$, which denotes the minimum detectable difference in magnetic field strength (in Tesla) discernible per second of total measurement time. This quantity is especially useful for comparing DC detectors and is generally used in the literature, but can also be useful for comparing RF sensors. It should be noted that δB_{min} will be different for different frequencies and most of these quantum sensors only work in the DC to low RF regime ($\sim Hz$). Sensitivities for each device will represent its sensitivity in the DC regime unless otherwise stated.

1.1.1 SQUID

Superconducting QUantum Interference Devices or SQUIDs are incredibly sensitive DC magnetic field sensors, which use superconducting loops for using Josephson junctions [13]. These junctions are highly susceptible to small changes in DC field around them, making them very useful for detecting current, voltage, inductance and magnetic susceptibility in samples. To implement this system to detect magnetic fields an input coil is placed around a SQUID Josephson junction, which is then connected to a a pickup coil with the sample inside it. When the sample is moved through the coil, the change in magnetic field will induce a current in the pickup coil which will induce a current in the input coil. This current will produce a reciprocal magnetic field at the Josephson junction, but far more concentrated producing a greater sensitivity than with a bare SQUID [14]. This amplification technique was an inspiration for implementing a similar method of amplification using trapped-ions, which I have detailed in section 5. The readout of a SQUID circuit is a voltage which can be detected and amplified to give the signal and this voltage is directly proportional to the current in the input coil. This essentially means that the SQUID detector can be used as a direct current-to-voltage converter.

Although highly sensitive these systems do have drawbacks. SQUIDs, because of their reliance on superconducting materials need to operate at either liquid Helium (4.2 K) or liquid nitrogen (77 K) temperatures to function, so generally require very bulky cryogenic systems making them unsuitable for field work. They also require substantial shielding as they are very susceptible to DC noise and stray noise making it difficult to use them outside a controlled laboratory environment.

1.1.2 Atomic Vapour Cells

Atomic vapour cells, also known as alkali-metal atomic magnetometers use the atomic-spin - dependent properties of different alkali vapours to detect DC magnetic fields. This works by directing a circularly polarised laser beam through a glass cell containing the vapour of a particular alkali gas (such as Caesium), which is resonant with the first absorption line of the gas. This will produce a spin alignment that will precess at a frequency (called the Larmor frequency ω_L) proportional to the modulus of an externally applied DC magnetic field, B_0, ($\omega_L = \gamma|B_0|$ where γ is the gyromagnetic ratio of the medium). If the precession is then driven by an applied RF field, B_{rf} (with a frequency of ω_{rf}), then the obsorption coefficient of the alkali medium changes, which will lead to a modulation of the transmitted optical intensity of the emitted light from the vapour cell. In this way, by applying a variable RF field to the cell to determine the Larmor frequency (when $\omega_{rf} = \omega_L$), the applied field B_0 can be calculated.

There are four principal techniques for atomic vapour cells, which are as follows: Coherent Population Trapping (CPT); Nonlinear-Magneto Optical Rotation (NMOR); Spin-Exchange Relaxation Free (SERF) regime; and Mx magnetometer. The CPT method is advantageous because it only uses optical light without applied RF fields. This involves applying two different lasers that have orthogonal polarisations that couple the Zeeman sub-levels in different hyperfine states. When the light is on resonance with the Zeeman levels, there is an observable dimming of light from the absorption into the vapour cell. By measuring the exact wavelength of light needed to be on resonance, the Zeeman splitting of the levels can be determined and hence the applied magnetic field. This method has demonstrated sensitivities of DC magnetic fields in the region of 1 $pT/\sqrt{Hz}$ in an unshielded environment [15]. NMOR is a technique, which involves directing light into the vapour cell, which when resonant with a particular transition inside the atoms produces a non-linear magneto optical rotation. The magnetic field can then be read out in the same fashion described in the previous paragraph, where this rotation produces a precession of the state. The magnetometers operating in the SERF regime are also based on NMOR principle. However, such magnetometers have limited sensitivities due to depolarization caused by various atoms interaction types. The dominant type of these interactions is the spin-exchange collisions that can change the hyperfine state of the atoms while preserving the total angular momentum of the colliding atom pair. This results in a decoherent precession of the atom ensemble in the presence of a magnetic field, which makes the measurement of the Larmor frequency difficult. However, decoherence due to spin-exchange collisions can be completely eliminated if the spin-exchange collisions occur faster than the precession frequency of the atoms. Traditional atomic magnetometers are fundamentally limited by spin-exchange relaxation. When two polarized atoms collide, the electrons can transition into the other hyperfine state and precess in the opposite direction from the bulk of the ensemble, thereby causing decoherence and loss of signal. Spin-exchange relaxation is suppressed if the spin-exchange collisions happen fast enough in a sufficiently low magnetic field. In such a regime, the spins do not have enough time to precess and decohere between collisions. To achieve the required density, potassium droplets are heated in the cell up to 180 °C. To reduce the precession frequency, the measurement cell containing the potassium is shielded from external magnetic fields by a factor of 106 using μ-metal magnetic shields [16]. Mx Vapour cell magnetometers rely on RF fields being driven at the atoms in the cell, then the phase difference between the RF wave and the optical light exciting the atoms can then be used to derive the Larmor frequency and hence the magnetic field applied [18].

CPT and SERF magnetometers are optical devices that usually require zero magnetic field or very low magnetic fields, which can be useful in some applications, where a very high DC field cannot be provided. Unfortunately SERF magnetometers also require very high temperatures and is far more susceptible to environmental noise, but otherwise have the highest sensitivity of the Atomic vapour cell techniques.

The fundamental limit of vapour cell magnetometers is given by their shot-noise limit: $\delta B = 1/\gamma\sqrt{nT_2Vt}$ where n is the density of atoms in the cell, γ is their gyromagnetic ratio, T_2 is the coherence time, V is the cell volume, and t is the total measurement time. The biggest limiting factor in this equation is usually the coherence time which is especially low compared to ion trap magnetometers, which leads to a sensitivity of usually around $\approx 300\ fTcm^{3/2}Hz^{-1/2}$. The fundamental shot noise limit is around $\sim aTcm^{3/2}Hz^{-1/2}$ but in practice this is almost always dominated by technical or environmental noise.

The bandwidth of these magnetometers is limited by the width of the resonance line, which decreases with the increased size of the cell. This means that as you reduce the bandwidth of the sensor you must increase the size of the cell and hence increase the noise. Therefore you cannot improve the signal to noise ratio in this way. Typically Mx magnetometers have demonstrated sensitivities of $6pT\sqrt{Hz}$ with a bandwidth of around 1 kHz; with SERF's it can provide $6fT\sqrt{Hz}$ with 200 Hz bandwidth. These magnetometers generally only operate in the DC regime and frequencies below 100 Hz as their sensitivity drops proportionally to $1/f$, where f is the operating frequency [17].

The dynamic range of these Mx mode detectors is around 500 nT for a cell with an internal size of 1 mm, which is determined by the resonance linewidth as with the other sensors. It is possible in principle to increase this, but would be difficult due to the high fields producing non-linear drive frequencies, with a large range. [18]

The SERF magnetometers use Helmholtz coils instead of shielding to maintain a constant magnetic field strength at the cell. This means that the system can be made more portable without bulky shielding, but is inherently less sensitive due to the noise produced by the DC from the coils. The coils are also tuned to the

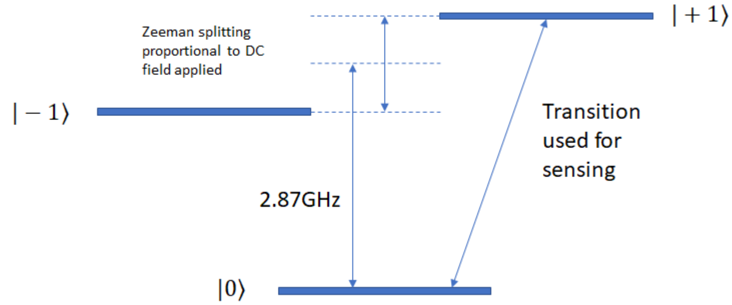

Figure 1: Diagram showing the $^3A_2$ ground state manifold showing the $m_s = 0$ ground state $|0\rangle$ and the two degenerate $m_s \pm 1$ $|{+1}\rangle$ and $|{-1}\rangle$.

magnetometer itself to cancel out ambient fields to remain in the spin-exchange suppression regime.

1.1.3 NV-Centres

N-V centre magnetometers consist of a single nitrogen atom placed in a diamond lattice as a substitute for a carbon atom and its nearest-neighbour vacancy. This produces two charge states at the vacancy: a neutral N-V^0 and the negatively charged version N-V$^-$, which is the state that is used for sensing.

This negatively charged state creates a spin triplet in the orbital ground state $^3A_2$, shown in figure 1. This consists of the $m_s = 0$ then two degenerate $m_s \pm 1$ states separated by 2.87 GHz. This splitting is defined by the quantisation axis of the N-V defect corresponding to the axis joining the nitrogen and the vacancy. This means that the Zeeman splitting of the $m_s \pm 1$ (The $|{+1}\rangle$ and $|{-1}\rangle$ states) is directly proportional to the DC field applied along the N-V axis of the centre.

This Zeeman splitting can be used to measure DC and AC magnetic fields by isolating a spin-1/2 system between the $|0\rangle$ and $|{+1}\rangle$ and sensing using this transition. This offers a great DC and low RF sensor for ambient conditions at room temperature, but is less effective in noisy unshielded environments.

To measure DC fields a Ramsey technique is used in many quantum sensors [19]. This involves preparing the system in the ground state $|0\rangle$, before applying a $\pi/2$ pulse to put the system in a 50/50 superposition state: $\frac{1}{\sqrt{2}}(|0\rangle + |1\rangle)$. The system is then allowed to precess over a free evolution time τ, which means that the system will accumulate a phase ϕ over that time to produce the state: $\frac{1}{\sqrt{2}}(|0\rangle + e^{i\phi}|1\rangle)$ where the phase is given by: $\phi = g\mu_B B_z \tau/\hbar$ where g is the coupling constant; μ_B is the permeability of the media; B_z is the magnetic field strength along the vacancy axis and $\hbar$ is the reduced Planck's constant. A second $\pi/2$ pulse is applied to go to the measurement basis. This then produces a probability distribution between the two states: $\sin\left(\frac{\phi}{2}\right)|0\rangle + \cos\left(\frac{\phi}{2}\right)|1\rangle$. The state can be measured by applying laser and checking for fluorescence. The sensitivity of this system is proportional to the free evolution time τ, but it is limited by the amount of time that the system can be left to precess before it interacts with the neighbouring carbon atoms causing decoherence. The average time it takes before this happens is called the coherence time T_2^* and the optimum free evolution time is τ T_2^*. This leads to a magnetic field strength sensitivity of:

$$\delta B_{DC} \approx \frac{\hbar}{g\mu_B C\sqrt{T_2^*}} \tag{1}$$

Where $1/C = \sqrt{1 + 2(\alpha_0 + \alpha_1)/(\alpha_0 - \alpha_1)^2}$ and $\alpha_m \approx (t_m\gamma)\eta_m$ which represents the number of photons collected where η_m is the collection efficiency and have a radiative decay of $\gamma = 15\ MHz$ with a total measurement time of t_m.

NV-centres can also be used to measure low frequency RF magnetic fields. This requires the measurement of an oscillating magnetic field $B(t) = B_{AC} \sin(\omega_{AC} t + \phi)$, where the free evolution time of the experiment τ is matched to the period of the oscillations of the magnetic fields $\tau = \tau_{AC} = 2\pi/\omega_{AC}$. The phase is chosen so that the nodes of the incoming field coincide with the MW π pulses. The sensitivity of this technique is given by: [19]

$$\delta B_{AC} \approx \frac{\pi\hbar}{2g\mu_B C\sqrt{T_2}} \tag{2}$$

The T_2 coherence time is extended by using the spin echo technique to: $T_2 \to T_2 n^s$ [20] Where n is the number of decoupling pulses and s relates to the purity of the sample and the prevalence of ^{13}C. For example with no ^{13}C in the crystal this results in an s value of $s = 0.37$. This also increases the measurement time to: $\tau_{AC} \to \frac{n}{2}\tau_{AC}$.

This means that for optimum sensitivity you must sense fields near: $\omega_{AC} = 2\pi/\tau_{AC}\ 1/T_2$. This means this technique can only be used optimally for short frequencies (~kHz). This can be overcome by applying very short echo pulses, which would increase the sensitivity at the cost of losing bandwidth.

1.1.4 Persistent Current Qubit

This system uses superconducting material similar to a SQUID but uses a single atom of superconducting material to produce a two-level system to sense DC and RF fields in a similar manner to N-V-centres or atomic vapour cells [21]. This method has a very high coupling to magnetic fields along with a relatively long coherence time producing impressive sensitivities of 3.3 $pT/\sqrt{Hz}$ even up to 10 MHz frequency. The downside to this magnetometer is that it can only operate at 43 mK, but otherwise compares favourably with other quantum magnetometers.

1.1.5 BEC-Atomic Magnetometer

This magnetometer involves trapping a string of cold Rubidium atoms in an optical trap and spin polarising the atoms. Observing its evolution over time you can ascertain the magnetic field strength along the ensemble. The advantage of having a string of atoms is that you can measure fields at each atom giving a spatial resolution of around $50\mu m$ along with sensitivities of $\approx 10\ pT/\sqrt{Hz}$. [22]

2 Theory of trapping and sensing using Yb ions

To properly appreciate the results of the experiments we have undertaken, this section will detail the underlying theory of ion trapping as well as the energy structure of ytterbium and how its internal state is manipulated in our experiments to sense RF and microwave fields.

2.1 Ion trapping

To conduct any sensing experiments using ions, they must first be trapped and cooled to a degree where coherent state manipulation can be carried out. There are several known options that can achieve this including optical tweezers [48], Penning traps [49] and Paul traps [50] among many others [51]. The two main ion trapping technologies are Penning and Paul traps, which both use electrostatic fields to trap ions. These techniques are relatively simple to construct and provide high trap depths [51]. In this section I will provide a summary of these techniques and expand on the 2-D Paul traps that are used in my experiment and the theoretical underpinnings of these traps. Much of the theory detailed in this section is based on the simulations and theoretical work completed by fellow PhD student Dr. Ethan Potter [39] and post-doctoral fellow Dr. Altaf Nizamani.

2.1.1 Penning and Paul trap basics

Penning traps and Paul traps both use electric fields to confine ions, but Penning traps use magnetic fields applied along the trap axis to trap the ions radially (with a Lorentz force) while the DC electrodes provide trapping axially. This allows for trapping in all three dimensions of space, a diagram showing a basic Penning trap is shown in figure 2. The trapped-ion cloud can be compressed by using a segmented DC electrode on an end-cap to apply a rotating electric field, which can apply a torque to the trapped particles causing them to contract [69]. However, it is not ideal for quantum sensing with trapped-ions due to the fact that these traps require very large magnetic fields (on the order of 1 T). Penning traps also usually require cumbersome superconducting magnets, which are wrapped around the trapping chamber and have to be kept at cryogenic temperatures. It is of course not ideal for a miniaturised system that would be used commercially. The high magnetic field strengths could also be a problem using our sensing scheme shown in section 2.3.1, which relies on tuning to a certain frequency by changing the Zeeman splitting of the state we are using to sense. Applying a 1 T magnetic field would therefore render it impossible to use the first order Zeeman splitting due to subsequent Zeeman splitting orders arising from high magnetic field.

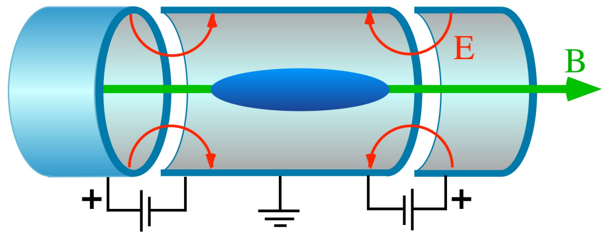

Figure 2: Diagram of a basic Penning trap with strong DC magnetic fields to confine the ions radially and DC end-caps trap the ions along the axis of the trap. Public domain image by Dhdpla.

To avoid using powerful magnetic magnetic fields for trapping, the obvious solution is to use electric fields exclusively, i.e. a Paul trap [50]. This trap encounters a problem however due to Gauss's law, which states that the curl of the electric field $E(z)$ in free space is always equal to zero: $\nabla \cdot E(z) = 0$, which can be expressed by the electric field potential $\phi(z)$: $E(z) = \nabla \cdot \phi(z)$, which together with the previous equation gives: $\nabla^2\phi(z) = 0$. This is the Laplace equation stated by Earnshaw's theorem [52]. As the electrostatic force, F, applied to a charged particle is defined by: $F = \nabla\phi$, which we can plug into Laplace's equation to give: $\nabla^2\phi = \nabla \cdot (\nabla\phi) = \nabla \cdot F = 0$. Hence there is no point in free space where there is an electrostatic nil, so no charged particle can ever be in equilibrium.

Earnshaw's theorem states crucially that a particle cannot be trapped at a certain point in time, but does not state that it cannot be trapped over a certain amount of time. This is exploited in the Paul trap by applying a trapping potential along a certain axis while ejecting it along the perpendicular axis, then before the ion is accelerated from the trap centre the electrode potentials are inverted to trap along the perpendicular axis and eject along the previously trapping axis. This means averaged over time there is a 'pseudo-potential' which produces an effective electrostatic nil at the centre of the trap. The canonical geometry of the Paul trap, uses four electrodes applying perpendicular electric fields, alternating 180 degrees out of phase, at an RF frequency. This traps the ion in two dimensions and is trapped in the third using two DC potential end caps. A diagram showing a simple quadrupole trap can be found in figure 3.

2.1.2 Pseudo-potential and secular frequency calculations

As detailed in the previous section, most Paul traps [53, 54, 55] involve two dimensional RF trapping with the DC potentials in the remaining dimension, as is the case with the 2-dimensional surface traps used on this project. In this section I will detail how the resulting pseudo-potential is calculated analytically and give a description of the resulting secular motion of the ion due to the dynamic nature of the applied fields. This knowledge is used to optimise trap voltages and maximise trap depths [53].

First, we use the one dimensional case where the electric field, $E(x,t)$, has a time t dependence of $\cos(\Omega t)$ where Ω is the frequency of the applied trapping RF. For an ion with a charge e and a mass of m, the electrostatic force it experiences is given by $F = -eE$. Combining this with $E(x,t) = E_0(x)\cos(\Omega t)$, where $E_0(x)$ is the electric field amplitude, we can retrieve the equation of motion for the system.:

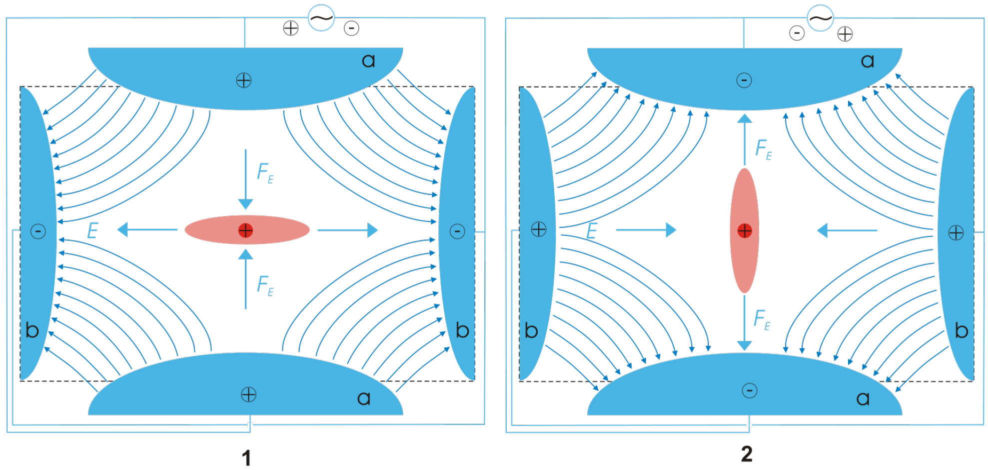

Figure 3: Diagram of a Quadrupole ion trap showing the forces exerted on the ion by the opposing electrodes generating electric fields to trap the ion along one axis at a certain time and eject it in another before flipping to an opposing direction to trap and eject in a perpendicular direction. There are two DC end caps one above and one below. Public domain image by .

$$m\frac{d^2x}{dt^2} = -eE_0(x)\cos(\Omega t). \tag{3}$$

This can be solved for the ion position given an initial position of x_0:

$$x(t) = \frac{e}{m\Omega^2}E_0(x)\cos(\Omega t) + x_0. \tag{4}$$

Equation 4 tells us that the motion is homogeneous and simple, meaning that the average force applied to the ion over all time will be zero so the ion will tend to stay trapped near the nil position. This is not quite the case near the centre of the trap as there is in fact a slight inhomogeneity from the electric field $E(x)$ around this position. It is this inhomogeneity that produces the secular motion in the ion. The analytical calculations can be determined by Taylor expanding the equation $E(x)$ around $x \approx x_0$:

$$E(x) = E(x_0) + \frac{\partial E(x)}{\partial x}(x - x_0) + O. \tag{5}$$

Where O is denoting higher terms, which can be ignored as they are negligible in our case and we can now plug in $F = -eE$ to give:

$$F(x) \approx -eE(x_0)\cos(\Omega t) - \frac{\partial E(x_0)}{\partial x}\frac{e^2}{m\Omega^2}E(x_0)\cos^2(\Omega t). \tag{6}$$

Averaged over a period we find that: $\langle\cos(\Omega t)\rangle = 0$ and $\langle\cos^2(\Omega t)\rangle = 1/2$, the resulting averaged force is:

$$\langle F(x)\rangle \approx -\frac{\partial E(x_0)}{\partial x}\frac{e^2}{m\Omega^2}E(x_0) = -e\frac{\partial\Psi(x_0)}{\partial x}. \tag{7}$$

The pseudo-potential $\Psi(x)$ is expressed by:

$$\Psi(x_0) = \frac{e}{4m\Omega^2} E^2(x_0). \tag{8}$$

When simulating how the trap behaves given an arbitrary electrode geometry it can be useful to express these equations in terms of all three spacial dimensions:

$$\Psi(x, y, z) = \frac{e}{4m\Omega^2} |\vec{E}(x, y, z)|^2. \tag{9}$$

$$\langle \vec{F}(x, y, z) \rangle = -e\nabla \cdot \Psi(x, y, z). \tag{10}$$

To solve these equations we can use the general expression for an applied electric RF potential generated by the electrodes:

$$\phi_{RF}(x, y, z, t) = \eta_{RF} V_{RF} \left(\frac{\alpha x^2 + \beta y^2 + \gamma z^2}{2r_0^2} \right) \cos(\Omega t). \tag{11}$$

Where r_0 is the is the distance between the RF rails and the trap centre; η_{RF} is a geometrical factor relating to the geometry of the RF electrodes which is equal to one when their shape is hyperbolic and decreases as the electrodes deviate from that shape [56]; α, β and γ are constants related to the RF rail geometries for the three dimensions [57]. For a linear trap like the one shown in figure 3 (which in this case is also analogous to the 2-D traps used in the experiment), the RF applies potentials in two perpendicular dimensions and nothing in the third. This results in: $\beta = -\gamma = 1$ and $\alpha = 0$, which can be substituted into equation 12 to give the RF potential for this geometry:

$$\phi_{RF}(y, z, t) = \eta_{RF} V_{RF} \left(\frac{y^2 - z^2}{2r_0^2} \right) \cos(\Omega t) \tag{12}$$

We can then take the spatial gradient of equation 12 to give the electric field vector:

$$\begin{aligned} \vec{E}(y, z, t) &= -\nabla \cdot \phi_{RF}(y, z, t) \\ &= -\frac{\eta_{RF} V_{RF}}{r_0^2} \cos(\Omega t)(y - z) \\ &= -\vec{E}(y, z) \cos(\Omega t). \end{aligned} \tag{13}$$

To get an expression for the pseudo-potential, we can substitute the spatial component of the electric field $\vec{E}(y, z)$ into equation 9:

$$\Psi(y, z) = \left(\frac{e}{4m\Omega^2 \frac{\eta_{RF}^2 V_{RF}^2}{r_0^4} (y^2 + z^2)} \right). \tag{14}$$

By examining this equation one can see the distinctive rotational saddle potential producing a bowl-like potential indicative of Paul traps described earlier. To ascertain the secular motion of the ion, we can average the force applied to the ion in this system:

$$
\begin{aligned}
\langle \vec{F}(y,z) \rangle &= -e\nabla \cdot \Psi(y,z) \\
&= -e\nabla \cdot \left(\frac{e}{4m\Omega^2(y^2+z^2)} \frac{\eta_{RF}^2 V_{RF}^2}{r_0^4} \right) \\
&= -\frac{e^2\eta_{RF}^2 V_{RF}^2}{2m^2\Omega^2 r_0^4}(x+y).
\end{aligned} \tag{15}
$$

The force experienced by the ion in the two dimensions acted on by the RF is described by equation 15. Hence the secular frequency of this system in the radial as well as y and z dimensions is:

$$
\omega_r = \omega_y = \omega_z = \frac{e\eta_{RF} V_{RF}}{2m\Omega r_0^2}. \tag{16}
$$

In a real trap any slight deviation from the optimum trap geometries will result in different secular frequencies from those described in equation 16.

Now that we have found the secular frequency induced by the RF electrodes, we can move onto the motion produced by DC end caps, which is applied along the x axis. The solution for the potential induced by this field is:

$$
\phi_{DC}(x,t) = \eta_{DC} V_{DC} \left(\frac{2x^2 - (y^2+z^2)}{2x_0^2} \right). \tag{17}
$$

Where x_0 is the distance between the centre of the trap and the DC electrodes and η_{DC} is a geometric factor given by the shape and placement DC end caps, which is equal to one for hyperbolic shaped electrodes. Otherwise the factor is less as the geometries deviate from hyperbolic as well as contributions from the geometry offset of the RF electrodes [58]. Using the same procedure as in the RF case the secular motion in the x direction due to the DC end caps is:

$$
\omega_x = \frac{\sqrt{2}e\eta_{DC} V_{DC}}{m x_0^2}. \tag{18}
$$

2.1.3 Trap parameters

Now to ascertain what the parameters we need when simulating our trap as well as making an estimate of the micro-motion, which is an intrinsic motion of the ion produced by interactions between the RF and DC fields. This motion is mostly confined to the y-z plane due to this being the plane that is acted upon by the RF. The following trapping parameters are calculated in relation to desirable stable ion trajectories by equating the ion motion to a set of Mathieu equations [59]. First we should combine the DC and RF potentials given by equations 17 and 12 respectively to produce an overall potential equation for the entire system:

$$
\Phi(x,y,z,t) = \eta_{RF} V_{RF} \left(\frac{y^2 - z^2}{2r_0^2} \right) \cos(\Omega t) + \eta_{DC} V_{DC} \left(\frac{2x^2 - (y^2+z^2)}{2x_0^2} \right) \tag{19}
$$

If we assume that the ion motion is uncoupled between the three spatial dimensions, we can equate the equations of motion for in the y and z planes, which results in:

$$\frac{d^2y}{dt^2} = -\frac{e}{m}\left(\frac{\eta_{RF}V_{RF}}{r_0^2}\cos(\Omega t) - \frac{\eta_{DC}V_{DC}}{x_0^2}\right)y \tag{20}$$

$$\frac{d^2z}{dt^2} = \frac{e}{m}\left(\frac{\eta_{RF}V_{RF}}{r_0^2}\cos(\Omega t) - \frac{\eta_{DC}V_{DC}}{x_0^2}\right)z. \tag{21}$$

These equations can be put into a Mathieu differential equation by making the following substitutions:

$$\Omega t = 2\zeta, \tag{22}$$

$$q_z = -q_y = \frac{2\sqrt{2}\omega_r}{\Omega} = \frac{2e\eta_{RF}V_{RF}}{m\Omega^2 r_0^2}, \tag{23}$$

$$a_z = -a_y = -\frac{4e\eta_{DC}V_{DC}}{m\Omega^2 x_0^2}. \tag{24}$$

This gives the following Mathieu equation:

$$\frac{d^2 i}{d\zeta^2} + (a_i - 2q_i\cos(2\zeta))i = 0. \tag{25}$$

Where $i = [y, z]$. This equation can have an infinite number of solutions, although only periodic solutions will create a stable trap. To find these solutions the Floquet theorem [59] is used to determine the solutions for x and y. For a linear trap $a_i < q_i^2 \ll 1$ and the numerical solutions are calculated by Wineland et al. [54] The solution gives a region of stability for a and q values that is very useful in the design and voltage optimisation of our chips.

One of these solutions arises when $a_i = 0$ and $q_i^2 \ll 1$, which is a common set of parameters when the DC voltage is zero at the trap position. The resulting ion motion along the z axis is calculated by Hughes et al. [53] and is given by:

$$z(t) = \left(1 + \frac{q_z}{2}\cos(\Omega t)\right) z_0\cos(\omega_z t). \tag{26}$$

We can use the substitutions made earlier for the q values for the Mathieu equation 24, which gives:

$$z(t) = \left(1 + \frac{\sqrt{2}\omega_z}{\Omega}\cos(\Omega t)\right) z_0\cos(\omega_z t). \tag{27}$$

Equation 27 gives insight into the motion of the ion in this system as there are two driving factors: one is the secular motion ω_z, which is the inherent motion of the ion in a potential well; and the micro-motion which is produced by the oscillating electric fields from the RF at a frequency Ω. From the derived solutions for the Mathieu equation [54], we know that when $q = \frac{2\sqrt{2}\omega_z}{\Omega} < 0.9$ the ion should remain trapped.

These parameters are invaluable when simulating what DC voltages are needed to maximise the trap depth and reduce heating from micro-motion and secular motion.

2.2 Laser ionisation, Doppler cooling and ytterbium energy manifold

The IQT group that I am a part of have focused very strongly on trapping ytterbium (Yb) ions for both quantum sensing and quantum computing applications. There are seven stable isotopes of Yb to choose from: ^{168}Yb, ^{170}Yb, ^{171}Yb, ^{172}Yb, ^{173}Yb, ^{174}Yb and ^{176}Yb. Of these we use $^{171}Yb^{+}$ as it is the only one of these isotopes that has a total nuclear spin of 1/2. Having a non-zero spin means that its energy structure contains hyperfine states whose splitting can be modulated using an applied B-field [3], which allows us to tune our sensor to a given RF or microwave frequency for detection. Many of these isotopes also have higher nuclear spins, but these produce more complex hyperfine states that are harder to address and control coherently. It is also useful to trap $^{174}Yb^{+}$, which has no nuclear spin, making it relatively simple to trap, as microwaves are not required to cool the ion unlike $^{171}Yb^{+}$. This is useful for setting the initial trapping parameters and voltages for the trap before moving on to $^{171}Yb^{+}$ trapping. The following section will give details of the $^{171}Yb^{+}$ and $^{174}Yb^{+}$ energy manifolds and how they are used for ionisation, Doppler cooling and coherent experimentation.

2.2.1 Ionisation

For ^{171}Yb or ^{174}Yb to be trapped in a Paul trap they must be ionised by removing the outermost electron in their electronic structure. First they are emitted from one of two atomic ovens, whose design is described in section 3.1.3. One oven contains natural Yb, which contains both ^{171}Yb and ^{174}Yb along with the other five naturally occurring isotopes[1]. The other oven contains Yb that has been enriched to contain over 95% ^{171}Yb.

When trapping runs are initiated one of these ovens is heated, which produces a flux of neutral Yb atoms, which is directed towards the expected trapping region of the chip. At the trapping region above the chip two laser beams are directed 90^{o} perpendicular to the oven: 399 nm and 369 nm. The 399 nm laser excites any neutral Yb atom's outermost electron in its beam path from its ground state $^{1}S_0$ to the $^{1}P_1$ where it is then ejected into the continuum using a 369 nm beam leaving a positively charged ion. This interaction can be seen graphically in figure 4.

The exact wavelengths used for ^{171}Yb or ^{174}Yb ionisation for the 399 nm laser does differ slightly between isotopes as shown in table 1. The exact wavelengths used can also differ significantly depending on the orientation of the ovens in relation to the laser. These effects are due to a Doppler shift and can be calculated by using [60].

2.2.2 Doppler cooling

Once the ions are ionised and trapped above the surface of the chip, they require any superfluous kinetic energy to be removed. This is because 'hot' ions cannot crystallise and cannot be addressed coherently. They can also be heated further due to interactions with lasers and collisions with atoms, risking the ion overcoming the trap depth and escaping.

To cool the ion we use Doppler cooling, which involves shining a laser that is slightly detuned from a certain transition. This is so that when the ion is moving towards the beam source, it is more likely to absorb a photon and then emit one in a random direction. This leads to a net force towards the centre of the trap and

[1] 14.3% 171Yb, 31.8% 174Yb, 53.9% other.

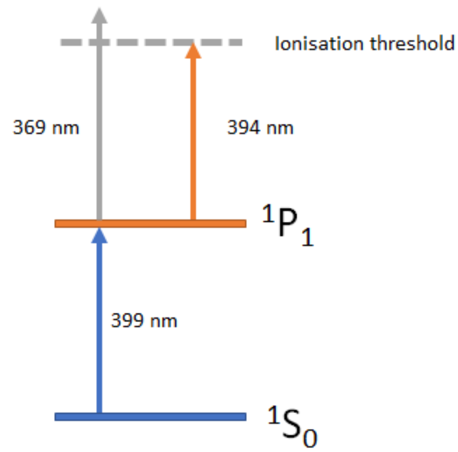

Figure 4: Diagram of the energy levels used to ionise both ^{171}Yb and ^{174}Yb, where a 399 nm laser beam is used to excite the outer most electron of the atom from a ground $^1S_0$ state to the $^1P_1$ state before being excited into the continuum by a 369 nm beam.

a reduction in the ions speed and hence kinetic energy and temperature.

The cooling cycle we chose for $^{174}Yb^+$ is given in figure 5. It uses an off-resonant 369 nm laser to drive the transition $^2S_{1/2} \leftrightarrow {}^2P_{1/2}$, which is used to Doppler cool the ion. Unfortunately once the ion has transitioned to the $^2P_{1/2}$ state, there is a small (0.5%) chance that the ion will decay into the $^2D_{3/2}$ state. Over time the ion will eventually escape the cooling cycle and will continue to heat. This is remedied by applying a 935 nm laser resonant with the transition $^3[3/2]_{1/2}$ state, where it can decay into the $^2S_{1/2}$ state and back into the cooling cycle. Additionally there is a small chance that the ion may collide with an air molecule in the vacuum chamber and cause a $^2D_{3/2} \rightarrow {}^2D_{5/2}$ transition. The state can then decay to the $^2F_{7/2}$ state; where a 638 nm laser can pump it to $^1[5/2]_{5/2}$, where it can freely decay back to $^2D_{3/2}$ and back into the cooling cycle. In our case we did not employ the 638 nm laser for our cooling cycle because the chances of the $^2D_{3/2} \rightarrow {}^2D_{5/2}$ state occurring is roughly once a day [35]. This seems to be acceptable for us as we want to simplify our system as much as possible, so the addition of another laser is quite an unnecessary burden.

The cooling of $^{171}Yb^+$ is slightly more complicated due to the additional 1/2 nuclear spin of the ion, which includes the addition of hyperfine states detailed in figure 6. The cooling cycle for $^{171}Yb^+$ remains quite unchanged from that of $^{174}Yb^+$ other than the fact that the 935 nm (and 638 nm if one wishes to use it) must be power broadened to cover all of the hyperfine states. There is a chance that the state may decay from $^3[3/2]_{1/2}\,|F=1\rangle$ to $^2S_{1/2}\,|F=0\rangle$, which can be put back into the cooling cycle using a 12.64 GHz microwave source to transition $^2S_{1/2}\,|F=0\rangle \leftrightarrow {}^2S_{1/2}\,|F=1\rangle$ [61]. This addition of a microwave source is why trapping $^{171}Yb^+$ is significantly more difficult than trapping $^{174}Yb^+$, which does not require any microwaves.

2.2.3 $^{171}Yb^+$ $^2S_{1/2}$ ground state manifold

The states used for all sensing experiments were within the $^2S_{1/2}$ ground state manifold, which is shown in figure 7. It is made up of four principal states: The ground state: $|0\rangle$ ($F=0$, $m_f=0$) and as well as the three hyperfine states: $|0'\rangle$($F=1$, $m_f=0$), $|+1\rangle$ ($F=1$, $m_f=+1$) and $|-1\rangle$($F=1$, $m_f=-1$). The hyperfine states are generated due to $^{171}Yb^+$'s 1/2 nuclear spin and hence their splitting is influenced by an applied B-field.

Ion isotope	Ionisation beam wavelength (nm)	Detection and cooling beam wavelength (nm)	Re-pumping beam wavelength(nm)
$^{174}Yb^{+}$	398.91127	369.52504	935.17976
$^{171}Yb^{+}$	399.91067	369.52604	935.18768

Table 1: Table displaying the resonant wavelengths of the 369 nm, 399 nm and 935 nm, measured on our system for both $^{174}Yb^{+}$ and $^{171}Yb^{+}$

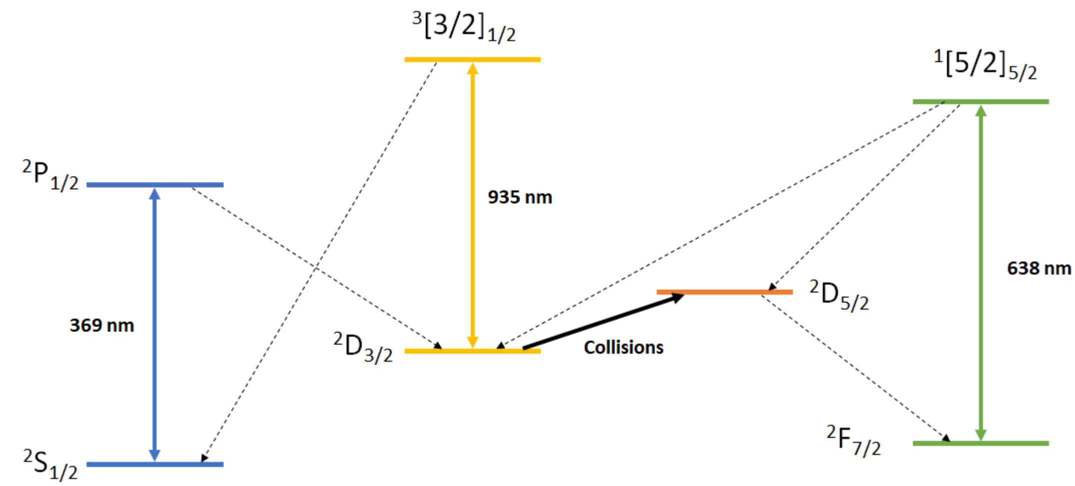

Figure 5: Diagram of the energy levels involved in the $^{174}Yb^{+}$ cooling cycle. Doppler cooling is carried out by driving the transitions betwen $^{2}S_{1/2}$ and $^{2}P_{1/2}$ using an detuned 369 nm beam. The electron can decay from $^{2}P_{1/2}$ to $^{2}D_{3/2}$, so a 935 nm repumping laser is used to drive the state to $^{3}[3/2]_{1/2}$ so it can decay back into the cooling cycle. There can also be collisions that cause a transition from $^{2}D_{3/2}$ to $^{2}D_{5/2}$, which can decay to the $^{2}F_{7/2}$ state. An additional 638 nm laser can be employed to transition the ion to the $^{1}[5/2]_{5/2}$ state where it can decay back into the cooling loop.

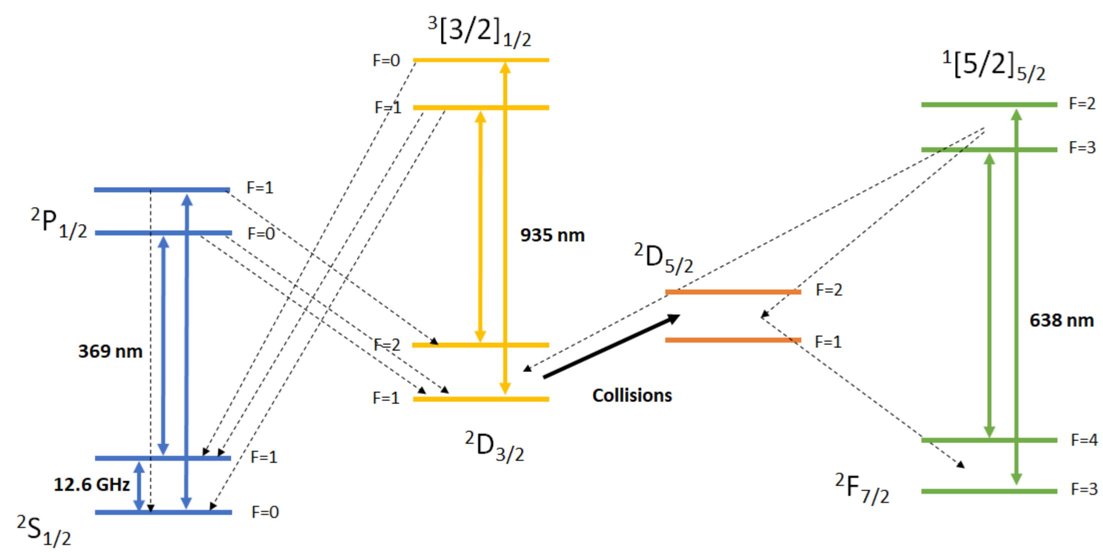

Figure 6: Diagram of the energy levels involved in the $^{171}Yb^{+}$ cooling cycle. Very similar to the cooling cycle of $^{174}Yb^{+}$ as shown in figure 5, but also includes a 12.64 GHz source to keep the ion in the cooling cycle when states decay into the $|F=0\rangle^{2}S_{1/2}$ ground state. The 935 nm and 638 nm lasers must also be power broadened so they can transition the ion between their different hyperfine states.

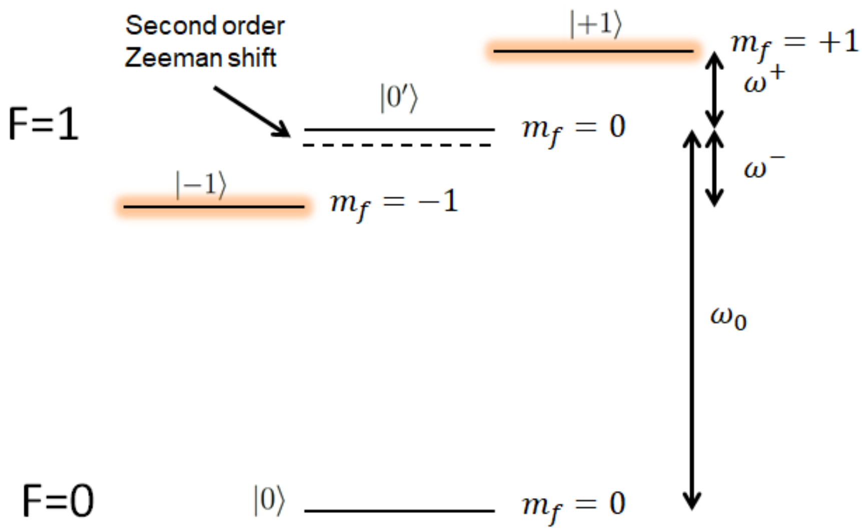

Figure 7: The hyperfine ${}^2S_{1/2}$ manifold for ${}^{171}Yb^+$, which contains four states: the $|F=0\rangle$ ground state denoted $|0\rangle$; the $|F=1\rangle$, $m_f=0$ state denoted $|0'\rangle$; and the two hyperfine states with $|F=1\rangle$ with $m_f=+1$ and $m_f=-1$, which are denoted $|+1\rangle$ and $|-1\rangle$ respectively.

When no magnetic field is applied to the system the $|-1\rangle$ and $|+1\rangle$ states are degenerate with the $|0'\rangle$ state and its splitting with the ground state $|0\rangle$ is called the 'clock' transition, which has a transition frequency of $\omega_{hf} = 2\pi \times 12.6428121$ GHz [61]. Once a DC B-field is applied to the ion the $|-1\rangle$ and $|+1\rangle$ states begin to split and the $|0'\rangle \leftrightarrow |0\rangle$ splitting will increase due to second order Zeeman splitting. The magnitude of these changes is calculated using the Breit-Rabi formula [62]: (The following calculations are based closely on the calculations by my colleague Dr. Joseph Randall in his thesis [63])

$$\begin{aligned} \omega_+ &= \frac{\omega_{hf}}{2}(1+\chi-\sqrt{1+\chi^2}), \\ \omega_- &= -\frac{\omega_{hf}}{2}(1-\chi-\sqrt{1+\chi^2}), \\ \omega_0 &= \omega_{hf}\sqrt{1+\chi^2}. \end{aligned} \tag{28}$$

Where ω_+ is the $|+\rangle \leftrightarrow |0'\rangle$ transition splitting; ω_- is the $|-\rangle \leftrightarrow |0'\rangle$ transition splitting and ω_0 is the $|0\rangle \leftrightarrow |0'\rangle$ clock transition splitting produced by second order Zeeman effects and:

$$\chi = (g_J - g_I)\frac{\mu_B B}{\hbar\omega_{hf}} \tag{29}$$

Where B is the applied magnetic field strength; μ_B is the Bohr magneton; g_I is the nuclear spin g-factor, which is ignored in this case because it is negligible compared to the electron spin g-factor g_J, which is $g_J \approx 2$. These splittings are important as they are the states used to sense both RF and microwaves, which can be tuned with an applied B-field. Graphs showing how these splittings change with the applied B-field are shown in figure 8.

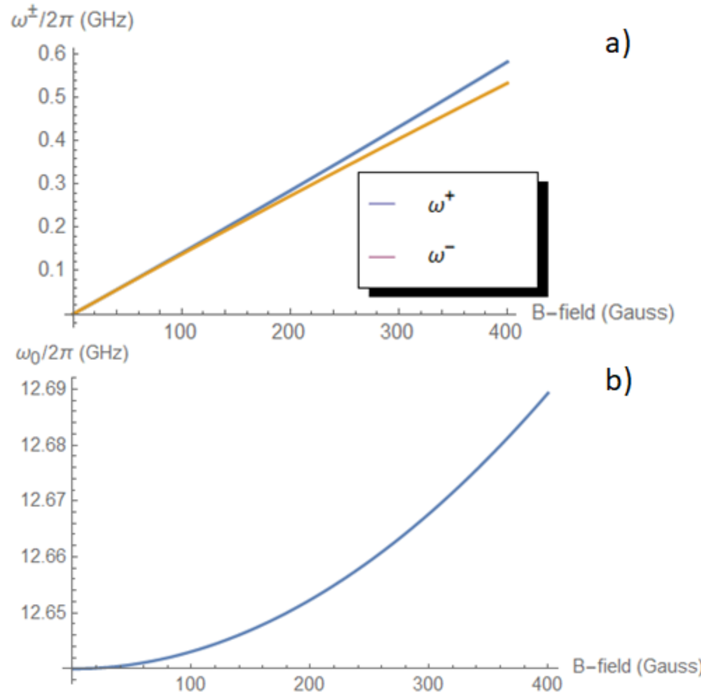

Figure 8: a) Graph showing how the energy splitting for the two hyperfine states between them and the $|0'\rangle$ state, changes with applied B-field to give the tuneability of this sensor. b) This shows how the splitting between the $|0\rangle$ and the $|0'\rangle$ state changes with the applied B-field, this effect is due to the second order splitting.

2.3 RF and microwave sensing using dressed states

2.3.1 Basis for RF and microwave sensing using trapped-ions

Fundamentally our quantum sensor detects oscillating magnetic waves by measuring how quickly they can drive a transition between two arbitrary quantum states. The sensing procedure described herein is derived from the work of Baumgart et al. [3] and the work of Dr. Joseph Randall [63] and will be summarised here. The two states that are used for sensing can be denoted by: $|\downarrow\rangle \equiv (0,1)^T$ and $|\uparrow\rangle \equiv (1,0)^T$, with the zero point energy half way between these two states. The Hamiltonian of this two state system is given by:

$$H_0 = \frac{\hbar\omega_0}{2}\left(|\uparrow\rangle\langle\uparrow| - |\downarrow\rangle\langle\downarrow|\right) \tag{30}$$

Where ω_0 is the transition frequency. As mentioned in the previous section, hyperfine states are utilised for our sensing experiments so the state is only coupled via magnetic dipole coupling to the electromagnetic radiation we wish to sense, with no interaction with the electric dipole. The total Hamiltonian of the system with an applied field is: $H = H_0 + H_I$ where H_I is given by:

$$H_I = -\vec{\mu}\cdot\vec{B}. \tag{31}$$

Where $\vec{\mu}$ is the magnetic moment and $\vec{B}$ is the applied magnetic field. The magnetic field can be expressed as:

$$\vec{B} = \vec{B}_0 \cos\left(\omega t - \vec{k}\cdot\vec{r} - \phi\right) \tag{32}$$

Where $\vec{B}_0$ is the amplitude of the magnetic field; $\vec{k}$ is the wavevector; $\vec{r}$ is the ion position; ω is the frequency of the applied field; ϕ is the phase of the wave and t is the time. The magnetic dipole approximation can be used to find $\vec{k}\cdot\vec{r}\approx 0$ due to the fact that RF and microwave wavelengths are generally many orders of magnitude greater than the ion's wavefunction. Now if we substitute equation 32 into the Hamiltonian for the system we retrieve:

$$\begin{aligned} H_I &= -\left(\langle\downarrow|\vec{\mu}\cdot\vec{B}_0|\uparrow\rangle|\downarrow\rangle\langle\uparrow| + \langle\uparrow|\vec{\mu}\cdot\vec{B}_0|\downarrow\rangle|\uparrow\rangle\langle\downarrow|\right)\cos(\omega t-\phi), \\ &= \hbar\Omega_0\left(|\uparrow\rangle\langle\downarrow| + |\downarrow\rangle\langle\uparrow|\right)\cos(\omega t-\phi). \end{aligned} \tag{33}$$

Where $\Omega_0 = \langle\downarrow|\vec{\mu}\cdot\vec{B}_0|\uparrow\rangle/\hbar = \langle\uparrow|\vec{\mu}\cdot\vec{B}_0|\downarrow\rangle/\hbar$ is the Rabi frequency, which describes the rate at which the ion transitions from the $|\downarrow\rangle$ state to the $|\uparrow\rangle$. Now it is useful to move to the interaction picture with respect to H_0 where $H\rightarrow H' = e^{iH_0t/\hbar}(H-H_0)e^{-iH_0t/\hbar}$, which gives:

$$H' = \frac{\hbar\Omega}{2}\left(|\uparrow\rangle\langle\downarrow|e^{i\omega_0 t} + |\downarrow\rangle\langle\uparrow|e^{-i\omega_0 t}\right)\left(e^{i\omega t}e^{-i\phi} + e^{-i\omega t}e^{i\phi}\right). \tag{34}$$

When the applied frequency ω is close to the resonant frequency ω_0 then this equation produces four terms. Two of these are slowly rotating with the detuning frequency: $\delta = \omega - \omega_0$ and two terms that rotate much faster at the rate: $\omega + \omega_0$. The rotating wave approximation can now be used, which assumes that: $\Omega_0 \ll \omega_0$, that allows for the faster rotating terms to be ignored going forward, to produce:

$$H' = \frac{\hbar\Omega}{2}\left(|\uparrow\rangle\langle\downarrow|e^{-i\delta t}e^{i\phi} + |\downarrow\rangle\langle\uparrow|e^{i\delta t}e^{-i\phi}\right) \tag{35}$$

Now we can use the Schrödinger equation: $i\hbar\frac{\partial}{\partial t}|\psi(t)\rangle = H'|\psi(t)\rangle$ to solve for an arbitrary spin state: $|\psi(t)\rangle = c_\downarrow(t)|\downarrow\rangle + c_\uparrow(t)|\uparrow\rangle$. From this, one can extract the unitary operator capable of describing how the state population changes through time. The Schrödinger equation can be solved with:

$$\dot{c}_\uparrow(t) = -\frac{i\Omega_0}{2}e^{i\delta t}e^{-i\phi}c_\downarrow(t), \tag{36}$$

$$\dot{c}_\downarrow(t) = -\frac{i\Omega_0}{2}e^{-i\delta t}e^{i\phi}c_\downarrow(t), \tag{37}$$

Now if equation 36 is differentiated in time and substituted into equation 37, then a 2nd order differential equation can be formed with respect to $c_\uparrow$:

$$\ddot{c}_\uparrow(t) - i\delta\dot{c}_\uparrow(t) + \frac{\Omega_0^2}{4}c_\uparrow(t) = 0 \tag{38}$$

This equation has the following general solution:

$$c_\uparrow(t) = e^{i\delta t}\left(ae^{-i\Omega_\delta t/2} + be^{i\Omega_\delta t/2}\right). \tag{39}$$

Where a and b are constants given by the initial state of the ion and $\Omega_\delta = \sqrt{\Omega_0^2+\delta^2}$. Now the $c_\downarrow(t)$ can be found by differentiating equation 39 with respect to t and substituting it with equation 36 to retrieve:

$$c_\downarrow(t) = \frac{e^{-i\delta t/2}e^{i\phi}}{\Omega_0}\left(\delta\left(ae^{-i\Omega_\delta t/2} + be^{i\Omega_\delta t/2}\right) - \Omega_\delta\left(ae^{-i\Omega_\delta t/2} - be^{i\Omega_\delta t/2}\right)\right). \tag{40}$$

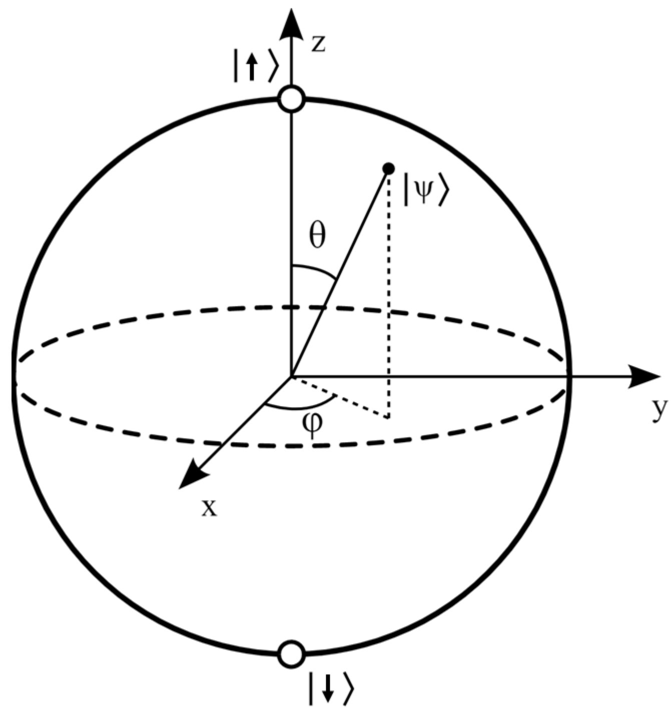

Figure 9: A pictorial representation of the transition between two states called a Bloch sphere. Using our unitary expression shown in equation 41 the angle deviating from the z-axis is $\theta = \Omega_0 t$ and the angle deviating from the x-axis over the x-y plane is given by the phase of the system ϕ. Diagram adapted from work by Smite-Meister under public domain.

This now provides all the information needed to produce the unitary operator, which can describe the state population's change through time. First the constants a and b must be determined using the two principal starting conditions: When the state is prepared in the $|\uparrow\rangle$ state at $t = 0$: $a = -b = (1 + \delta/\Omega_\delta)/2$; and when the state is prepared in the $|\downarrow\rangle$ state at $t = 0$: $a = -b = \Omega_0 e^{-i\phi}/2\Omega_\delta$. These initial conditions can then be input into equation 39 and equation 40 to produce the unitary operator:

$$U(\delta, \Omega_0, \phi, t) = \begin{pmatrix} e^{i\delta/2}\left(\cos(\Omega_\delta t/2) - \frac{i\delta}{\Omega_\delta}\sin(\Omega_\delta t/2)\right) & -\frac{i\Omega_0}{\Omega_\delta} e^{i\delta t/2} e^{-i\phi}\sin(\Omega_\delta t/2) \\ -\frac{i\Omega_0}{\Omega_\delta} e^{-i\delta t/2} e^{i\phi}\sin(\Omega_\delta t/2) & e^{-i\delta/2}\left(\cos(\Omega_\delta t/2) + \frac{i\delta}{\Omega_\delta}\sin(\Omega_\delta t/2)\right) \end{pmatrix} \tag{41}$$

A useful pictorial tool that can explain what is happening is the Bloch sphere shown in figure 9. This shows how the angles $\theta = \Omega_0 t$ and ϕ manifest themselves as the system evolves through time, with or without an applied field. This also shows how pulses of both θ and ϕ can manipulate the state coherently.

Finally one can calculate the probability of the state being in the $|\uparrow\rangle$ state if prepared in the $|\downarrow\rangle$ state:

$$P_\uparrow(t, \delta) = |c_\uparrow|^2 = \frac{\Omega_0^2}{\Omega_\delta^2}\sin^2(\Omega_\delta t/2) = \frac{\Omega_0^2}{2\Omega_\delta^2}\left(1 - \cos(\Omega_\delta t)\right) \tag{42}$$

This provides a good basis for understanding how this sensor works going forward as this can be applied to any two-level state including the bare and dressed states we use for sensing that will be detailed in the following sections.

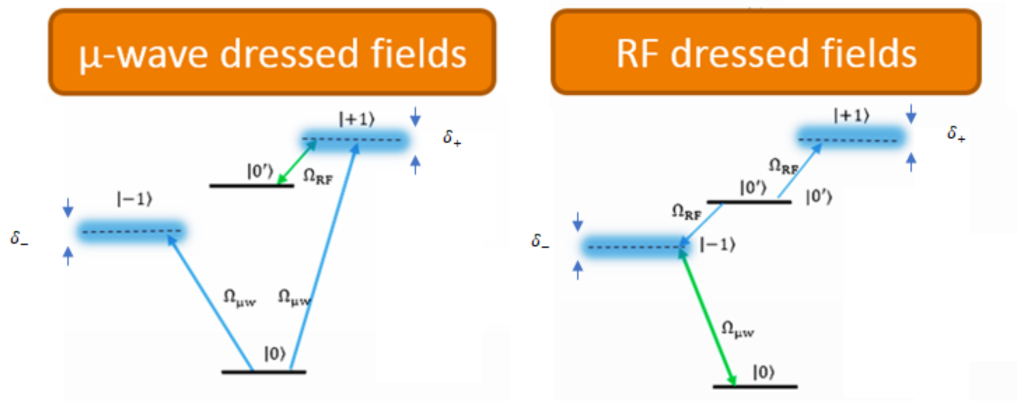

Figure 10: Diagram showing the two dressing fields annotated in blue to indicate the dressing fields and green indicating the state we use to sense. δ symbolises the detuning of the dressing fields, which should be as small as possible for ideal sensing.

2.3.2 Dressed states

The $^2S_{1/2}$ manifold shown in figure 7 shows multiple transitions that can be used to measure magnetic fields by measuring their Rabi frequency Ω in the manner described in section 2.3.1. This includes the $|0'\rangle \leftrightarrow |+1\rangle$ transition for sensing RF (1 MHz - 150 MHz) and the $|0\rangle \leftrightarrow |-1\rangle$ for sensing microwaves (12.5 GHz - 12.7 GHz). This is called 'bare' state sensing, without dressing fields, which is a simple procedure, but because it relies on the hyperfine states, hence the system is very sensitive to small fluctuations in DC field. These noise induced fluctuations change the splitting so the resonant frequency of the transition is changing constantly. The result is decoherence of the quantum superposition between the two states so measurements can only be carried out for a few microseconds, which is detrimental to the sensitivity as is described later in section 2.4.2.

To overcome this we employ dressed states for sensing both RF and microwaves in the manner described in figure 10. These fields should stabilise the sensor allowing for far higher coherence times and hence sensitivities. To examine this theoretically we can examine a Hamiltonian where there are two states $|-1\rangle$ and $|+1\rangle$ both being driven to an intermediate state $|0\rangle$. This in analogous to both the RF and microwave sensing methods shown in figure 10 (Though in the RF dressed state case we use $|0'\rangle$ instead of $|0\rangle$). These three states in vector form are: $|0\rangle \equiv (0,0,1)^T$, $|-1\rangle \equiv (0,1,0)^T$ and $|+1\rangle \equiv (1,0,0)^T$. There are also two fields driving the transitions $|0\rangle \leftrightarrow |-1\rangle$ and $|0\rangle \leftrightarrow |+1\rangle$, which have the Rabi frequencies Ω_+ and Ω_-, with the detuning δ_+ and δ_- and phase ϕ_- and ϕ_+ respectively. Now using the same method to produce the Hamiltonian for equation 33 the following Hamiltonian can be produced for this dressed state system:

$$H_{ds} = \frac{\hbar\Omega_-}{2}\left(|-1\rangle\langle 0| e^{-i\delta_- t}e^{i\phi_-} + |0\rangle\langle -1| e^{i\delta_- t}e^{-i\phi_-}\right) + \frac{\hbar\Omega_+}{2}\left(|+1\rangle\langle 0| e^{-i\delta_+ t}e^{i\phi_+} + |0\rangle\langle +1| e^{i\delta_+ t}e^{-i\phi_+}\right) \quad (43)$$

One can now move to the interaction picture with respect to: $H_\delta = \hbar(\delta_- |-1\rangle\langle -1| + \delta_+ |+1\rangle\langle +1|)$, which gives:

$$H'_{ds} = e^{iH_\delta t/\hbar}(H_{ds}(t) - H_\delta)e^{-iH_\delta t/\hbar} \tag{44}$$

$$= \frac{\hbar}{2}\begin{pmatrix} -2\delta_+ & 0 & \Omega_+ e^{i\phi_+} \\ 0 & -2\delta_- & \Omega_- e^{i\phi_-} \\ \Omega_+ e^{-i\phi_+} & \Omega_- e^{-i\phi_-} & 0 \end{pmatrix} \tag{45}$$

This derivation was derived from work by Fewell et al. [65], where more derivation for the eigenenergies and eigenstate coefficients are given. In our case we use dressing fields that are in phase ($\phi_- = \phi_+ = 0$), the fields are on resonance ($\delta_- = \delta_+ = 0$) and they have the same intensity at the ion ($\Omega_- = \Omega_+ = \Omega$). Using these simplifications we can derive the eigenstates of this system:

$$\begin{aligned} |D\rangle &= \frac{1}{\sqrt{2}}\left(|{+1}\rangle - |{-1}\rangle\right), \\ |u\rangle &= \frac{1}{2}|+\rangle + \frac{1}{2}|-\rangle + \frac{1}{\sqrt{2}}|0\rangle, \\ |d\rangle &= \frac{1}{2}|+\rangle + \frac{1}{2}|-\rangle - \frac{1}{\sqrt{2}}|0\rangle. \end{aligned} \tag{46}$$

With the eigenenergies:

$$\begin{aligned} E_u &= \frac{\hbar\Omega}{\sqrt{2}}, \\ E_d &= -\frac{\hbar\Omega}{\sqrt{2}}, \\ E_D &= 0. \end{aligned} \tag{47}$$

So as you can see the energy of the dressed state system E_D is independent of the Rabi frequency (and its noise) of the dressing fields. To understand how this uncouples the system from magnetic field noise, one can introduce a Hamiltonian, which represents the magnetic field fluctuations coupling with the 1st order sensitive hyperfine states:

$$H_n = \hbar\lambda_0(t)(|{+1}\rangle\langle{+1}| - |{-1}\rangle\langle{+1}|), \tag{48}$$

Where $\lambda_0(t)$ is an arbitrary time-dependent function, that represents the random varying noise. So if we switch to the dressed state basis:

$$H_n = \frac{\hbar\lambda_0(t)}{\sqrt{2}}(|D\rangle\langle u| + |D\rangle\langle d| + |u\rangle\langle D| + |d\rangle\langle D|) \tag{49}$$

This Hamiltonian with the eigenenergies from equation 47 shows that the three states are separated by an energy gap of $\hbar\Omega/\sqrt{2}$, so this means that magnetic field noise can only interact with the system if it has a frequency near $\Omega/\sqrt{2}$, so it is useful to use very powerful dressing fields that produce high Rabi frequencies. These fields will produce systems that are only susceptible to high frequency $\gg$kHz noise, which is usually far less intense than DC and kHz noise present in most environments.

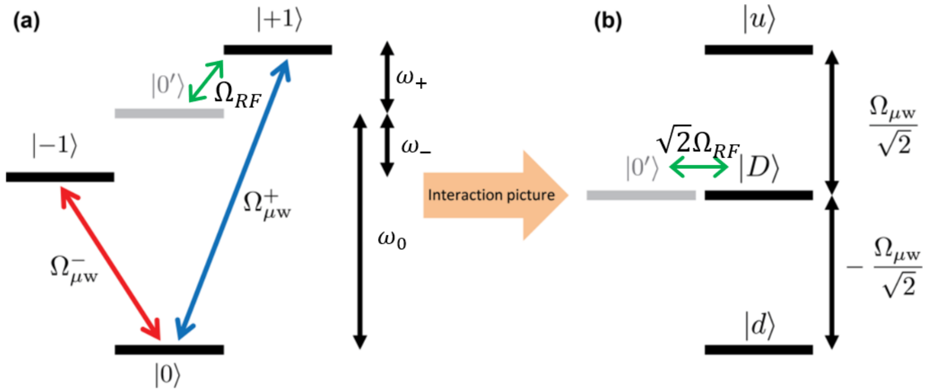

Figure 11: Energy levels involved in the sensing of RF fields Ω_{RF} utilising microwave dressing fields $\Omega^{-}_{\mu w}$ and $\Omega^{+}_{\mu w}$. This generates three dressed state energy levels $|D\rangle$, $|u\rangle$ and $|d\rangle$ shown in b). These states have an energy splitting of $\pm\hbar\Omega_{\mu w}/\sqrt{2}$.

2.3.3 Sensing RF

As described earlier in section 2.3.1, to sense RF radiation (1 MHz - 150 MHz) one should apply two microwave fields $\Omega^{-}_{\mu w}$ and $\Omega^{+}_{\mu w}$ to drive the transitions $|0\rangle \leftrightarrow |-1\rangle$ and $|0\rangle \leftrightarrow |+1\rangle$ respectively. An opportunity to sense the fields driving these transitions is presented, between $|0'\rangle \leftrightarrow |+1\rangle$, which in the interaction picture is the $|0'\rangle \leftrightarrow |D\rangle$ transition, which can be seen in figure 11. As we use the hyperfine states this allows us to modulate the frequency splittings ω_0, ω_- and ω_+. This allows the system to be tuned to any frequency we wish, by changing the applied B-field.

Using our general Hamiltonian for an arbitrary dressed state derived in equation 43, we can derive the Hamiltonian for this dressed state system while assuming that the dressing fields are in phase ($\phi_- = \phi_+ = 0$), the fields are on resonance ($\delta_- = \delta_+ = 0$) and they have the same intensity at the ion ($\Omega^{-}_{\mu w} = \Omega^{+}_{\mu w} = \Omega_{\mu w}$). This gives:

$$H_{\mu w} = \frac{\hbar\Omega_{\mu w}}{2}(|+1\rangle\langle 0| + |-1\rangle\langle 0| + |0\rangle\langle +1| + |0\rangle\langle -1|). \tag{50}$$

This produces the following eigenstates:

$$|D\rangle = \frac{1}{\sqrt{2}}(|+1\rangle - |-1\rangle) \tag{51}$$

$$|u\rangle = \frac{1}{2}|+1\rangle + \frac{1}{2}|-1\rangle + \frac{1}{\sqrt{2}}|0\rangle \tag{52}$$

$$|d\rangle = \frac{1}{2}|+1\rangle + \frac{1}{2}|-1\rangle - \frac{1}{\sqrt{2}}|0\rangle \tag{53}$$

Using this one can express the Hamiltonian in terms of the dressed states:

$$H_{\mu w} = \frac{\hbar\Omega_{\mu w}}{\sqrt{2}}(|u\rangle\langle u| - |d\rangle\langle d|). \tag{54}$$

This shows that the energy splitting between $|u\rangle$ and $|d\rangle$ and $|D\rangle$ are given by $\frac{\hbar\Omega_{\mu w}}{\sqrt{2}}$ and $-\frac{\hbar\Omega_{\mu w}}{\sqrt{2}}$ respectively as shown in figure 11. Rotations between the $|D\rangle$ and $|0'\rangle$ on the Bloch sphere and can be driven by

RF transitions $|0'\rangle \leftrightarrow |{+1}\rangle$ and $|0'\rangle \leftrightarrow |{-1}\rangle$. The resonant frequencies are quite similar as shown in figure 8 at low applied DC fields, whose differences arise from second order Zeeman effects.

Now one can produce a Hamiltonian expressing a system that is being driven by an RF field between $|0'\rangle \leftrightarrow |{+1}\rangle$, with a detuning of δ_{RF}, an phase ϕ_{RF} and a Rabi frequency Ω_{RF}:

$$H_{RF} = \frac{\hbar\Omega_{RF}}{2}\left(|{+1}\rangle\langle 0'| e^{-i\delta_{RF}t}e^{i\phi_{RF}} + |{-1}\rangle\langle 0'| e^{i(\delta_{RF}-\Delta\omega_{2nd})t}e^{-i\phi_{RF}} + H.c.\right), \tag{55}$$

Where $\Delta\omega_{2nd} = \omega_+ - \omega_-$ is the second order Zeeman effect, which produces the difference in splitting of ω_+ and ω_-. H.c. is the Hermitian conjugate. Using the dressed state eigenstates shown in equation 46 we can now switch to the interaction picture in terms of the dressed states:

$$\begin{aligned} H'_{RF} = &\frac{\hbar\Omega_{RF}}{2\sqrt{2}}\left(|D\rangle\langle 0'|\left(e^{-i\delta_{RF}t}e^{i\phi_{RF}} - e^{i(\delta_{RF}-\Delta\omega_{2nd})t}e^{-i\phi_{RF}}\right) + H.c.\right) \\ &+ \frac{\hbar\Omega_{RF}}{4}(|u\rangle\langle 0'|\left(e^{-i\left(\delta_{RF}-\frac{\Omega_{\mu m}}{\sqrt{2}}\right)t}e^{i\phi_{RF}} - e^{i\left(\delta_{RF}-\Delta\omega_{2nd}+\frac{\Omega_{\mu m}}{\sqrt{2}}\right)t}e^{-i\phi_{RF}}\right) \\ &+ |d\rangle\langle 0'|\left(e^{-i\left(\delta_{RF}+\frac{\Omega_{\mu m}}{\sqrt{2}}\right)t}e^{i\phi_{RF}} + e^{i\left(\delta_{RF}-\Delta\omega_{2nd}=\frac{\Omega_{\mu m}}{\sqrt{2}}\right)t}e^{-i\phi_{RF}} + H.c.\right). \end{aligned} \tag{56}$$

This Hamiltonian shows that the two transitions: $|0'\rangle \leftrightarrow |{+1}\rangle$ and $|0'\rangle \leftrightarrow |{-1}\rangle$ each couple with the three dressed states. So there are six transitions in total with three dressed state pairs with a frequency separation of $\Delta\omega_{2nd}$. This stipulates a few conditions for optimal sensing on the $|0'\rangle \leftrightarrow |D\rangle$ transition: if the dressing fields are not a lot more intense than the RF $\Omega_{RF} \ll \Omega_{\mu w}$, then the sensing field will drive the off-resonant transitions $|0'\rangle \leftrightarrow |u\rangle$ and $|0'\rangle \leftrightarrow |d\rangle$; The RF Rabi frequency Ω_{RF} should be far less than $\Delta\omega_{2nd}$ so the dressed state pairs do not become degenerate; The case when $\Delta\omega_{2nd} \approx \Omega_{\mu w}/\sqrt{2}$, should be avoided as the $|0'\rangle \leftrightarrow |u\rangle$ and $|0'\rangle \leftrightarrow |d\rangle$ transitions will begin to have overlapping transition frequencies.

If we use these limitations in our Hamiltonian equation 56, we can remove the 2nd order Zeeman effects and are left with an expression that only describes $|0'\rangle \leftrightarrow |D\rangle$:

$$H'_{RF} = \frac{\hbar\Omega'_{RF}}{2}\left(|D\rangle\langle 0'| e^{-i\delta_{RF}t}e^{i\phi_{RF}} + |0'\rangle\langle D| e^{i\delta_{RF}t}e^{-i\phi_{RF}}\right). \tag{57}$$

Where $\Omega'_{RF} = \Omega_{RF}/\sqrt{2}$ is the Rabi frequency of the $|0'\rangle \leftrightarrow |D\rangle$ transition. As described earlier this dressed state system renders the system immune to small fluctuations in the B-field producing the Zeeman splitting. This is apparent as any small fluctuation that is not large enough to produce a second order Zeeman effect will produce a detuning $\delta_+ = -\delta_- = \delta$, for the hyperfine states from equation 28. There is a contracting detuning from the $|0'\rangle \leftrightarrow |D\rangle$ transition $\delta_{RF} = \delta$, which means the effective RF resonant frequency does not change at all unless the change in B-field is significant (such as when tuning the sensor to a new sensing frequency deliberately).

One can finally calculate how the state population should change in time in a similar manner in which we calculated it for the general case for equation 42. If we assume that the phase of the RF is zero, then the state population in the dressed state $|D\rangle$ is:

$$P_D(\delta_{RF}, t) = \frac{\Omega'^2_{RF}}{2(\Omega'^2_{RF} + \delta^2_{RF})}\left(1 - \cos\left(\sqrt{\Omega'^2_{RF} + \delta^2_{RF}}t\right)\right). \tag{58}$$

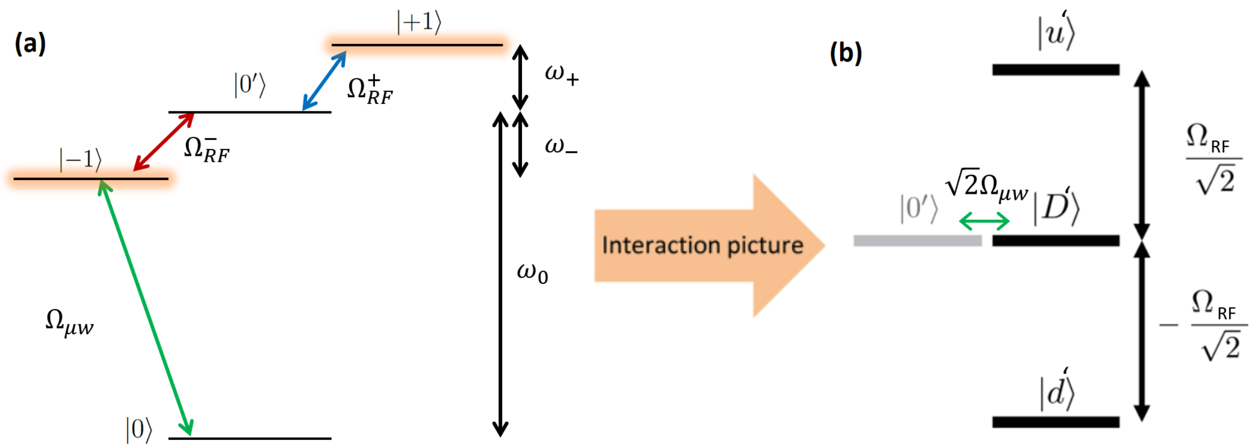

Figure 12: a). Energy levels involved in the sensing of microwave fields $\Omega_{\mu w}$ utilising RF dressing fields Ω^{-}_{RF} and Ω^{+}_{RF}. This generates three dressed state energy levels $|D'\rangle$, $|u'\rangle$ and $|d'\rangle$ shown in b). These states have an energy splitting of $\pm\hbar\Omega_{RF}/\sqrt{2}$.

2.3.4 Sensing microwaves

Sensing with microwaves is a very similar procedure as sensing with RF as the states involved are identical other than the fact you can use the $|0'\rangle$ as an intermediary state between the $|+1\rangle$ and $|-1\rangle$ instead of $|0\rangle$. This is done by applying an RF field (Ω_{RF}) to drive the $|0'\rangle \leftrightarrow |+1\rangle$ and $|0'\rangle \leftrightarrow |-1\rangle$ transitions as shown in figure 12.

The theory for this system is analogous to that for RF sensing, by replacing $|0\rangle$ with $|0'\rangle$ and swapping $\Omega_{\mu w}$ with Ω_{RF} so will not be repeated here. The resulting interaction picture Hamiltonian is:

$$H'_{\mu w} = \frac{\hbar\Omega'_{\mu w}}{2}\left(|D'\rangle\langle 0|\, e^{-i\delta_{\mu w}t}e^{i\phi_{\mu w}} + |0\rangle\langle D'|\, e^{i\delta_{\mu w}t}e^{-i\phi_{\mu w}}\right). \tag{59}$$

As you can see this equation is almost identical to equation 57 describing the Hamiltonian for the RF sensing system.

2.4 Sensitivity determination

As described in the previous subsection, the applied RF and microwaves that are sensed with the experiment drive oscillations between two states. The frequency of these oscillations is called the Rabi frequency Ω and is proportional to the strength of these fields. By measuring the Rabi frequency of the transition one can determine the intensity of the field driving that transition and therefore the experiment works as a RF and Microwave sensor. A major question arises however: exactly how sensitive is this detector and in particular to what accuracy can you determine the magnetic field strength of the field you wish to sense per second of experimental time. It is also useful to know the parameters that you need to get the minimum sensitivity possible. In this section I will detail how to introduce noise to the system that we have constructed in section 2.3, and how this can be used to determine the sensitivity of the system as well as find what parameters used to maximise the aforementioned sensitivity.

2.4.1 Noise characterisation and coherence time

We must first set up a Hamiltonian for this system that includes noise acting on the system. This can be RF waves with a frequency of $\Omega/\sqrt{2}$, which produce noise as described in section 2.3.2 or from other sources. This noise manifests in a tendency for the quantum superposition of the state during measurement to decay into a mixed state and so lose all the information gleaned from the RF or microwave field.

If we first assume that there is a two-level system as laid out in section 2.3.1 with a Hamiltonian H_{TLS}, one can then find a solution for the wave function, which can then be used to extract an equation that describes the decoherence of the system. This is based on the work by Cywiński et al. [66]. The pure dephasing Hamiltonian is the Hamiltonian of the two-level system without noise $\hat{H}_{TLS}$ plus the Hamiltonian of the time dependent noise $\hat{H}_{noise}(t)$:

$$\hat{H} = \hat{H}_{TLS} + \hat{H}_{noise}(t) = \frac{1}{2}[\Omega + \beta(t)]\hat{\sigma}_z \tag{60}$$

Where Ω is the energy splitting of the two-level system, $\hat{\sigma}_z$ is a Pauli matrix and $\beta = \mu_B B_0 \cos(\omega_f t + \phi_f)$ is a time varying magnetic noise, with a frequency ω_f and a phase ϕ_f. μ_B is the Bohr magneton and B_0 is the maximum magnetic field noise amplitude.

If we now set up an initial state of our two-level system for this Hamiltonian: $|\psi(0)\rangle = a|\uparrow\rangle + b|\downarrow\rangle$ where $|a|^2 + |b|^2 = 1$, we can carry out a free induction decay experiment on this system where where the system is left to precess over time before a fluorescence based measurement is carried out. Using the Hamiltonian equation 60 the resulting state after a time τ is:

$$|\psi\rangle = e^{-\Omega/2} e^{-i/2\int_0^\tau \beta(t)dt} a|\uparrow\rangle + e^{\Omega/2} e^{i/2\int_0^\tau \beta(t)dt} b|\downarrow\rangle \tag{61}$$

Using this state we can determine the off diagonal terms of the qubit density matrix, which are:

$$\rho_{\uparrow\downarrow}(t) = e^{-\Omega/2} e^{-i/2\int_0^\tau \beta(t)dt} \rho_{\uparrow\downarrow}(0) \tag{62}$$

Where $\rho_{\uparrow\downarrow}(0) = ab^*$. We can now use this to define the coherence of the qubit:

$$f(t) \equiv \frac{|\langle\rho_{\uparrow\downarrow}(t)\rangle|}{|\langle\rho_{\uparrow\downarrow}(0)\rangle|} \tag{63}$$

When wanting to a maximise the coherence of a two-level system a series of spin-echo π pulses are applied to the system to cancel out the effects of noise on the system. This 'dynamic decoupling' method is explained in Joe Randall's thesis [63]. So if one applies n ideal π pulses along the x-axis to the system within a time interval $t' \in [0, t]$ with a coherence $f(t)$ and these pulses are carried out at times $t_1, t_2 ... t_n$, then this results in a qubit evolution operator:

$$\hat{U}(t) = e^{-i\hat{\sigma}_z/2\int_{t_n}^{t}[\Omega+\beta(t')]dt'}(-i\hat{\sigma}_x)e^{-i\hat{\sigma}_z/2\int_{t_{n-1}}^{t_n}[\Omega+\beta(t')]dt'} \cdots \times (-i\hat{\sigma}_x)e^{-i\hat{\sigma}_z/2\int_0^{t_1}[\Omega+\beta(t')]dt'} \tag{64}$$

Where $\hat{\sigma}_x$ is the Pauli matrix which exchanges the amplitudes of $|\uparrow\rangle$ with $|\downarrow\rangle$ with each pulse. Now applying this matrix to the coherence equation 63, this gives us:

$$f(t) = |\langle \exp(-i \int_0^t \beta(t') f(t;t') dt') \rangle| \tag{65}$$

A solution for this equation is:

$$f(t) \equiv e^{-\chi(t)} \tag{66}$$

The Gaussian approximation of the function $\chi(t)$ can be expressed in terms of the spectral density of the noise $S(\omega)$ [66]:

$$\chi(t) = \int_0^\infty \frac{d\omega}{2\pi} S(\omega) |\tilde{f}(t;\omega)|^2 = \int_0^\infty \frac{d\omega}{\pi} S(\omega) \frac{F(\omega t)}{\omega^2} \tag{67}$$

Where $\tilde{f}(t;\omega)$ is the Fourier transform of $f(t;t')$ with respect to t' and $F(\omega t) = \frac{\omega^2}{2}|\tilde{f}(t;\omega)|^2$ is the filter function, which encapsulates the effect of the pulses on the coherence of the system.

Now if we assume a flat spectral density so $S(\omega) = 1$ we can use the sum rule to produce:

$$\int_{-\infty}^{+\infty} \frac{d\omega}{\pi} \frac{F(\omega t)}{\omega^2} = \int_{-\infty}^{+\infty} f^2(t;t') dt' = t \tag{68}$$

From equation 68 and equation 67 we can ascertain that the pulses only prevent decoherence produced by low frequency noise, because of the $1/\omega^2$ term, so $S(\omega) \approx S(0)$. leading to a solution for equation 67: $\chi(t) = S(0)t/2$ for all pulse sequences when $t \gg 1/\omega_n$, where ω_n is the frequency at which the noise begins to decay. An equation for the coherence of the system can now be derived:

$$f(t) = e^{-S(0)t/2} \tag{69}$$

In our case $S(0) = 2/T_2$ where T_2 is the coherence time of the system, which denotes the rate at which the system decoheres from a superposition.

Now we can try and ascertain what kind of coherence time we should expect for our system. As stated earlier we will assume that noise frequencies are low $\omega \to 0$ hence $F(\omega t)/\omega^2 \to t^2/2$. Now if we assume an exponential decay in noise amplitude with frequency, which gives $S(\omega) = 2\pi A/|\omega|$, where A is the amplitude of the noise spectrum, this provides us with a solution for equation 67:

$$\chi(t) \approx At^2 \left(\ln \left(\frac{1}{\omega_f + t} \right) + O(1) \right) \tag{70}$$

Where $O(1)$ is the integral constant from equation 67. Now from [66] we know that $\chi(T_2) = 1$, so by setting $t = T_2$ and rearranging equation 70 for T_2 we get:

$$T_2 = \frac{e^{O(1) - 1/AT_2^2}}{\omega_f} \tag{71}$$

We can now assume that A is very large so $1/AT_2^2 \ll O(1)$, which finally gives us:

$$T_2 = \frac{e^{O(1)}}{\omega_f} \tag{72}$$

This results in our expectation value for the coherence time, so for RF sensing using Yb ions one can use the data from Baumgaut et al. [3] to get an experimental value of $e^{O(1)} = 2.1 \times 10^7 s$. So for instance for a transition frequency of $\omega_f = 14MHz$ this should give a coherence time of $T_2 = 1.5s$.

2.4.2 Sensitivity

Now the nature and origin of decoherence is understood, we can apply it to our population equations in section 2.3.3 to find the sensitivity we should expect from our system. First a generalised version of equations 58 and 59 can be made, which shows the probability distribution of a two state system. An e^{-t/T_2} decoherence term from section 2.4.1 can now be included, which describes how the Rabi oscillations tend to damp towards $P(t \gg T_2) \to 0.5$. This can be written as:

$$P(t, \delta) = \frac{\Omega^2}{2(\Omega + \delta^2)} \left(1 - e^{-t/T_2} \cos\left(\sqrt{\Omega^2 + \delta^2} t\right)\right). \tag{73}$$

Where Ω is the Rabi frequency of the applied field, δ is the detuning of the transition, T_2 is the coherence time and t is the measurement time.

Now that we have an expression for the probability distribution over time we can calculate the error associated with determining the Rabi frequency of a given measurement. From Baumgart et al. [3] we know the definition of the standard deviation of the probability ΔP is:

$$\frac{\Delta P}{\delta \Omega} = \left|\frac{\partial P}{\partial \Omega}\right|. \tag{74}$$

We can then rearrange this equation in terms of the minimal detectable change in Rabi frequency:

$$\delta \Omega = \frac{\Delta P}{\left|\frac{\partial P}{\partial \Omega}\right|} \tag{75}$$

It can now be assumed that the sensed field is on resonance ($\delta = 0$), we can differentiate equation 73, with respect to Ω to get:

$$\left|\frac{\partial P}{\partial \Omega}\right| = \left|te^{-t/T_2} \sin\left(\Omega t\right)/2\right|. \tag{76}$$

To find ΔP one can now use the standard deviation for a probabilistic experiment repeated n times, with perfect state detection fidelity [3]:

$$\Delta P = \sqrt{P(1-P)/n} \tag{77}$$

Now by inserting equation 73 into equation **??**, with no detuning we get:

$$\Delta P = \sqrt{\frac{1 - e^{-2t/T_2}\cos^2(\Omega t)}{4n}} \tag{78}$$

By now plugging in equation 78 and equation 76 we can get an expression for the Rabi frequency error:

$$\delta\Omega = \frac{1}{t\sqrt{n}}\sqrt{\frac{1 - e^{-2t/T_2}\cos^2(\Omega t)}{e^{-2t/T_2}\sin^2(\Omega t)}} \tag{79}$$

Now this equation can be simplified from the observation that when the Rabi oscillation is at its steepest, the measurement is the most sensitive, because a small change in Rabi frequency will cause a larger displacement of the data point there. This means that we can set $\Omega t = N\pi/2$ where N is any odd integer, which gives:

$$\delta\Omega = \frac{e^t/T_2}{t\sqrt{n}} \tag{80}$$

From this we can now calculate the shot noise limited sensitivity for $\delta\Omega$, which was calculated by: [3, 67, 68]

$$S_\Omega = \delta\Omega\sqrt{T_{tot}} \tag{81}$$

Where $T_{tot} = N(t + T_{add})/n_i$ is the total experimental time; N is the total number of measurements; t is the individual measurement time; T_{add} is the additional time required between measurements such as for laser cooling, detection and state preparation and n_i is the number of ions used during the experiment. To maximise sensitivities, it is desirable to have a large measurement time t, which should be around 1 s, which is significantly less than our usual T_{add}, which is usually on the order of 10 - 100 ms. Hence we can assume that $T_{add} \ll t$, which simplifies equation 81 to:

$$S_\Omega = \frac{e^{t/T_2}}{\sqrt{n_i t}} \tag{82}$$

From an observation of this function it can be deduced that it has a single minima, which would give us the maximum sensitivity for a given experimental time t. We can calculate this by differentiating this equation in terms of t and setting it equal to zero to give $t_{opt} = T_2/2$, where t_{opt} is the optimal experimental time. This is because we ideally want long experiment times so that the field we wish to sense has more time to interact with the ion to produce a signal, but also increases the chance of an ion decohering and being unable to extract useful information out of the system.

We can now define the sensitivity of the sensor in terms of the minimum magnetic field detectable by the sensor per second of total experimental time. We can do this by using equation 31 to equate the magnetic field to Rabi frequency, which gives:

$$\delta\Omega = \frac{\mu}{\hbar\sqrt{2}}\delta B \tag{83}$$

Where δB is the uncertainty of the sensed magnetic field strength and μ is the amplitude of the magnetic moment. This is given by $\mu = g_J\mu_B J$ where $g_J \approx 2$ is the electron g-factor; μ_B is the Bohr magneton and

J is the total angular momentum quantum number given by $J = L + S$ where for the ${}^2S_{1/2}$ hyperfine manifold of ${}^{171}Yb^+$ $L = 0$ and $S = 1/2$ so $J = 1/2$. We can now substitute equation 83 into equation 81 to give:

$$S_B = \frac{\hbar e^{t/T_2}}{\mu_B}\sqrt{\frac{2}{n_i t}} = \frac{\hbar\sqrt{2}}{\mu_B} S_\Omega \tag{84}$$

3 Demonstrator experimental set-up

My project's purview has been to demonstrate RF and microwave sensing using trapped-ions and to miniaturise the various components to package into a device for commercial applications (see section 6). To this end I (and my colleagues on the sensor team) have endeavoured to deploy a demonstrator system capable of trapping individual ions on a microfabricated chip trap and apply RF and microwave pulses for coherent manipulation of the ion to conduct sensing experiments.

The construction of the various constituents of this system as well as the final assembly make up the bulk of the work that I have done on this project and the following sections will detail my personal efforts to build the demonstrator system and which parts were solely only my work and others that were completed in collaboration with my team members.

3.1 Vacuum system

The vacuum system is the core of our experiment, it contains the ion-trapping chip where all the ions used for RF and microwave sensing are trapped, as well as the supporting electronics to provide the RF and DC potentials needed for trapping. The various subsystems inside the vacuum chamber are displayed in figure 13 for reference. The following section will detail the parts used inside the vacuum chamber, how they arranged, their purpose and the rationale behind the choices we made in the design. The chamber and internal structure was designed by Dr. Altaf Nizamani and was assembled by myself in collaboration with Dr. Ethan Potter and Dr. Altaf Nizamani.

3.1.1 UHV chamber

All quantum sensing experiments conducted during my PhD were done within the vacuum chamber, which was built especially for quantum sensing. The chamber, was designed by Dr. Altaf Nizamani and was built to fulfil the following specifications:

- 100 pin D-sub DC electrical feedthrough.
- Two high current electrical feedthroughs for the separate $^{171}Yb^{+}$ and $^{174}Yb^{+}$ atomic ovens rated for up to 10 A.
- RF feedthrough rated for up to 100 MHz for providing trapping RF on chip.
- Mounting for the internal PCB electronics and chip.
- Laser access through two windows coated to provided maximum transmissivity for 369 nm, 399 nm and 935 nm wavelengths. Arrayed so that the beam can be made parallel to the chip.
- Bracketing for the atomic ovens to place them in the optimal position and to provide a ground for the electrical current for the ovens.
- Ion gauge to provide accurate measurement for the vacuum pressure.
- Ion pump to provide below 1×10^{-10} mbar pressure.
- Stainless steel valve for closing the vacuum to the turbo pump to bring the chamber down to ultra-high vacuum.

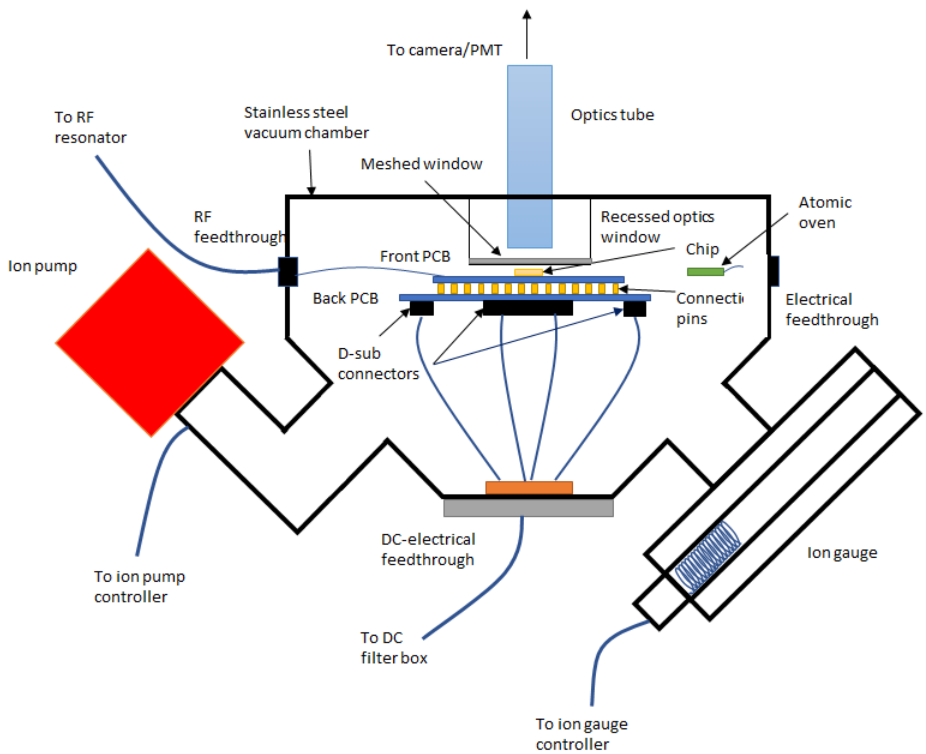

Figure 13: Diagram showing the various components within the stainless steel vacuum system. Displaying the chip, which is positioned just below the recessed window, which is covered in a fine stainless steel mesh to prevent charge build up. The chip's DC connections are wire-bonded to the front PCB, which is connected to the back PCB using pressure pins, before being wired to the 100-pin DC electrical feedthrough using UHV bakeable D-sub cables. The RF for the trapping potential is provided via a separate RF compatible feedthrough and connected to the front PCB via a SMP connector, before being wirebonded to the chip. The atomic oven is mounted directly below the chip to provide the stream of neutral ytterbium to be ionised at the chip. The ion pump and ion gauge are connected to the vacuum system via two stainless steel T-piece vacuum chamber parts and actively pump the system and measure the vacuum pressure respectively. Not to scale.

- A recessed optical window in front of the chip. This is to ensure that the optics tube can be as close as possible to the ions on the chip.

To fulfil the UHV specifications all the materials used inside the system were checked against ultra-high vacuum (UHV) compatible materials list for Laser Interferometer Gravitational-Wave Observatory (LIGO) experiment [38]. The core of our chamber is a 6" spherical octagon[2] welded to a DN40CF cluster[3] made from type 304 stainless steel.

The 100 pin feedthrough[4] was installed to the rear of the system as shown in figure 13 and consists of a 28 pin and a 76 pin D-sub connection equalling 104 possible DC connections. Custom bakeable cables were designed and built to break the 76 pin D-sub into three 25 pin D-sub connectors that can connect to the back PCB (see sections 3.1.6). The 28 pin D-sub has a separate cable to convert it to a 25 pin D-sub connector to make it compatible with the back PCB connectors. This means that only 100 of the 104 connections can actually be utilised on the chip itself. The reason for this number of connections is that some of Dr. Ethan Potters sensing chip designs for multi ion sensing were expected to require this many connections, more information on this can be found in his thesis [39].

The atomic ovens are mounted on brackets that were designed by Dr. Altaf Nizamani to direct the neutral Yb flux towards the chip position and can be manually moved to the correct elevation relative to the chip carrier and then held in place with two bolts, while the system is open. Information on the atomic oven design can be found in section 3.1.3. These ovens are supplied with current through two barrel connectors that are connected to a high current electrical feedthrough[5], which is rated for 16 A.

The trapping RF is supplied from an RF 50 Ω SMA feedthrough[6], which is connected to the chip via several wirebonds on the front PCB. The front PCB is connected to the RF feedthrough via a custom made coax cable[7] with an SMP connector[8] and an SMA cable[9] on the feedthrough side.

3.1.2 System preparation

After all components of the system outlined at the beginning of this section, were designed and ordered, they need to be prepared and assembled correctly to assure that they are compatible with Ultra High Vacuum (UHV)[38], which requires less than 1×10^{-9} mbar pressure at the chip position. This requires a robust process of cleaning with different chemicals and baking in our specially built oven.

Before assembly all the different stainless steel vacuum components were meticulously cleaned using the following method. Each component was unpacked inside our own class 1000 clean room, which is designed to minimise the amount of dust in the environment that could compromise the vacuum. The individual components were then submerged in acetone in a glass container. The container was then lowered into an ultrasonic bath, which is designed to dislodge dirt particles and dissolve them with ultrasound waves in water. The components are sonicated for 10 minutes before being removed from the beaker and placed in another beaker filled with isopropyl alcohol (IPA). The component is then sonicated again for 10 minutes submerged in IPA to remove any

[2] Kimball Physics MCF600-SphOct-F2C8
[3] MCF450-WeldClstr-E1C4
[4] Kurt J. Lesker IFDGG501056AX
[5] Kurt J. Lesker EFT0243032
[6] Allectra 242-SMAD50-C40
[7] RS Pro 794-7206
[8] Rosenberger19K201-302L5
[9] TE Connectivity 1056456-1

acetone residue that may remain. After this the component is removed and rinsed in ethanol before being left to dry for a few minutes. For more sensitive components such as the chip and the viewports were simply rinsed in acetone and dried with a nitrogen gun.

Once all the components have been cleaned they are wrapped in aluminium foil to allow for transport outside the clean room without the risk of dust falling into the components. Then the stainless steel vacuum system components are transported to our dedicated vacuum system oven built by former group member Dr. James Siverns [37]. This oven was designed to bake the moisture out of the walls of the chamber and to vaporise any grease or dust on the pieces. The oven is then ramped up in temperature using heaters controlled by a Python programme written by former group member Nikolaus Lorenz. This is to assure that the thermal expansion and contraction from rapid temperature changes does not cause the viewports to break or damage other sensitive internal components. The programme ramps up the temperature for about a day up to 200 °C and then keeps it at that temperature for two weeks before ramping it down slowly to room temperature.

Once the initial bake was complete the vacuum parts were brought back to the cleanroom for assembly. Each of the vacuum system part flanges have 'knife edges' where they should connect to other vacuum parts, which are designed to press into soft copper gaskets when one is placed between two vacuum parts you wish to put together. The parts are then bolted together using nuts and bolts and tightened evenly to avoid a lop-sided seal. The flanges connected to the octagon/cluster had their bolts screwed directly into the system.

Once the entire system was sealed we began a leak test, which involved installing a residual gas analyser (RGA) onto the system and sealing its sensor head inside the system. Then our turbo pump[10] was attached to the valve, which was opened and the pump turned on. After a few hours of pumping we would examine the pressure and if it was not in the 10^{-6} mbar region it would tell us there was a major leak and would begin tightening bolts until the pressure began dropping again. If the pressure was within acceptable parameters then we would proceed with the leak test. This involves using a helium spray gun with a needle head to spray helium into all the places on the chamber which are liable to leak such as the gaskets of the flange connections and the viewports, that can have micro-cracks that leak. The RGA is connected to a computer that can display the partial pressure of any atoms in the chamber with a certain atomic mass. So while we are spraying with the helium we look for a helium peak on the computer. If we spray in all the vulnerable spots on the chamber without any helium peaks then we can safely assume that there are no leaks on the system.

Once the leak test is complete we can disconnect the RGA and the turbo pump and reseal the system before taking the entire system to the oven for a second bake. Once the system is installed in the oven it is connected to the turbo pump via the valve and the ion gauge and ion pump controllers are plugged in. The system is then wrapped in foil to ensure that the heat is transferred to the system as slowly as possible, to avoid viewport breakages. The magnets that are attached to the ion pump are removed as they are not rated to 200 °C and is not needed initially. The turbo pump is then turned on before opening the valve to pump down the system for a few hours before the bake. Once the pressure has fallen to an adequate level the oven controller will begin ramping up the temperature to 200 °C as with the previous bake. The pressure should increase due to the outgassing from the chambers walls during the ramp, but over the following week the pressure will slowly decrease and settle. Once the pressure has plateaued (usually over twelve hours), the oven can be ramped down to around 50 °C. This is done so that the oven can be opened to install the oven magnets and the pressure difference from opening the oven will not be too great. The ion pump is then activated and the oven ramped up

[10] Leybold Turbolab

to around 150 °C (just below the magnets limit of 160 °C). Again the pressure should increase rapidly due to the activation, but should settle and drop to even lower pressures than before. Once the pressure has plateaued again after a few days the system can be ramped down to 50 °C once again, so the oven can be opened and the valve to the turbo pump can be sealed. Once the valve is closed the ion pump is solely maintaining the pressure in the system and finally the ion gauge can be activated and outgassed. This is done by ramping up the system yet again to 150 °C and increasing the current applied to the coils inside the ion gauge, which ejects the material that may be attached to them. Over the next few days the pressure should settle again and then the final ramp down can begin to get down to room temperature.

Once the ramp down is complete the system can be briefly disconnected from the ion gauge and the ion pump before being transported to its desired location on the optics table. The system is reconnected to the ion pump and ion gauge as quickly as possible to avoid any great reductions in internal pressure. Once they are connected and the pressure has stabilised the current on the ion gauge should be set. There is a trade-off with this parameter as high currents generally give a more accurate reading, but they also mean a higher minimum pressure inside the system. This is from the heat of the coils inside the ion gauge causing outgassing. Once an optimal current has been chosen the system is left to see how low the pressure will go outside the oven, which in our case was just above 10^{-11} mbar.

3.1.3 Atomic oven

The atomic ovens are the source of neutral ytterbium, which are then ionised to produce Yb^+, which can be trapped above the surface of the chip. They have a simple construction shown in figure 14 using a 16 mm piece of 17 G surgical tubing[11], which has the last 4 mm of its length flattened with pliers. This crushed tab is then spot welded to a 3 mm by 5 mm piece of Constantan foil[12]. The opposite end of the foil is then spot welded to a piece of single core copper wire, which is then connected to an electrical feedthrough via a barrel connector. The tube is held in place with a bracket that directs the atomic flux towards the trapping position and provides a ground for the current to flow to from the cable. The ytterbium is loaded into the oven by cutting it into small pieces or flakes with a scalpel, before dropping them into the tube and pressing them in to ensure they are as close to back as possible and so the Yb does not fall out. The steel tube provides the high resistance load that produces heat when a high current of generally up to 8 A is is applied to it. This heat increases the temperature of the oven up to 420 K and hence the vapour pressure of the ytterbium producing a flux of neutral atoms to emit from the tube [35]. This set-up is very effective due to its simplicity and reliability already demonstrated with the macroscopic trap experiment in our laboratory [37, 36].

As shown in figure 14 the atomic ovens are placed very deliberately so that the lip of the tube is just below the surface of the chip. This is done due to the fact that that if the tube is facing down onto the chip, the Yb flux will be directed onto its surface. This would cause the chip to become coated in Yb and there is evidence that this can adversely effect the electrical properties of the chip. Greater justification for this method can be found in Dr. David Murgia's thesis [35].

We used an oven that used natural ytterbium, used for initial trapping and an enriched oven loaded with 95% ^{171}Yb that was used for coherent experiments and sensing measurements (more details can be found in section 2.2). To test these ovens a fluorescence test is carried out to check whether the ovens are functioning

[11] Stainless Tube and Needle Co. 17 G Thin Wall 304/316
[12] Goodfellow. Constantan® - Resistance Alloy - Foil. 0.1 mm thickness. 245-709-96

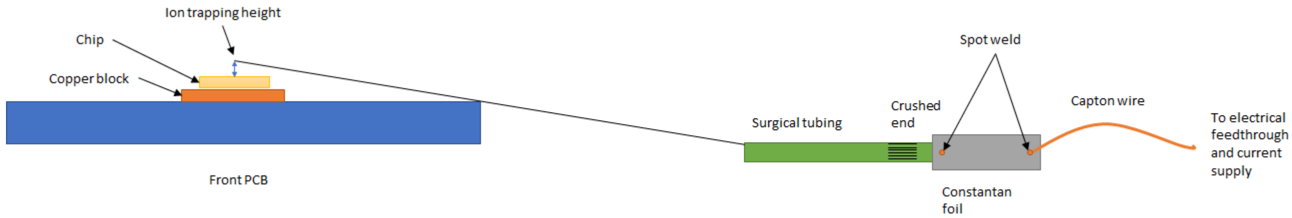

Figure 14: This shows how the atomic ovens in the system are constructed from surgical tubing, Constantan foil and single core copper wire all spot welded together. As well as the rationale for how they are positioned in the system so that the neutral Yb flux is rises up towards the trapping position of the chip and not down onto the chip surface, which could coat it in Yb and possibly effect the properties of the chip.

as intended and to measure exactly what the ionisation frequency is for the two isotopes for our system. This is very useful as it limits the amount of parameter space needed when trying to trap initially. To carry this test out we directed a 399 nm laser directly into the oven to produce a strong fluorescence beam. Then we increased the current applied to the oven up to 0.8 A to ablate the ytterbium oxide layer on the surface of the ytterbium in the oven from when the oven was exposed to air. Once this layer has been ablated the neutral Yb flux should begin to flow and by tuning the laser around the wavelengths, we would expect we eventually saw a powerful 399 nm beam begin to fluoresce along the beam path.

3.1.4 Optical access view-port and mesh

Most of the parts that made up the vacuum system are made up of ‘off the shelf’ parts, from LewVac as detailed in section 3.1.1. This is not the case for the main optical view-port, which is a custom design made by Dr. Altaf Nizamani and coated for increased 369 nm transmissivity. This window is made to be recessed into the chamber so that the chip is only 5 mm away from the chamber window. The advantages of this are detailed in section 3.4, but in short it increases the number of photons that can be collected from the ion per second, during state detection, which minimises the required detection time.

The proximity of the ion to the window also presents a problem, because the window is made of dielectric silica material and so has a tendency to build up static electric charges across its surface. This is a problem for our ion as it at such close proximity would cause a large shift in DC field at the ion causing decoherence on our sensing experiment, which results in a loss of sensitivity (see section 2). This effect was calculated by Dr. David Murgia in his thesis [35] and was found to be noticeable for his recessed window which is very similar to ours. There are two possible solutions to this problem: one is that windows can be coated with Indium Tin-oxide (ITO), which is conductive so will ground any charges; or a wire mesh, that if pressed against the window will collect any charge build-up and ground it to the system. The main problem with both of these solutions is that the conductivity of the window will not only prevent charge accumulation, but also acts as a barrier to RF and microwave radiation. This is a problem for device that is designed to sense RF and microwave radiation and would prevent the delivery of microwave and RF through the front view-port for sensing and coherent state manipulation. We opted for using a mesh, because unlike with ITO coating, a mesh can have a hole cut in it around the centre so that we can have optical access and to allow RF and microwaves to be delivered. The optimal size of the hole so that charge build up is kept at a level that is not noticeable at the ion is done in Dr. David Murgia’s thesis [35] and was used to calculate the optimal size for our hole.

3.1.5 Ion pump and ion gauge

As detailed in section 3.1.1 after the system is pumped down to roughly 1×10^{-7} mbar the ion pump[13] is needed to reduce the pressure inside the chamber even lower down to UHV levels ($> 1 \times 10^{-9}$ mbar). The ion pump we are using is attached to the main chamber via a T piece so there is enough room for the entire pump without limiting the space available in the main chamber. This ion pump works by ionising the latent gas within the system allowing the ions to be accelerated under a strong electric potential into a cathode. This cathode acts as getter, which absorbs this latent gas and maintains a constant low pressure. As described in section 3.1.2 when the pump is exposed to air the getter is saturated with air particles rendering it useless for future pumping. This is why it is necessary to pump the system down from normal pressure to 10^{-7} mbar, before activating the pump. Activation is the process of heating the cathode to remove the particles bonded to the getter, which are then removed by the turbo pump. Once activation is complete the pump can then operate again as normal, although after multiple activations there is a significant degradation in the performance of the pump.

The ion gauge[14] is what we have used for making precise UHV pressure measurement down to 10^{-13} mbar. The ion gauge we used was a hot-filament ionization gauge, which works by emitting electrons from heated filament. These electrons are attracted to an anode grid with a large positive voltage applied. A fraction of these accelerating electrons will collide with gas atoms causing them to become ionised and are attracted to a negative cathode wire. When they hit the cathode it induces a small current in the wire, which can then be amplified and detected. As shown in section 3.1.2 when the pump is brought to UHV vacuum it must be activated to remove any contaminants on its surface to allow it to function properly at UHV.

3.1.6 Internal electronics

The chip is mounted on a copper block attached to two custom PCBs, as can be seen in figure 13. The chip is attached to a custom designed copper block using epoxy[15], which acts as a heat sink to prevent destructive heat build-up from high power RF used for producing trapping potentials. This copper block is screwed into the front PCB and the front PCB is screwed into the back PCB, which is mounted onto custom made brackets attached groove grabbers on the side viewports. Both the front and back PCBs core are made of Rogers RO4350B material with a Electroless nickel immersion gold finish. This was chosen for its UHV compatibility and its ease of use for wirebonding. Both the front and back PCBs were designed by Dr. David Murgia [35].

The chips DC channels are wirebonded to the front PCB using the wirebonding machine the IQT clean room. The DC electrodes were wirebonded multiple times and were shorted to neighbouring channels on the front PCB. This was done to allow me to check the channels are still connected to the chip by checking for the shorts on the external feedthrough. The RF rail and ground plane were also wirebonded, with multiple contingency wirebonds. The RF rail on the front PCB is attached to the vaccum system via an SMP connector attached to the rail using epoxy. The circular DC pads seen at the top and bottom of figure 15 are connected to the reverse of PCB, that are in physical contact with a set of gold pins[16], which connect the front PCB to the back PCB.

The back PCB contains the low-pass filter used to attenuate any noise picked up between the back PCB and the low-pass filters in the filter box outside the system (see section 3.5). To this end we employed a

[13] NexTorr D200-5
[14] EPIMAX PVCX Gauge
[15] Epoxy Technology EPO-TEK H21D
[16] Mill Max 0852-0-15-20-83-14-11-0

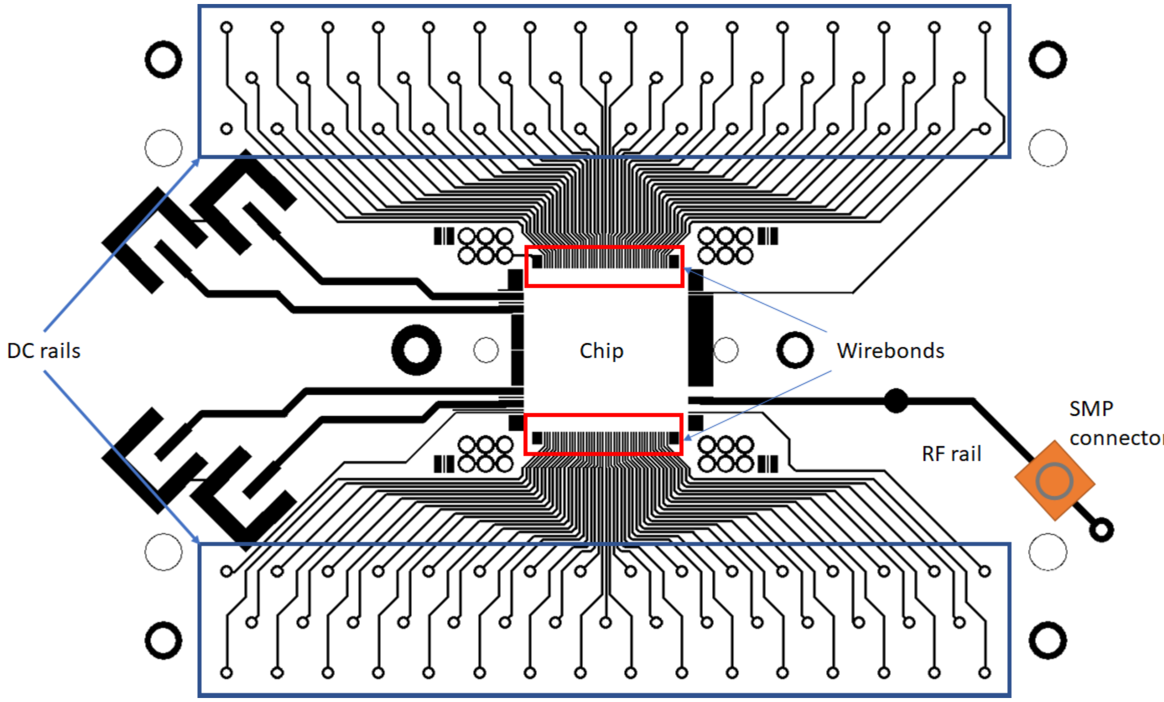

Figure 15: This a schematic of the face-up side of the front PCB. This shows DC pads where the DC potentials are introduced from the reverse side and where they are wirebonded to the chip in the centre. The position of the RF rail and the SMP connector which provides the RF voltage, is indicated. Design by Dr. David Murgia [35].

set of 620 pF capacitors[17] bridging each DC channel to ground and a 1 kΩ resistor on the track (position shown in figure 16). The track then connects to the gold pins mentioned above. This low pass filter provides a cut off frequency of 260 kHz, to remove RF signals from the DC channels disturbing the ion. The pins, capacitors and resistors were all fixed on the PCB using lead-free solder paste[18], which has better UHV compatibility, than regular solder paste.

3.2 Lasers and optical set-up

The principal lasers we used during experiments were 369 nm, 399 nm and 935 nm. The 369 nm laser as shown in section 2 is used for the doppler cooling of the ion as well as state detection. It is generated by an MSquared Ti:sapphire laser (SOLSTIS CW), which produces 739 nm light, that is directed through a SHG crystal (ECD-X) frequency doubler, to produce 369 nm light. The 399 nm and 935 nm lasers are both produced by separate Toptica DL pro lasers and all three of these lasers are fibre coupled to our table using custom made single-mode, polarisation maintaining fibres[19]. Many of the experiments in our laboratory use 635 nm light as well as there is a chance that ion will become trapped in a state that it can be re-pumped out of using this laser. The chance of this means that it will only happen on average once a day of trapping [35], so we determined that it was not worth the added complexity of an additional laser so did not include it within our system. All three lasers wavelengths are monitored by a wavemeter[20], which are monitored and locked by a LabView programme developed by PhD. student David Bretaud. The locking programme interfaces with the Toptica laser controller[21] for the

[17] Presidio Components VP0505NP0621K150V4M1R6
[18] Multicore 96SCLF320AGS88
[19] Thorlabs PM780-HP-CUSTOM
[20] HighFinesse WS-7
[21] Toptica SYS DC 110

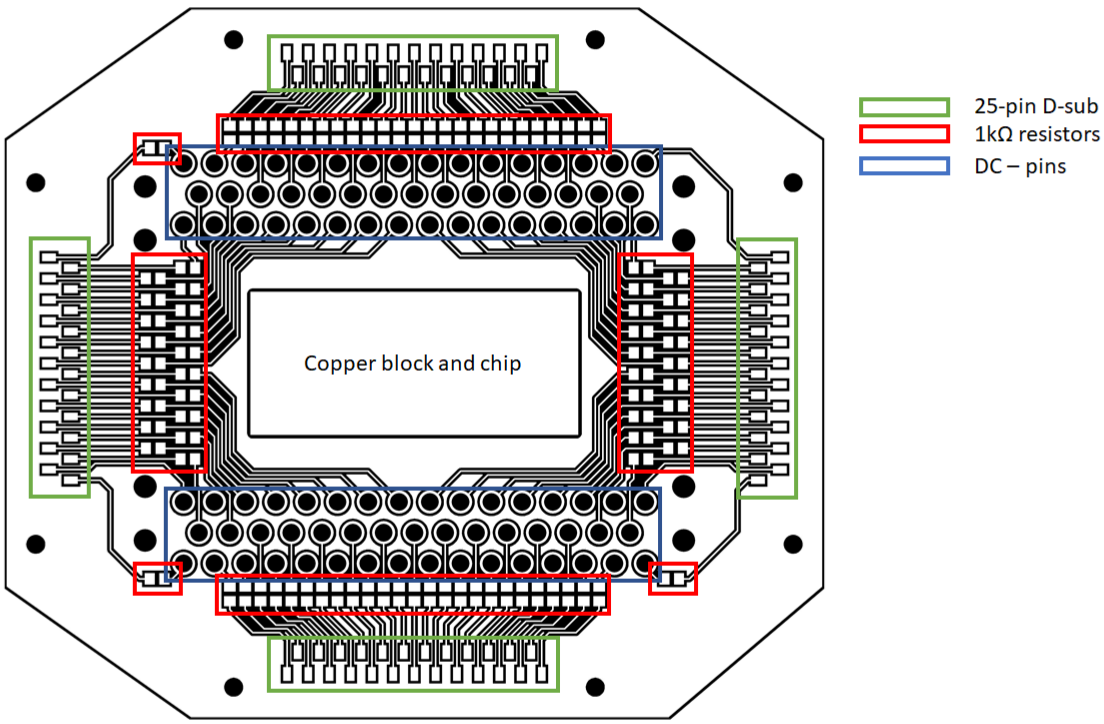

Figure 16: This a schematic of the face-down side of the back PCB. This shows the position of the pads where the gold pins that connect the front PCB by sticking out the back of this PCB, where the capacitors are situated. The position of the four soldered 25 pin D-sub connectors are shown, which brings the DC voltages from the DC feedthrough. The DC tracks then have to go through a resistor before going onto the gold pins. Design by Dr. David Murgia [35].

399 nm and 935 nm lasers. The 369 nm laser is locked more accurately using a locking procedure developed by my colleague Dr. Tomas Navickas [40]. The original laser layout was designed and assembled by my colleague Dr. Ethan Potter.

3.2.1 369 nm laser set-up

The 369 nm laser is principally used for Doppler cooling, state preparation and readout, therefore it must be very precisely locked and modulated far more than the other three lasers. This requires an Acousto-Optic Modulator[22] (AOM) and an Electro-Optic Modulator[23] (EOM) to be able to accurately modulate the freuency of the laser by around 100 MHz. The AOM/EOM set-up is situated near the source of the 369 nm laser light due to spatial constraints on the optics table, this set-up is shown in figure 17. The beam profile after going through the AOM/EOM optics is usually non-Gaussian, which is undesirable for aligning the beam to the trapping position and avoiding scatter off the chip. After the AOM/EOM optics the beam is directed into a fibre coupler, which is then coupled to another coupler on the table with the vacuum system. The resulting output beam will be Gaussian even with an non-Gaussian input. A diagram showing how the AOM/EOM system is set up is shown in figure 17.

The AOM works by applying a laser through a crystal, which has a AC electric current applied to it. This splits the incident laser into multiple beam 'orders' starting with the 0 order which has the same beam path as the original beam as well as the same wavelength. The subsequent orders are angled away from the zero order with shifted frequency. The magnitude of the frequency shift can be modulated by changing the RF power and frequency of the AC source, which is supplied by the AOM driver[24]. The angle of the beam into the AOM was optimised to maximise the strength of the 1st order beam out of the AOM. The 1st order is then isolated and passes through a 100 mm lens to focus the beam onto a prism that reflects the beam back along the beam path and is collimated by the same lens. The laser is then directed back into the AOM, which then produces the same splitting effect and the first order is then isolated again. This double pass procedure is done to allow the frequency to be changed without moving the beam itself as the spitting effect is cancelled out by the double pass.

After the AOM the beam is directed at the EOM, which is a device used to add side bands to the input laser. The EOM RF signal is provided by an EOM driver system[25]. The laser is usually attenuated by the EOM so the angle and polarisation of the input beam needs to be adjusted, hence the inclusion of a half waveplate and a quarter waveplate just before the EOM. After the EOM the beam is coupled to a single mode polarisation maintaining fibre using one of our home built couplers with a collimating lens. The coupling is polarisation dependent so a half wave plate is utilised just before the coupler. The fibre is then fed across the laboratory to the experiment table over about 15 m.

3.2.2 Beam combination

The 935 nm and 399 nm lasers are produced on separate tables from the experiment and supply laser light to multiple experiments. This is not usually an issue as most of the experiments in our laboratory use the same Yb isotope for experiments and hence transition frequency, which does not need to be changed (unlike 369 nm). Each laser is fibre coupled into one of our custom made couplers and is optimised using a mirror directing the

[22] Isomet AOM 1206C-833
[23] QUBIG EO-T2100M3
[24] Isomet 630C-110-G AO Driver
[25] QUBIG RF generator + amplifier

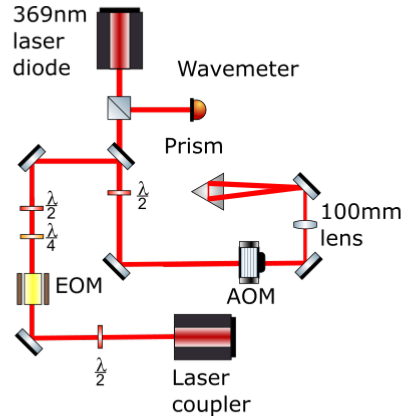

Figure 17: Diagram of the AOM/EOM optics before the fibre coupler to the experiment. The 369 nm laser is initially directed into the AOM, which splits the beam into multiple orders of which the first order is isolated and focused with a 100 mm lens. This focuses the beam onto a prism that reflects the beam back along itself through the lens and back into the AOM. The beam is then split again into orders with the first isolated and directed into an EOM before being directed into a coupler.

beam into the coupler and the coupler itself, which is mounted onto a mirror holder.

The output of the 369 nm coupler is collimated with a lens and is put through a 100 mm focal length lens to focus the beam onto a 100 μm pin-hole before collimating the beam again at the other side. This is done to produce a clean Gaussian beam profile from the 369 nm. Also by changing the distance between the second lens and the pin hole, the size of the beam that is collimated can be modulated. This is especially important for the 369 nm as we require a strong beam that will not scatter off the chips surface and cause charge build up, which could disturb the ion. More detail on the exact design and justification of this telescope set-up can be found in Dr. Ethan Potter's thesis [39].

The 369 nm laser is then directed into a dicroic beamsplitter, which transmits 369 nm light and reflects 399 nm light. The 399 nm laser coupler collimates the 399 nm beam and then is directed into the beamsplitter, where it is combined with the 369 nm beam. The combined beam is then combined with the 935 nm laser at a cold mirror, which transmits 935 nm light and reflects the combined 369 nm and 399 nm beams. The three beams are combined on the cold mirror and directed to a gimbal mounted mirror, which reflects the combined beams into the chamber. Just before the chamber there is a 150 mm lens that focuses the beams to a point at the trapping position. The minimum spot sizes at the trap position for the 369 nm, 399 nm and 935 nm beams was 20 μm, 100 μm and 100 μm respectively. This maximises the laser power at the trapping position and minimises the laser scatter off the surface of the chip, which would produce charges that could build up disturbing the ion. The angle and position of the combined beam into the system is done with a gimbal mounted mirror attached to a three dimensional translation stage[26]. The stage can adjust the displacement of the beam in and out of the chip and the mirror can be adjusted to angle the beam up and down the surface of the chip. The vertical angle into the system can be adjusted as well by adjust the gimbal mirror mount in conjunction with angling the cold mirror. Although this does mean that the beams have to be recombined. The total beam combination optic set-up can be seen in figure 18 as it was redesigned by myself and Dr. Tomas Navickas.

[26]Mitutoyo Digital Micrometer 350-351-30

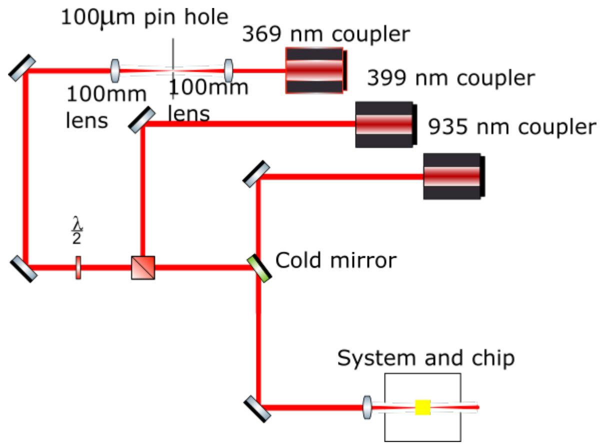

Figure 18: Laser diagram of immediate set-up outside the system. The 369 nm, 399 nm and 935 nm lasers are all fibre coupled to the table using single mode optical fibres and custom made fibre coupler with lenses that are adjusted to collimate the beams. The 369nm lens is put though a 100 mm lens and then a 100 μm pinhole and then collimated with another 100 mm lens on the other side on a one dimensional stage. The 369 nm and 399 nm beams are combined in a dicroic beams splitter before combining with the 935 nm using a cold mirror before being directed into the system using a gimbal laser mirror. The beam is finally focused with a 150 mm lens onto the trapping position.

3.3 Experimental control system

3.3.1 FPGA box

The control system for our experiment is used for conducting coherent experiments, by providing pulses of 369 nm, RF and microwaves, at incredibly precise times to manipulate the internal state of the ion. The principal component of our control system is the field-programmable gate array[27] (FPGA), which produces and receives all the Transistor to Transistor Logic (TTL) pulses required for a coherent experiment. The sequences are dictated to the FPGA using a PC using ARTIQ Python based scripts (see section 3.3.2), which can also collect and interpret data from the experiment. The TTL pulses from eight different output channels go to two Direct digital synthesis (DDS) boxes that produce RF signals for coherent manipulation and for frequency mixing to produce microwaves as detailed in section 3.3.3.

The FPGA is utilised in our system to produce TTL pulses that can turn the RF and microwave sources off and on in nano-second precision, which is crucial to maximise the fidelity of the experiments. The FPGA can also receive TTL packets from the PMT (see section 3.4) to count individual photons that may be only nanoseconds apart. This speed is crucial to be able to do state detection very quickly and with high fidelity. Python scripts are loaded onto the board using a an ethernet connection to the master control PC. The FPGA then runs the pulse sequence and sends TTL packets into a custom made breakout PCB (see figure 19). This breaks the input and output channels into separate shrouded headers[28] that connect to ribbon cables and on to the input and output buffers. This system was designed by Dr. Simon Webster in collaboration with Christopher Ballance from the University of Oxford and was assembled and tested by myself.

The input and output buffers are used to invert the signals being produced and received by the FPGA. These are made from custom PCB boards designed by Christopher Ballence and assembled by myself. A diagram

[27] Xilinx FPGA KC705
[28] Farnell-T812112A100CEU

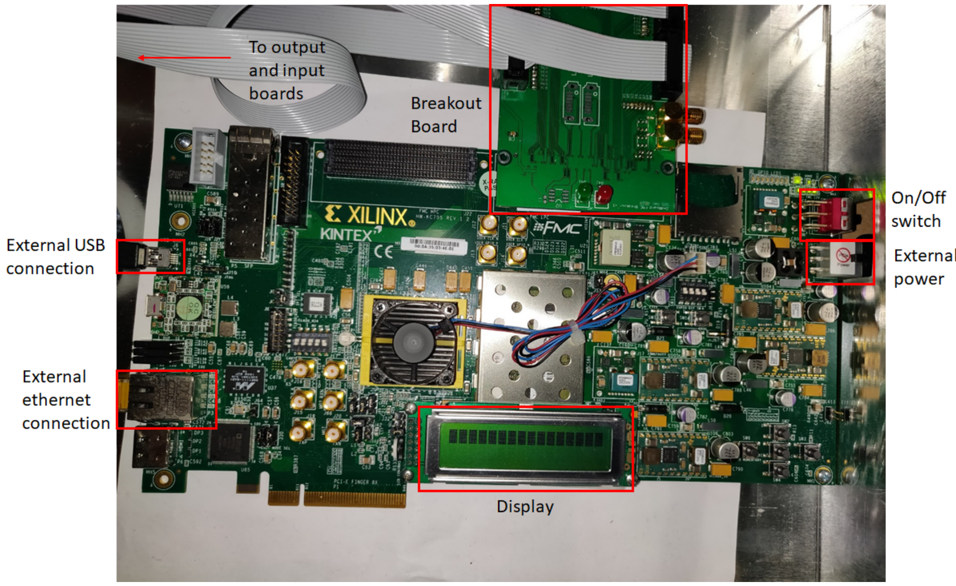

Figure 19: The FPGA board used for our experiment installed in the control box. The breakout board where the TTL pulses are received and output is labelled. Signals are then taken to the output/input boards via ribbon cables. USB and Ethernet connectors are shown that allow me to control the board from the control PC. The display is used during troubleshooting the board.

showing the output board design is shown in figure 20 as well as a simple circuit diagram of one of the four channels on the board. This output buffer works by receiving signals from the shrouded header[29], which are pulled up to the 3.3 V supply of the board via a 100 kΩ resistors. This is done to ensure that board always receives a well defined signal. The signal then goes into an output inverter[30], which outputs a high signal when the input is low and vice-versa. The resulting output goes through a 33 Ω resistor to prevent current spikes from connecting the output to ground or a high capacitance component. This is then connected to a external BNC connectors[31], which pass signals to the DDS boxes (see section 3.3.3) to switch on and off the RF and microwave sources to the trap with nanosecond precision to produce pulse sequences. Two decoupling capacitors were utilised on the board's power supply to insure the rise time is as fast as possible.

The input boards are very similar to the output board (as seen in figure 21) and use all the same components except for a different input inverter[32]. In this case the circuit is in reverse where TTL signals are received from the BNC connectors and are pulled down to ground via 33 Ω resistors to avoid current spikes and the output is connected to the shrouded header, which goes to the FPGA.

3.3.2 ARTIQ

Advanced Real-Time Infrastructure for Quantum physics (ARTIQ) is a piece of software that has been developed by M-labs specifically for quantum related experimental set-ups, which is used by many quantum groups in the UK and abroad such as at Oxford University and NIST. ARTIQ uses scripts written in Python to simultaneously run pulse sequences for experiments via the FPGA (see section 19), set RF and microwave frequencies using the DDS boxes (see section 3.3.3) and also run analysis in real time. The ARTIQ dashboard programme provides

[29]Farnell T821112A1S100CEU
[30]Farnell SN74AC04PW
[31]Toby B-P225-DC-50-R
[32]Farnell SN74LVC04APW

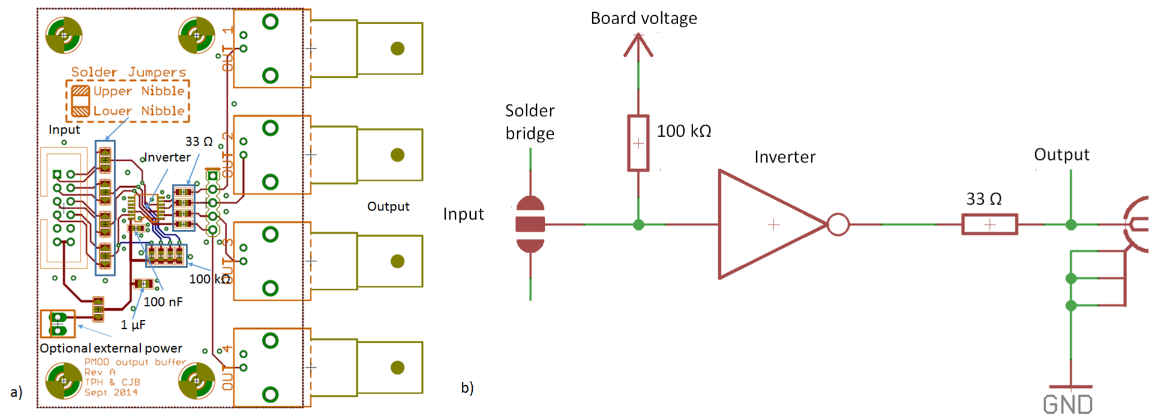

Figure 20: a) PCB diagram showing the layout of output buffer boards. The signals from the FPGA are taken from the 2 by 6 shrouded header and the channels that are needed are selected using the solder jumpers. The signals are then given the opposite of their original value (high signals become low and low signals become high) using an inverter. The outputs of this inverter then go to through a 33 Ω resistor before reaching the output BNC connectors. The Inverter is powered using a 3.3 V supply from the FPGA. Also the use of resistors and capacitors to ground is used as a low pass filter to avoid noise and drift. b) A simple circuit diagram of one of the four output channels described above.

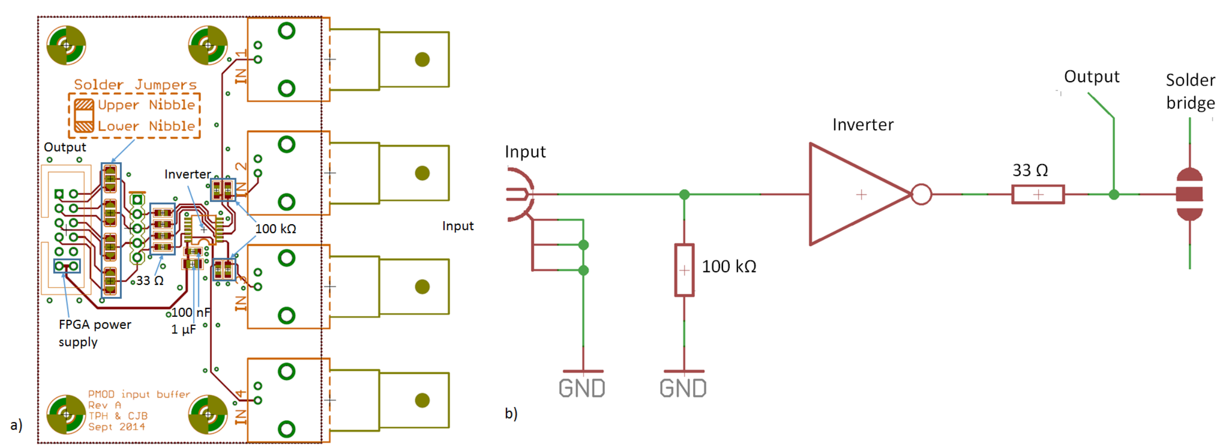

Figure 21: a) PCB diagram showing the layout of input buffer boards. The signals for the FPGA are introduced via external BNC connectors. These four channels are connected to 100 kΩ resistors that go to ground, which provide a drain for the input. The signals are then given the opposite of their original value (high signals become low and low signals become high) using an inverter. The outputs of this inverter then go to through a 33 Ω resistor before reaching the output shrouded header, which connects to the FPGA. Also the use of resistors and capacitors to ground is used as a low pass filter to avoid noise and drift. b) A simple circuit diagram of one of the four input channels described above.

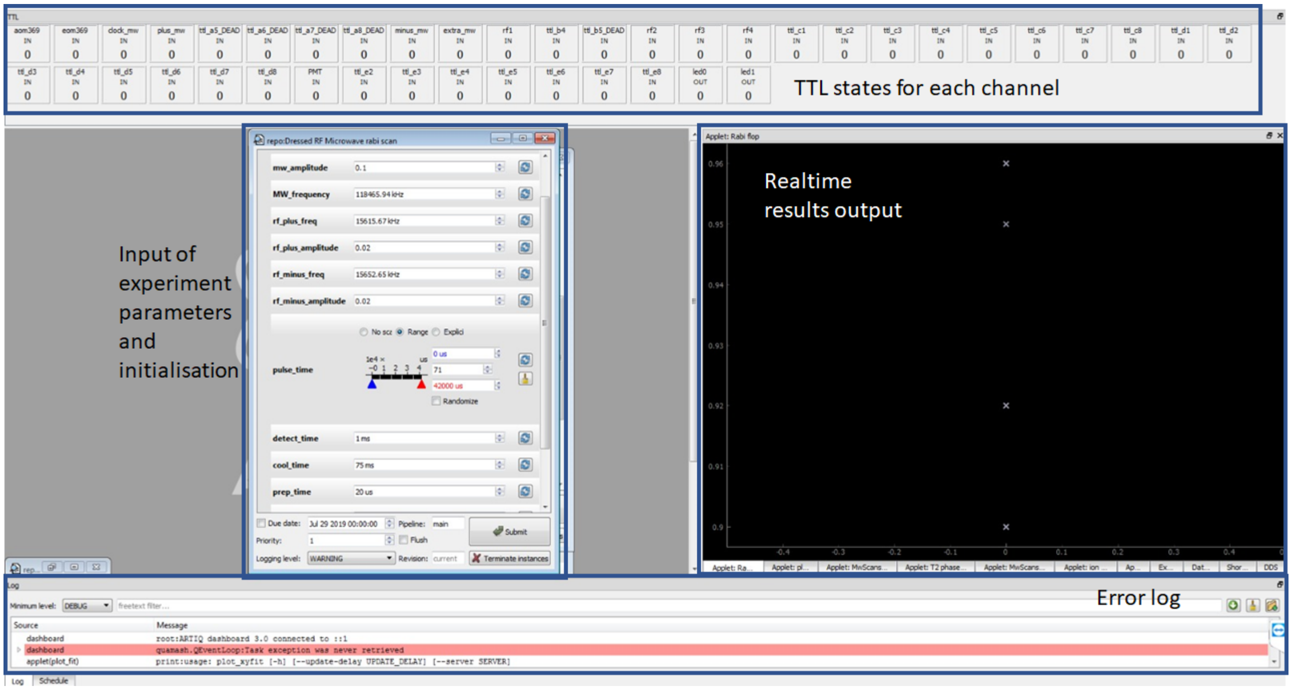

Figure 22: This is a screenshot of the ARTIQ dashboard, where all experiments are set, run and monitored. The top bar shows all the TTL inputs and outputs, while showing their respective states, to indicate whether or not the sequences are operating as intended. The panel to the left shows an experimental input window for dressed state microwave frequency scan for measuring the π time of a certain microwave transition. Here all the different initial experimental parameters can be input, as well as swept parameters and the number of steps in that sweep. To the right is where the plotted data is displayed from the computer building up probability distributions of the state of the ion after each experiment. This data can show the state probability against the swept parameter and even do basic analysis and plotting. The bottom panel is for error and load logging.

a useful interface to upload Python scripts to and change experimental parameters on the fly, as well as adjust swept parameters (see figure 22). I used ARTIQ Python scripts to run analysis at the end of each experiment to extract useful parameters such as the peak frequency of a given transition and its π time and incorporate these parameters into future experiments automatically. This allowed for far more scope for the automation of the experiment leading to faster data collection and more efficient working. Our ARTIQ framework was developed in collaboration with my colleague Dr. Simon Webster and Christopher Ballance from Oxford University as well as myself. The initial set-up software development was done by Dr. Simon Webster, but all final experiments, which were used for data collection were written in Python by myself. More information on the exact experimental sequences carried out in my Python scripts are shown in section 4 and the actual code that was used can be found in the appendix A.

3.3.3 DDS

The FPGA controls the TTL pulses that control when the RF and microwaves fields are applied to the ion with nano-second accuracy (see section 3.3.1). However it is the Direct Digital Synthesizer (DDS) evaluation boards[33] that set the microwave and RF frequencies at the beginning of each experiment. This is done via a USB connection to control computer, which runs all the ARTIQ pulse sequences (See section 3.3.2). With the

[33] Analog Devices AD9959

frequencies selected the board produces them using a external 25 MHz clock frequency source[34]. In constructing the DDS box I attempted to use an oscillator crystal soldered onto the board instead of the external source, but found the resulting signals too unstable at the intended frequencies I wanted. The board produces four separate channels that are each amplified using +15 db amplifiers[35]. This is done to give the RF enough power to reach the minimum requirements for the RF switches[36], which can switch the RF on and off in nano-seconds. These switches are controlled by TTL pulses generated by the FPGA (See section 3.3.1). The original DDS layout was designed by Dr. Anna Webb and adapted by myself.

The four signals are then wired to external BNC connectors and cabled onto the optics table near the system. These four signals are then joined together using a RF combiner[37] so they can be emitted from the same RF coil. Just before the RF coil the signals are amplified a final time by a +43 db RF amplifier[38] to give the RF enough power to produce a strong signal at the ion. Finally the combined amplified signals are sent to an RF coil wrapped around the detection optics next to the main optics window, so that the RF can be delivered through the wire mesh covering most of the window (see section 3.1.4). A diagram of this set-up can be found in figure 23.

To produce the microwaves that are needed for the experiment we use an identical DDS box with the same components and assembly. The four outputs are combined as with the RF DDS outputs on the optics table near the vacuum system. They are subsequently mixed using a microwave mixer[39] with a 12.64 GHz signal from a vector signal generator[40]. This means we can apply microwaves to the ion without changing the microwave source frequency as we only need to use microwaves up to 100 MHz around the Yb clock frequency of 12.64 GHz. After mixing the resulting signal is amplified using a microwave amplifier[41], before reaching the microwave horn[42]. The horn is mounted on a waveplate mount with rotation adjustability inside the main viewport next to the detection optics tube. This is necessary as it allows me to adjust the incoming polarisation of the microwaves, for Doppler cooling on the ion by addressing the individual hyperfine states of the $^2S_{1/2}$ ground state of $^{171}Yb^+$. A diagram showing this set-up including the microwave components is shown in figure 23.

3.4 State detection system

To make state detection measurements there is a need to reliably ascertain the state of the ion after each experimental run, so that the state probability can be accurately determined. To this end an optical system was designed by Dr. Ethan Potter and Dr. Altaf Nizamani, then assembled and aligned by Ethan Potter. After changes to the experimental layout on the optics table I disassembled the optics system before reassembling it in its new location and subsequently realigning it.

A diagram of the state detection system is shown in figure 24. We acquired a custom made optics system[43], which is designed to collect as many photons from a fluorescence at the ion as possible. Hence the objective lens is placed as close to the chip as physically possible to maximise the detection angle of the photons

[34] Stanford Research Systems DS345
[35] Mini Circuits ZFL-750+
[36] Mini Circuits ZASW- 2-50DR+
[37] Mini Circuits ZMSC-4-3+
[38] Mini Circuits LZY-22+
[39] Marki Microwave T3-03-16M
[40] Hewlett Packard HP-83712B Synthesized CW Generator
[41] Microwave Amps AM51-12-6S-43-43
[42] Flann Microwave 18240-10
[43] EKSMA Optics PLCA1

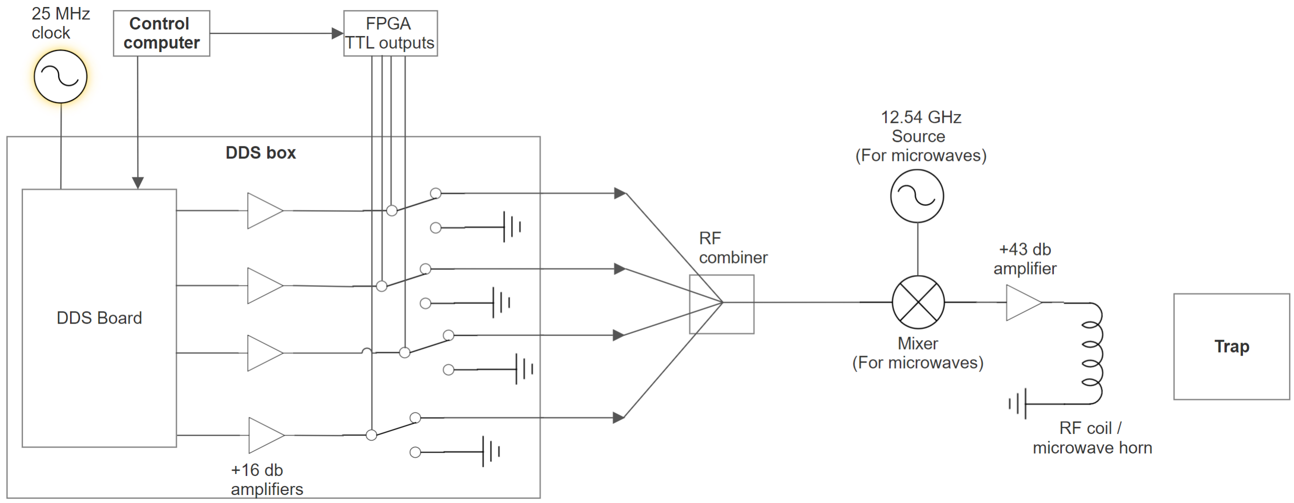

Figure 23: A schematic of one of the DDS boxes that can generate the RF and microwave signals for the experiment. This signal can have any frequency between 1 MHz and 500 MHz with a power of up to 0 dBm and is produced using a 25 MHz external clock frequency. These signals are then amplified before being connected to the TTL switches that are controlled by the FPGA. Each channel is then wired onto the optics table where all four channels are combined. The microwaves are produced by mixing the combined RF channels with a 12.54 GHz source, before being amplified a final time. The other four channels of RF are fed into an RF coil, which delivers the frequencies to the ion.

leaving the chip. The objective lens is housed in a plastic case[44] as opposed to the usual metal casing for the rest of the optics tube. This is to allow the microwaves and RF delivery to the chip as the horn and RF coil are in close proximity to the objective and could deflect these waves if made from metal. An adjustable iris is placed at the focus of the objective so that the light from the ion trapping region of the chip can be isolated. This helps to increase the fidelity of our experiments. A doublet then focuses the light to our detection apparatus through a narrow bandpass filter[45] to allow 369 nm light to pass while eliminating other wavelengths. This again allows us to run our experiment without low light levels and increases the fidelity of the experiments.

Their were two different methods we employed for detecting ion fluorescence: one is using a CCD camera[46], or a Photo-multiplier tube[47] (PMT). These devices are selected by using a flipper mirror that can direct the light straight through to the PMT or can be directed at the CCD camera at a 90 degree angle. The CCD camera is used principally to image the trap for calibration and finding the rough trapping position. Once trapping runs begin the CCD camera is used to detect when trapping has occured and to find the ion height for future experiments. After initial calibration and trapping, the CCD camera becomes less useful for coherent experiments due to its low refresh rate and quantum efficiency meaning the detection time would have to be substantially longer. The PMT however is ideal for coherent experiments due to its ability to count individual photons that are only nanoseconds apart, allowing for shorter detection times and higher fidelities. More details on the exact design of the optical system as well as justification for these decisions can be found in Dr. Ethan Potters thesis [39].

[44]Ketron 1000PEEK
[45]Semrock FF01-370/36-25
[46]Andor iXon+
[47]Hammamatsu H11870-01

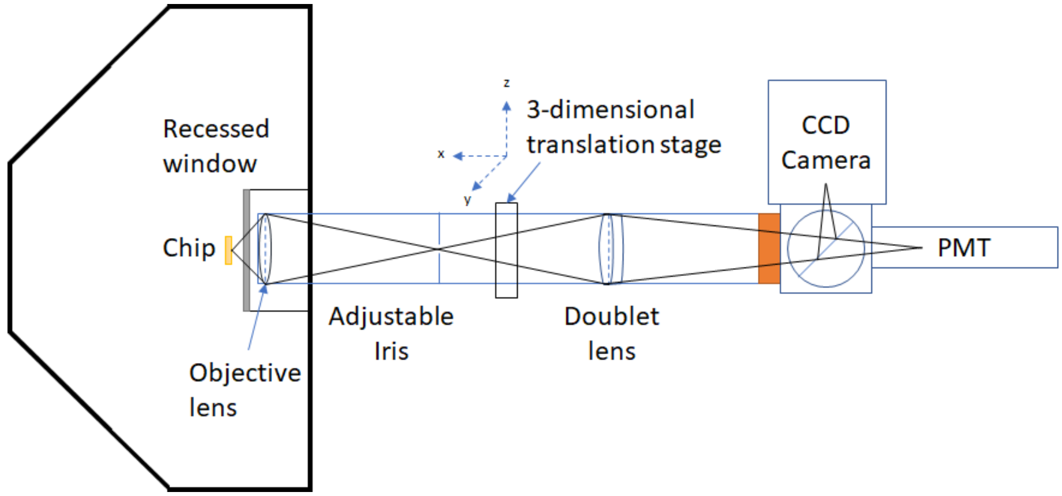

Figure 24: This is a diagram of the state detection system for the system, this shows the vacuum system with the ion trapping microchip to the left. The optics tube has an objective lens for collecting the light from the ion and is positioned right against the glass of the viewport. At the focus of this objective there is an adjustable iris used to remove any extraneous light. A doublet is then used to focus the light through a 369 nm filter onto a flipper mirror which can direct the light onto the CCD camera or the PMT. The entire tube position is adjusted using a 3-axis translation stage for optical alignment.

3.5 DC System

As detailed in section 2.1 both RF and DC potentials are needed to use a Paul trap to trap Yb^+ ions. The DC voltages for the system are required to be very precise and very stable with as little high frequency noise as possible. Each of these channels needs to be generated and adjustable before being filtered and finally wired into the system where the DC channels are applied to the chip.

The DC voltages are generated using a voltage card[48] installed in our dedicated DC control computer. This card is capable of generating 16 unique DC voltages capable of producing voltages from +10 V to -10 V, which is more than enough for our chips which generally only require voltages between -5 V and +5 V (see section 2.1). The output of this voltage card is a 45 pin D-sub which is then connected to a custom made breakout box built by myself, which breaks out the D-sub using a PCB into 16 individual SMA connectors. Only eight channels are used for the trapping potentials and two are used for AOM control, the remaining DCs are redundancies.

Between the generation of the DC voltages and the vacuum system there is a significant length of cable, with multiple connectors and a PCB. All of these components add RF noise to the system from the environment, which can be very destructive to the ion trap as it will cause the ion to oscillate and heat up until it leaves the trap. This problem is resolved by constructing a set of low-pass filters for each DC channel to remove the RF noise of the voltage they may have accumulated, leaving only the DC values. The filters are a four stage low-pass filter designed by Dr. Bjoern Lekitsch, the circuit diagram of this design is found in figure 26. I used PCBs designed by Dr. David Murgia to produce a filter box with up to 100 possible filtered connections. The SMA connections are filtered before being output through headers, which are connected to a PCB designed by myself, that convert the 100 channels into a 78 and 26 pin connectors. These can then be directly interfaced with the vacuum system DC electrical feedthrough, through two short D-sub cables to minimise noise after the filtering. To verify that the filtering had reduced the amount of RF noise to an adequate level a computer controlled

[48] Analog Devices AD9959/PCB

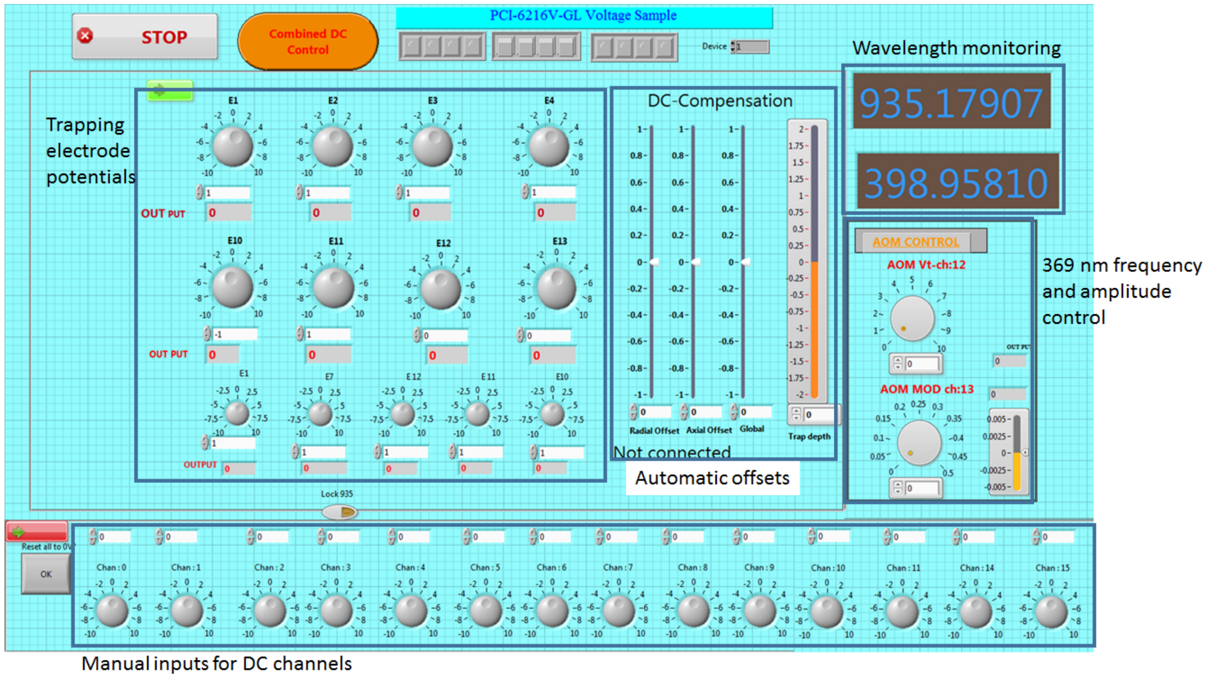

Figure 25: The LabVIEW interface for control over both the DC system and the AOM. The eight large dials in the top left indicate the applied DC potential for the electrodes used for trapping. Here the electrode potentials can be maunually set and monitored. The four sliders near the centre of the panel from left to right: radial offset, which uses rotation electrodes from the centre; the axial offset displaces the ion from the exact centre of the four trapping electrodes; and trap depth, which attempts to change the relative trap depth of the whole system. The bottom panel is used to monitor and change all the available DC channels available. The two dials to the far right are used to control the AOM controller (See section 3.2.1), the top dial is used to control the wavelength of the 369 nm laser and the bottom dial is used for changing the relative intensity of the beam. The top right panels monitor the wavelengths of the 935 nm and 399 nm beams.

spectrum analyser[49] was used, the results are shown in figure 27 and show the substantial reduction.

The DC potentials were designated using a LabVIEW programme installed on the computer with the DC output card. This programme was initially designed by MSc student Ben Sayers to directly control all 16 channels, but was subsequently improved by post-doctoral fellow Dr. Altaf Nizamani to include automatic axial, radial and trap depth shifts to the trap without the need for simulations. This newer interface is shown in figure 25. This programme also utilises two channels for the purpose of AOM control used to change the RF intensity and frequency sent to the AOM to modulate the output frequency and intensity of the 369 nm laser. More details can be found in section 3.2.1.

3.6 Trapping RF generation

RF is a critical component in the ability to trap using our 2-D surface traps as detailed in section 2.1. Generating RF for trapping voltages can be quite challenging as there is need to produce relatively large voltages efficiently at the chip. This is due to the fact that there must be near perfect impedance matching between the RF source/amplifier and the small electrical load of the microchip. An RF resonator circuit is employed to provide this matching and to avoid the RF from reflecting back from the chip and damaging the circuit. A capacitive

[49] SignalHound USB-SA44B

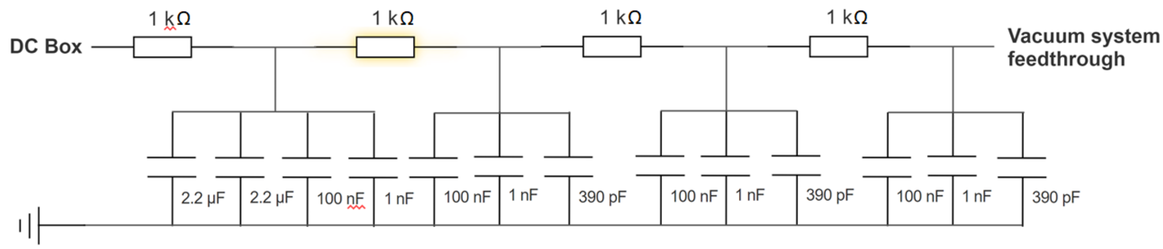

Figure 26: Circuit diagram denoting the low pass filter used to remover high frequency noise. Designed by Dr. David Murgia.

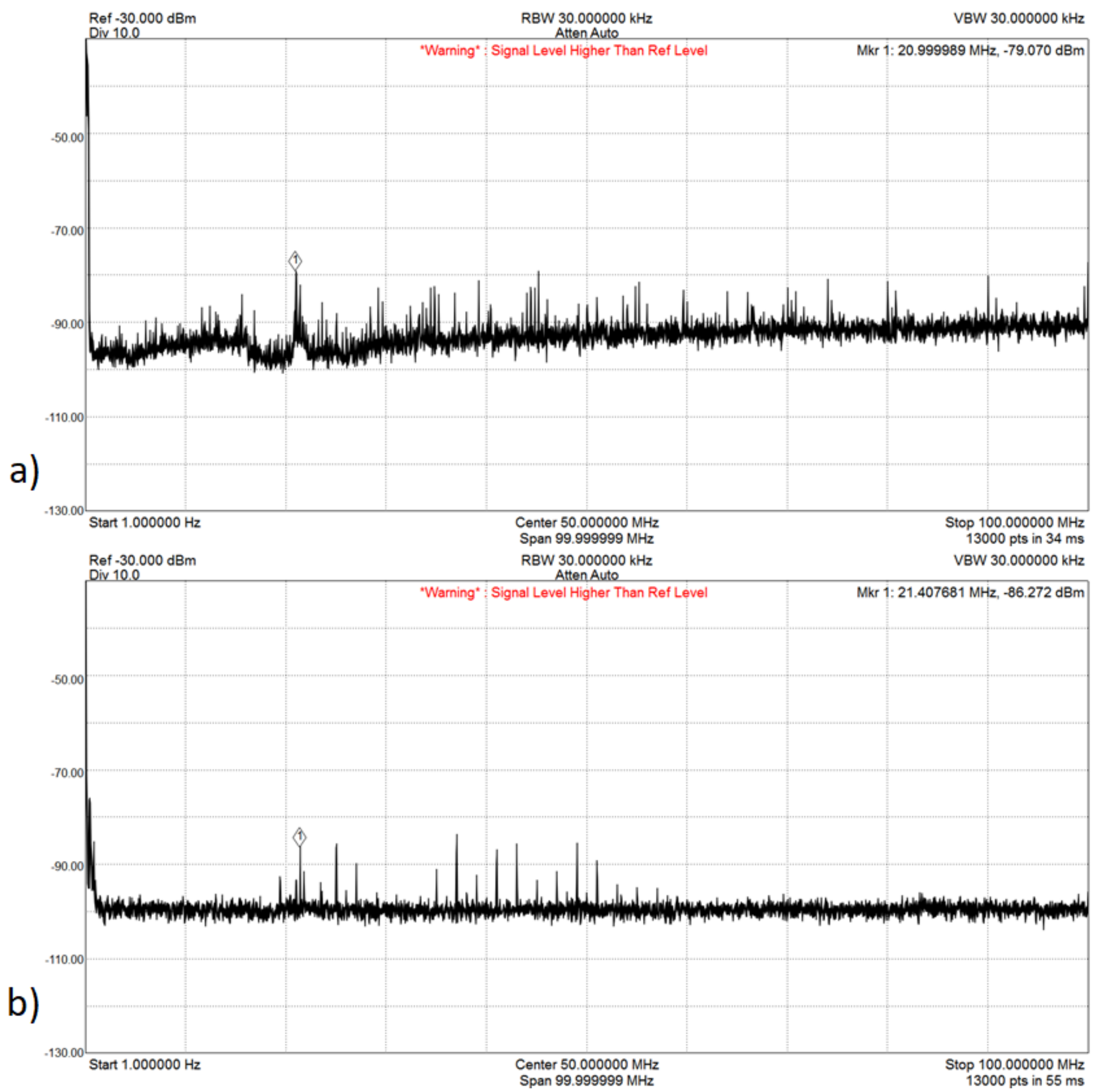

Figure 27: a) RF noise spectrum of the output of the DC breakout box without filtering showing a peak noise value of around -79 dBm b) An RF noise spectrum of the output of the filter box after applying a DC value to it, this results in a maximum RF noise value of -86 dBm.

divider is also used to monitor the RF frequency and amplitude applied to the chip. This system for trapping RF delivery was designed and built by Dr. Ethan Potter and more details on the design and reasoning for these design decisions can be found in his thesis [39]. A diagram displaying the RF delivery circuit is displayed in figure 28.

The RF is produced by a signal generator[50] before being being put through a 40 dB RF amplifier[51]. The resulting amplified signal is then put through the resonator, which is a cylindrical copper can with a large copper coil attached to the input through to ground. The output is a smaller coil made of copper wire, which is situated inside the larger coil. The quality factor Q of this resonator is optimised by adjusting the shape and position of the smaller coil (which can be reshaped by hand quite easily), before being put inside the can. The resonator can is then attached to a Vector Network Analyser[52] (VNA), which can determine the Q of the circuit. The output coil can then be repeatedly adjusted until the optimal Q is achieved.

Immediately after the resonator there is a T junction that diverts a portion of the RF power for measurement by a capacitive divider. A capacitive divider is a simple circuit shown in figure 28, which is a small capacitor between the input and output and a larger capacitance to ground between the input and output, in our case 0.2 pF and 20 pF. The purpose of this circuit is to take a small portion of the RF signal out of the resonator, so that it can be measured by an oscilloscope. The signal on the oscilloscope can be used to determine the amplitude of the RF being applied to the chip. The frequency at the oscilloscope and the chip should be identical, but the amplitude is determined by applying a multiplication factor to the measured amplitude on the oscilloscope. The desired ratio chip to divider ratio should be small enough that there is a measurable signal at the oscilloscope to ensure the proper amplitude is applied to the trap, but large enough that the vast majority of the power is sent to chip and that the power limits of the oscilloscope are not exceeded. This ratio is determined by the ratio of the two capacitors used in the capacitive divider, so in our case: 20 pF/0.2 pF=100. This is a very rough estimate and assumes that the capacitance of the oscilloscope port is negligible.

[50] Rigol DG4062
[51] MiniCircuits ZHL-5W-1+
[52] Farnell ZNLE3

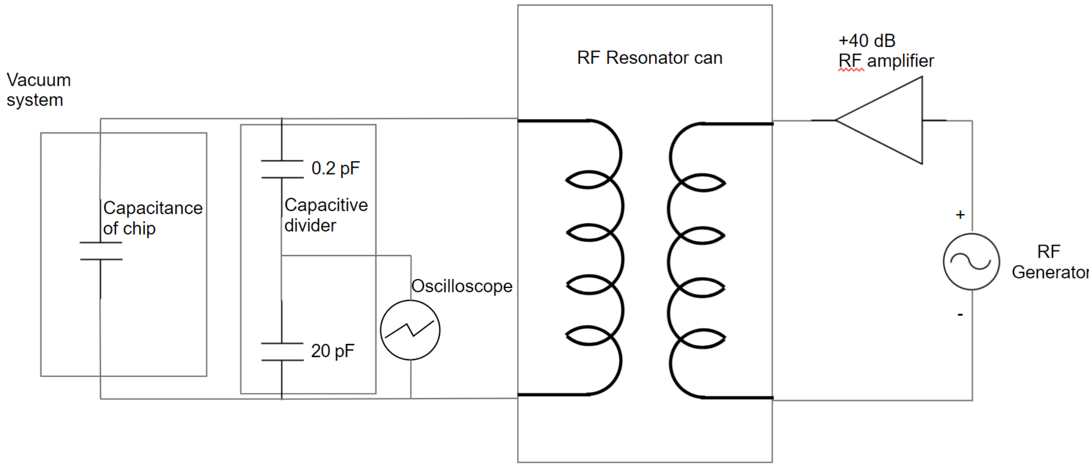

Figure 28: Circuit diagram displaying how the trapping RF is generated and amplified. A Resonator is used to impedance match the RF signal to the chip to ensure maximum power transfer. A capacitive divider is also shown in the circuit to monitor the voltage being applied to the chip using an oscilloscope.

To determine the exact ratio experimentally, the circuit from figure 28 was rearranged, where instead of connecting to the chip, the cable is attached to another port of the oscilloscope instead. A very small voltage is then applied so as not to damage the oscilloscope and a ratio can be taken of the first oscilloscope channel and the second. Multiple voltage measurements are taken from the two ports with different power being applied as the ratio generally changes linearly with increased applied power. After a number of measurements are carried out, the ratio at the desired trapping voltage can be determined by extrapolating up to that voltage. This measurement can be made even more accurate by measuring the exact capacitance of the chip, external and internal cabling and add an equal amount of capacitance to the connection to the second oscilloscope port to simulate the load of the chip.

4 Results

So far I have described how the system was built and how it works as a sensor. Now I will show how this was employed to measure RF and for the first time for ion trap quantum sensors microwaves! I will go through the procedures we went through to contain Yb ions and optimise the trap, before measuring the coherence time of the system and conducting sensing experiments to ascertain the exact sensitivity of the system. The work of collecting this data and working on the system day-to-day was in collaboration with my colleague, Dr. Ethan Potter, who conducted much of the data analysis seen in this section, while I focused on writing the Python code necessary to conduct the pulse sequences needed to run the experiments.

4.1 $^{174}Yb^{+}$ and $^{171}Yb^{+}$ trapping and trap optimisation

In this section I will detail how we initially trapped both $^{174}Yb^{+}$ and $^{171}Yb^{+}$, as well as ascertain various trap parameters such as micro-motion and secular frequency. The reasons for trapping $^{174}Yb^{+}$ before $^{171}Yb^{+}$ are detailed in section 2.2.2, but in short are because of the need for microwaves for Doppler cooling, and due to the ion's sensitivity to the polarisation of the microwaves and 369 nm laser. Once trapped, the parameters for the optics and laser positioning can be optimised to make the subsequent trapping of $^{171}Yb^{+}$ far easier. The micro-motion (see section 2.1.3) of the system is also measured and compensated for by applying proper DC voltages.

4.1.1 Trapping $^{174}Yb^{+}$

Once all the apparatus was assembled as described in section 3, (with the exception of the Helmholtz coils; RF and microwave emitters and generation; and control system) we began trapping $^{174}Yb^{+}$. This procedure begins with overlapping the 369 nm, 399 nm and 935 nm beams and focusing them at the expected trap position. RF and DC trapping parameters for the system were simulated by Dr. Ethan Potter [39], to ascertain which DC electrodes should be used and what potentials should be applied to them, as well as RF frequency and potential for the RF rails. The 399 nm laser had a laser power of roughly 200 μW and the 935 nm was around 8 mW. These powers were quite high to produce a power broadening effect, so if our applied wavelengths are somewhat detuned from resonance, there will still be sufficient power on resonance to address the ion. The 369 nm laser power was around 100 μW for initial trapping as it is not ideal to apply this wavelength at high power to the chip as any scatter from the chip can interfere with the optics and possibly produce a charge build-up, which could interfere with the trap. To avoid this scatter we built a laser telescope (As described in section 3.2.2) for the 369 nm beam to constrict the beam waist to around 50 μm. Just before trapping is carried out a fluorescence test is done using the natural atomic oven (more detail in section 3.1.3), to check the oven is functioning as intended and to find the 399 nm fluorescence wavelength for both $^{174}Yb^{+}$ and $^{171}Yb^{+}$. This is so we can apply our 399 nm laser with confidence we are applying the correct wavelength. The 369 nm beam is detuned with the AOM to be around 50 MHz away from resonance for optimal Doppler cooling rate.

Trapping runs are done in a very systematic manner to sweep the various parameters, which are unknown for optimal trapping these include:

- 369 nm wavelength.
- 935 nm wavelength.
- Trap position in the y, z direction (see figure 29).

- Detection optics focal point position.
- DC and RF voltages applied to the trap.

The 935 nm wavelength parameter can be safely ignored as the power of 8 mW will mean the laser would be sufficiently power broadened, so there is very little chance that the drift from the wavemeter or the Doppler shift associated with the system will effect the wavelenth to disallow trapping. Also we can have a measure of confidence in the DC and RF parameters although they were changed at one point, which resulted in an almost immediate trapping event. The Trapping procedure went as follows:

1. Set the y, z position of the combined focused lasers at the centre of the expected trap position as well as the detection optics (see figure 29).
2. Open the iris just before the system window (We blocked the beams between the runs to avoid exposing high intensity beams to the trap unnecessarily, which could produce charge build-up or damage the chip surface).
3. Turn on DC supplies to the natural oven and apply 6 A of current and wait around 45 seconds for the oven to heat up to sublimation temperature.
4. Observe trapping region on the camera to check for a ion cloud.
5. After a couple of minutes begin tuning the 369 nm beam around 10 MHz either side of the original detuning.
6. After around four minutes from when the oven was activated move the detection optics objective in and out of the expected trap height to observe ions that may be out of focus.
7. At five minutes turn off the oven and close the laser iris to rest the trap for five minutes to avoid coating the trap with Yb.
8. Flush the RF by turning off the source for the trapping RF and turning it back on again. This is to make sure that any ions that were trapped, but went into a dark state are removed from the trap so new ions can take its place.
9. Manually change the wavelength of the 369 nm beam using the laser controller and repeat points 2. - 8. repeat this for ten different wavelengths, spread over 50 MHz either side of the expected wavelength.
10. Change the beam position in the manner described in figure 29 then repeat point 9.

Once an ion is observed on the camera, one should use the objective lens position to try and produce a crisp image of the ion, to confirm it is an ion and not some artefact or scatter from the laser beam. The final test to make sure we are observing an ion is to block only the 935 nm laser, which as described in section 2.2.2 is a repumping laser, so this should result in the ion going into a dark state and stop fluorescing. Once we can establish that you can turn the ion fluorescence on/off with the 935 nm beam, it is clear an ion has been trapped, so we immediately turn off the oven and the 399 nm beam, so no new ions are trapped and could destabilise the one we already have trapped.

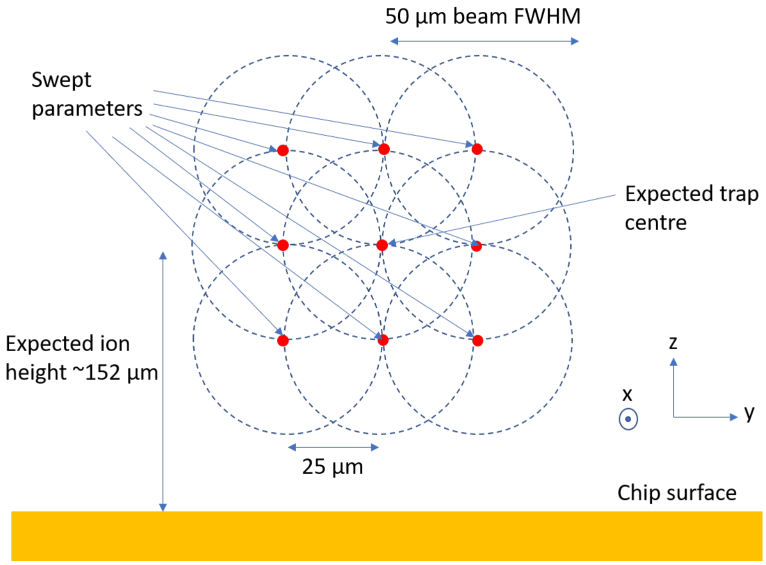

Figure 29: Diagram of the different laser positions we used when sweeping parameters to find the optimal laser position for trapping. This involved directing the beam at the centre of the expected trapping region, before moving on to the surrounding regions in the y-z plane in 25 μm steps.

4.1.2 Micro-motion and secular frequency measurements

Before any Micro-motion or secular frequency measurements were attempted, we first tried to make sure our detection fidelity was as high as possible. First we centred the camera on to the ion so that the focus was at the centre of the iris as shown in figure 24, so that only the ion is visible and the camera does not observe any scatter from the chip. This should increase our detection signal to noise ratio as well as allow us to operate experiments without the system being in complete darkness. We can then turn on the PMT (see section 3.4), and measure the number of counts per second measured by the PMT, when the ion is trapped and fluorescing and when it is in a dark state (such as when the 935 nm laser is blocked). This gave us a signal to noise ratio of around 50.

Micro-motion is described in detail in section 2.1.3, and manifests in stray DC fields that displace the ion. To compensate, we first reduced the trap RF to around 0.3 its original value, which increases the relative effect of the DC-offset. This results in the ion moving in the direction that the field is applying a force on the ion, this results in a dimming of the ion as it will be obscured by the detection optics iris. We then changed the DC values to put the ion back into its original position, by optimising the photon count on the PMT to put the ion back into the centre of the iris. The RF power is then restored to its original power, which should displace the ion again as the new trap nil should have been displaced by the DC changes. The objective lens is then moved to the new trap position as well as the laser position. This entire process is then repeated until there is no change in trap position as you decrease and increase the trapping RF power.

The secular frequency is the intrinsic harmonic motion for a given trap geometry is described in section 2.1.3. The calculated secular frequencies from simulations carried out by Dr. Ethan Potter [39] and these values can be found in table 2. The secular frequencies were measured experimentally using the RF coil described in section 3 used for the coherent manipulation of the ion's state. We applied an RF signal to the trapped-ion with a frequency around the expected secular frequencies and watch for an effect on the CCD camera. The measured values we determined are also shown in table 2.1.3. As you can see there is a significant discrepancy between

	Expected theoretical values	Experimental results
Axial secular frequency $\omega_x/2\pi$ (kHz)	326.3	214
Radial secular frequency $\omega_y/2\pi$ (kHz)	1,346	1,091
Radial secular frequency $\omega_z/2\pi$ (kHz)	1,473	950

Table 2: Table of expected and measured values for the axial an secular frequency of the trap. Theoretical calculations from Dr. Ethan Potters thesis [39].

our expected values and the real values. This can be explained by small differences in the DC potentials from micro-motion compensation efforts shown in the previous paragraph. Also it is known that a number of the electrodes on the chip are not connected to the external electrical feedthrough (see section 3.1) and hence are floating allowing arbitrary DC potentials to accumulate, which will effect the secular frequencies.

4.1.3 Trapping $^{171}Yb^{+}$

After trapping $^{174}Yb^{+}$, to do actual sensing measurements we have to trap $^{171}Yb^{+}$. This adds a new level of complexity as microwaves have to be applied and attention has to be taken to the polarisation of both the microwaves and laser light for cooling. First the enriched oven is fluorescence tested as described in section 3.1.3 to determine that the oven is functioning and what the wavelength is exactly for the 399 nm ionisation laser (given in table 1).

Once this is carried out a microwave horn is directed into the system in a manner described in section 3.3.3 and mounted on a waveplate holder to change the polarisation of the microwaves. This is done to ensure a closed cooling cycle, with microwaves that must be emitted, which address the $^2S_{1/2}\,|F=0\rangle$ ground state to $^2S_{1/2}\,|F=1\rangle$ state transition and their hyperfine levels. The hyperfine splitting is generated by a B-field from a set of Helmholtz coils around the vacuum system assembled by Dr. Ethan Potter [39]. This B-field, was modulated to produce ≈ 9.114 G, which produced a hyperfine splitting of $\approx 2\pi \times 12.7$ MHz. We applied three different microwave frequencies to address each of three aforementioned $|F=1\rangle$ states these were: 12.6428 GHz, 12.6555 GHz, 12.6301 GHz. As can be seen in figure 30 each of these transitions has a different polarisation so the microwave horn is angled to try and provide a mix of all three in equal measure. The power of this horn is also rather high at 10 W to ensure the transitions are sufficiently power broadened to drive these transitions even if they are detuned (while also making precautions to make sure no one is working on the optics table as trapping runs are carried out).

As can be seen in figure 30 the polarisation of the 369 nm cooling laser is also important for driving all three $^2S_{1/2}\,|F=1\rangle \leftrightarrow {}^2P_{1/2}\,|F=0\rangle$ transitions. A half-waveplate is employed just before the system to change the polarisation to be a mixture of all three polarisations like with the microwaves. Once all these tasks are completed trapping runs are carried out very similarly to trapping $^{174}Yb^{+}$ except in this case the optimal laser position should already be known from trapping $^{174}Yb^{+}$. During trapping runs we also changed the polarisations of the 369 nm laser and the microwaves in case we did not get the right polarisation mixture.

4.2 Initial experiments

Once $^{171}Yb^{+}$ had been trapped it was important for us to optimise the state preparation, detection and the fidelity of our experiments. This will help us determine our sensitivity in line with the theory done in section 2.4.2.

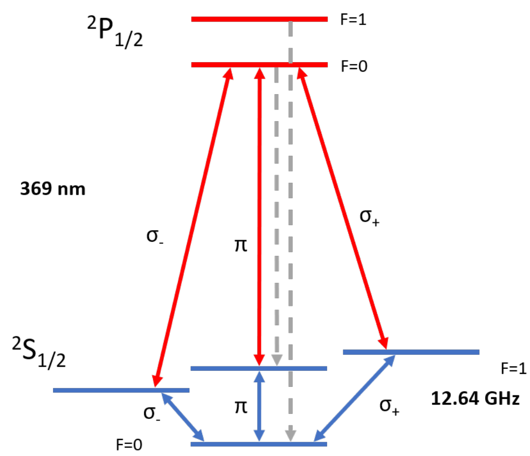

Figure 30: Diagram of the of the cooling cycle between $^2S_{1/2}$ and $^2P_{1/2}$ states, which is just part of the full cooling cycle shown in figure 6. This shows the three polarisations (σ_-, σ_+ and π) needed to make the transitions for 12.64 GHz and 369 nm when cooling $^{171}Yb^+$

4.2.1 State preparation and detection

The theory in section 2 assumed that at the beginning of each experiment the ion was prepared in one of two states perfectly and at the end of the experiment the ion's state should be determined. To go about this one must start from the basis that the ion is being cooled in the manner shown in figure 30. From this the 935 nm repumping laser and the microwaves are turned off. This is to ensure an ion in the $^2S_{1/2}\,|F=0\rangle$ ground state we want to prepare into is not excited into the $^2S_{1/2}\,|F=1\rangle$ state. Then the EOM (see section 3.2.1) is used to add 2.1 GHz sidebands to the 369 nm cooling laser. This is to drive the $^2S_{1/2}\,|F=1\rangle \leftrightarrow {}^2P_{1/2}\,|F=1\rangle$ transition and not the $^2S_{1/2}\,|F=1\rangle \leftrightarrow {}^2P_{1/2}\,|F=0\rangle$ transition. Once the ion is in the $^2P_{1/2}\,|F=0\rangle$ state it can decay down to the ground state $^2S_{1/2}\,|F=0\rangle$ so over time the ion should fall into this state exclusively and hence will stop fluorescing. Figure 31 shows how quickly this state preparation happens being around $t_p \approx 30$ μs. A diagram showing this interaction is shown in figure 32.

At the end of any given measurement using microwave dressed states as described in section 2.3.2 the system should be left in a superposition of $|D\rangle$ and $|0'\rangle$. So if we want to collapse the wavefunction to determine which state the ion is in then we must differentiate these two states experimentally. To this end we first apply a π pulse to make the transfer $|0'\rangle \rightarrow |0\rangle$ if the state was in $|0'\rangle$ otherwise there is no effect. Now if we apply an on resonant 369 nm beam then if the state was in the dressed state $|D\rangle$ then it will drive all the hyperfine states: $\{|+1\rangle\,|-1\rangle\} \leftrightarrow {}^2P_{1/2}\,|F=0\rangle$. This will result in the ion fluorescing and emit 369 nm photons, which can be detected by the state detection system (either the PMT or CCD camera, see section 3.4). The Python code used to prepare the state is shown is shown in the appendix A.1.

4.2.2 State detection fidelity

When calculating the sensitivity of this sensor it is important to know how reliably the sensor can accurately prepare the state as well as read it out. The uncertainty of these two procedures discussed in the previous subsection are hard to distinguish, so are taken together into as single State Preparation And Measurement (SPAM) error. This is calculated by carrying out a state detection fidelity experiment, which involves preparing the ion into either a bright or dark state and then running a state preparation readout. This experiment is run multiple times and the number of photons collected by the PMT is measured over a certain detection time.

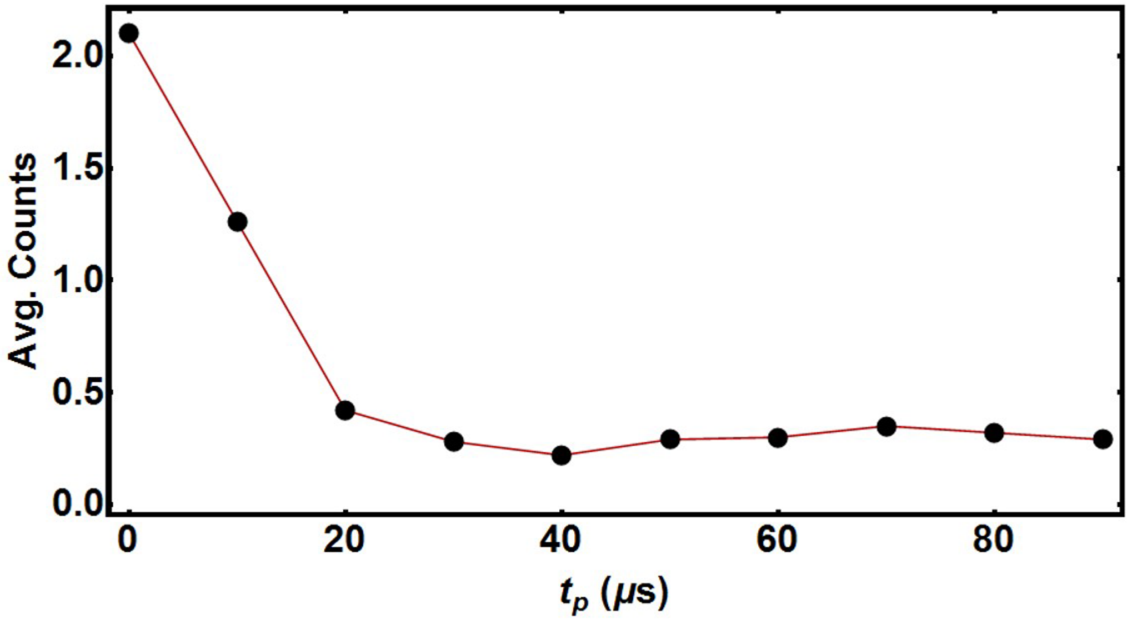

Figure 31: This graph shows how the fluorescence of the ion decreases with time after the EOM applies sidebands to the 369 nm cooling laser, which prepares the state in the ground state. Each data point represents 100 experimental repetitions each with a 1 ms detection time. The photon can be seen to decay rapidly to 20-30 μs before levelling out. The number of photons never reaches zero due to the intrinsic dark count of the PMT as well as 369 nm laser scatter from the chip just behind the ion position. This plot was generated by Dr. Ethan Potter [39].

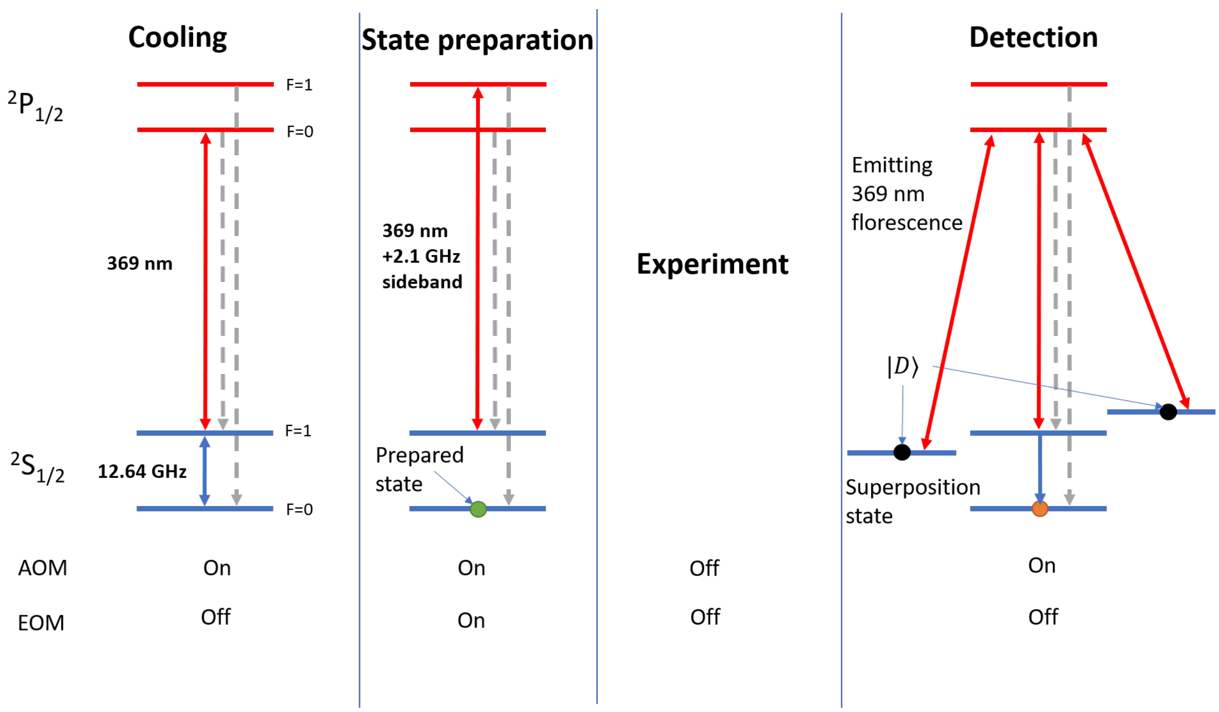

Figure 32: Diagram of the different lasers and microwaves used for the cooling, state preparation and state detection procedures used at the beginning and end of each experiment. This also shows you whether the AOM (which turns the 369 nm laser on and off) and the EOM (which adds sidebands to the 369 nm laser) are employed at each step.

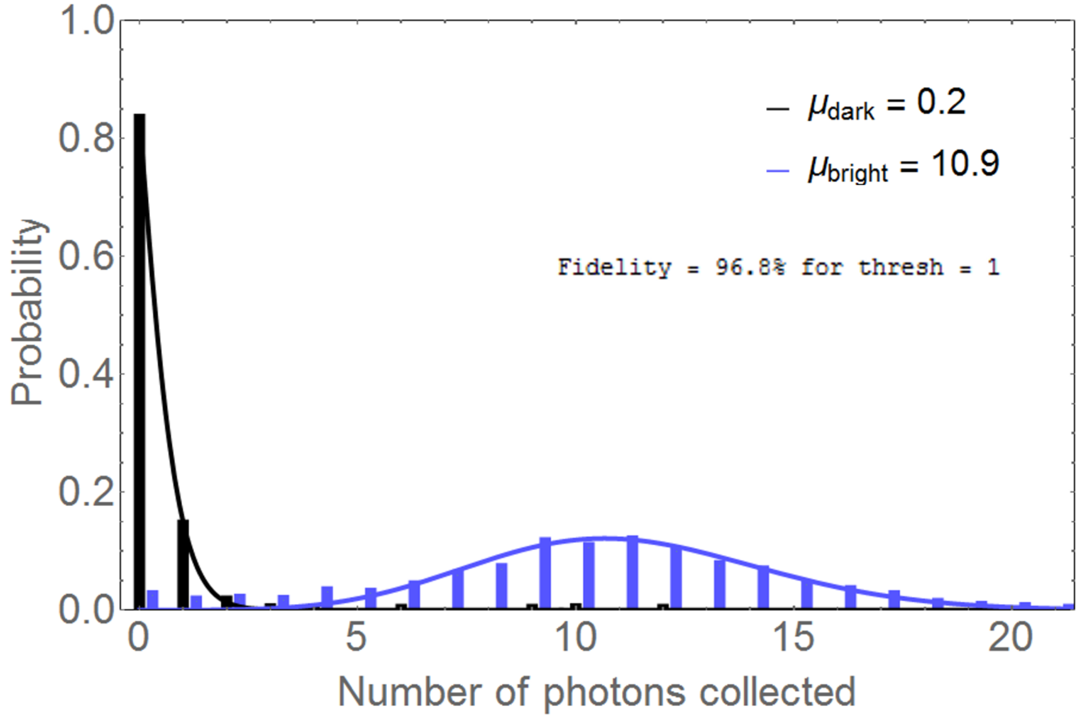

Figure 33: A histogram showing the results of a state detection measurement experiment to determine the optimum detection time (in this case 1 ms) and the fidelity of our experiment. This graph has two plots, one when the state is prepared in the dark state and the other in the bright state, each has 1000 measurements. μ_{dark} and μ_{bright} are the average photon count detected by the PMT for all the dark and bright experiments respectively. Data taken from Dr. Ethan Potters thesis [39].

These photon numbers from all experiments are fitted to histograms, one for the dark state and one for the bright state. These histograms are fitted to the general Poissonian function:

$$f_{Poisson}(n) = \frac{\mu^n}{n!}e^{-\mu}. \tag{85}$$

Where n is the number of photons and μ is the average photon number. A 100% fidelity measurement would have the two histograms have no overlap so one could always get a bright state measurement when the system is prepared in the bright state and vice-versa for the dark state. The reason for the overlap is usually due to crosstalk on the 369 nm possibly making the $^2S_{1/2}\,|F=0\rangle \leftrightarrow {}^2P_{1/2}$ transition, which as seen in figure 32 could result in a dark state preparation being read as bright. More details on how the fidelity was calculated and the state detection fidelity experiment can be found in Dr. Ethan Potters thesis [39]. An example of the results of a typical state detection fidelity experiment is shown in figure 33.

4.3 Experiment sequences

In this project we have succeeded in measuring RF and microwave coherence times and sensitivity, this was achieved by conducting hundreds of experiments with several dozen separate pulse sequences developed by myself and run on our ARTIQ system mentioned in section 3.3.2. Almost all these different sequences however contain three basic experiments that will be detailed in this section. These are: the frequency scan for determining the transition frequencies for all the transitions in the $^2S_{1/2}$ manifold; Rabi oscillation measurements, for determining the π time of each of the transitions in the $^2S_{1/2}$ manifold; and the Ramsey experiment for measuring the coherence time of the system. Code for how the control system sweeps different parameters for all three of the below experiments shown in appendix A.3.

4.3.1 Frequency scans

One of the most important parameters one needs before making any RF or microwave measurements is the exact frequency of all the relevant transitions for the $^2S_{1/2}$ manifold of $^{171}Yb^+$. This is relevant for ensuring the state preparation has a high fidelity for making the microwave π pulse required, as well as provide accurate frequencies for the dressing fields. To carry out this experiment the usual SPAM procedure is utilised for cooling, state preparation and detection detailed in section 4.2. Then microwaves or RF are applied to whatever transition we wish to probe, with some frequency near what we expect it to be, for a time we roughly expect to be the π time of the transition. A state detection is carried out and the experiment is repeated between 50 - 100 times to build up a probability of the ion being in one state or the other. Once we have a probability we can repeat the entire experiment, with a stepped RF frequency, which is repeated over the range of frequencies we expect the RF resonant frequency to be. When all of these data points are made they should produce a Gaussian distribution, assuming that we swept over the transition resonance. A graphical representation of this experimental procedure can be found in figure 34. The probability distribution of this experiment is expressed by:

$$P_{|F=1\rangle}(\delta) = \frac{A}{2}\frac{\Omega^2}{\Omega^2+\delta^2}\left(1-\cos\left(t_\pi\sqrt{\Omega^2+\delta^2}\right)\right) \tag{86}$$

Where Ω is the Rabi frequency; $\delta = \omega_r - \omega$ is the detuning where ω_r is the resonant frequency of the transition and ω is the applied field frequency; t_π is the π time of the transition with this field and A is the fringe contrast. This is derived from equation 42, with greater derivation detail in Dr. Ethan Potters thesis [39]. In most cases this equation can be approximated to a simple Gaussian, which were used to plot these functions in Python:

$$P(\omega) = A_g e^{-\frac{(\omega-\omega_r)^2}{2c^2}} \tag{87}$$

Where A_g and c are constants. Once the experiment is finished an analysis programme I wrote will plot the Gaussian and determine the peak frequency of the transition, which can then be loaded into the system memory for later experiments.

4.3.2 Rabi oscillation measurements

To actually make a magnetic field measurement as described in section 2.3.1 a Rabi frequency measurement must be made. These measurements are also important for measuring the π time as $t_\pi = \pi/\Omega$. This is the time it takes to make transfer the state population from one state to another, which is useful for preparing or measuring states and conducting frequency scans (see section 4.3.1). This is done by carrying out SPAM to prepare the state before applying a pulse of on resonant microwaves or RF (usually starting with $t = 0$, with no change in state), before doing a state detection and repeating the experiment 50 times to build a state probability. This is then repeated with longer and longer pulse times to give a probability distribution over time. After finishing the experiment it gives a sine wave described by equation 42, which for an on resonant applied field gives:

$$P_\uparrow(t) = A\sin^2(\Omega t/2) \tag{88}$$

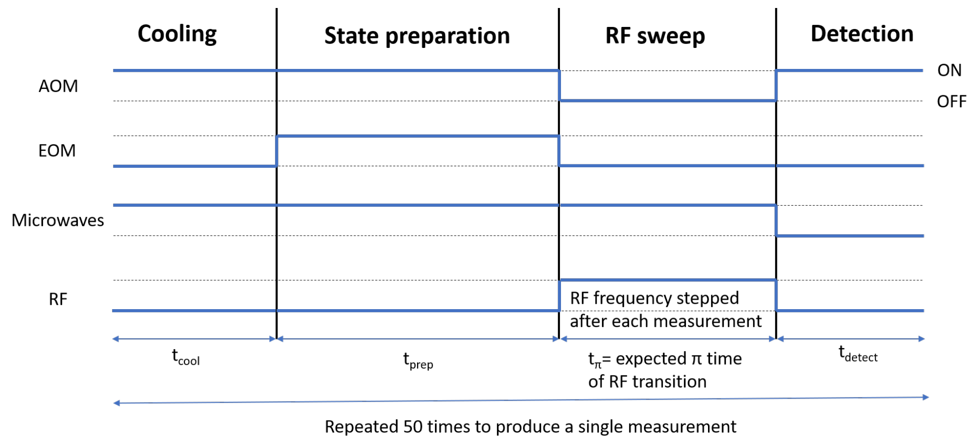

Figure 34: This shows the pulse sequence needed to carry out a basic RF frequency scan by running the SPAM sequence before applying a π RF pulse to the ion and carrying out a state detection. After many repetitions to build up a probability distribution the applied RF frequency is changed and the repetitions are carried out many times with different frequencies to show how the state population changes with frequency.

Where A is the amplitude of the Rabi oscillation and should be ≈ 1 for an on resonant wave. My Python script (see appendix A.2) then runs analysis on this data to plot it using equation 88 as a line of best fit to determine value for Ω and hence t_π can be determined. A diagram of the pulse sequence used for this experiment is shown in figure 35.

4.3.3 Ramsey experiments

As discussed in section 2.4.1 the coherence time of an experiment is integral in measuring the sensitivity of the sensor. This is due to the fact that the coherence time is indicative of the optimum sensing time to give the best sensitivity per second of total experimental time. To actually measure this coherence time we use a Ramsey experiment for measuring the T_2^* and T_2 coherence times.

To measure the T_2^* time the usual cooling and state preparation is carried out before a $\pi/2$ pulse is carried out on the transition we want to measure. This puts the state into a $50/50$ superposition state, where it is left to precess over time while allowing the ion to decohere within that time. After this delay there is a second $\pi/2$ pulse with a different phase compared to the first pulse. State detection is then carried out and the measurement is carried out 50-100 times to give a probability distribution and then the entire experiment is repeated with different phase differences from 0 to 2π. When plotted with phase against state population this should give a sine wave described by:

$$P_\uparrow(\phi) = p_{off} + \frac{a}{2}\sin(\phi + \phi_{off}). \tag{89}$$

Where a is the fringe contrast; P_{off} is the population offset; ϕ is the phase and ϕ_{off} is the phase offset. This equation comes from the Unitary operator of the two state system from equation 41. For a very short delay time the fringes on this sine wave are quite small, but once this experiment is repeated for longer delay times these fringes become smaller and smaller as $P_\uparrow(t \to \infty) \to 0.5$. This fringe decay with delay time can be fit to the exponential decay of decoherence which is proportional to e^{-t/T_2^*} (see section 2.4.1) so the T_2^* time can be determined. This calculation was carried out by Dr. Ethan Potter, with more details in his thesis [39].

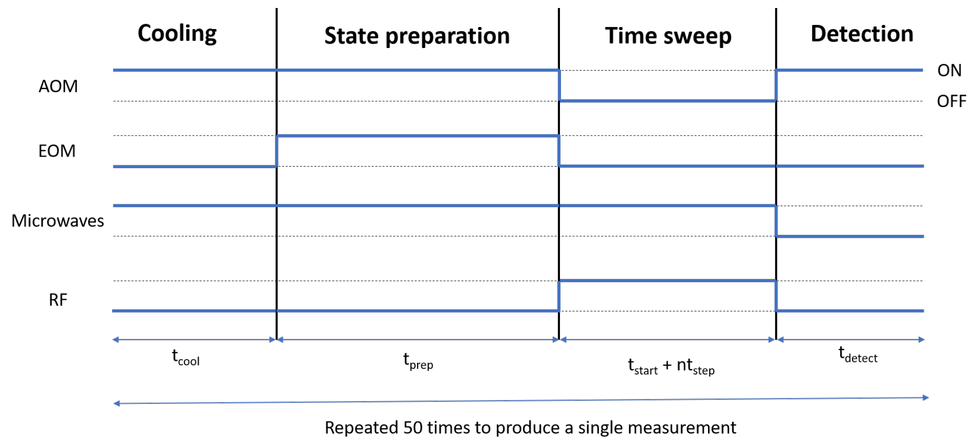

Figure 35: This shows the pulse sequence needed to carry out a basic Rabi measurement by running the SPAM sequence before applying a RF pulse to the ion and carrying out a state detection. After many repetitions to build up a probability distribution the experiment is carried out again with a longer pulse time. This is done with many pulse times to build a probability distribution with pulse time.

This T_2^* is a good indicator for coherence, but as I detailed in section 2.4.1 we can use dynamic decoupling to cancel out magnetic field noise. The T_2 experiment remains largely unchanged other than after the first $\pi/2$ pulse and half the delay time a π pulse in phase with the first pulse is carried out then we wait for the second half of the delay and then the final $\pi/2$ pulse is applied with its phase change. Otherwise the experiment is the same with the same increases in delay and measurement of fringes. This generally leads to a longer coherence time, which we can use in our long sensitivity measurements for the optimum experimental time (see section 2.4.2). This pulse sequence can be seen in figure 37.

4.4 Bare state sensing results

To conduct sensitivity measurements using dressed states, information must be gleaned from the bare states of the ion. That being the individual transitions inside the $^2S_{1/2}$ manifold for $^{171}Yb^+$, by determining the resonant frequency of the relevant transitions as well as the π times associated with pulses from our microwave and RF emitters on our system. The prime transition we care about is the 'clock', $|0\rangle \leftrightarrow |0'\rangle$ transition, where our accuracy for the frequency and π time is crucial for our state detection fidelity (see section 4.2.2). Then the microwave dressed states are measured $|0\rangle \leftrightarrow \{|+1\rangle, |-1\rangle\}$ for maintaining the integrity of the dressed state throughout a measurement. This is also true for the RF dressed states $|0'\rangle \leftrightarrow \{|+1\rangle, |-1\rangle\}$ as well as the $|0'\rangle \leftrightarrow |+1\rangle$ and $|0\rangle \leftrightarrow |-1\rangle$ transitions used for RF and microwave field measurements respectively. It is also useful to make T_2^* and T_2 measurements of the bare sensing transitions to give us a picture of what kind of noise is effecting the system. As if there is a large difference on coherence time between the bare states and the dressed states that tells us there must be significant low frequency noise effecting the system that is being mitigated by the dressed states.

4.4.1 Bare state clock state measurements

Usually at the beginning of every day a clock ($|0\rangle \leftrightarrow |0'\rangle$) measurement is made. We initially make a frequency scan around the expected value of the transition resonance, which is calculated using the 2nd order Zeeman splitting (see section 2.3.3). Once we have the resonant frequency we can conduct a Rabi experiment to determine

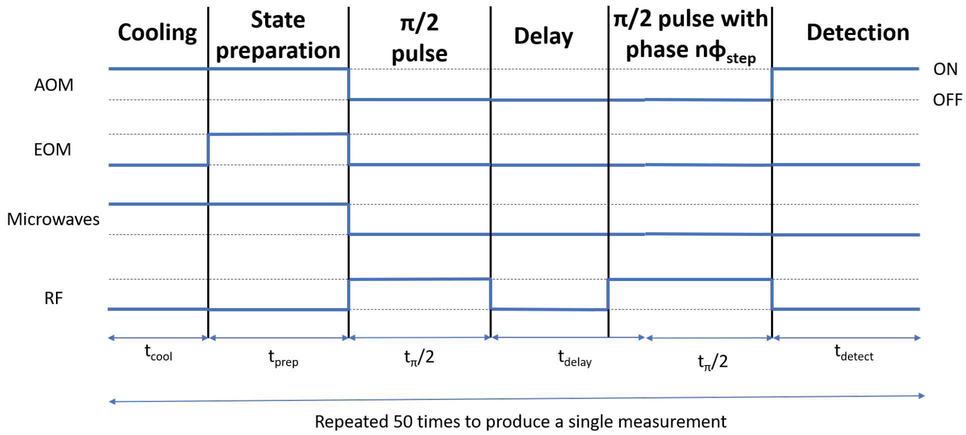

Figure 36: This shows the pulse sequence needed to carry out a T_2^* measurement on an RF transition by running the SPAM sequence before applying an RF$\pi/2$ pulse to the ion. There is then a delay before a second $\pi/2$ RF pulse, which has a phase difference with the first RF $\pi/2$ pulse, before state detection is carried out. This is repeated 50-100 times to give a state probability, before the whole experiment is repeated many times with greater differences in phase between the two $\pi/2$ RF pulses from 0 to 2π

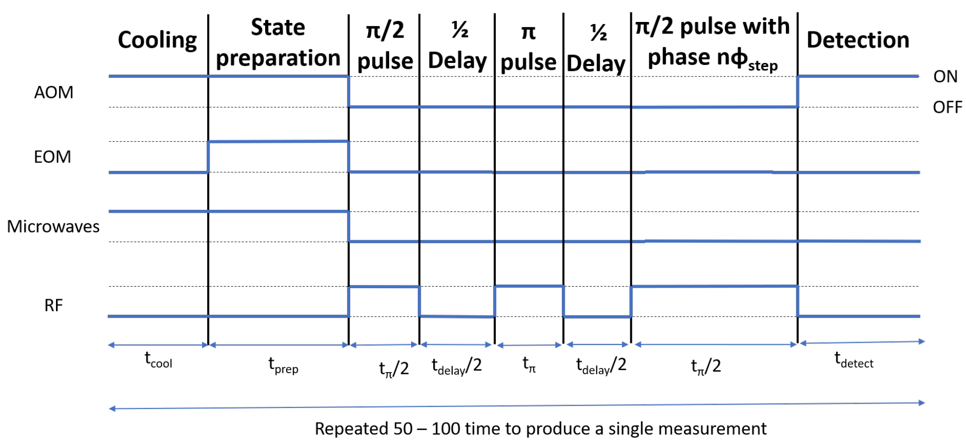

Figure 37: This shows the pulse sequence needed to carry out a T_2 measurement on an RF transition. This is very similar to the sequence shown in figure 36 except that between the two $\pi/2$ pulses there is a π pulse in phase with the first pulse. The delay time is split half and half either side of the π pulse.

the t_π time for this transition with the microwave source being used. The results of a typical frequency scan an Rabi frequency measurement are shown in figure 38, which shows how we fit the data to equation 86 to determine the Rabi frequency of the transition Ω.

4.4.2 Bare state hyperfine state measurements

The first order Zeeman splitting produces the hyperfine transitions $|0\rangle \leftrightarrow \{|+1\rangle, |-1\rangle\}$ and $|0'\rangle \leftrightarrow \{|+1\rangle, |-1\rangle\}$, which must all be measured to determine their resonant frequency and Rabi frequency of these transitions. Estimates of the the resonant frequencies of these transitions can be determined from calculating the first order Zeeman splitting generated by an applied B-field given by equation 28.

Initially these transitions are examined individually for resonant frequency for later experiments and can be seen in figure 39 and figure 40 for the microwave and RF dressing fields respectively. The Rabi frequencies of the transitions used for the two transition for the RF ($|0\rangle \leftrightarrow \{|+1\rangle, |-1\rangle\}$) and microwave ($|0'\rangle \leftrightarrow \{|+1\rangle, |-1\rangle\}$) dressing fields must be matched to maximise the coherence time of the sensing experiments for reasons outlined in section 2.3.2. This presents a problem, because when both dressing fields are applied simultaneously the Rabi frequency of each dressing field shifts slightly from what it would be if it was probed in isolation. So to remedy this each of the Rabi measurements shown in figures 39 and 40 were both done with the other dressing field being applied with roughly the same Rabi frequency. The Rabi frequency is then modulated using the DDS RF and microwave source (see section 3.3.3). This is repeated until both fields express the same Rabi frequency within the error of our measurements.

4.4.3 Bare state coherence time measurements

Examining the T_2^* and T_2 times for the bare states and the clock state were important for testing our procedures for the more complex dressed state Ramsey experiments. They are also useful to identify what kind of noise the system is being exposed to, to cause decoherence.

Initially a coherence time measurement was made for the T_2^* and T_2 times for the $|0'\rangle \leftrightarrow |0\rangle$ clock transition, which is shown in figures 41 and 42 respectively. Here the T_2^* time was found to be 0.60(6) s and the T_2 was 3.81(3) s, with a 2nd order Zeeman splitting of 7.9 kHz. The large discrepancy in the two coherence times is indicative of a problem with slowly changing B-field noise effecting the transition. This is because of the π used in the T_2 experiment cancels out these slowly oscillating noise fields [71]. The most likely source of this noise is the Helmholtz-coils used to generate the B-field to produce the Zeeman splitting on the ion, which was designed and built by Dr. Ethan Potter [39]. It is possible that small fluctuations in resistance in the copper wire from changes in temperature are causing problems with the delivery of B-field and introducing noise. This is a possible avenue to improving the coherence time of the entire system in future.

After the clock state measurements, the coherence times of the 1st order sensitive Zeeman states was measured. These times were expected to be significantly lower due to these states being sensitive to the 1st order Zeeman splitting. The results of these measurements for both the $|0\rangle \leftrightarrow |-1\rangle$ and $|0\rangle \leftrightarrow |+1\rangle$ transitions for both T_2^* and T_2 measurements can be found in figures 43 and 44 respectively. The coherence times for the the $|0\rangle \leftrightarrow |-1\rangle$ transition was: $T_2^* = 1.54(2)$ ms and $T_2 = 4.86(2)$ ms. The coherence times for the the $|0\rangle \leftrightarrow |+1\rangle$ transition was: $T_2^* = 2.47(8)$ ms and $T_2 = 4.31(1)$ ms. The similarity in coherence time between the two transitions can be explained by the fact that they are produced by the same 1st order Zeeman effect so any discrepancies between them are probably due to experimental error. The difference between T_2^* and T_2 times for both transi-

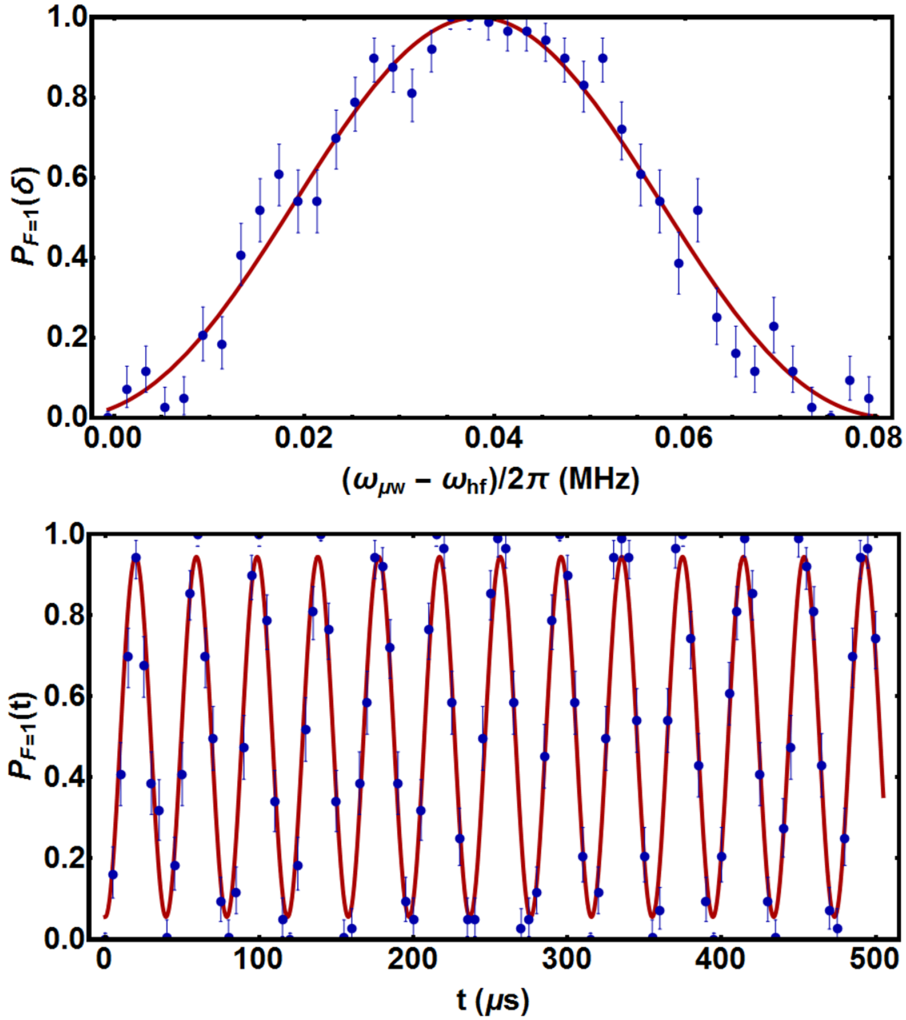

Figure 38: Top). This is a frequency scan of the $|0\rangle \leftrightarrow |0'\rangle$ transition around the expected resonance. With $P_{F=1}(t)$ indicating the state population for the $|0'\rangle$ state. The x axis is given by the difference in resonant frequency due to the second order Zeeman splitting: $(\omega_p - \omega_{hf})/2\pi = 39.1$ kHz. The data points are fitted to a line given by equation 86. From this fit the resonant frequency ω_r can be extracted. Bottom) The resonant frequency is used to produce a Rabi experiment shown here, which produces a sine wave described by equation 88, which has a frequency equal to the Rabi frequency Ω. The measured π time for this experiment was: 19.72 μs. The error bars for both plots was determined from the standard error probability. These plots were generated by Dr. Ethan Potter [39].

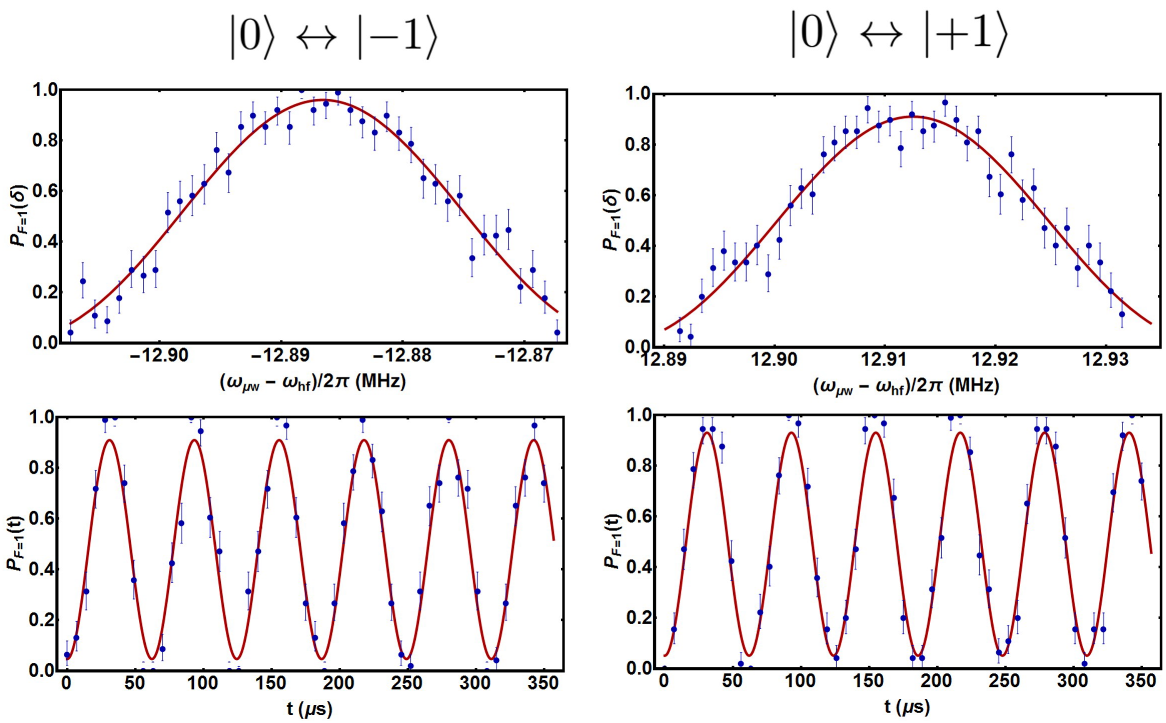

Figure 39: Top). These are frequency scans of the $|0\rangle \leftrightarrow |-1\rangle$ left). and $|0\rangle \leftrightarrow |+1\rangle$ right). transitions plotted with a line of best fit generated by equation 86. This is showing how the population of the $F = 1$ state varies with detuning from the clock resonant frequency ω_{hf}. In this case the splitting was found to be 12.8835 MHz and 12.9112 MHz for the $|0\rangle \leftrightarrow |-1\rangle$ and $|0\rangle \leftrightarrow |+1\rangle$ transitions respectively. Bottom). These are two Rabi oscillation measurements for the $|0\rangle \leftrightarrow |-1\rangle$ left). and $|0\rangle \leftrightarrow |+1\rangle$ right). transitions. These are plotted with a sine wave line given by equation 88 with a Rabi frequency Ω. This shows how the state population of $|0\rangle$ changes with microwave pulse time. The two Rabi frequencies were found to be $\Omega/2\pi = 16.065$ kHz and $\Omega/2\pi = 16.140$ kHz for the $|0\rangle \leftrightarrow |-1\rangle$ and $|0\rangle \leftrightarrow |+1\rangle$ transitions respectively. The error bars for both plots was determined from the standard error probability. These plots were generated by Dr. Ethan Potter [39].

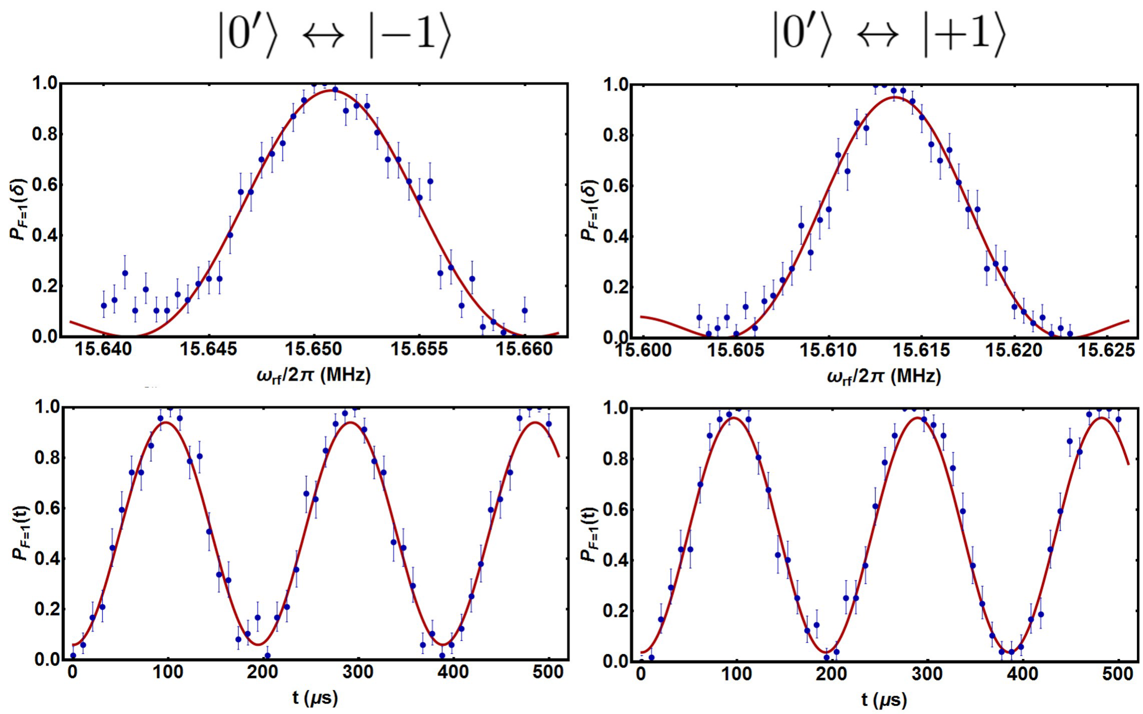

Figure 40: Top). These are frequency scans of the $|0'\rangle \leftrightarrow |-1\rangle$ left). and $|0'\rangle \leftrightarrow |+1\rangle$ right). transitions plotted with a line of best fit generated by equation 86. This is showing how the population of the $F = 1$ state varies with applied RF frequency. In this case the splitting was found to be 15.6507 MHz and 15.6136 MHz for the $|0'\rangle \leftrightarrow |-1\rangle$ and $|0'\rangle \leftrightarrow |+1\rangle$ transitions respectively. Bottom). These are two Rabi oscillation measurements that for the $|0'\rangle \leftrightarrow |-1\rangle$ left). and $|0'\rangle \leftrightarrow |+1\rangle$ right). transitions. These are plotted with a line generated by the sine wave equation 88 with a Rabi frequency Ω. This shows how the state population of $|0\rangle$ changes with RF pulse time. The two Rabi frequencies were found to be $\Omega/2\pi = 5.149$ kHz and $\Omega/2\pi = 5.186$ kHz for the $|0'\rangle \leftrightarrow |-1\rangle$ and $|0'\rangle \leftrightarrow |+1\rangle$ transitions respectively. The error bars for both plots was determined from the standard error probability. These plots were generated by Dr. Ethan Potter [39].

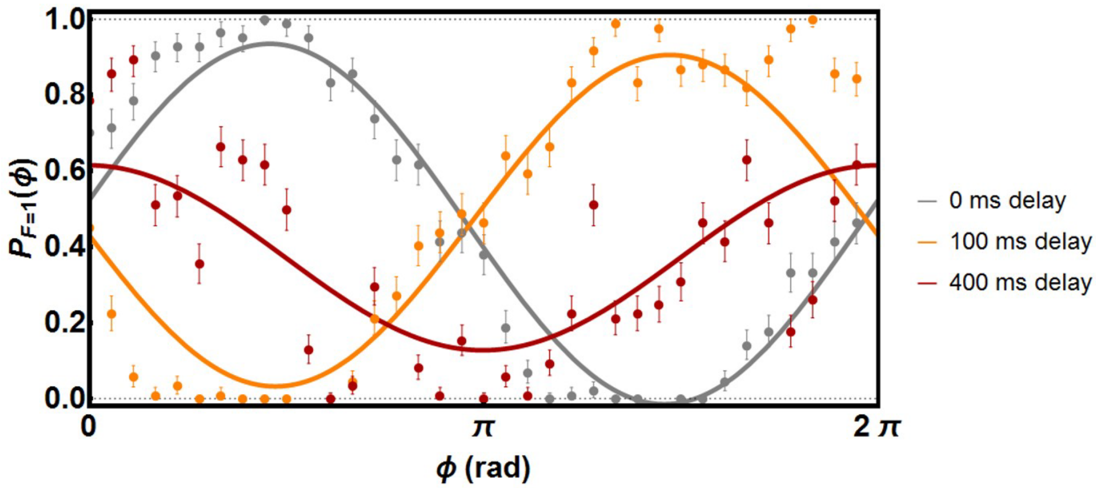

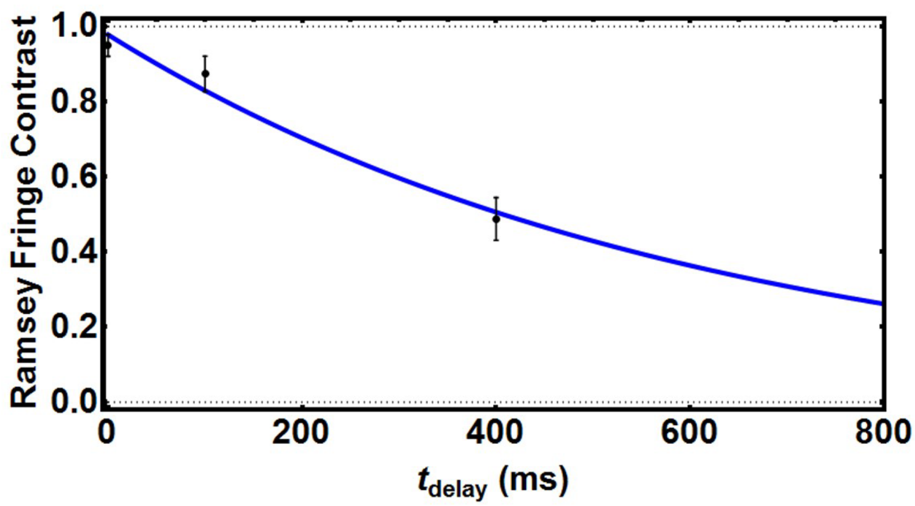

Figure 41: Top). Results of a T_2^* experiment (see section 4.3.3) for the $|0\rangle \leftrightarrow |0'\rangle$ 'clock' transition, with the state population of the $|0'\rangle$ state plotted against the phase ϕ of the second $\pi/2$ pulse. The different coloured plots are related to the delay time between the two pulses and are modelled using equation 88 to extract the fringe contrast a. bottom). A plot of the Ramsey experiment plots fringe a against the delay time, where the errors are given by the standard error of the top plots. The line is plotted with an exponential coherence decay function e^{-t_{delay}/T_2^*}, which gives a coherence time of $T_2^* = 0.60(6)$ s. These plots were generated by Dr. Ethan Potter [39].

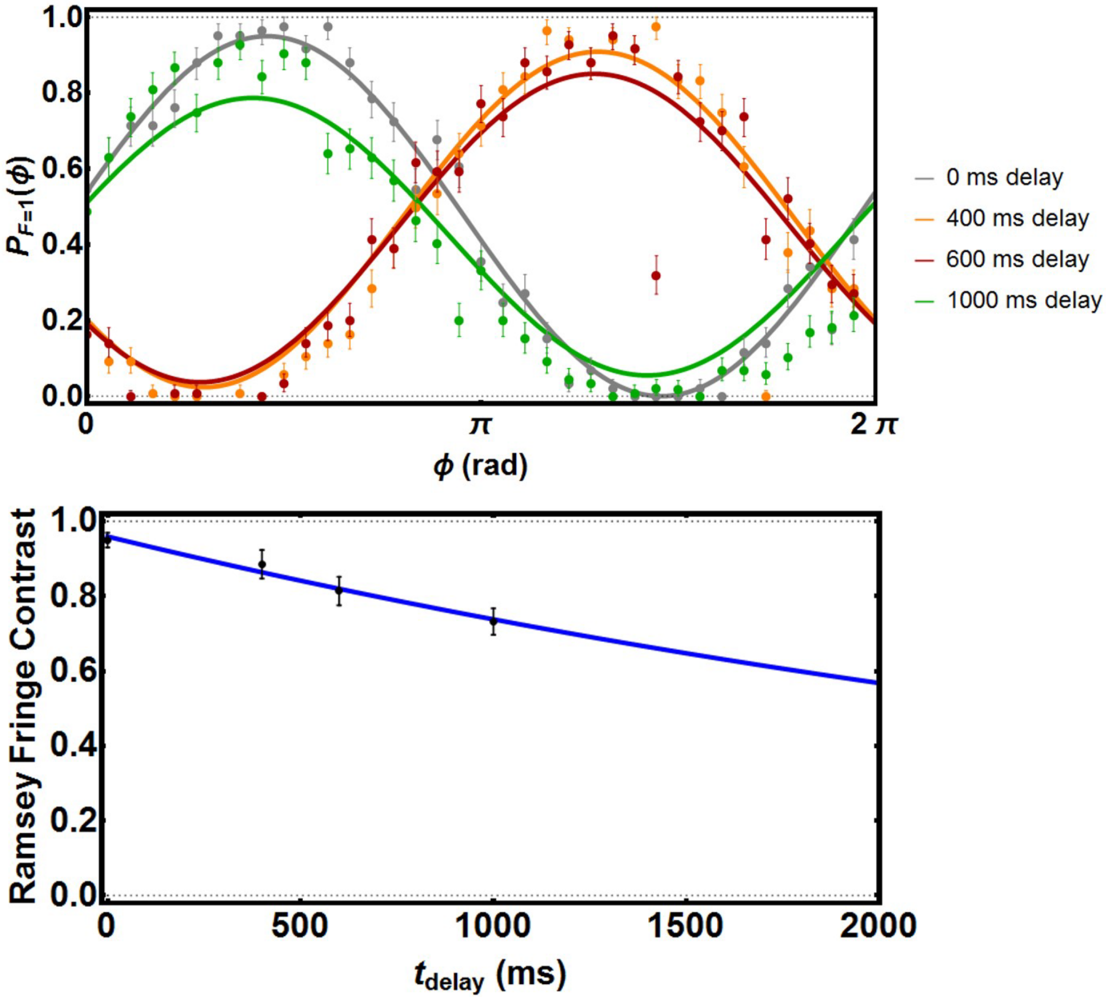

Figure 42: Top). Results of a T_2 experiment (see section 4.3.3) for the $|0\rangle \leftrightarrow |0'\rangle$ 'clock' transition, with the state population of the $|0'\rangle$ state plotted against the phase ϕ of the second $\pi/2$ pulse. The different coloured plots are related to the total delay time between the two pulses (not including the π decoupling pulse) and are modelled using equation 88 to extract the fringe contrast a. bottom). A plot of the Ramsey experiment plots fringe a against the delay time, where the errors are given by the standard error of the top plots. The line is plotted with an exponential coherence decay function e^{-t_{delay}/T_2}, which gives a coherence time of $T_2 = 3.81(3)$ s. These plots were generated by Dr. Ethan Potter [39].

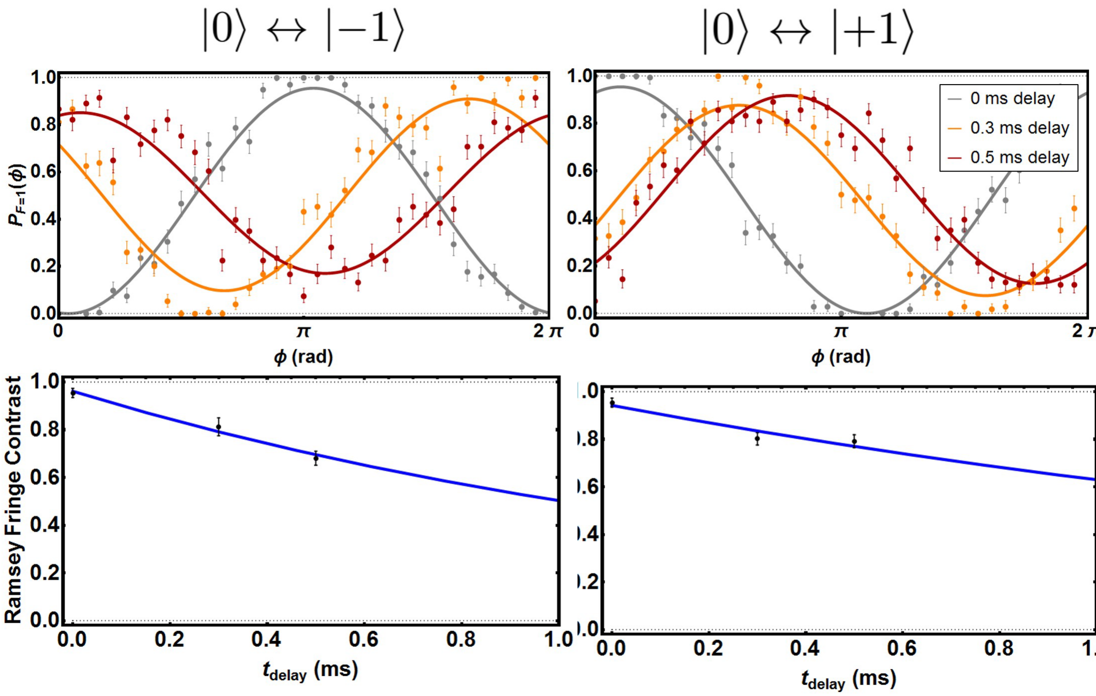

Figure 43: Top). Results of a T_2^* experiment (see section 4.3.3) for the $|0\rangle \leftrightarrow |-1\rangle$ and $|0\rangle \leftrightarrow |+1\rangle$ hyperfine transitions on the left and right respectively. The state population of the $|0'\rangle$ state is plotted against the phase ϕ of the second $\pi/2$ pulse. The different coloured plots are related to the delay time between the two pulses and are modelled using equation 88 to extract the fringe contrast a. bottom). Plots of the Ramsey experiment fringe a against the delay time, where the errors are given by the standard error of the top plots. The line is plotted with an exponential coherence decay function e^{-t_{delay}/T_2^*}, which gives a coherence time of $T_2^* = 1.54(2)$ ms for the $|0\rangle \leftrightarrow |-1\rangle$ transition (left) and $T_2^* = 2.47(8)$ ms for the $|0\rangle \leftrightarrow |+1\rangle$ transition (right). These plots were generated by Dr. Ethan Potter [39].

tions is probably due to the noise affecting the system to be generally be the fast oscillating noise that generally drives 1st order Zeeman effects. This is because T_2 experiments generally remove slowly oscillating B-field effects.

4.5 Dressed state RF sensing

As detailed in section 2.3.2 dressed states will provide far greater sensing capability compared to the simple bare states experiments detailed in the previous section. This is due to their inherent noise cancelling capability, so rapidly oscillating B-field fluctuations that cause 1st order Zeeman effects on the ion are cancelled out and will not cause the ion to decohere. This dressed state system was adapted from the technique used for maintaining high coherence time when using $^{171}Yb^+$ ions for quantum gates [64].

The resonant frequencies and t_π times measured in section 4.4 can now be employed to generate microwave dressing fields on transitions $|0\rangle \leftrightarrow |+1\rangle$ and $|0\rangle \leftrightarrow |-1\rangle$, with on resonant fields with matching Rabi frequencies. This produces a dressed state $|D\rangle$, which allows for RF sensing using the $|0'\rangle \leftrightarrow |D\rangle$ transition. This experimental procedure is summarised in figure 45. As with the bare states, the $|0'\rangle \leftrightarrow |D\rangle$ transition's resonant frequency can be tuned, by changing the applied DC field from the Helmholtz coils.

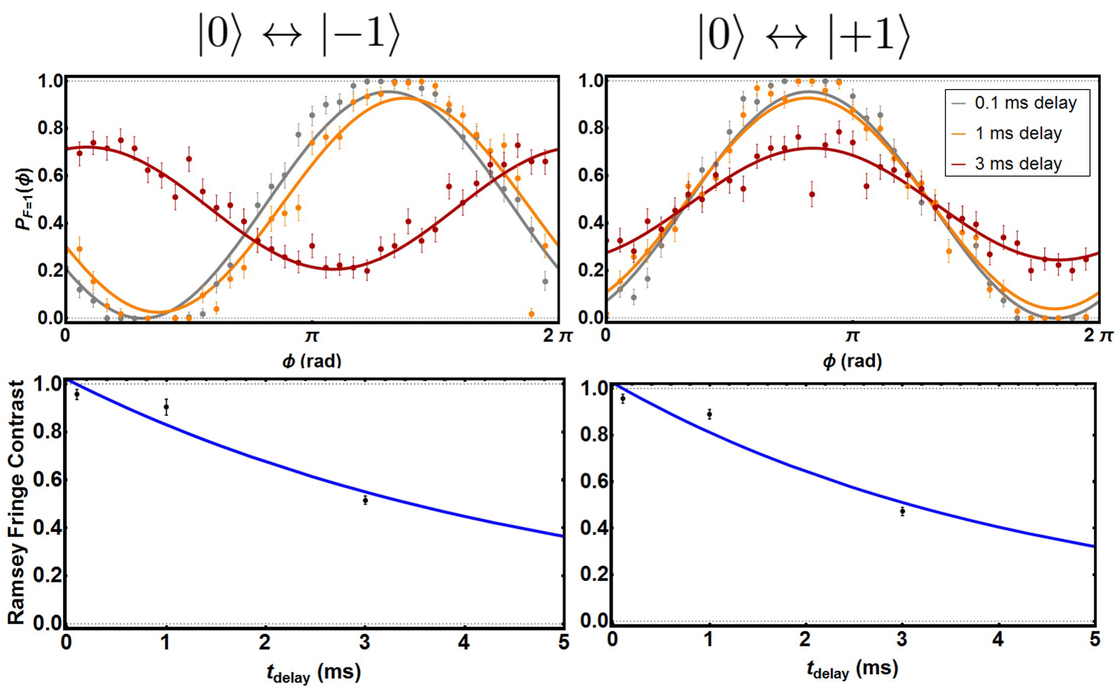

Figure 44: Top). Results of a T_2 experiment (see section 4.3.3) for the $|0\rangle \leftrightarrow |-1\rangle$ and $|0\rangle \leftrightarrow |+1\rangle$ hyperfine transitions on the left and right respectively. The state population of the $|0'\rangle$ state is plotted against the phase ϕ of the second $\pi/2$ pulse. The different coloured plots are related to the delay time between the two pulses (not including the π decoupling pulse) and are modelled using equation 88 to extract the fringe contrast a. bottom). Plots of the Ramsey experiment fringe a against the delay time, where the errors are given by the standard error of the top plots. The line is plotted with an exponential coherence decay function e^{-t_{delay}/T_2}, which gives a coherence time of $T_2 = 4.86(2)$ ms for the $|0\rangle \leftrightarrow |-1\rangle$ transition (left) and $T_2 = 4.31(1)$ ms for the $|0\rangle \leftrightarrow |+1\rangle$ transition (right). These plots were generated by Dr. Ethan Potter [39].

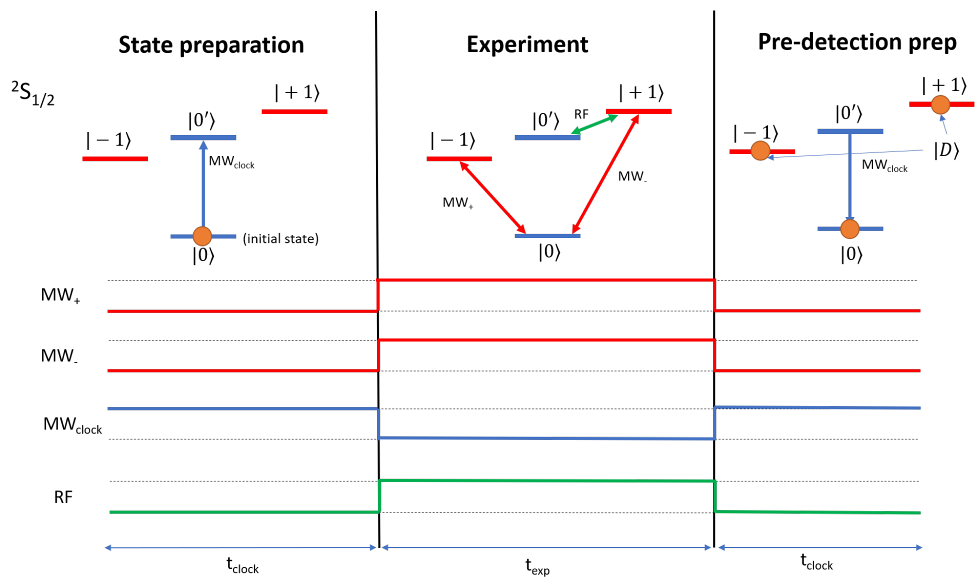

Figure 45: This shows the pulses used during an microwave dressed state sensing experiment as well as show how these pulses influence the ions $^2S_{1/2}$ manifold states. Once the state has been prepared normally as detailed in section 4.2.1 into the $|0\rangle$ state the state is transferred into the $|0'\rangle$ state using a microwave clock pulse. Once the state is prepared in the $|0'\rangle$ state the experiment can begin, which is initiated by applying microwave dressing fields MW_- and MW_+ to set up the dressed state $|D\rangle$. The ion is then exposed to an RF field resonant with the transition we wish to sense with: $|0'\rangle \leftrightarrow |D\rangle$. After finishing our experiment the dressing fields are removed leaving the state in superposition of $|D\rangle$ and $|0'\rangle$. During a fluorescence measurement the $|D\rangle$ and $|0'\rangle$ states will both produce fluorescence, because they are both in F=1 states of the $^2S_{1/2}$ manifold. To be able to distinguish between them there is another clock π pulse applied to the ion to transfer $|0'\rangle \rightarrow |0\rangle$ so if the state was originally in the $|0'\rangle$ after the experiment then the ion will no longer fluoresce under 369 nm light.

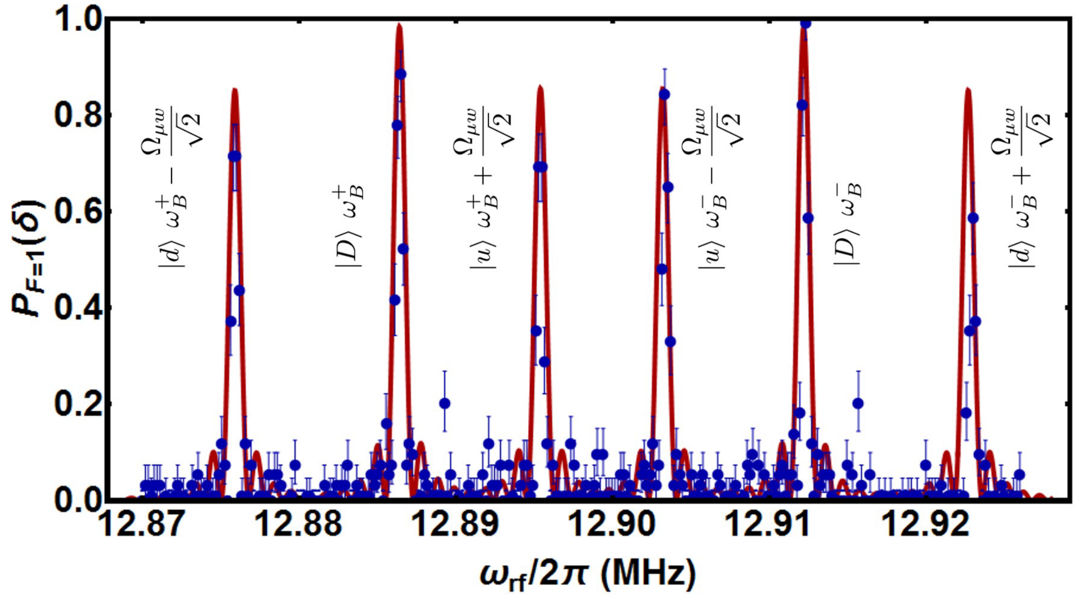

Figure 46: This is plot of the population of the F=1 state of the $^2S_{1/2}$ manifold after a frequency sweep experiment (see section 4.3.1) against the frequency ($\omega_{RF}/2\pi$) of an applied RF pulse with a pulse time of 975 μs. This is after preparing the ion into the $|0'\rangle$ state as shown in figure 45. The red line is fitted individually for each of the six peaks using equation 86. The difference in peak heights is explained by the fact that the same pulse time was used for all six peaks while their relative Rabi frequencies are different. The six peaks are produced from the three dressed states $|u\rangle$, $|d\rangle$ and $|D\rangle$, which are all paired with the transitions from the $|+1\rangle$ (ω_B^+) and $|-1\rangle$ (ω_B^-) states. From these peak frequencies we can calculate the Rabi frequency of the dressing fields $\Omega_{\mu w}/\sqrt{2} \approx 2\pi \times 9.8$ kHz and the 2nd order Zeeman shift $(\omega_B^- - \omega_B^+)/2\pi = 25.8$ kHz. This plot was generated by Dr. Ethan Potter [39].

4.5.1 Dressed state RF frequency scan

The first step once on resonant dressing fields are applied is to identify all the different dressed state transitions with the $|0'\rangle$ state. These are the transitions with the three dressed states $|u\rangle$, $|d\rangle$ and $|D\rangle$, but also due to interactions detailed in section 2.3.2, each of these transitions is paired with the $|+1\rangle$ and $|-1\rangle$ states. This gives a total of six transitions that can be used for sensing. These six transitions were identified using a wide frequency scan shown in figure 46. These transition frequencies will allow us to make sure that the various states are not overlapping leading to cross talk and make sure we are using the transition $|0'\rangle \leftrightarrow |D\rangle$ as this state will experience less decoherence (see section 2.3.2). The error bars for both plots was determined from the standard error probability (more details can be found in Dr. Ethan Potters thesis[39]).

4.5.2 Dressed state RF sensing coherence time measurements

Before Rabi oscillation measurements can be undertaken we had to ascertain how long our measurements should be when attempting sensitivity measurements. There must be a balance between long measurements to collect as much information about the field as possible, while being short enough that decoherence does not become an issue. This is all detailed in section 2.4.1, where the optimal sensing time was found to be $T_{opt} = T_2/2$. Hence it is crucial to make accurate coherence time measurements before magnetic field measurements are carried out.

To this end we carried out T_2^* and T_2 measurements in a similar manner as with the bare state. The

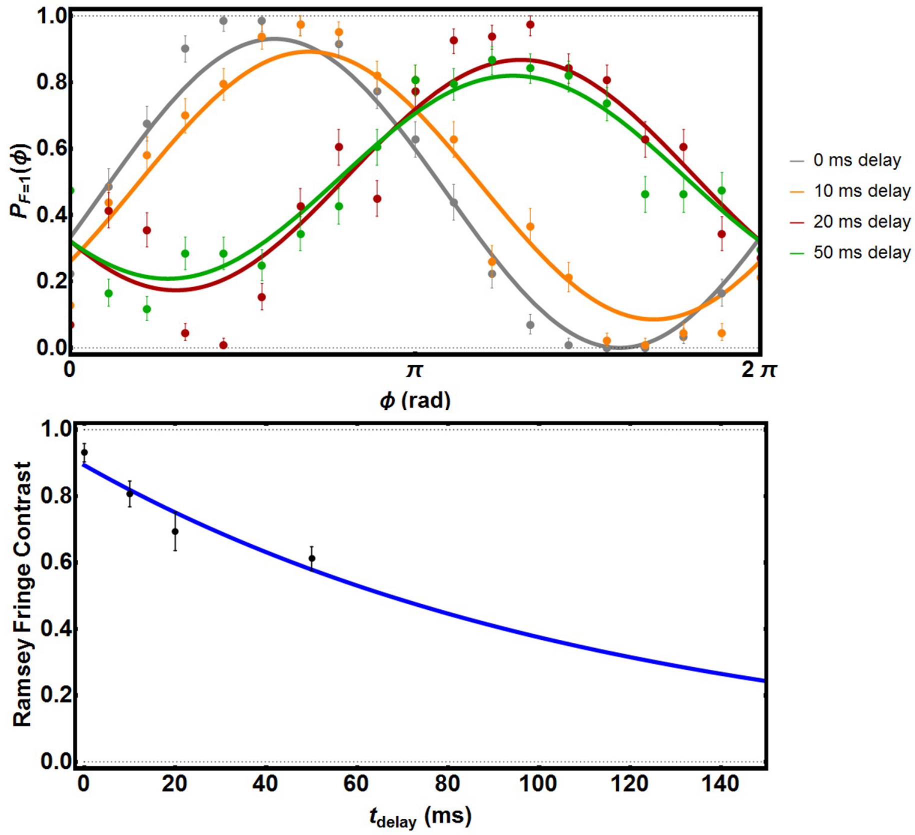

Figure 47: Top). Results of a T_2^* experiment (see section 4.3.3) for the $|0'\rangle \leftrightarrow |D\rangle$ transition with the state population of the F=1 state plotted against the phase ϕ of the second $\pi/2$ pulse. The different coloured plots are related to the delay time between the two pulses and are modelled using equation 88 to extract the fringe contrast a. bottom). A plot of the Ramsey experiment plots fringe a against the delay time, where the errors are given by the standard error of the top plots. The line is plotted with an exponential coherence decay function e^{-t_{delay}/T_2^*}, which gives a coherence time of $T_2^* = 0.11(5)$ s. These plots were generated by Dr. Ethan Potter [39].

state is prepared in the $|0'\rangle$ state in the manner shown in figure 45 and using the $|0'\rangle \leftrightarrow |D\rangle$ via ω_B^+ transition for the $\pi/2$ and π pulses described in section 4.3.3. The T_2^* without the spin echo was found to be 0.11(5) s and the T_2 time was 0.64(5) seconds, with the results of these experiments shown in figures 47 and 48.

As can be seen the coherence times of these experiments are orders of magnitude greater than the bare state measurements made in section 4.4.3. There is still a significant difference in coherence times T_2^* and T_2, this is probably due to the slow magnetic field drift of the Helmholtz coils mentioned in section 4.4.3. Even with this there is a significant difference in the coherence time compared to the work of Baumgart et al [3]. The source of this discrepancy was investigated by Dr Ethan Potter in his thesis [39], where he believed that it was noise in the microwave and RF generation and mixing apparatus (see section 3.3.3). This would result in drifting Rabi frequencies that could cause decoherence in the system. This was partially confirmed by an experiment he undertook to examine the noise when the microwave and RF emitters were coupled to our Virtual Network Analyser (VNA), which saw a 0.1 dBm oscillation in the microwave fields. This offers a possible avenue to improve coherence time in the future, by improving the apparatus and isolating sources of noise.

Another possible source of decoherence is background RF populating the $|u\rangle$ and $|d\rangle$ states. This

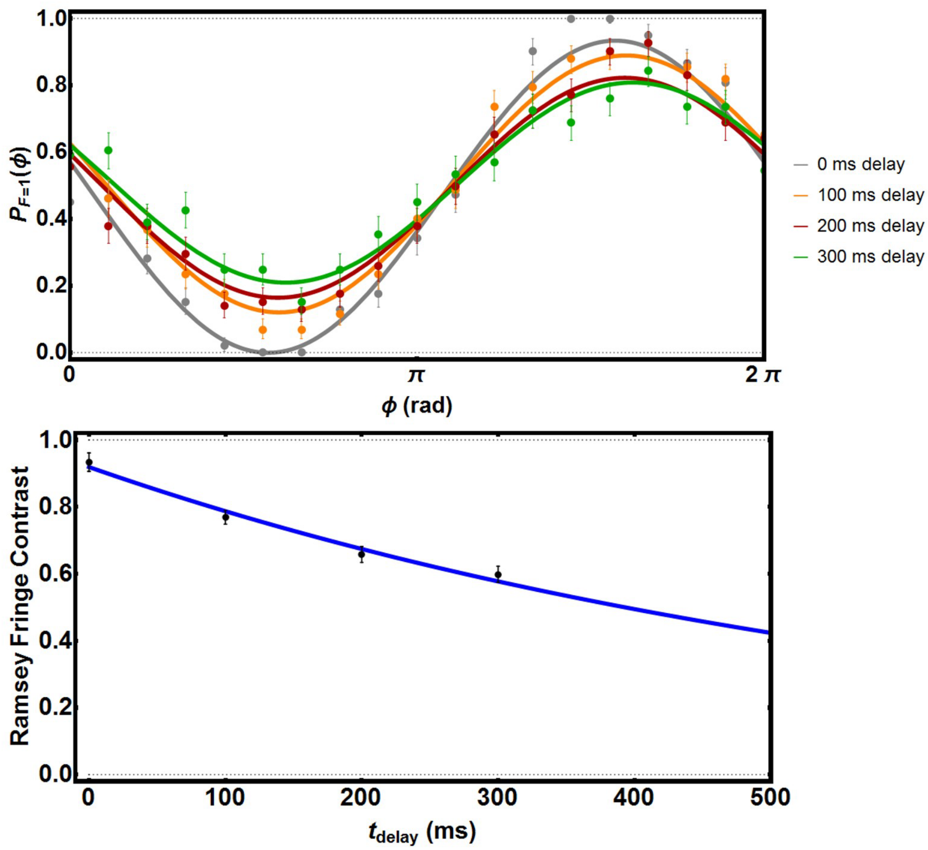

Figure 48: Top). Results of a T_2 experiment (see section 4.3.3) for the $|0'\rangle \leftrightarrow |D\rangle$ transition, with the state population of the F=1 state plotted against the phase ϕ of the second $\pi/2$ pulse. The different coloured plots are related to the total delay time between the two pulses (not including the π decoupling pulse) and are modelled using equation 88 to extract the fringe contrast a. bottom). A plot of the Ramsey experiment plots fringe a against the delay time, where the errors are given by the standard error of the top plots. The line is plotted with an exponential coherence decay function e^{-t_{delay}/T_2}, which gives a coherence time of $T_2 = 0.64(5)$ s. These plots were generated by Dr. Ethan Potter [39].

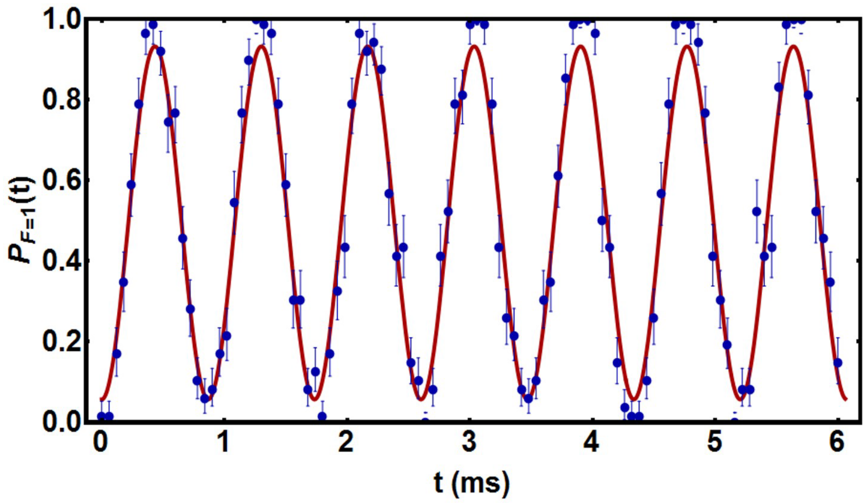

Figure 49: This is a Rabi oscillation experiment plot with the $F = 1$ state population after an experiment against the exposure time to the field driving the $|0'\rangle \leftrightarrow |D\rangle$ transition. Each data point is an average population probability taken from 50 individual measurements. This data was fitted to a sine function (red line), which is described by equation 88. This fit gives a Rabi frequency of $\Omega_{RF}/2\pi = 1.153$ kHz. This plot was generated by Dr. Ethan Potter [39].

would be caused by RF fields around the frequency of $\Omega_{\mu w}/\sqrt{2}$ where $\Omega_{\mu w}$ is the Rabi frequency of the matched microwave dressing fields. The rate at which this decoherence occurs is given by the T_1 time, which was not measured in this project, but is detailed in Dr Randall's thesis [63]. Experiments could be carried out in future to measure this T_1 to determine if this effect is a major contributing factor to the decoherence that is being experienced on our system.

4.5.3 Dressed state RF Rabi oscillation measurements

Once coherence time measurements have been made, sensing experiments can finally be carried out. These sequences are described in section 4.3.1, while the system is prepared and readout in the way described in figure 45. The only difference with these sensitivity measurements is that they are significantly longer typically measuring hundreds of milliseconds to be similar to the coherence times measured in section 4.5.2. The long sensitivity measurements will be detailed in the following section, but an example of the beginning of a long Rabi experiment is shown in figure 49.

4.5.4 Dressed state RF sensitivity measurements

As detailed in section 2.4.2 using long Rabi oscillations the Rabi frequency can be determined to a high accuracy (equation 82). From this the intensity of that RF field can be determined using equation 83.

We initially wished to conduct sensing measurements over many oscillations with experimental times over hundreds of milliseconds to be close to the optimal sensing time of $T_2/2$, but we were unable to do this within the constraints of the project. This was because ions that are exposed to RF for a long time during experiments, are not being cooled by the off-resonant 369 nm laser, so there is a significant chance of the ion will either de-crystallise, (so it can no longer be observed or manipulated coherently) or it is ejected from the trap entirely. More work investigating this phenomena was done by Dr. Ethan Potter in his thesis [39].

	RF field sensing with microwave dressing fields	
$T_{add}(ms)$	76	
n	30	
$T_2(s)$	0.64(5)	
	Experimental results	Theoretical limit with T_2 time
$\delta\Omega'_S$ (Hz)	6.16±0.236	0.770
δB (pT)	99.0±3.80	12.4
S $(pT/\sqrt{Hz})$	7.826 ±1.63	3.58
S_B $(pT/\sqrt{Hz})$	126±26.2	57.5

Table 3: Table summarising the results for 15.6161 MHz RF sensing, with microwave dressing fields and comparing these results with the theoretical limits of the system given the T_2 time measured for sensing this RF frequency. T_{add} is the total of the cooling, state preparation and detection times of the experiment; n is the number of experimental repetitions per data point; T_2 is the coherence time of the system measured in section 4.5.2; $\delta\Omega'_S$ is the sensitivity of the Rabi frequency measurement; δB is the sensitivity of the RF field strength measurement; S_Ω is the sensitivity of the Rabi frequency measurement per second of total experimental time; S_B is the sensitivity of the RF field strength measurement per second of total experimental time.

The actual RF sensing measurements that were used for the sensitivity calculations are given in figure 50. Here the resonant frequency of the $|0'\rangle \leftrightarrow |D\rangle$ transition was determined so an on resonant field could be applied to the system to produce Rabi oscillations. These oscillations were fitted to equation 88 to determine the Rabi frequency of $\Omega_{RF}/2\pi = 1.165$ kHz, which gives a magnetic field strength of $B_{RF} = 1.177 \times 10^{-7} T$ using equation 83, from section 2.4.2.

The data shown in figure 50 can be used to find the maximum sensitivity in terms of Rabi frequency. This is shown in figure 51, where the data points in figure 50 were compared to the line of best fit, to give their standard error. This shows how the sensitivity generally increases with time, with our best sensitivity being $\delta\Omega'_{RF} = 6.156 \pm 0.236$ Hz, which indicates a magnetic field sensitivity of $\delta B = 9.8997 \pm 0.3795 \times 10^{-11}$ T.

As detailed in section 2.4.2 this does not represent the real sensitivity of the system S_Ω given by equation 81, which is the sensitivity of the Rabi frequency measurement per second of total measurement time T_{tot}. The data in figure 51 can be used to produce figure 52 using equation 83. From this S plot the maximum sensitivity was extracted and found to be $S_\Omega = 7.8 \pm 1.626$ $Hz/\sqrt{Hz}$, which gives a magnetic field sensitivity of 126 ± 26 $pT/\sqrt{Hz}$. As mentioned previously, there was an issue with the ion heating, which meant we had to apply very long cooling steps during experiments, so $T_{add} > t$. This lead to the results shown in figure 52 to be very far from the theoretical limit. This does leave a lot of room for improvement then if a way can be found to limit the heating on the ion and hence reduce T_{add}. A summary of all the RF sensing results can be found in table 3 as well as a comparison with the theoretical limits of the system given our measured coherence time.

The Python code used for the frequency scans, Rabi oscillation measurements and Ramsey experiments, using microwave dressing fields is shown in the appendix A.4.

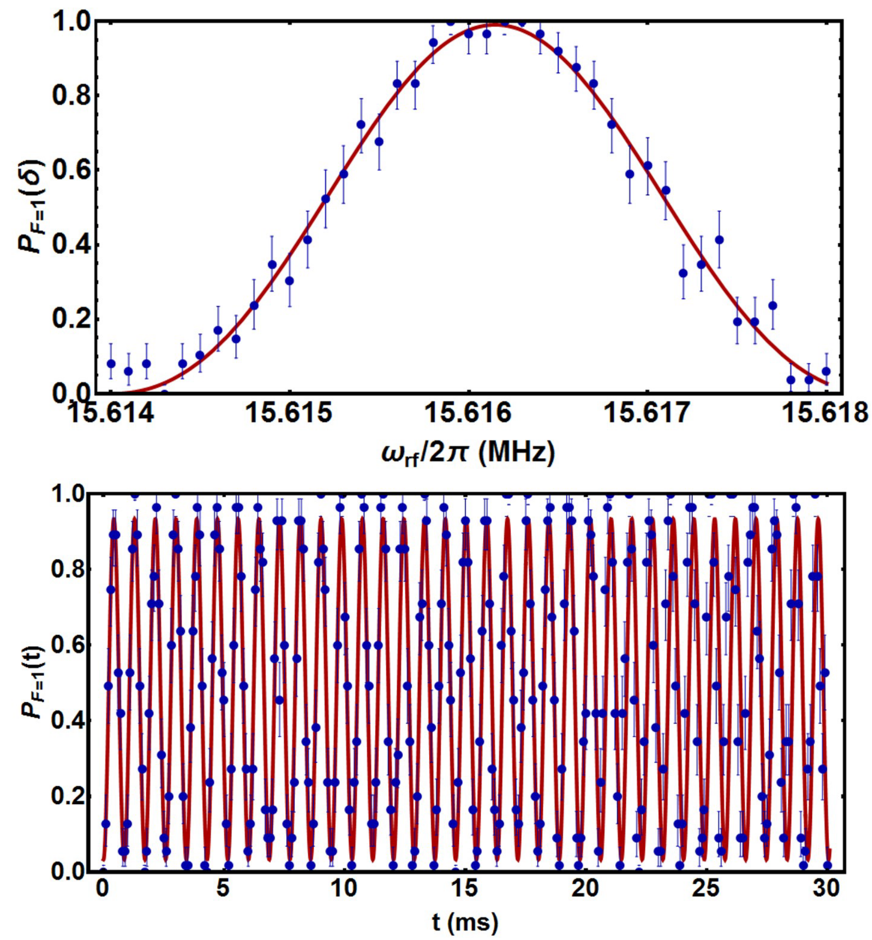

Figure 50: Top). A frequency scan of the transition we used for RF sensing: $|0'\rangle \leftrightarrow |D\rangle$. With the population of the F=1 state of the $^2S_{1/2}$ manifold of the $^{171}Yb^+$ against the applied RF frequency $\omega_{rf}/2\pi$. The applied RF pulse lasted 429.36 μs and each data point consists of 50 separate measurements. The red line is a fit of the data using equation 86, which is used to extract a peak resonant frequency of $\omega_p/2\pi = 15.6161$ MHz. Bottom). This is a Rabi frequency measurement by collecting data over a long interaction time and by making many measurements at different times to build enough data to make a good estimate of the Rabi frequency. The red plot line was plotted using a sine wave function described by equation 88. From this equation we can extract the Rabi frequency of this measurement $\Omega_{RF}/2\pi = 1.165$ kHz, which using equation 83 gives us a magnetic field strength of $B_{RF} = 1.177 \times 10^{-7}T$. These plots were generated by Dr. Ethan Potter [39].

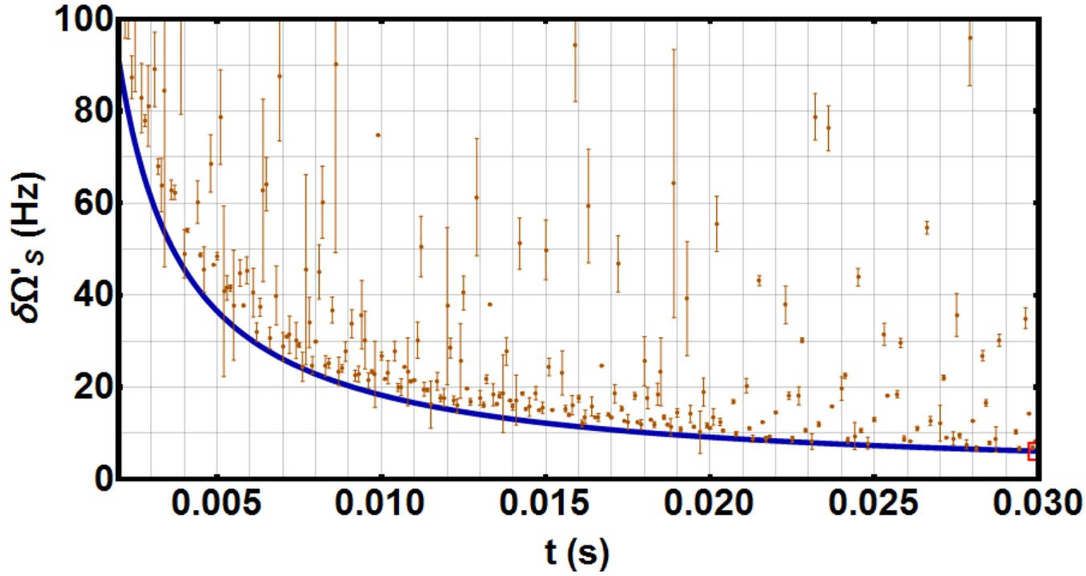

Figure 51: This is a graph of the minimal Rabi frequency resolution $\delta\Omega_S$ for each data point from figure 50. Each orange data point was calculated by measuring the standard deviation of each data point in figure 50 to the best fit line using equation 75. The blue line represents the best possible sensitivity values theoretically possible according to equation 80. The red square to the far right of the graph shows the best sensitivity that was achieved with this experiment, taken after a measurement time of 0.03 s, which gave a Rabi frequency resolution of $\delta\Omega'_{RF} = 6.156 \pm 0.236$ Hz, which gives a minimal magnetic field change of $\delta B = 9.8997 \pm 0.3795 \times 10^{-11}$ T. The errors on these measurements were calculated using the asymmetry of the population measurement errors. This plot was generated by Dr. Ethan Potter [39].

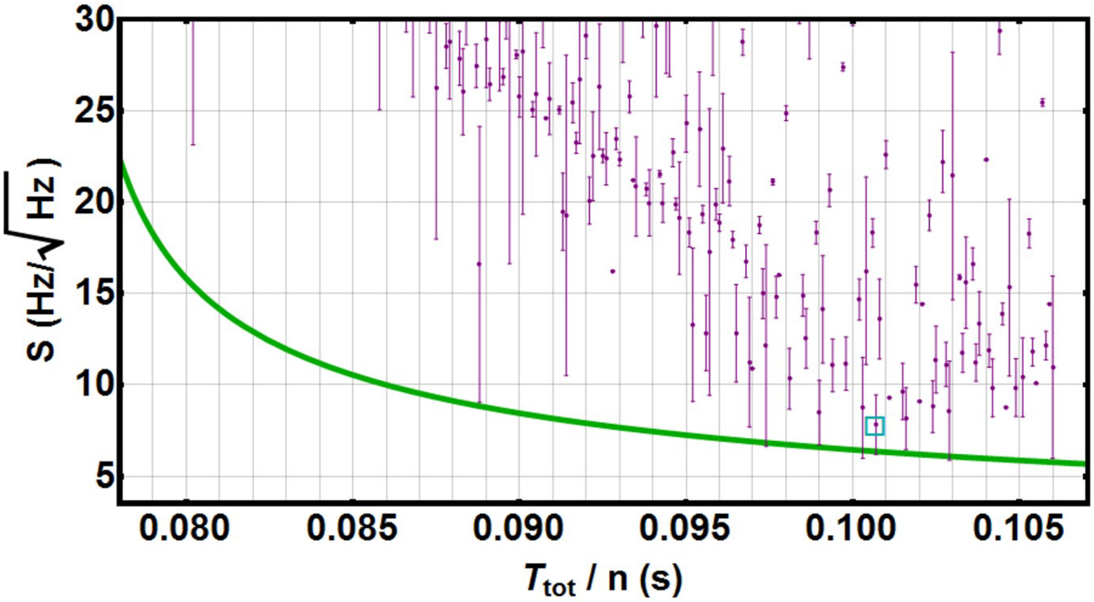

Figure 52: Sensitivity measurements derived from the data used in figure 51. The purple data points are generated using the equation 81 to give the Rabi frequency sensitivity per second of total experimental time. n is the number of measurements per run, which was 30. T_{tot} was the total experimental time given by $T_{tot} = n(t+T_{add})/n_i$; where $T_{add} = 76$ ms is the time needed for cooling, preparing and detecting the ions state during each run; $n_i = 1$ is the number of ions used in the experiment. The green line is the theoretical limit of the system and calculated using equation 82 for the ideal case when $T_2 \to \infty$. The best sensitivity measured in this data set is indicated by the cyan box, which was taken with total experimental time of $T_{tot}/n = 0.1007$ s and gave a sensitivity of $S_\Omega = 7.8 \pm 1.626\ Hz/\sqrt{Hz}$, which gives a magnetic field sensitivity of $126 \pm 26\ pT/\sqrt{Hz}$. This plot was generated by Dr. Ethan Potter [39].

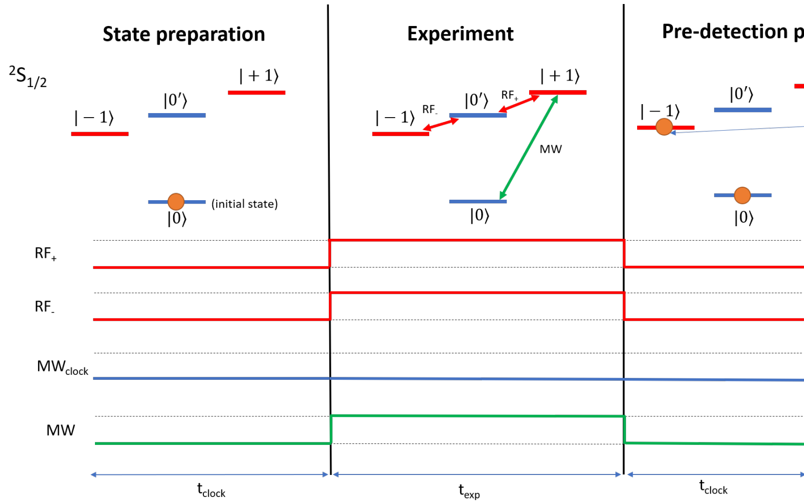

Figure 53: This shows the pulses used during an RF dressed state sensing experiment as well as show how these pulses influence the ions $^2S_{1/2}$ manifold states. This procedure is significantly more straightforward than with microwave dressing fields shown in figure 53 as the state is already prepared in the correct state from the procedure shown in figure 45. The state is prepared in the $|0\rangle$ state so the experiment can begin, which is initiated by applying RF dressing fields RF_- and RF_+ to set up the dressed state $|D'\rangle$. The ion is then exposed to an RF field resonant with the transition we wish to sense with: $|0\rangle \leftrightarrow |D'\rangle$. After finishing our experiment the dressing fields are removed leaving the state in superposition of $|D'\rangle$ and $|0\rangle$. A 369 nm laser pulse is then used after the experiment to produce fluorescence if the state is left in the F=1 $|D'\rangle$ state.

4.6 Dressed state microwave sensing

As detailed in section 2.3.2 dressed states will provide far greater sensing capability compared to the simple bare states experiments detailed in the previous section. This is due to their inherent noise cancelling capability so fast oscillation B-field fluctuations that cause 1st order Zeeman effects on the ion are cancelled out and will not cause the ion to decohere. This dressed state system was adapted from the technique used for maintaining high coherence time when using $^{171}Yb^+$ ions for quantum gates [64].

The resonant frequencies and π times measured in section 4.4 can now be employed to generate RF dressing fields on transitions $|0'\rangle \leftrightarrow |+1\rangle$ and $|0'\rangle \leftrightarrow |-1\rangle$, with on resonant fields with matching Rabi frequencies. This produces a dressed state $|D'\rangle$, which allows for RF sensing using the $|0\rangle \leftrightarrow |D'\rangle$ transition. This experimental procedure is summarised in figure 53. The transition also has the utility that it can have its resonant frequency tuned by changing the applied B-field to choose certain frequencies to sense while ignoring others.

4.6.1 Dressed state microwave frequency scan

The first step once on resonant dressing fields are applied is to identify all the different dressed state transitions with the $|0\rangle$ state. These are the transitions with the three RF dressed states $|u'\rangle$, $|d'\rangle$ and $|D'\rangle$. Unlike the microwave dressing fields, there is a 1st order Zeeman splitting between the transition pairs for $|+1\rangle$ and $|-1\rangle$ so the frequency splitting is very wide and would be impractical to do a frequency scan over all six states, so three of the states are shown in figure 54. These transition frequencies will allow us to make sure that the various states are not overlapping leading to cross talk and make sure we are using the transition $|0\rangle \leftrightarrow |D'\rangle$ as this state will experience less decoherence (see section 2.3.2).

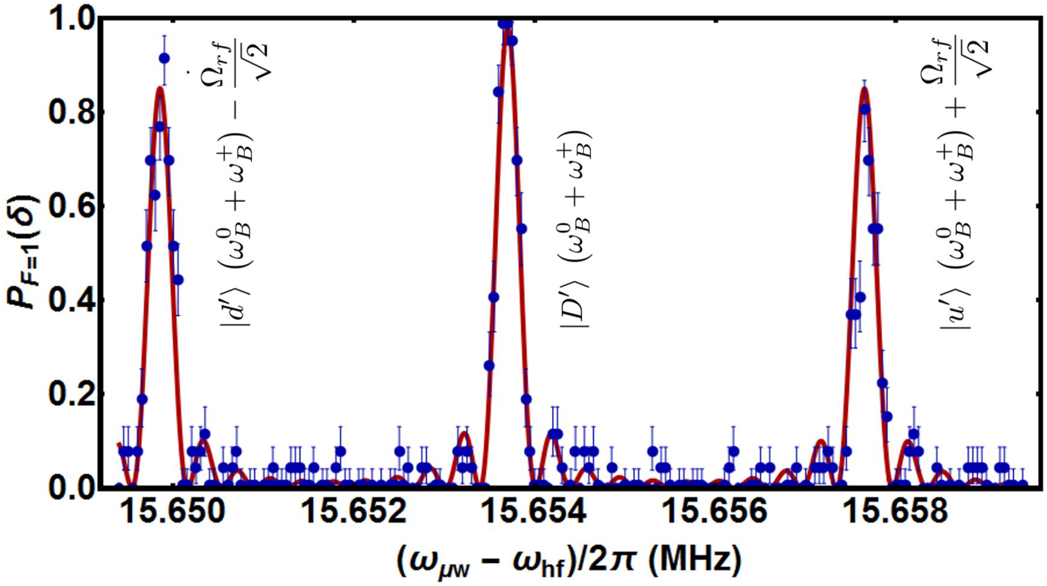

Figure 54: This is plot of the population of the F=1 state of the $^2S_{1/2}$ manifold after a frequency sweep experiment (see section 4.3.1) against the frequency splitting ($\omega_{\mu w}/2\pi$) of an applied microwave pulse with a pulse time of 2.795 ms. The red line is fitted individually for each of the three peaks using a Gaussian like function (equation 86). The difference in peak heights is explained by the fact that the same pulse time was used for all three peaks while their relative π times are different. The three peaks are produced from the three dressed states $|u'\rangle$, $|d'\rangle$ and $|D'\rangle$. From these peak frequencies we can calculate the Rabi frequency of the dressing fields $\Omega_{RF}/\sqrt{2} \approx 2\pi\times 3.9$ kHz. This plot was generated by Dr. Ethan Potter [39].

4.6.2 Dressed state microwave sensing coherence time measurements

As with microwave dressed states shown in section 4.5.2, the coherence time is needed to make optimal sensitivity measurements. We used the same experimental procedure as before, but applying pulses to the $|0\rangle \leftrightarrow |D'\rangle$ transition instead. The T_2^* without the spin echo was found to be 0.35(8) s and the T_2 time was 1.15(3) seconds, with the results of these experiments shown in figures 55 and 56 respectively.

The coherence time measurements give very similar results to that for microwave dressed state, which is to be expected as the two systems are analogous to one another. The coherence time discrepancy between the T_2^* and T_2 times is explained in the same manner as with microwave dressed states (see section 4.5.2).

4.6.3 Dressed state microwave Rabi oscillation measurements

Microwave Rabi oscillation measurements are conducted in the same manner as with RF Rabi oscillation measurements detailed in section 4.5.3. An example of a short RF measurement can be seen in figure 57.

4.6.4 Dressed state microwave sensitivity measurements

As detailed in section 2.4.2 using long Rabi oscillations the Rabi frequency can be determined to a high accuracy (equation 82). From this the intensity of that RF field can be determined using equation 83 in a very similar manner as with RF sensitivity measurements detailed in section 4.5.4. We also experienced the same overheating problem as before so we were limited to making measurements up to only 50 ms, which can be seen in figure 58. It does show however the increase in sensitivity with greater measurement time.

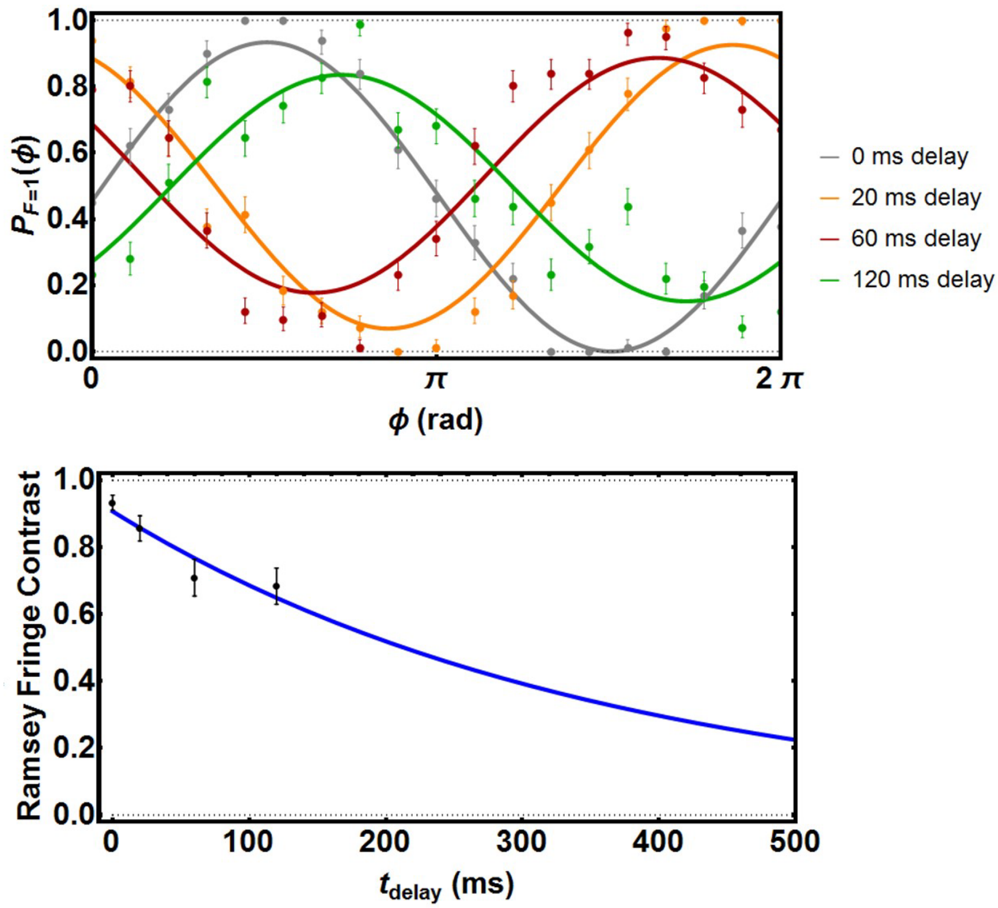

Figure 55: Top). Results of a T_2^* experiment (see section 4.3.3) for the $|0\rangle \leftrightarrow |D'\rangle$ transition with the state population of the F=1 state plotted against the phase ϕ of the second $\pi/2$ pulse. The different coloured plots are related to the delay time between the two pulses and are modelled using equation 88 to extract the fringe contrast a. bottom). A plot of the Ramsey experiment plots fringe a against the delay time, where the errors are given by the standard error of the top plots. The line is plotted with an exponential coherence decay function e^{-t_{delay}/T_2^*}, which gives a coherence time of T_2^* =0.35(8) s. These plots were generated by Dr. Ethan Potter [39].

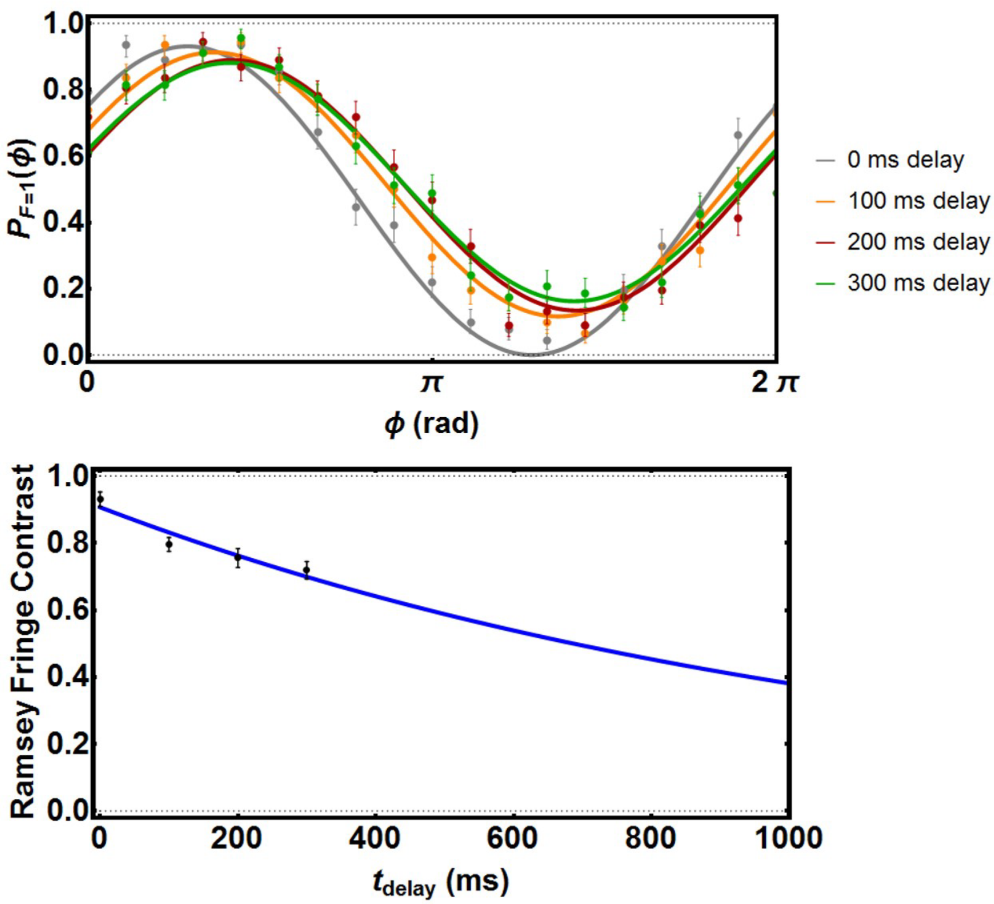

Figure 56: Top). Results of a T_2 experiment (see section 4.3.3) for the $|0\rangle \leftrightarrow |D'\rangle$ transition, with the state population of the F=1 state plotted against the phase ϕ of the second $\pi/2$ pulse. The different coloured plots are related to the total delay time between the two pulses (not including the π decoupling pulse) and are modelled using equation 88 to extract the fringe contrast a. bottom). A plot of the Ramsey experiment plots fringe a against the delay time, where the errors are given by the standard error of the top plots. The line is plotted with an exponential coherence decay function e^{-t_{delay}/T_2}, which gives a coherence time of T_2 =1.15(3) s. This plot was generated by Dr. Ethan Potter [39].

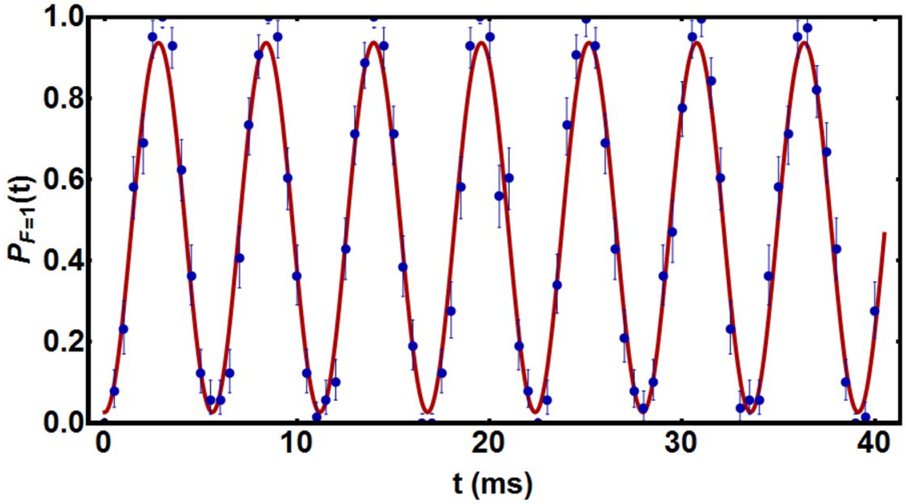

Figure 57: This is a Rabi oscillation experiment plot with the $F = 1$ state population after an experiment against the exposure time to the field driving the $|0\rangle \leftrightarrow |D'\rangle$ transition. Each data point is an average population probability taken from 50 individual measurements. This data was fitted to a sine function (red line), which is described by equation 88. This fit gives a Rabi frequency of $\Omega_{RF}/2\pi$ =179 Hz. This plot was generated by Dr. Ethan Potter [39].

The actual microwave sensing measurements that were used for the sensitivity calculations are given in figure 58. Here the resonant frequency of the $|0\rangle \leftrightarrow |D'\rangle$ transition was determined so an on resonant field could be applied to the system to produce Rabi oscillations. These oscillations were fitted to equation 88 to determine the Rabi frequency of $\Omega_{\mu 2}/2\pi$ =0.176 kHz, which gives a magnetic field strength of $B_{RF} = 1.178 \times 10^{-8}T$ using equation 83.

From the data collected in figure 58 the maximum sensitivity in terms of the Rabi frequency can be determined. This is shown in figure 59, where the data points in figure 58 were compared to the line of best fit, to give their standard error. This shows how the sensitivity generally decreases with time, with our best sensitivity being $\delta\Omega'_{\mu w} = 4.101 \pm 0.405 \; Hz/\sqrt{Hz}$ which indicates a magnetic field sensitivity of $\delta B = 6.5942 \pm 0.6512 \times 10^{-11}$ $T/\sqrt{Hz}$.

As detailed in section 2.4.2, this does not represent the real sensitivity of the system S_Ω given by equation 81, which is the sensitivity of the Rabi frequency measurement per second of total measurement time T_{tot}. The data shown in figure 59 can be used to produce figure 60 using equation 83. From this S plot the maximum sensitivity was extracted and found to be $S_\Omega = 6.34 \pm 0.687 \; Hz/\sqrt{Hz}$, which gives a magnetic field sensitivity of $102 \pm 11.0 \; pT/\sqrt{Hz}$. As mentioned previously, there was an issue with the ion heating, which meant we had to apply very long cooling steps during experiments, so $T_{add} > t$. This lead to the results shown in figure 52 to be very far from the theoretical limit. This does leave a lot of room for improvement then if a way can be found to limit the heating on the ion and hence reduce T_{add}. A summary of all the microwave sensing results can be found in table 4 as well as a comparison with the theoretical limits of the system given our measured coherence time.

The Python code used for the frequency scans, Rabi oscillation measurements and Ramsey experiments, using RF dressing fields is shown in the appendix A.5.

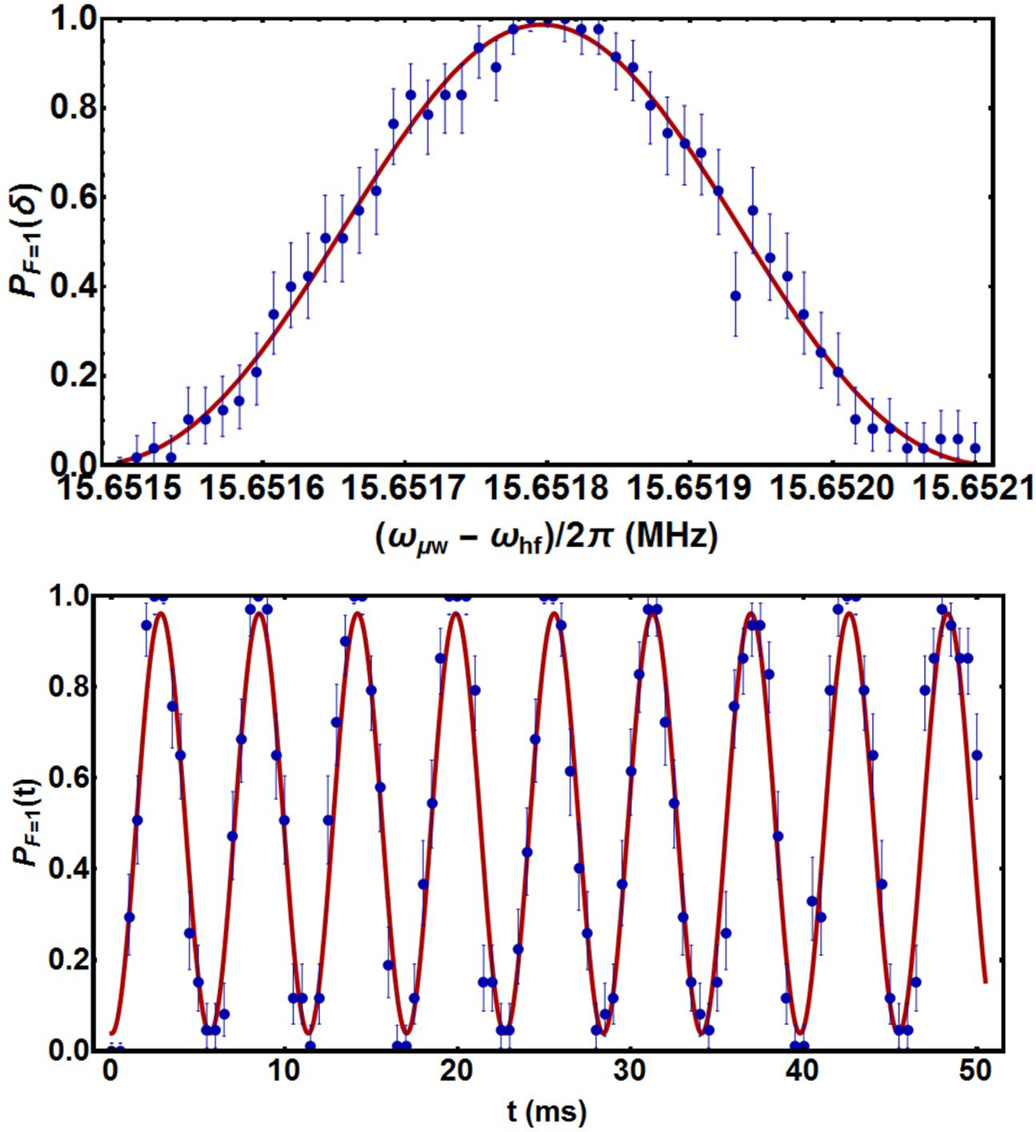

Figure 58: Top). A frequency scan of the transition we used for microwave sensing: $|0\rangle \leftrightarrow |D'\rangle$. With the population of the F=1 state of the $^2S_{1/2}$ manifold of the $^{171}Yb^+$ ion against the applied RF frequency $\omega_{\mu w}/2\pi$. The applied microwave pulse lasted 2841.72 μs and each data point consists of 50 separate measurements. The red line is a fit of the data using a Gaussian like function equation 86. Bottom). This is a Rabi frequency measurement by collecting data over a long interaction time and by making many measurements at different times to build enough data to make a good estimate of the Rabi frequency. The red plot line was plotted using a sine wave function described by equation 88. From this equation we can extract the Rabi frequency of this measurement $\Omega_{\mu w}/2\pi$ =0.176 kHz, which using equation 83 gives us a magnetic field strength of $B_{RF} = 1.178 \times 10^{-8}T$. These plots were generated by Dr. Ethan Potter [39].

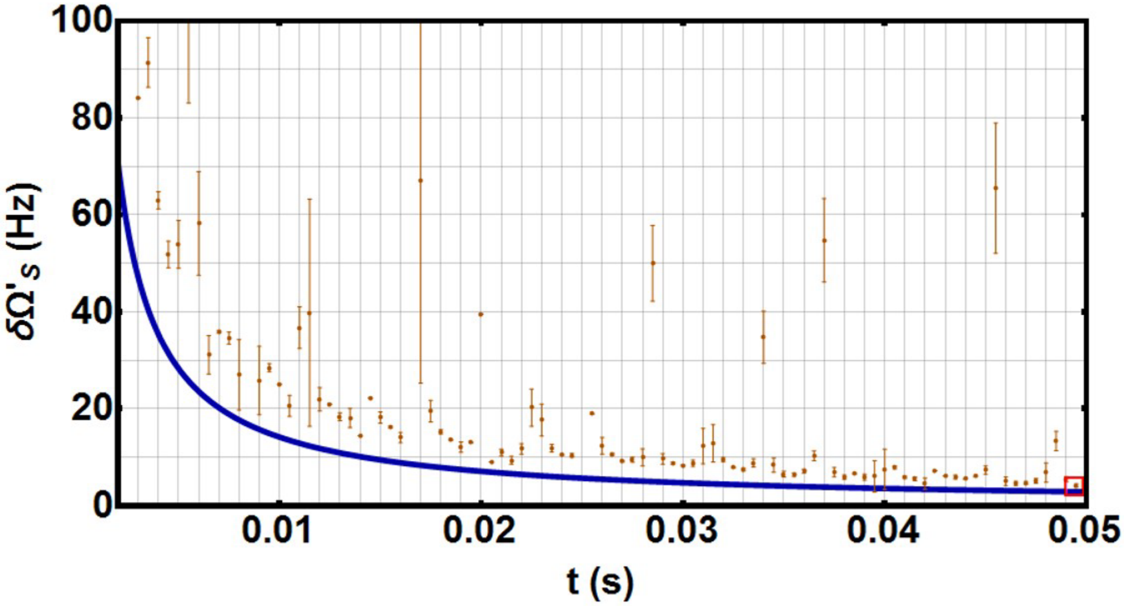

Figure 59: This is a graph of the minimal Rabi frequency resolution $\delta\Omega_S$ for each data point from figure 58. Each orange data point was calculated by measuring the standard deviation of each data point in figure 58 to the best fit line using equation 75. The blue line represents the best possible sensitivity values theoretically possible according to equation 80. The red square to the far right of the graph shows the best sensitivity that was achieved with this experiment, taken after a measurement time of 0.0495 s, which gave a Rabi frequency resolution of $\delta\Omega'_{RF} = 4.101 \pm 0.405$ Hz, that gives a minimal magnetic field change of $\delta B = 6.5942 \pm 0.6512 \times 10^{-11}$ T. The errors on these measurements were calculated using the asymmetry of the population measurement errors. This plot was generated by Dr. Ethan Potter [39].

	microwave field sensing with RF dressing fields	
T_{add} (ms)	76	
n	50	
T_2 (s)	1.15(3)	
	Experimental results	Theoretical limit with T_2 time
$\delta\Omega'_S$ (Hz)	4.10±0.405	0.334
δB (pT)	65.9±6.51	5.37
S $(pT/\sqrt{Hz})$	6.35 ±0.687	2.62
S_B $(pT/\sqrt{Hz})$	102±11.0	42.1

Table 4: Table summarising the results of the 12.658 GHz microwave sensing, with RF dressing fields and comparing these results with the theoretical limits of the system given the T_2 time measured for sensing with this RF frequency. T_{add} is the total of the cooling, state prep and detection times of the experiment; n is the number of experimental repetitions per data point; T_2 is the coherence time of the system measured in section 4.6.2; $\delta\Omega'_S$ is the sensitivity of the Rabi frequency measurement; δB is the sensitivity of the microwave field strength measurement; S_Ω is the sensitivity of the Rabi frequency measurement per second of total experimental time; S_B is the sensitivity of the microwave field strength measurement per second of total experimental time.

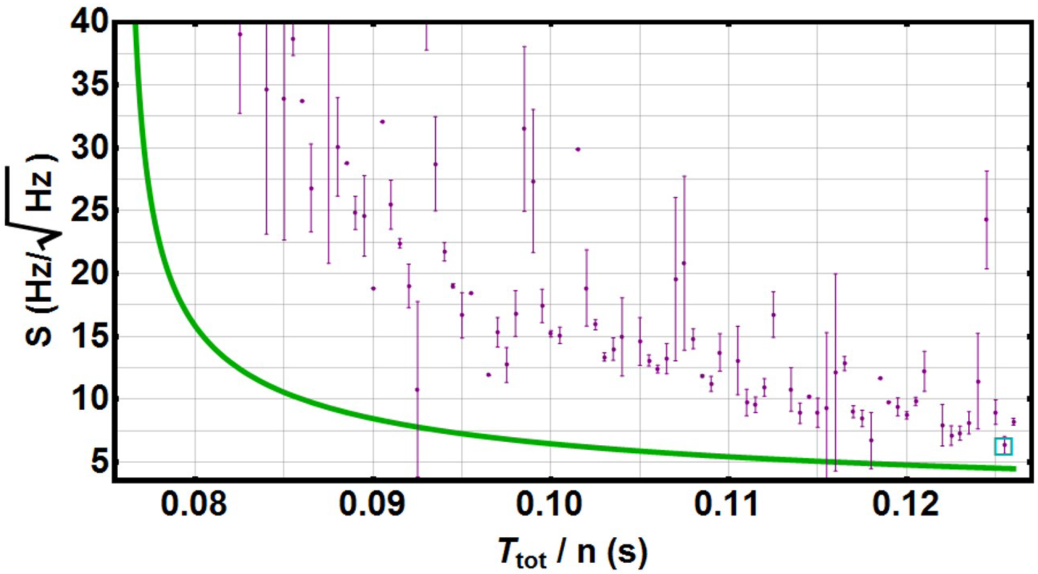

Figure 60: Graph of the sensitivity of the measurements from figure 51 per second of total experimental time. The purple data points are generated using the equation 81 to give the Rabi frequency sensitivity per second of total experimental time. n is the number of measurements per run, which was 30. T_{tot} was the total experimental time given by $T_{tot} = n(t + T_{add})/n_i$; where $T_{add} = 76$ ms is the time needed for cooling, preparing and detecting the ions state during each run; $n_i = 1$ is the number of ions used in the experiment. The green line is the theoretical limit of the system and calculated using equation 82 for the ideal case when $T_2 \to \infty$. The best sensitivity measured in this data set is indicated by the cyan box, which was taken with total experimental time of $T_{tot}/n = 0.1255$ s and gave a sensitivity of $S_\Omega = 6.35 \pm 0.6876\ Hz/\sqrt{Hz}$, which gives a magnetic field sensitivity of $102 \pm 11.0\ pT/\sqrt{Hz}$. This plot was generated by Dr. Ethan Potter [39].

5 Coil-ion coupling technique and future experiments

Although I have succeeded in achieving many milestones in terms of demonstrating RF and microwave sensing using trapped-ions, I believe there is still a lot to build on experimentally. The below objectives will need to be completed before we can demonstrate that this sensor has real potential to make an impact in the commercial space. These include demonstrating tuneability; showing sub-millihertz bandwidths and coupling the ion to an antenna system for unprecedented sub femto-Tesla RF detection.

5.1 Tuneability demonstration

One of the main advantages of this sensor over many classical and quantum sensors is its ability to be quickly tuned to particular frequencies, with a very small bandwidth of around 1 Hz. This allows it to ignore frequencies that are not useful to the user and only examine frequencies which are of interest.

This tuneability arises from the Zeeman splitting effect shown in section 2, whereby a DC field is applied to lift the degeneracy of the $m_f = \pm 1$ hyperfine states and allow us to sense between states $|0'\rangle$ and $|+\rangle$ as shown in figure 8. This relies on an assumption that the field is small and so will scale differently with very large splitting, conversely with very small splitting, there is the possibility that the the ω_+ and ω_- states will begin to overlap and produce crosstalk reducing the quality of the signal. Additionally, as shown in section 2.4.1 the coherence time T_2 is inversely proportional to the energy splitting, so as the splitting becomes larger and subsequently the driving frequency becomes higher, sensitivity will be reduced as shown in figure 61.

So far our experiments have demonstrated sensing at a single RF frequency and a single microwave frequency, so the tuneability of the sensor has so far been undemonstrated. With some effort it should be possible to use the procedure for sensing as outlined in section 2 and then repeat the process for multiple RF and microwave frequencies, by changing the applied DC field and hence the energy splitting of the system. This would provide us with a set of data showing how tuned frequency affects sensitivity. This would be a great achievement and demonstrate tuneability for the first time for a quantum sensor in the Microwave and RF regime. This would also help us determine what applications have the greatest potential, by showing which frequencies the sensor excels at compared to rival systems. A significant effort would have to be undertaken however due to the significant number of long measurements needed to be able to produce a single reliable sensitivity measurement, which will have to be repeated many times with different frequencies to provide a convincing demonstration of tuneability.

5.2 Multi-ion sensing

All experiments detailed in section 4 were all conducted using a single ion, carrying out experiments one after another. It is possible to do experiments with many ions, all sensing in an ensemble, which according to equation 82 in section 2.4.2, will result in an increase in sensitivity proportional to $\sqrt{n}$ where n is the number of ions used for sensing.

If we could scale up to a hundred ions, then this would result in a roughly 10 fold increase in sensitivity (as shown in section 2), opening up a number of possibilities for applications such as RADAR and NQR, which involve picking up very weak signals (more details in section 7). Using an ensemble of ions also reduces the amount of time necessary to make an initial measurements, as many individual state measurements are needed

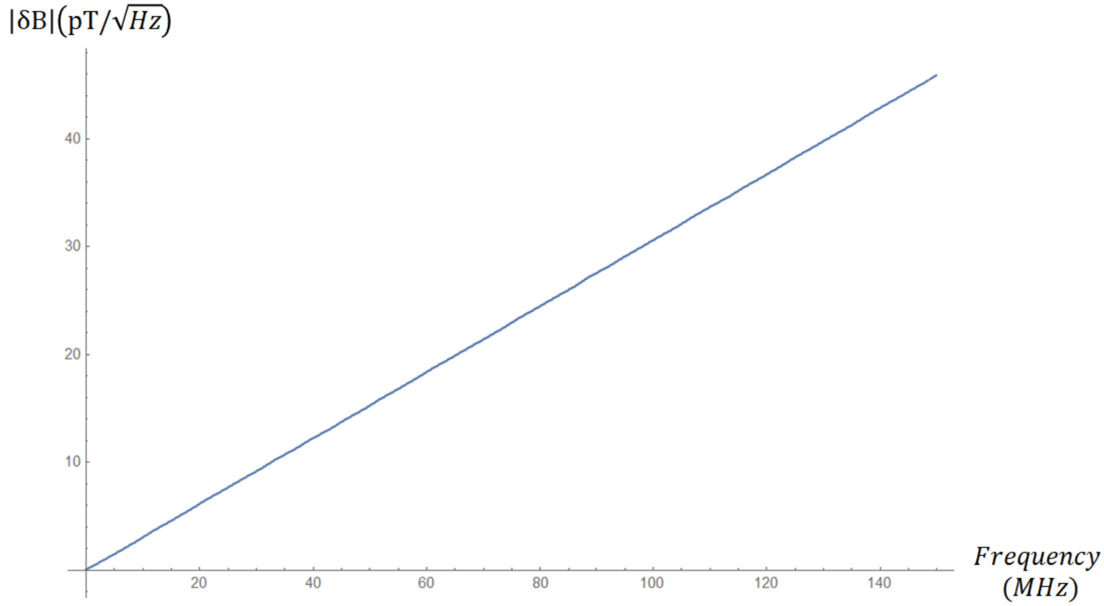

Figure 61: Graph showing how the sensitivity of the sensor should decrease with increasing frequency

to make a single data point, which could be done with a few dozen ions measured simultaneously.

Our group has already demonstrated multi ion trapping of $^{174}Yb^{+}$ using our current linear chip after first trapping, shown in figure 62. This was not used for initial sensing experiments using $^{171}Yb^{+}$, but could in principle be used to demonstrate multi-ion sensing with several ions. Although if we wish to sense with more ions then we will need a different chip, such as the one designed by Dr. Altaf Nizamani called the Dual rail chip (shown in figure 63), which is designed specifically to accommodate large ensembles of several dozen ions. This chip has already been installed demonstrated trapping on a different experiment and would be a valuable next step in terms of improving the number of ions for sensing simultaneously.

There would have to be a few new additions made to the current experimental set-up to allow for multi-ion sensing. As shown in section 3.4 we have a single channel PMT, which is very accurate at allowing us to sense with a single ion, but cannot distinguish between separate ions. To solve this problem we would need either a new multi channel PMT or a CCD camera with sophisticated programming software to pick out individual ions. The multi-channel PMT option would provide us with a far better fidelity and detection time with PMTs generally having very low dark counts than CCDs and can detect individual photons within nano-seconds of one another.

I have also worked with Laser 2000 to develop a beam shaper capable of turning the Gaussian beam shape of our lasers into a flat sheet. A graph showing how the output beam profile changes with input beam diameter is shown in figure This is done so that all the ions trapped on the surface of the dual rail chip can be addressed with the same beams with a similar level of intensity. This device has been designed manufactured and been delivered to us, but still requires some testing to verify it is fit for purpose. More details on this device can be found in section 6.1.2.

The drawbacks would be a limited number of channels for these PMTs, which would mean you would only be able to sense using a few dozen ions at once without multiple PMTs. This would also require very

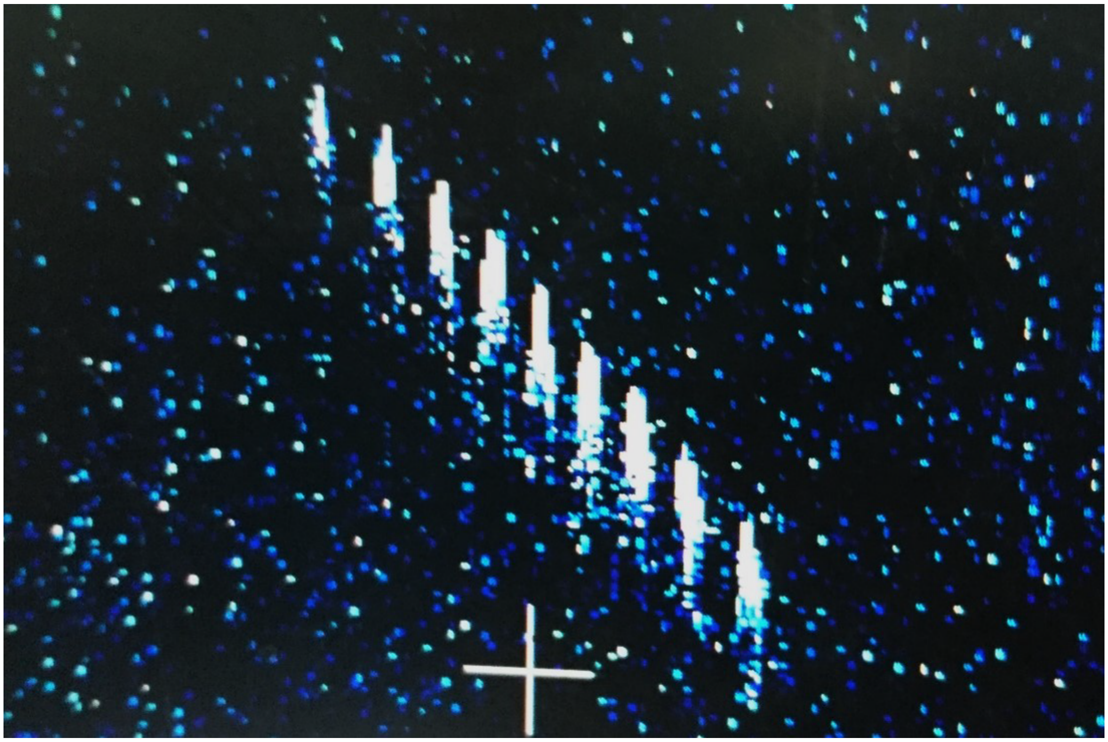

Figure 62: CCD picture of a string of $^{174}Yb^{+}$ ions on our linear chip. This could be repeated in future experiment to make an initial demonstration of the sensitivity increase with additional ions. This would demonstrate only a modest increase in sensitivity though and would require a new chip with greater capacity for more ions to increase the sensitivity further.

expensive and elaborate optics able to focus each ions light onto an individual PMT channel and would be very sensitive to small movements on the system and liable to drift. A CCD camera could be used, but would require significant software development to be able to find individual ions and distinguish them from one another. There has already been some developments in this field by my colleague, Dr. Adam Lawrence, which I would recommend building upon.

5.3 Qdyne sensing using trapped-ions

Using ion traps for RF and microwave detection already offers very competitive signal linewidth determination capabilities, as we have a very long coherence time of up to ≈1 s. As the relationship between linewidth and coherence time is $\delta\nu \propto T_2^{-1}$ this means we typically are able to achieve line widths of around 1 Hz, which compares very favourably with other quantum and even classical sensors that can only typically provide a frequency resolution of around 1 kHz (see section 1.1). This opens up many applications that require very precise frequency resolution such as NMR and RADAR detection.

Even with this already impressive frequency resolution it should be possible to push this a lot further and even into μHz regime using a technique called Qdyne developed by Simon Schmitt et al. [24]. Qdyne also known as the quantum heterodyne detection scheme, uses a well known classical spectroscopical technique, called heterodyning. This involves mixing a given unknown wave with a known clock wave and extracting information about the unknown wave such as phase and frequency, by observing the resulting mixed function. Qdyne takes this classical technique and applies it to a quantum sensor to produce a sensor far better at determining linewidth

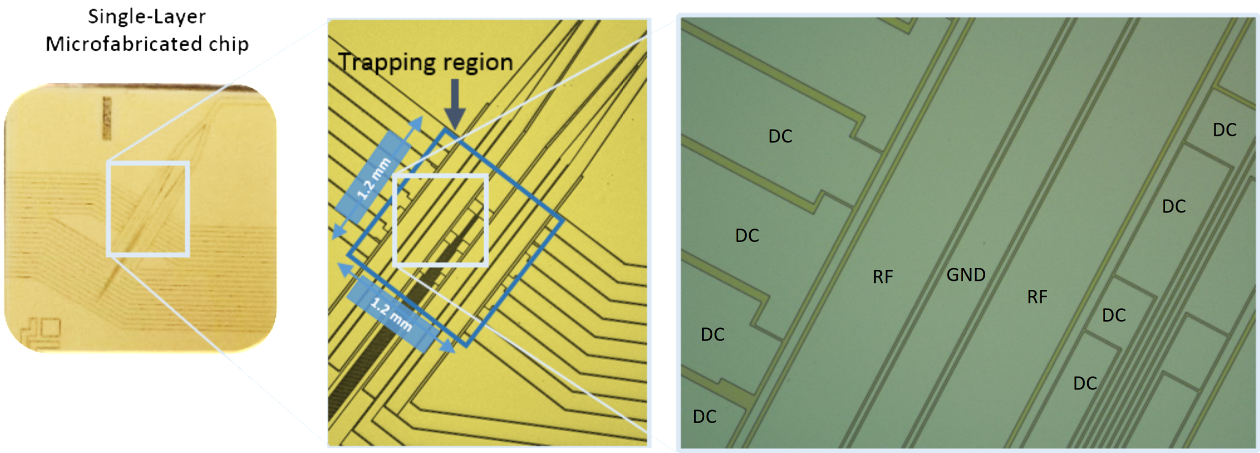

Figure 63: Picture of new dual rail ion trap chip capable of trapping up to a hundred ions simultaneously, showing the dimensions of the trapping area and the position of the RF rails and DC electrodes for producing the pseudo-potential required for trapping.

than either technique in isolation. Details on exactly how this is done is shown in [24], but in summary suppose you want to measure an oscillating magnetic field in time t, which drives a two-level system $|0\rangle$ between $|1\rangle$:

$$H(t) = k\sigma_z \sin(2\pi\nu t + \phi), \tag{90}$$

Where k is the interaction strength, σ_z is the Pauli spin-z operator, ϕ is an arbitrary phase of the magnetic field and ν is the frequency of the wave. The initial phase of a measurement is relevant to the result of the experiment. A dynamic decoupling scheme is used to eliminate drift and noise from the measurement as detailed by Alexander Stark et al [25]. This means applying a series of π pulses in sequence with a separation of roughly $1/2\nu$ as shown in figure 64. Then a detection sequence can check the state and then a subsequent measurement is taken precisely synchronised with the first measurement so information on the phase of the detected wave can be determined. These measurements can be chained together as many times as necessary, but eventually you are limited by the clock stability. This is then repeated a number of times to build up a probability distribution with the change of phase. By heterodyning with the external clock we can measure the signal phase evolution in time and then by applying Fourier transform to the result the frequency space of the signal can be determined (see figure 65). One interesting thing to note is that the decrease in determinable frequency linewidth using this technique is $T^{-3/2}$, which is far better than the T^{-1} relationship using conventional quantum sensing techniques.

Simon Schmitt et al. [24] demonstrated this technique with N-V centres, which as shown in section 1.1.3 is a simple two-level qubit. This is very similar to the two-level system detailed in section 2. I am currently in collaboration with Professor Alex Retzker's group to investigate applying this method to ion trap sensing and whether it can be modified to make magnetic field measurements with extremely long measurement times to allow for increased sensitivity.

This would require a number of upgrades to the system including a very stable clock for timing the measurements of our experiment, but this would result in a revolutionary increase in linewidth for our sensor.

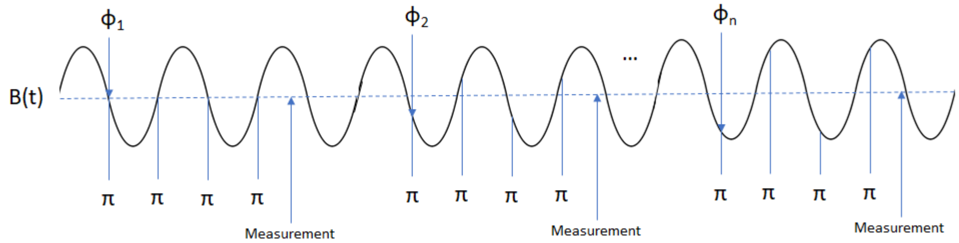

Figure 64: Diagram illustrating the pulse sequence required for Qdyne. The state is first prepared and a sequence of decoupling π pulses are generated before a measurement, which is precisely synchronised with a local oscillator so the subsequent measurement can be initiated with a precise phase displacement to the first measurement. Figure adapted from Alexander Stark et al [25]

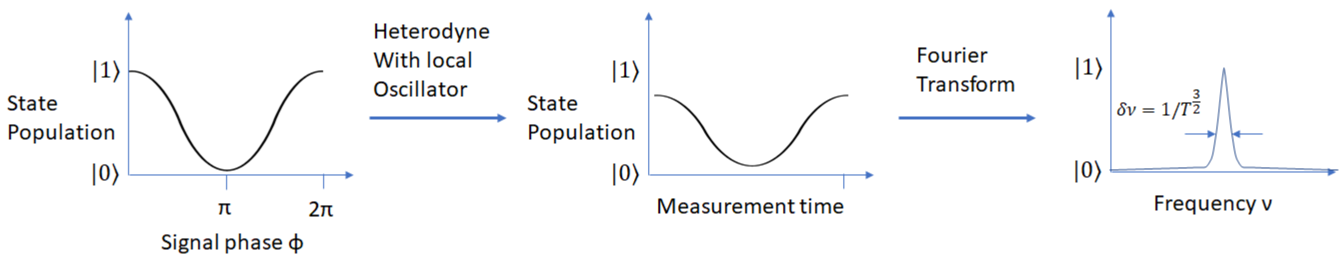

Figure 65: After repeated phase and population measurements are taken, the phase can be heterodyned with a local oscillator to produce a state change distribution with phase change. Fourier transform is then applied to the results of this experiment to extract information about the frequency of the signal. Figure adapted from Alexander Stark et al [25]

5.4 RF Coil Coupling Theory

The tunable RF ion quantum sensor is highly competitive in the RF and microwave frequency domain compared to other quantum sensors. Nevertheless, there is a significant advantage that RF pick-up coils/antennas and microwave radar dishes have over quantum sensor devices. This is due to the fact that quantum devices take measurements at a single point in space as opposed to an RF coil for example which collects an RF signal from a wide area given by the radius of the coil. This then generates a current, which can then be amplified and detected. This amplification and detection however adds a significant level of noise compared to what can be achieved using our quantum sensor. We have therefore developed a method which combines elements of classical sensors with our quantum sensor and obtain a system which is far more effective than either traditional sensors or a 'bare' quantum sensor. In principle we can use a normal aerial or RF coil, which can receive the RF field and induce a current in a wire. This wire is then plugged into our vacuum system and fed into a small coil located close to the trapped-ions. This concentrates the detected magnetic field into a small area around the ion causing a significant amplification of the received magnetic field. This effectively means we are using our device to replace the amplifier and detector system, yet maintain the use of the front end antenna system. This is expected to offer significant advantages over traditional RF and microwave detection systems resulting in the ability to detect smaller signals in noisier environments. A simplified schematic of the antenna-ion set-up is shown in figure 66. The subsequent discussion and calculations are work that I have done to demonstrate the feasibility of this idea.

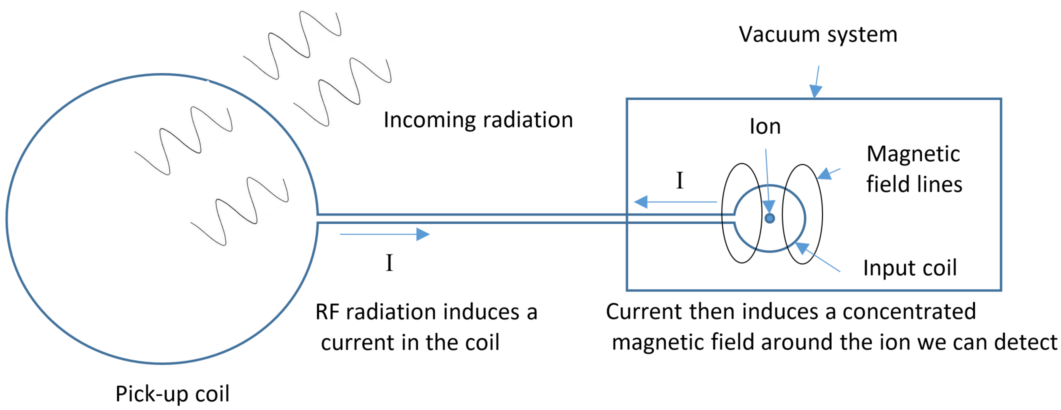

Figure 66: Diagram showing how RF radiation can induce a current in a coil, which induces a current in the input coil around an ion inside the vacuum system causing an amplification in magnetic field, greatly enhancing the sensitivity of the sensor.

5.4.1 Minimum Power Calculation

First we want to try and calculate the minimum sensitivity of this system in terms of power in dBm (which is the logarithmic power scaled to 10 mW, that is commonly used in RF and microwave detection literature). We can do this by assuming that there is perfect impedance matching between the input and output coil and that the current is roughly the same for the external and input coil (which is true according to our simulations). We can then assume the power being dissipated by the input coil P is driving a current I, which produces a B field as shown below.

$$B = \frac{\mu_0 I}{2R}. \tag{91}$$

Where μ_0 is the permeability of free space and R is the total resistance of the coil. To find the total resistamce we can first calculate the radiation resistance R_{rad} of a coil:

$$R_{rad} = \eta \frac{8}{3}\pi^3 \left(\frac{A}{\lambda^2}\right)^2.$$

$$\eta = c\mu_0, \lambda = \frac{c}{f}, A = \pi r^2.$$

$$R_{rad} = \frac{8\mu_0 \pi^5}{3c^3}(rf)^4. \tag{92}$$

Where c is the speed of light, μ_0 is the permeability of free space, λ is the wavelength of the radiation to detect, f is its frequency, A is the area of the coil and r is the radius of the coil. There are also two more resistances in the coil: The DC resistance of the wire itself with a diameter d and a resistivity ρ.

$$R_{DC} = \frac{8r\rho}{d^2}. \tag{93}$$

Where ρ is the resistivity of the wire and d is the diameter of the wire. The RF resistance from the skin effect of the wire is:

$$R_{AC} = \frac{2r}{d}\sqrt{\pi \mu_0 f \rho}. \tag{94}$$

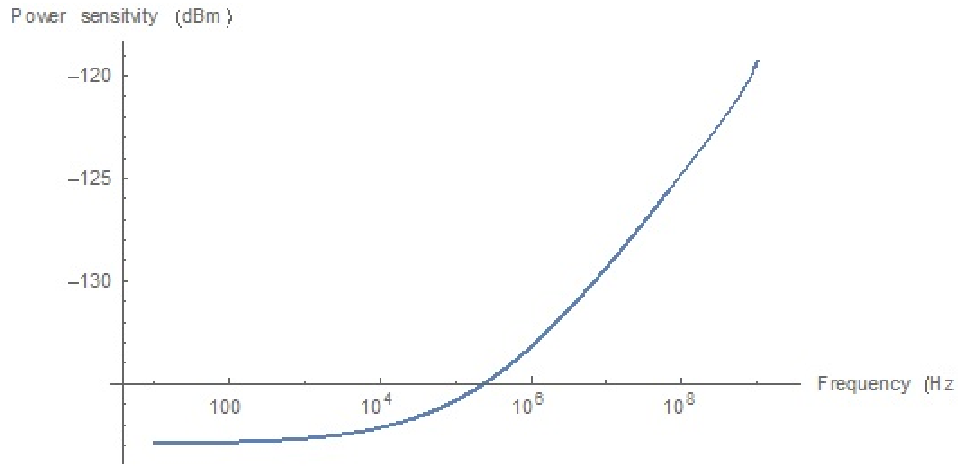

Figure 67: Graph showing how the Power sensitivity changes with frequency of the signal

The total resistance is $R = R_{rad} + R_{dc} + R_{ac}$. Then we can use $P = I^2 R$ to get:

$$P = \left(\frac{2rB}{\mu_0}\right)^2 R.$$

$$P = \left(\frac{2rB}{\mu_0}\right)^2 \left(\frac{8\mu_0\pi^5}{3c^3}(rf)^4 + \frac{8r\rho}{d^2} + \frac{2r}{d}\sqrt{\pi\mu_0 f\rho}\right). \tag{95}$$

And finally converting to dBm from watts:

$$P_{dBm} = 10\log_{10}\left(\frac{2rB}{\mu_0}\right)^2 R$$

$$P_{dBm} = 10\log_{10}\left(\left(\frac{2rB}{\mu_0}\right)^2 \left(\frac{8\mu_0\pi^5}{3c^3}(rf)^4 + \frac{8r\rho}{d^2} + \frac{2r}{d}\sqrt{\pi\mu_0 f\rho}\right)\right) + 30 \tag{96}$$

This provides us with a good idea of what we need to optimise to maximise power sensitivity, this includes the radius of the coil, although it is constrained by the fact it must be significantly bigger than the diameter of the wire; the frequency of the radiation being detected, although it is not a very significant factor at lower frequencies, as it only starts to attenuate the signal at high frequencies, as seen in figure 67. The most important factor to optimise is the magnetic field sensitivity of the ion which scales very well with the power sensitivity as shown in figure 68. The following graphs were made using equation 96 with the following values:

$r = 5\ mm$
$f = 80\ MHz$
$d = 500\ \mu m$
$\rho = 1.59 \times 10^{-8}\ \Omega m$ (Resistivity of Silver)
$B = 10\ pT\sqrt{Hz}^{-1}$

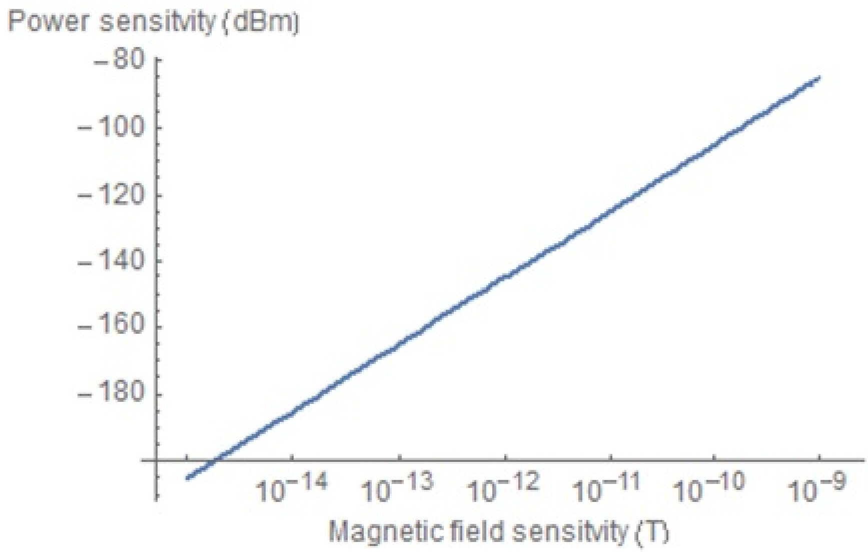

Figure 68: Graph showing how the Power sensitivity changes with the magnetic field sensitivity of the ion trap sensor

5.4.2 Johnson noise calculation

Noise from coil

One possible problem with this technique is that a coil system is inherently noisier than a bare ion as the coil itself introduces thermal noise to the ion introducing a noise floor to the system [34]. To calculate this we can first use the equation for Johnson voltage noise produced by the DC and AC components of the resistance of the coil [6]:

$$V_{noise} = \sqrt{4kT(R_{AC} + R_{DC})\Delta f}. \tag{97}$$

Where k is the Boltzmann constant, T is the temperature of the coil and Δf is the bandwidth of the ion sensor. From this we can use: $V_{noise} = I_{noise}R$ where R is the total resistance of the coil to find the current noise in the coil:

$$V_{noise} = \frac{\sqrt{4kT(R_{AC} + R_{DC})\Delta f}}{R_{AC} + R_{DC} + R_{rad}}. \tag{98}$$

We can now use equation 94 to get the magnetic field noise at the ion:

$$B_{noise} = \frac{\mu_0}{r}\frac{\sqrt{4kT(R_{AC} + R_{DC})\Delta f}}{R_{AC} + R_{DC} + R_{rad}}. \tag{99}$$

Using the same numbers as were used to produce figures 67 and 68 the magnetic field noise at the ion is calculated to be around 70 fT, which is well below our expected sensitivity of 10 pT so the noise floor introduced by the coil should not diminish sensitivity.

Noise From Vacuum System

If we assume that we want to enclose our ion in a vacuum system made of stainless steel then we might expect Johnson Noise from the chamber to occur and possibly disturb our ion. We can approximate the magnitude of this magnetic field in the DC regime, assuming our chamber is roughly spherical and use the following formula: [7]

$$\delta B = \frac{1}{\sqrt{2\pi}} \frac{\mu_0 \sqrt{kT\sigma t}}{a}. \tag{100}$$

Where σ is the conductivity of the material; t is the thickness of the vacuum system and a is the radius of the spherical chamber. If we estimate for a small vacuum chamber that we would ultimately use in the field, then we use a value of $t = 5$ mm and $a = 15$ cm then we get a value of $\delta B = 1.81 \times 10^{-30}$ T. This is obviously very small, which does make sense given the macroscopic dimensions of the system. If we look at the frequency dependency of this noise, which we would be interested in as we are using RF and microwave frequencies for sensing principally. It turns out that the frequency dependency is quite complicated and changes with frequency, material used and geometry. The relationship is always proportional to $f^{-1/n}$ where n is an integer of usually 1 to 4 [7]. We will always expect high frequencies to attenuate the noise significantly so as we start with such a negligible noise level it would only increase in negligibility as the frequency is increased.

Noise from chip

We might expect the noise to be significantly larger coming from the chip with it being in close proximity to the ion, so we should use another equation from [7] for noise generated from an infinite plane:

$$\delta B = \frac{1}{\sqrt{6\pi}} \frac{\mu_0 \sqrt{kT\sigma t}}{a}. \tag{101}$$

For a chip which has a thickness of 5 μm and an ion height of 200 μm and we assume it is made out of gold then the total magnetic field noise is: $\delta B = 7.82 \times 10^{-29}$ T, which is significantly larger than for the vacuum system, but still far less than the sensitivity of the ion, therefore insignificant, especially if we calculate frequency dependency.

5.4.3 Signal amplification calculation

An important parameter we would like to know is exactly how much the signal will be amplified using this ion-coil coupling technique compared to just the ion on its own. This will involve calculating what the minimum amount of magnetic field strength at a small antenna will require to produce a measurable signal at the ion within a second of detection time. This calculation will be used to determine the feasibility of various applications in section 7.

First we can use the Poynting vector to estimate the total power of the magnetic field at the external antenna [8]:

$$P_{in} = \frac{1}{2} E_0 H_0. \tag{102}$$

Where E_0 and H_0 are the amplitudes of the incident electric and magnetic fields respectively and E_0 is defined by:

$$E_0 = H_0 Z_0. \tag{103}$$

We can then plug equation 103 into equation 102 and rearrange to get P_{in} in terms of E_0 and the constant Z_0 (the impedance of free space):

$$P_{in} = \frac{E_0^2}{2Z_0}.$$

$$E_0^2 = 2Z_0 P_{in}. \tag{104}$$

We can now do the same calculation but in terms of the magnetic field flux density B_{ext} instead:

$$P_{in} = \frac{1}{2} Z_0 H_0^2$$

.

$$H_0 = \frac{B_{ext}}{\mu_0}$$

.

$$P_{in} = \frac{Z_0 B_{ext}^2}{2\mu_0^2}. \tag{105}$$

As P_{in} is the power per unit area the total electrical power received by the antenna is given by:

$$P = P_{in} A_{eff}. \tag{106}$$

Where A_{eff} is the total effective area of the antenna (the total area that collects the magnetic field). We can equate this to the electrical power equation: $P = I^2 R$. First, the voltage that is induced in the antenna is proportional to the electric field amplitude:

$$V = E_0 h_{eff} \tag{107}$$

Where h_{eff} is the effective height of the antenna. For a small antenna the effective area can be approximated to be around:

$$A_{eff} = \frac{3\lambda^2}{8\pi}. \tag{108}$$

Now if we assume that the current is the same at the load (at the ion input coil) as at the external antenna (as simulated in section 5.4.4), we can plug equation 108 and equation 105 into equation 106 and then equate to equation 95:

$$\left(\frac{2rB_{in}}{\mu_0}\right)^2 R = \frac{Z_0 B_{ext}^2}{2\mu_0^2}\frac{3\lambda^2}{8\pi}. \tag{109}$$

Now rearrange to get the amplification ratio:

$$\left(\frac{B_{ion}}{B_{ext}}\right)^2 = \frac{3Z_0}{\pi R}\left(\frac{\lambda}{8r}\right)^2$$

$$\frac{B_{ion}}{B_{ext}} = \frac{\lambda}{8r}\sqrt{\frac{3Z_0}{\pi R}}$$

$$\frac{B_{ion}}{B_{ext}} = \frac{c}{8rf}\sqrt{\frac{3Z_0}{\pi R}} \tag{110}$$

Using the same numbers as before this leads to an amplification factor on the order of 10^4 at around 20 MHz, which is a significant amplification. How this method can be applied to the applications of drone detection and explosive sensing can be found in section 7.

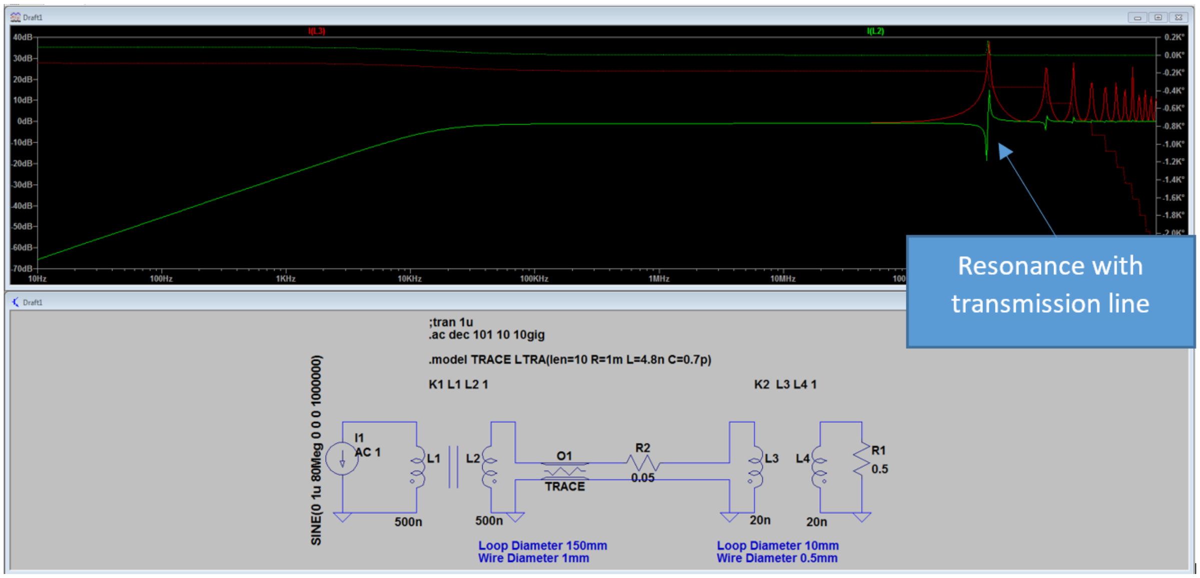

Figure 69: LT simulation of input coil and pick-up coil system with impedance matched electronics. The above figure represents the frequency response to impedance with 0dB representing perfect impedance matching. The two lines represent: Green, AC current in input coil; Red, AC current in output coil.. The below diagram shows the the circuit used to simulate the system, where the input magnetic flux is represented by the L1 and L2 transformer; L2 is the pick-up coil inductance; L4 and L3 is the input coil; L4 and R1 represents the radiation resistance. R2 represents the resistance and a noise source of the construction. Green: AC current in input coil; Red: AC current in output coil.

5.4.4 LT Simulation

One of the crucial assumptions made in the previous section was that the pick-up coil and the input coil are impedance matched to one another to ensure efficient power transfer from one coil to the other. This will require a system of inductors to ensure perfect impedance on each side. The quality of the match should be affected by the frequency of the signal being transferred, so this could effect our ability to tune the sensor to various frequencies. It is very difficult to calculate this frequency dependency analytically, so my colleague, Iain Hunter, produced a simulation of this system for me using LTspice, which is an electronic circuit simulation tool commonly used by electronic engineers.

This very simple LTspice simulation demonstrating the frequency response of the double inductance separated by a transmission line as shown in figure 69. This simulation shows the frequency response of magnetic flux input to current in the output coil. It shows that for frequencies of interest, 10 to 100 MHz, the current induced in the input coil is transferred of the current of the output coil.

This simulation is very simple and is not intended to show the complete system accurately over all frequencies. The inductances have been calculated at 80MHz.

6 Portable system

The original purview of the entire sensing project at IQT was to build a system to demonstrate sensing using trapped-ions, the construction of which was detailed in section 3. This was meant to provide a platform to prototype the technologies towards building a miniaturised version that could in principle be taken out of the laboratory for magnetic field sensing. As the project progressed however we found it difficult to find applications for a portable near-field RF and microwave sensor that would be competitive against other quantum sensors and classical devices. Eventually we decided to take the project in a different direction by concentrating on using the currently operational demonstrator system as a far field detector using the ion-coil technique detailed in section 5.4. Applications involving detection from a large stationary platform with a plentiful supply of power are detailed in section 7.

Before this pivot however there was significant work done towards building a portable quantum sensor, even if many of the subcomponents did not come to full fruition due to either time constraints from working on the demonstrator or from issues with funding industry led component projects. Although the final device has not been completed in its entirety significant progress was made in drawing up requirements for the various subsystems of the portable platform and preliminary designs which are detailed below. This project was designed to be industry led with the sensing group providing the specifications, so much of the design work was undertaken by them. A model of how we envisioned the final version of the portable with all the subsystems and the dimensions us shown in figure 70.

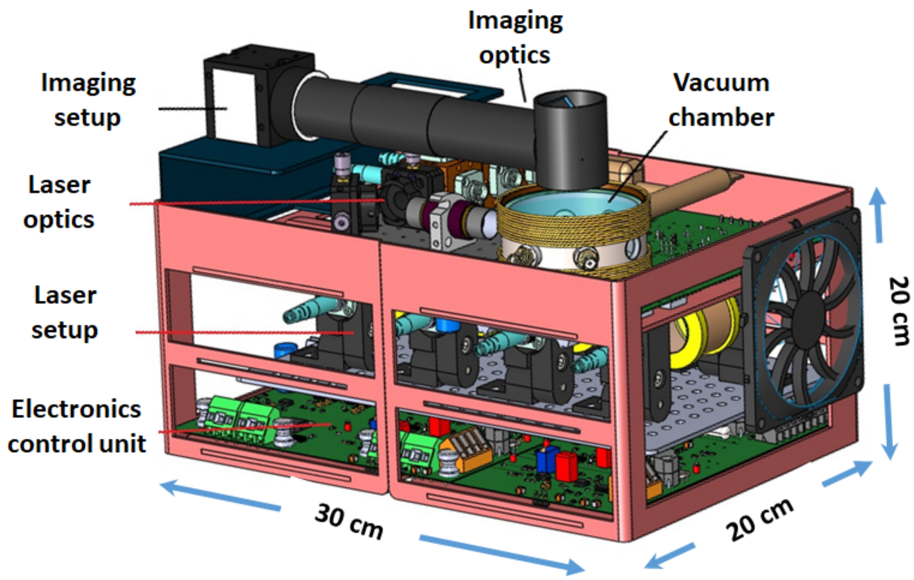

Figure 70: A 3-D model of the current design of the portable system with all the key components labelled and dimensions shown.

6.1 Lasers and optical set-up

6.1.1 Laser diodes

The lasers for the portable system were one of the most difficult components from a design perspective due to the required protection for each of the lasers and locking apparatus for maintaining a stable wavelength. As described in section 2 we need three principal lasers for sensing with Yb^+ ions: 369 nm, 399 nm and 935 nm lasers. Initially all three of these lasers were meant to be produced inside the Birmingham quantum hub (See section 1). Unfortunately they were unable to provide a 369 nm solution so the responsibility for its development fell to us. The specifications we would be looking for with our lasers are:

- >20 mW power after isolator
- Highly stable, acoustically inert
- Tuneable with AOM by 100 MHz
- Linewidth <1 MHz
- Low frequency noise
- RF modulation
- Small and compact Faraday Isolator ∼cm
- Faraday isolators tuned to specific wavelength, >30 dB suppression

- Fibre coupled
- Compact size, ideally confined to a 20 cm by 30 cm breadboard.

The 399 nm[53] and 935 nm[54] lasers are readily available for our purposes to provide a miniaturised platform for laser production and modulation. These off the shelf devices are perfect for our purposes as we only need a small laser power of around ≈10 mW. These modules provide inbuilt temperature and current control for precise frequency and intensity control from the central control board.

The 369 nm has been the main sticking point for this sub-project as there are very few companies that offer 369 nm diodes and none that we know of have full miniaturised laser stabilisation methods such as the ones for 399 nm and 935 nm. Fortunately Toptica offer a 20 mW 369 nm diode[55]. Unfortunately there is no miniature all-in-one stabilisation and temperature control for this model, so we would have to build our own device capable of doing these things. Fortunately there are many examples of this in the literature that we could emulate effectively [43, 42]

An alternate solution would also be to have a separate device to supply all three of the lasers as well as locking and frequency control, which could then fibre couple the beams into the quantum sensor device. This would mean that there would be a lot less space constraints within the device itself, but could alienate a few of our prospective end users that require extreme spatial constraints such as BP (see section 7.4). This set-up is used in many portable quantum sensing platforms in development at the moment [41].

6.1.2 Optomechanics

As shown in section 3.2 the optomechanics required for Yb ionisation, cooling and manipulation can be rather complex and usually require significant table space. Of course for the proposed portable device one does not have the luxury of vast table space and must share two levels of 30 cm by 20 cm space, with the vacuum system; detection optics; imaging and laser generation. I intended to use the LINOS Nanobench line of optomechanics[56], which provides half inch diameter optics solution we could use for: mirrors, waveplates,beamsplitters, fibre couplers, lenses and their relevant optics holders. This should vastly decrease the amount of space needed, although no designs have been drawn up yet pending other components completion.

Our new generation of chips shown in section 5.2, as well as speculative future chips, can trap many ions over an area of up to 5 mm by 5 mm. This poses a problem for our beam delivery system, which for the 369 nm beam on the demonstrator (which is designed for sensing with a single ion) has a spot size of $\approx 20\ \mu m$. This would make it impossible to address all the ions with the same beam. One could try to solve this problem by making the beam larger, but would result in a beam profile overlapping with the chip, which would produce a charge build-up over its surface (more details in section 3.2.2). As all the beams that would be used will have a Gaussian head-on profile, this would also mean that the the ions that are further from the centre of the beam would be addressed with far less beam intensity.

A solution we found for this problem was to employ beamshaper optics designed by the company Laser 2000. This device can input a collimated Gaussian beam and output a modified beam, which focuses the beam

[53] NICHIA Tunable Laser Module CORE - NUV611T
[54] 935 DFB laser with hermetic TO package, Monitor diode, Thermoelectric Cooler and Thermistor - EYP-DFB-0935-00080-1500-TOC03-0005
[55] Toptica - # LD-0375-0020-2
[56] QIOPTIQ

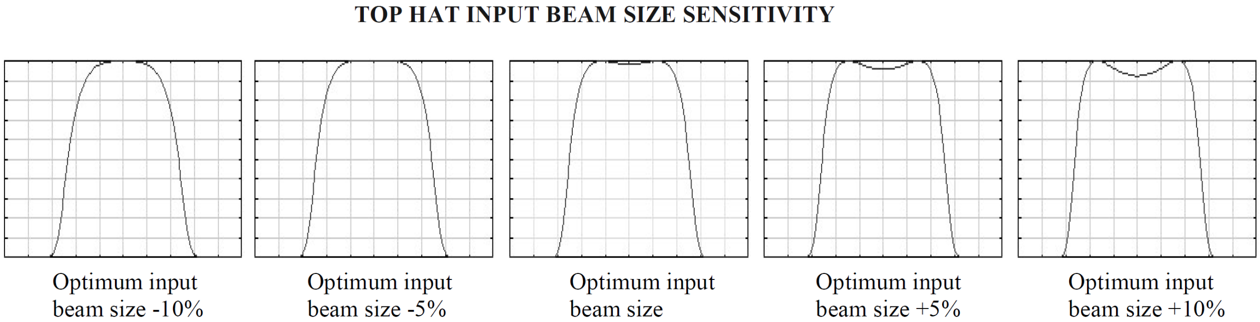

Figure 71: Simulation data supplied by Laser 2000 showing how the system is sensitive to input beam size, and what the beam shape will be with relative size of input beam

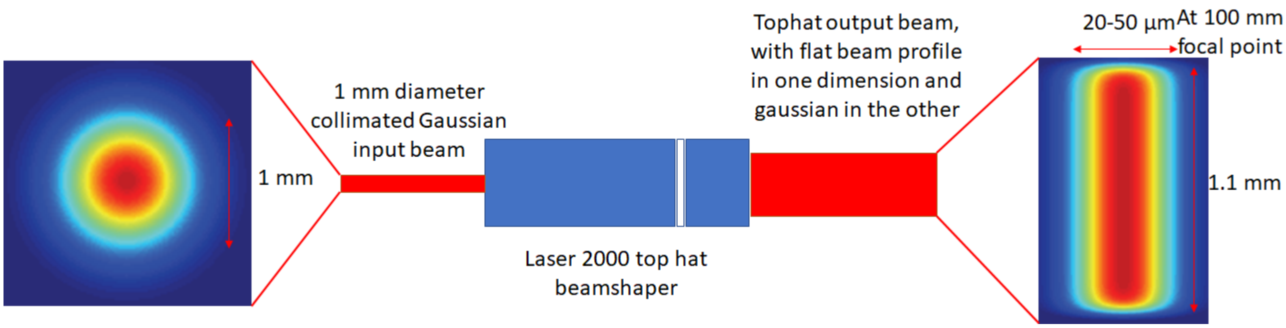

Figure 72: Diagram showing how a 1 mm gaussian input beam is modified using a laser 2000 beamshaper to produce a Tophat beam profile at the ion trapping position

to the chip position. At this focal point the beam has a tophat configuration where the beam profile is flat at the ion height of the chip, but is Gaussian in the dimension pointing perpendicular to the surface of the chip. A diagram of how this works can be seen in figure 72. This effectively produces a laser 'sheet' across the surface of the chip, so when the beam is placed at the ion height all of the ions are addressed with the same laser intensity. It also means that less light is wasted scattering off the chip or flying above the ion height. The device we requested from Laser 2000 was designed to input a 1 mm FWHM Gaussian beam, which must be carefully made as even a small deviation distorts the tophat profile as seen from simulation data provided by Laser 2000 in figure 71. This device has been delivered and ready to be used when the project transitions to using multi-ion chips. The output tophat beam would be 1.1 mm across and 20 - 50 μm thick at the focal point.

6.1.3 Wavemeter and laser locking

As stated in section 3.2 we used a HighFinesse WS-7 wavemeter for measuring the wavelengths of our three principal lasers for our experiment. This device is very effective at measuring all three wavelengths simultaneously and assisting in locking the wavelengths to particular transitions. This device is however almost as big as our proposed 'shoe-box' sized package shown in figure 70, so would be impracticable for our portable system.

A solution investigated by previous undergraduate student Tom Whitmore in his report [44] involved a system where the beams to be measured are directed into a series of mirrors at an angle, after a prism, with a small CCD array at the end. This could mean that the beam could have an effective path length of several meters even with a small volume to work with. The long beam length means that even minuscule changes in wavelength will cause a relatively large displacement in beam position at the the CCD. This method has been

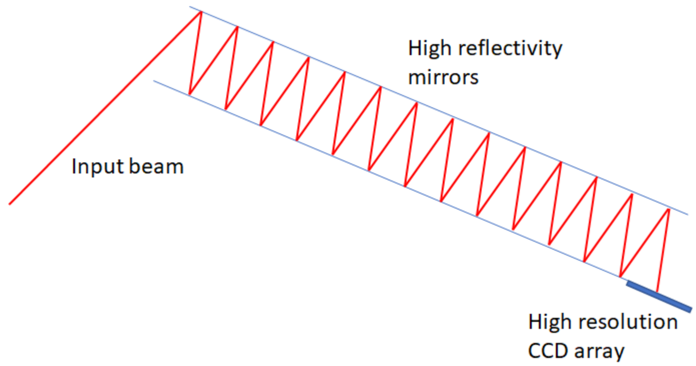

Figure 73: Diagram showing the principle of the mirror wavemeter where the beam to be measured is put through a mirror cavity to accrue a very long beam length before falling on a CCD camera.

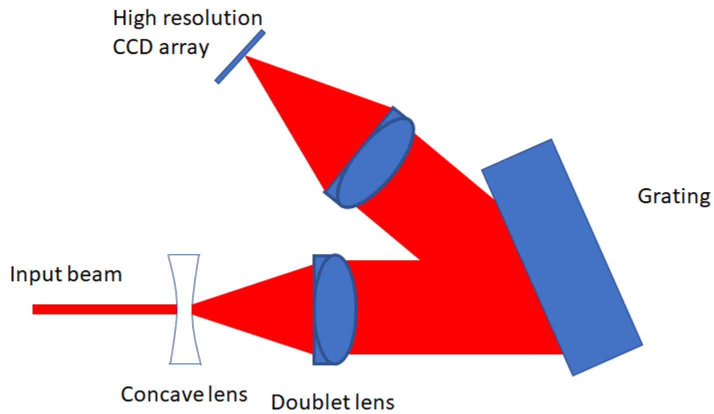

Figure 74: Diagram of the proposed grating configuration for the portable wavemeter where a beam is expanded onto a grating where it is deflected and focused onto a CCD camera.

theoretically determined to produce sub-picometre sensitivities. A diagram displaying this method is shown in figure 73.

Another method under consideration shown in the literature uses a grating to displace the light over a camera, in a similar manner to the mirror technique, as seen in figure 74 [45]. The grating affects the angle of the beam which is reflected strongly related to its wavelength. This method has been demonstrated to have a wavelength accuracy of ≈0.1 pm covering a space of only 50 cm by 20 cm, with space for further optimisation.

6.2 Control system

The control system is one of the most complex parts of the portable set-up, with the multitude of tasks that would have to conduct simultaneously. The current control set-up on the demonstrator system is split over three desktop computers; an FPGA; two DDS boxes with surrounding RF switches; three laser controllers (each with their own current, voltage and temperature control); Two RF generators and a microwave generator. All these devices use a large amount of power and some of these components are even larger than the entire proposed portable quantum sensor shown in figure 70. These components need to be compressed into a single control board or several smaller boards that can be stacked on top of one another and fit within the 5 cm × 30 cm × 20 cm volume allocated to it in figure 70.

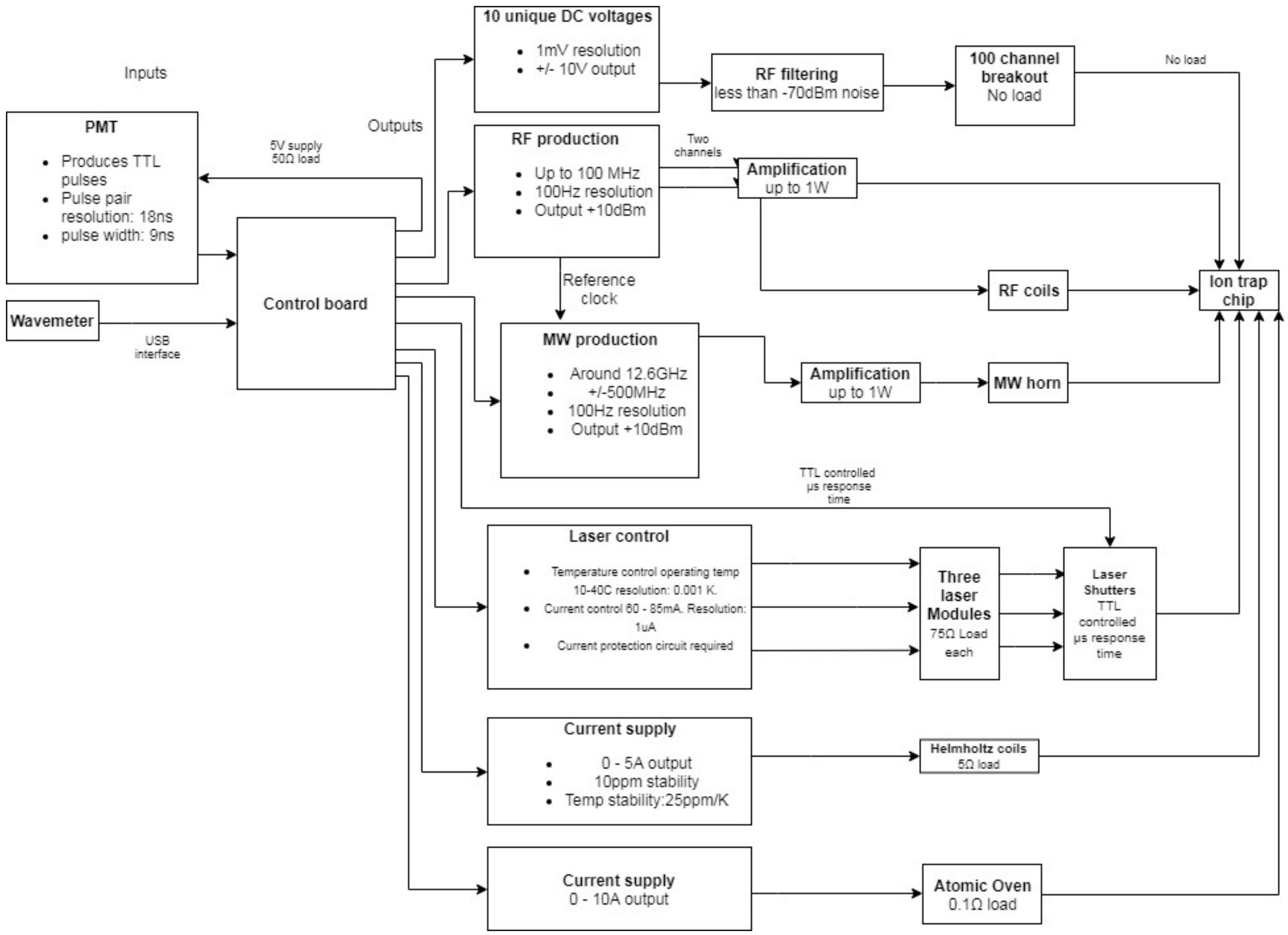

Figure 75: A flow diagram showing all the different components of the control board and their respective requirements, as well as how the different components of the control system interact with the experiment. This was used by Enterpoint Ltd to produce the first designs for the board.

This presents a significant engineering challenge especially while maintaining the high level of accuracy many of these components need in order to trap multiple ions and run coherent measurements with high fidelity. A flow diagram showing the relevant requirements of each subsystem within the control board are shown in figure 75. The development of this board was outside the capabilities and expertise of our group, so we outsourced construction of this system to the custom board design company called Enterpoint Ltd. Enterpoint Ltd were involved in the design phase with a plan for phased development with different iterations of the board to be received by myself and tested. I have decided to shelve this project for the time being as the development costs would require significant external funding and the project is currently pivoting away from the portable system development onto far-field detection using the ion-coil technique shown in section 5.4

6.3 Chip RF resonator

As seen in section 3.6 an RF signal is produced and amplified for the chip RF to generate the pseudo-potential required for trapping (as detailed in 2.1). There is a need for impedance matching between the chip and the RF source. On the demonstrator system this is done with a resonator can, which impedance matches the RF source to the chip, as shown in section 3.6. This can is far to large in terms of volume and weight, so an alternate approach is required. To solve this problem my colleague Dr. Ethan Potter proposed a PCB based system that uses an RF resonator crystal oscillator, which has Q factors of up to 70. This means that the entire resonator could be replaced by a PCB only 5 cm by 5 cm in are. More details on the construction of this device as well as the results of various experiments to establish its effectiveness can be found in Dr. Potter's thesis [39].

6.4 Vacuum System

The vacuum system for the portable device was the part of the project that went through the most iterations and the most effort from members of the quantum sensor team. This system has similar requirements to the demonstrator vacuum system as shown in section 13, but crucially needs to be substantially smaller in volume. Also the pumping should be passive, which should be possible with the far smaller volume using getters. A list of requirements for this is shown below:

- Compact size: $<$50 cubic centimetre.
- Low or no attenuation to B-field signals (DC-GHz range).
- Pressure down to $<10 \times 10^{-10}$ Torr.
- Low power to maintain pressure level, or self sustainable system, for example using non-evaporable getter element inside the chamber.
- Material: 304/316 S.S, titanium, ceramics (preference).
- Bakeable to $>$150 ^oC.
- $\sim$100 DC electrodes feedthrough ($\pm$10 V).
- RF Power feedthrough for RF trapping voltage 200 Vac.
- Microwave power feedthrough.
- Current feedthrough 2 A.
- AR coated viewports for 369 nm, 399 nm, 935 nm (laser access viewports) and 369 nm for imaging viewport (Front viewport). Quartz fused Silica or ZK7 glass viewport.
- Possible ITO coating on front viewport.
- Possibly in vacuum optics.
- In vacuum RF and microwave delivery.

At the beginning of the sensor project in 2014 companies were contacted to design a system with the above requirements. Eventually ColdQuanta was chosen by then post-doctoral fellow leading the project Dr. Altaf Nizamani. ColdQuanta first designs are shown in figure 76. These designs were very extreme in terms of minimal volume for the vacuum chamber, this was an advantage due to the smaller need for ion pumping and the ability to passively pump the system almost indefinitely. The system would be brought down to 10^{-7} mbar using a turbo pump before being pinched off from the copper pipe feeding into the system. The ion getter pump could then take over and bring the system to ultra-high vacuum. The metal parts were intended to be either Titanium or steel and the parts would be put together with their ColdQuanta's electron beam welding technology, while the glass would be connected with anodic bonding. The second version was designed to minimise the

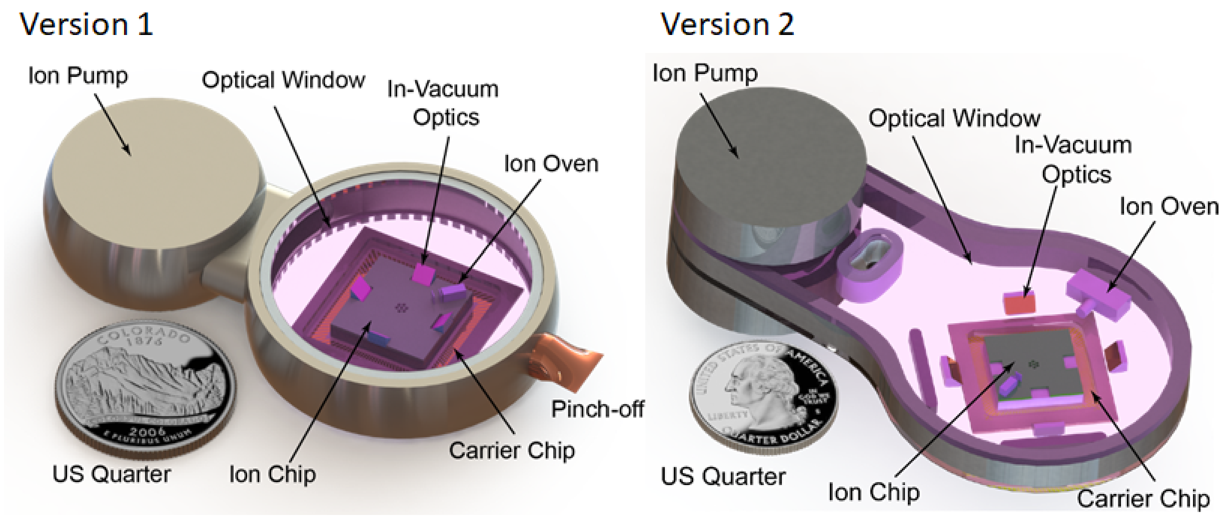

Figure 76: These are the two initial designs drawn up by ColdQuanta. Both are separated into two connected modules, one with the ion pump getter to maintain the vacuum of the second glass module, which contains the chip with the laser beams directed from above onto mirrors that direct it parallel to the chip at the ion height. The second version uses a slightly smaller volume to limit the amount of pumping power required for the getter.

chamber depth even more and bring the chip closer to the window to allow for better collection fidelities for the detection optics. Unfortunately ColdQuanta were unable to build these systems for us due to the very high development costs involved and the lack of other other customers who would be interested in this product. Also our funders at the quantum hub wished for us to work with a company that was based in the UK/EU. One of the other major problems with this system and subsequent designs was designing a electrical feedthrough that could accommodate the up to 100 DC connections plus chip RF and high current oven connections. This would require a unique custom solution for a chamber that would be so small.

As seen in figure 76 a specialised chip holder is designed for these systems, which is shown close up in figure 77. This chip holder's most notable feature is the mirrors used to deflect beams incoming perpendicular to the chip to make the beam parallel to the chip at the ion height before being deflected back the way it ingressed. This means that there is no need for an additional viewport on the side of the chamber for laser ingress and so the chamber can be made extremely narrow. The problem with this system is that the detection optics tube has to be small enough to allow for a laser beam to be fired at one of the mirrors on the chip holder. This also adds added complication to an already difficult laser alignment process. This design also includes a speculative design and placement for a miniaturised atomic oven to supply the required Yb flux.

Shortly after the shelving of the ColdQuanta system we were contacted by Torr Scientific Ltd (TSL) who were working with the Birmingham hub vacuum systems package to produce miniaturised vacuum systems for all the different quantum sensing experiments in the hub that have need of UHV environments for their systems. The general purpose system they developed is shown in figure 78. This package is substantially larger than the ColdQuanta designed system, but is still within our design requirements. This system has separate feedthroughs for the oven and chip RF to utilise 'off the shelf' parts for less engineering difficulties. This is also true for the ion pump which is housed in a separate chamber from the chip and connected to it with a copper pipe, which increases the pumping volume, but reduces the engineering complexity. As with the ColdQuanta design, the system should be connected to a turbo pump and then be pinched off, before the ion pump is activated to bring the system to UHV.

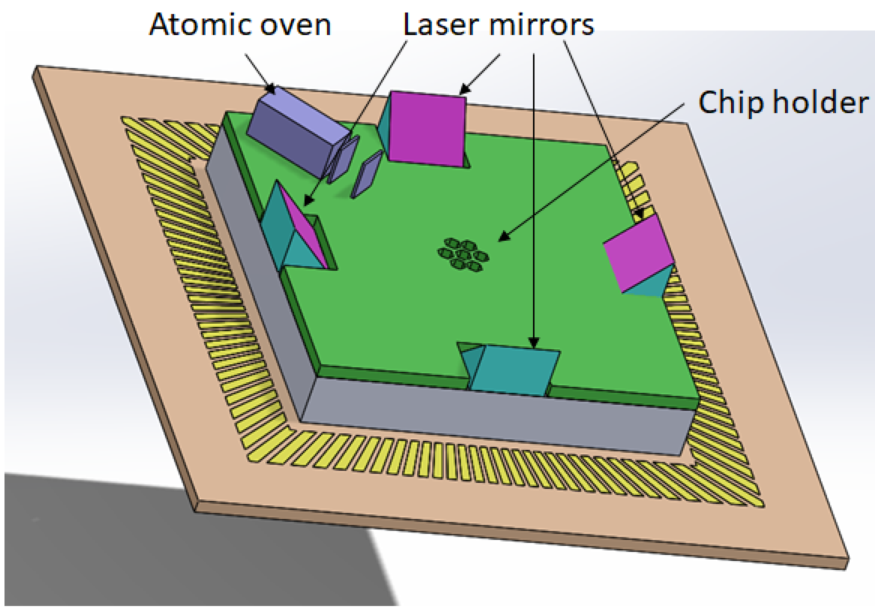

Figure 77: Chip holder used in the first ColdQuanta designs showing how the laser mirrors can direct the beam over the chips surface. This also shows a miniaturised atomic oven used placed near the chip.

The internal structure of the ion trapping chamber saw substantial changes from the ColdQuanta system as seen in figure 79. The major differences are that the laser is directed through two side windows over the chip. This reduces the complexity of the system, but substantially increases the volume of the chamber and also means that the chip's surface is 10 mm away from the chamber window, which is twice the distance on the demonstrator system and will reduce the detection fidelity of our state detection system.

Figure 80 shows the two subsequent versions, which were designed by Dr. Altaf Nizamani, and were given to TSL. These designs use a boxed chamber which integrate all the electrical connections into a single feedthrough behind the chip. Version three also puts the ion pump into the chip chamber as well to limit the amount of pumping vacuum. Ultimately these designs were scrapped in favour of the first design due to its availability and the companies incentive to build a system with demand from other groups.

Unfortunately this TSL system had a critical flaw as it had been assumed that RF and microwaves could enter the system unimpeded, when making calculations for commercial applications. When my colleague Weikang Fan made simulations of this we found that the stainless steel vacuum system would substantially attenuate the RF and microwave signals we wished to sense. Even through the glass viewport, there would be substantial attenuation of any RF or Microwave signals, as there would have to be fine steel mesh placed over the viewport similar to what was done in the demonstrator system in section 3.1.4. This was determined through an experiment that was conducted by myself by setting up two RF coils and placing a wire mesh between them, then attaching them to a VNA. The power transfer of 1.895 MHz RF can be compared to the case when the mesh is not there to find the attenuation. This experiment was repeated with two microwaves horns operating at 12.6 GHz microwaves. It was found that with RF and microwaves were both attenuated by around -0.5 dBm (around 15%). This is significant attenuation, which would effect our ability to compete with other quantum sensors and classical devices.

To resolve this problem we decided to work on designing a system which was made mostly out of

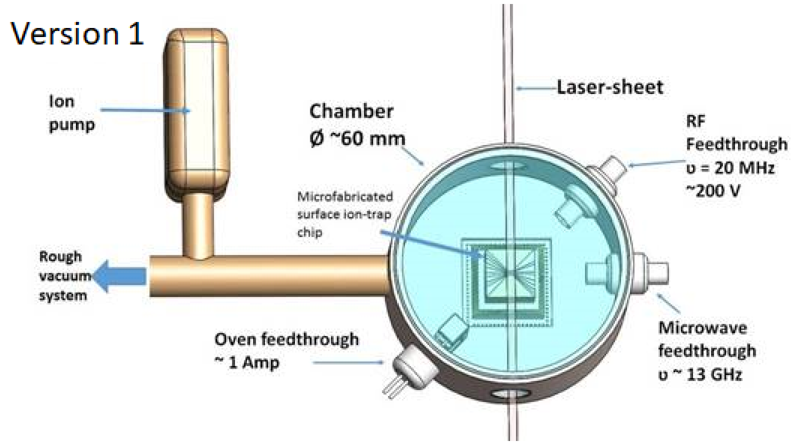

Figure 78: First iteration of TSL using an 'off the shelf' design. This diagram shows the various feedthroughs for the microwaves, RF and oven, as well as the laser access. Also note that the ion pump is external to the main chamber for easier construction.

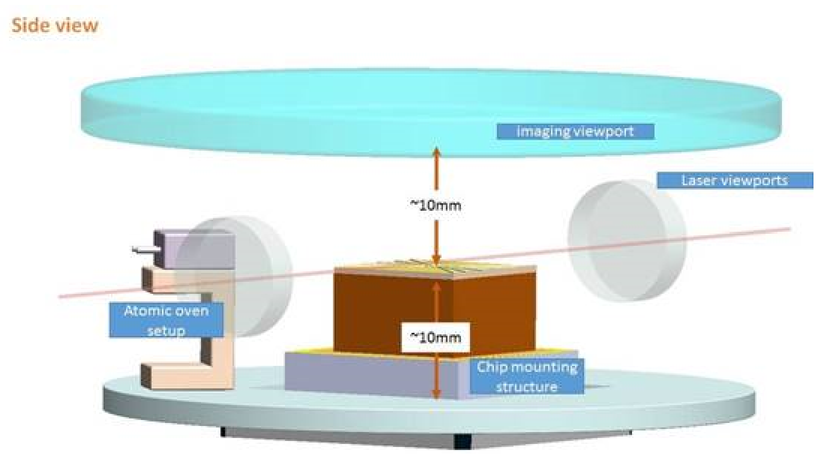

Figure 79: Diagram showing the internal structure of the TSL chamber showing the chip mounting, atomic oven, laser access and optical access.

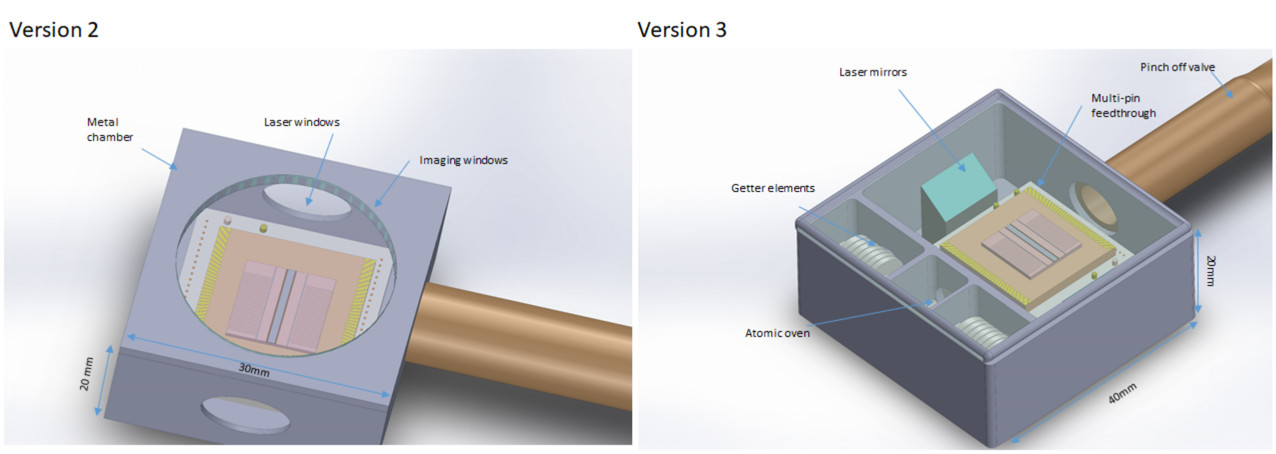

Figure 80: The next two TSL versions (designed by Dr. Altaf Nizamani) showing a box chamber instead of cylindrical and version 3 with a getter pump integrated into the box with the chip to reduce the total volume of the system and hence the pumping power required.

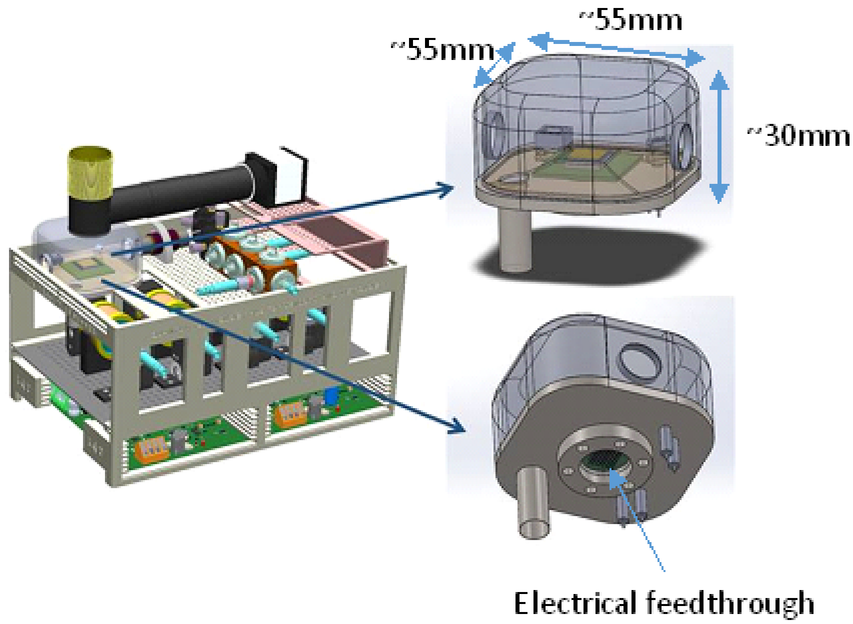

Figure 81: IQT design for a glass vacuum system to allow for the detection of external RF and microwave fields. Here is shown mounted on inside our model for the entire portable system.

dielectric material such as glass or ceramic. One of these designs is shown in figure 81. This chamber was to be made almost entirely out of glass with a metal bottom plate where the electrical feedthrough would be located as well as two IR coated windows to allow laser light to interact with the ions. The glass chamber presented quite a significant engineering problem however, because as far as we could find no vacuum company had made a system like this out of glass that could achieve UHV. The design was eventually abandoned after the discovery of the pick-up coil amplification idea (see section 5.4), which meant that RF and microwaves could be collected from outside the system and wired to the ion, hence bypassing the vacuum system entirely.

After this discovery we contacted e2v teledyne (post merger) and started discussions on designing a system that could be made mostly out of stainless steel or Titanium and use one of their 'off the shelf' chambers as a baseline to work off of. This led to a design that could accommodate the additional RF and microwave feedthroughs needed for an ion-coil interaction device as described in section 5.4 as well as a microwave emitter for microwave signal amplification. It would also maintain a 5 mm window to chip distance for optimal state detection fidelity. We were ultimately quoted for the development of this system, but due to budgetary constraints and the projects changing direction towards demonstrating the ion-coil technique with the current demonstrator system.

6.5 State detection system

The state detection system for the portable system will be relatively unchanged from that of the demonstrator system. Although the optics tube which houses the objective and doublet shown in section 3.4 would be far to large to fit comfortably in our portable system (as shown in figure 70) as it is 65 cm long. Fortunately we have a design requested from EKSMA optics shown in figure 82 made especially for the portable system and only has a length of 30 cm from the ion to the CCD camera.

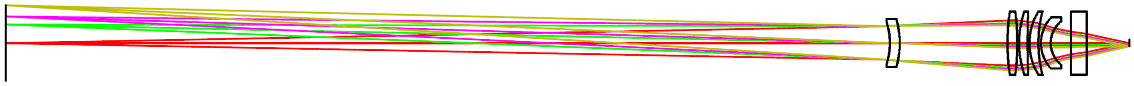

Figure 82: to scale optical ray simulation showing a 300 mm long optics system designed for the portable system by EKSMA optics, with window of vacuum chamber included in the simulation

In the current demonstrator set-up both the PMT and CCD camera is arranged for state detection as described in section 3.4. The CCD camera was used for initial ion trapping and testing for ascertaining trap parameters, while the PMT was used principally for coherent experiments. For the portable system it was decided that the CCD camera would only be needed as it is far more useful for multi-ion sensing, being able to differentiate between individual ions to check their state. A PMT would be a poor choice for this as the only way it could differentiate different ions is with a multi-channel PMT. This would require special optics to direct the light of each individual ion onto a particular PMT channel, which would require complex and sensitive optics. Also, PMTs would not be able to accommodate 100's of channels for 100's of ions, that would be required for sensing using the dual rail chip. A CCD camera would require significant software development to be able to differentiate different ions, but this work has already begun in our laboratory by my colleague Dr. Adam Lawrence.

6.6 Miniaturised Atomic Oven

A project to find the optimal design for a miniaturised oven for the portable system was undertaken by undergraduate student Ronnie Parker under my direct supervision. This project was done to compare the various known methods of producing an ytterbium atomic flux from an oven, as is shown on the demonstrator system in section 3.1.3. The methods investigated were: Indirect Electrical Heating; Direct Electrical Heating; Electromagnetic Induction Heating and Laser Ablation. Each of these methods were analysed to determine their strengths and weaknesses and make exact theoretical expectations for the resulting power need and costs involved in implementing these methods. The most advantageous method was then chosen and used to design a atomic oven system that fulfils the below criteria:

- An Yb oven that produces significantly collimated atomic beams for an ion trap without coating the electrodes.
- Miniaturised dimensions, and so must have a maximum volume of at most 5x5x5 mm.
- Can be controlled via a computer, utilising a small micro-controller circuit.
- Power consumption as low as possible; no higher than 100 mW.
- Be able to mount into the miniaturised vacuum system.
- must be heated to 300 ^oC to produce sufficient Yb flux

6.6.1 Sublimation techniques

Indirect electrical heating

Indirect electrical heating is a common atomic sublimation technique, which involves putting a large DC current through a plate or wire that heats the Yb containing vessel, which leads to sublimation. There are two main methods for this, one where the current is put through a wire that is wrapped around the Yb vessel in a coil

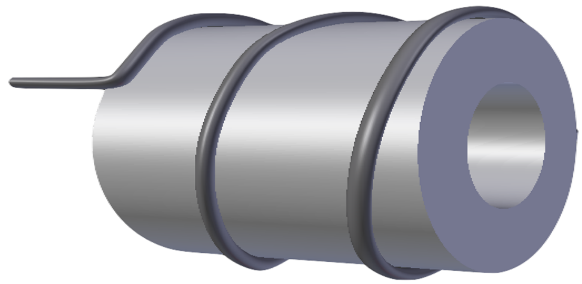

Figure 83: Example of a design for a indirect heating element for an atomic oven. A large current is put through a high resistance wire (typically made of tungsten) that is wrapped around the oven tube that contains the Yb. The wire should heat the vessel, which then heats the Yb producing an atomic flux.

as shown in figure 83. This is typically surrounded in insulating material to increase the power efficiency of the device. Using the model shown in figure 83 the current and power efficiency was determined to be 0.250 A and 0.019 W respectively. The other technique is to use an electrically resistive plate or coil at one end of the oven near the Yb to concentrate the heat.

The advantages of this technique are:

- Can be miniaturised to 5x5x5 mm
- Typically uses Tungsten as a filament, which is regularly used as a heating element, so engineering companies will have experience with its use.
- Our group already know how to build this type of oven so should be relatively easy to construct.
- High power efficiency with both methods.
- Using a thin wire induces a smaller DC field than other techniques that may disturb the ion allowing the oven to be brought closer to the chip.
- Simple design makes it easier to design and install in a system, as well as greater reliability

The disadvantages are:

- Small design parameters mean that the coil must be very thin, fragile and hard to fabricate.
- When wrapping the wire around the tube there are inefficiencies from not concentrating the heating at the Yb.
- May require microfabrication, which could be difficult to engineer and expensive.

Direct heating

Direct heating is the sublimation method used in our demonstrator system and is detailed in section 3.1.3. This method runs a current directly through the Yb carrying vessel itself to produce the heat necessary. This system however needs to scaled down to the 5 mm^3 size needed and should be surrounded by an insulator to increase efficiency.

The advantages of this technique are:

- Can be miniaturised to 5x5x5 mm.
- Our group already know how to build this type of oven so should be relatively easy to construct.
- Simple design means that should be easy to mount in any system we choose.
- Using a steel tube has a relatively low temperature coefficient so power delivery will not change much as temperature increases.

The disadvantages are:

- A lot more mass is generally heated using this method than with the indirect heating method, by heating up the entire tube.
- Generally requires a very high current to produce a good flux, 8 A for example is generally needed for the demonstrator system.
- The high currents could also degrade the materials over time reducing the lifetime of the oven.

Electromagnetic induction heating

Electromagnetic induction heating is quite similar to the indirect electrical heating method as they both involve wrapping a wire around the barrel of a Yb containing vessel. However the wire is not designed to produce heat through resistive heat but instead uses an AC current in the wire that produces eddy currents in the Yb itself to induce heating directly. This is based on work done by Zavitsanos and Carlson et al [46], which used the technique to sublimate carbon. We calculated the power required for our miniaturised design would be 2.7 W, which is far higher than what we require for our portable system.

The advantages of this technique are:

- Does not require complex microfabrication, cutting down on developmental costs
- Simple design means that should be easy to mount in any system we choose.
- Varying the applied AC frequency could provide scope for increased efficiency.

The disadvantages are:

- This method requires the production of high power AC current, which would require a variable RF source and amplifier. This would add significant complication to the set-up compared to a simple DC supply.
- According to current calculations based on the literature [46] the power efficiency of this method is substantially less than other methods.

Laser Ablation

The final technique we examined was laser ablation, where a high power laser beam is directed and focused into an insulated ytterbium containing vessel. This laser would be used to liberate the atoms at the outer most layer of the Yb, one at a time using a pulsed laser. To produce a sufficient flux we calculated that we would require a pulsed laser beam with a frequency of 9.7 MHz imparting 1 μJ of energy per pulse. This is analogous to a continuous beam with around 10 W of power being absorbed into the Yb.

The advantages of this technique are:

- This method provides very precise heating delivering energy directly to the Yb, while causing minimal heating to surrounding components.
- Can be produced in house as most of the components needed are readily available in our lab.
- Unlike other methods the Yb flux is produced almost instantaneously after activating the laser, this will reduce ion loading times by a number of seconds per run.
- The Yb receptacle can be miniaturised to 5x5x5 mm and the laser diode and supporting optics can be arrayed outside the vacuum system.

The disadvantages are:

- Unlike other methods there is significant amount of equipment required outside the system including: mirrors, lenses, a laser diode etc.
- Significant changes may need to be made to the miniaturised vacuum system to allow for an additional laser to interact with the oven.
- All the laser related components would significantly increase the cost, complexity and total volume occupied compared to other methods.
- Requires very high amounts of laser power.

6.6.2 Portable oven design

Ultimately we decided on a microfabricated indirect heating design shown in figure 84. This simple design uses a microfabricated tungsten coil shown in figure 86, which is placed at the back of a small ceramic cylinder (see figure 85) with the Yb. When the filament has a DC current applied to it will heat up to around 300 ^{o}C and begin ablating the Yb. An end cap is used with an aperture to constrict the beam so the atomic flux is concentrated at the ion trap position.

Ceramic was chosen to thermally insulate the oven so almost all the heat energy produced by the filament is concentrated inside the Yb to minimise the required current needed to produce a sufficient atomic flux. The calculated required current for the oven was 232 mA, which would require 15 mW of power from a DC current source. This design should take 7 seconds to heat up to the desired temperature from room temperature. So if the oven was loaded with 5 mg of Yb, this would lead to speculative lifetime of over quarter of a million trapping runs. This would be important as most of our designs for vacuum systems cannot be opened again once sealed, so the ovens cannot be refilled as they are done in the demonstrator system.

The design for the heating element was passed to Takeishi Electric Company Ltd who specialise on microfabricating metal components and CoorsTek Inc for the ceramic parts. We were in talks for them to produce these designs, but decided against moving the project further for the time being, due to budgetary concerns and the new focus away from the portable system.

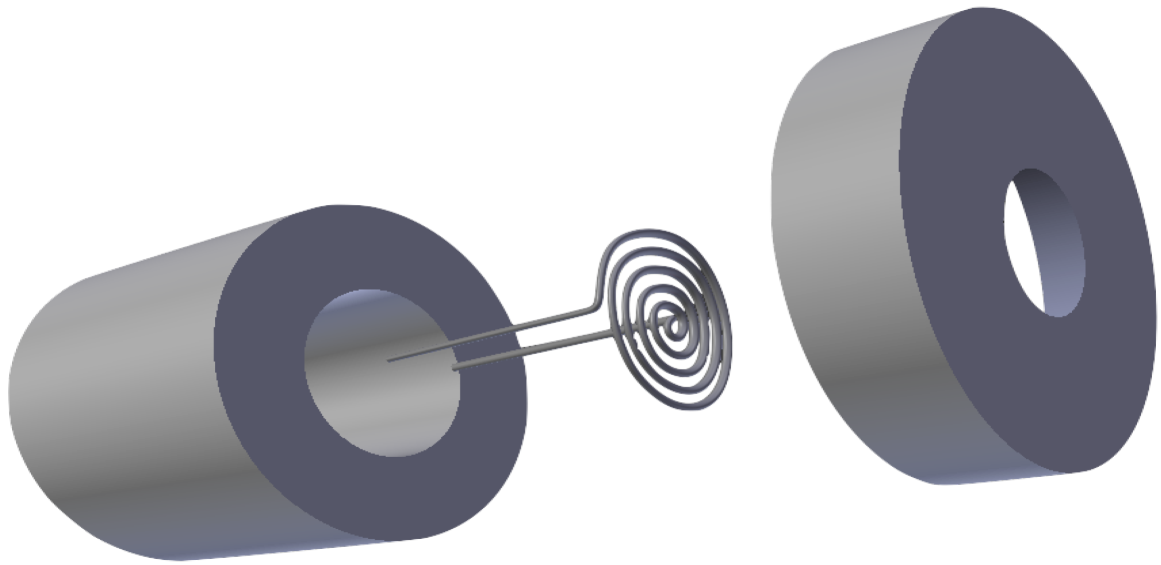

Figure 84: Design showing the three principal parts of our proposed oven. With the vessel to the left, then tungsten filament placed at the back of the oven near where the Yb will be deposited. Finally an end cap to the right which is fixed to the Yb containing vessel to provide a constricting apperture to produce a collimated Yb flux.

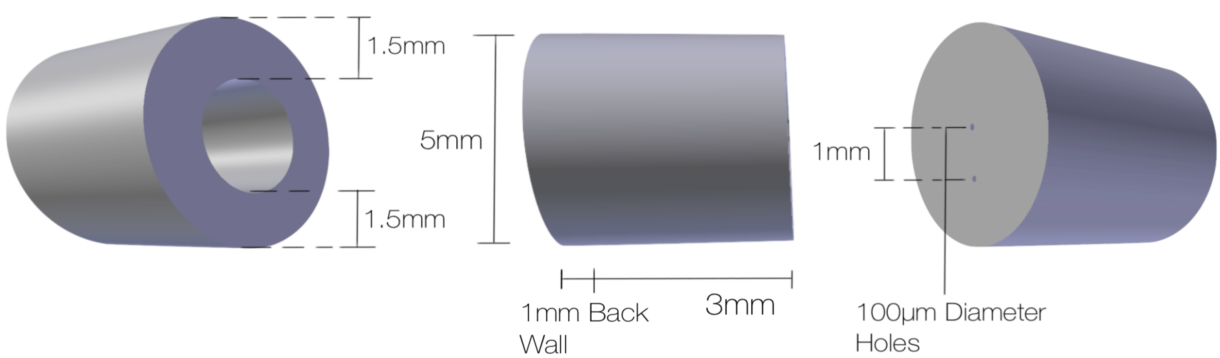

Figure 85: Diagram showing the dimensions of the ceramic Yb container part of the oven including the small holes needed to wire in the back to connect the filament

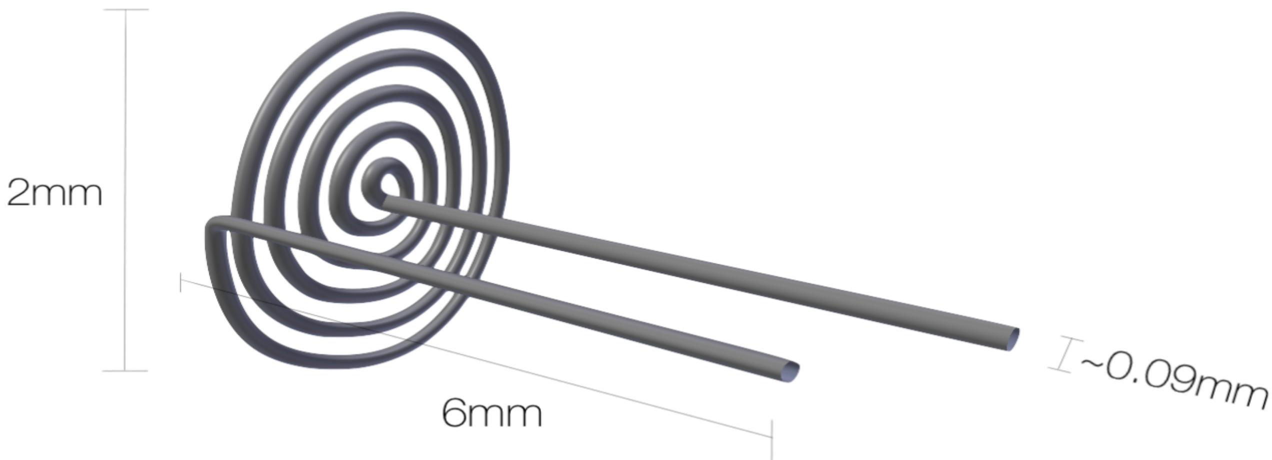

Figure 86: Diagram of the filament used to the sublimate the Yb. This shows the very small dimensions of the coil needed to produce optimal heating.

For more details on the exact calculations and reasoning for our oven design Ronnie Parkers dissertation is available on request [47].

7 Applications

Quantum sensing with trapped-ions has great potential to be revolutionary in the realm of RF and microwave sensing with its ability to focus on very narrow bandwidths with unparalleled sensitivity. In this section I will detail the different applications that I have considered along with calculations and reasoning to demonstrate the feasibility of these applications.

7.1 Classical RF sensors

Classical RF sensors have been in use since the late 19th century and have changed little in basic principle since that time. A coil or antenna arrayed in the open, which collects RF radiation over a cross section related to the size of the array, is generally used. The radiation then produces an AC electrical current in the antenna, which is then fed into a amplifier to increase the magnitude of the signal, so it is detectable, before being recorded. Although quantum sensors are beginning to make headway in some of these markets their sensitivities remain very high compared to classical sensors for radiation in the low RF regime [31].

This technology is used for essentially every RF and Microwave detection application, including radio communications, aircraft detection, NMR medical scanners and electronics defect detection. It is highly developed and finely tuned technology after over a century of development. Although they still have limitations, such as their need for electronics for both amplification and detection, which both add significant noise, reducing the signal to noise ratio (SNR) and hence the minimum detectable signal, which result in a lower sensitivity. Also classical sensors have limited minimum bandwidth, which is generally around 1-10 kHz for most systems, but can go down to 10 Hz with bulky and expensive electronics used in NMR detectors [26].

To make accurate comparisons for our novel ion trap sensor compared to a conventional system we can use our calculations for the effective area of the aerial from section 5.4 equation 108 and the Poynting vector power equation 105 and plug them into equation 106 to calculate the amount of electrical power in a conventional antenna induced by an oscillating magnetic field flux density B:

$$P = \frac{3Z_0}{\pi}\left(\frac{B\lambda}{4\mu_0}\right)^2 \tag{111}$$

Where $Z_0 = 377\ \Omega$ is the impedance of free space; λ is the wavelength of the radiation and μ_0 is the permeability of free space.

From this we can calculate the SNR of the system assuming that the main source of noise is the Johnson noise in the antenna from section 5.4.2.

$$P_{noise} = 4kT\Delta f \tag{112}$$

Where k is Boltzmann's constant, T is the noise temperature of the system and Δf is the bandwidth of the system. Hence the SNR for a classical antenna sensor is:

$$SNR_{con} = \frac{P}{P_{noise}}$$

$$SNR_{con} = \frac{3Z_0}{kT\Delta f}\left(\frac{B\lambda}{8\mu_0}\right)^2 \tag{113}$$

This equation will be used for calculations for drone detection and NQR applications.

7.2 Drone Detection

There is an ever increasing threat from drones being used to infiltrate restricted areas where they can be used for malicious purposes or pose a risk, especially recently in the UK [32]. One area we are considering is at airports where privately owned drones can pose a risk to planes through collisions and could even be used by terrorists to deliver explosives. Another area is around prisons where there is a serious problem of drones being used to drop drugs and weapons into prisons and supplying the illicit black-market in prisons.

Current technology for the detection of drones is done via the traditional RF pickup technique using a simple antenna and a RF receiver to detect the signals that are used by the drones base controller to interact and control the drone such as detailed in section 1 and section 7.1. Due to the inherently wide bandwidth of RF receivers this exposes the detector to large amounts of noise compromising the SNR, hence limiting its range. This is especially a problem in busy industrial or commercial centres such as airports or city centres.

The obvious solution to this problem is to narrow the bandwidth of the receiver, but for conventional receivers this is difficult to achieve below 10 kHz as the electronics become more expensive and less stable and can end up attenuating the signal as well as the noise. So the industry is in the need for a new solution that provides a narrow bandwidth and hence low noise solution [26]. The requirements are summarised by:

- Able to work in a high noise environment.
- Narrow bandwidth.
- High sensitivity to signals.
- Long range.
- High directivity.

At the moment the state of the art detection methods are little more complex than the base stations used to control the drones, which involve using a small dipole or loop antenna to collect the RF radiation generated by a small low power transmitter from the drone (usually around 100 mW). This radiation induces a small AC current in the antenna which is then amplified and then received by the system and recorded by a computer. The problem with this method is that these devices have an inherent bandwidth (typically 10 kHz) in which they are sensitive. The broader the bandwidth, the more noise there is being detected, which will drown out weaker signals reducing range. This is especially a problem in built up areas with high RF noise. These simple antennas do have an inherent directivity, but are quite limited and only have a detection angle on the order of 90 degrees. To increase the directivity you would have to increase the size of your antenna or add an array of small antennas, but this would increase the electrical resistance of your system, which induces noise and hence reduces the SNR. Also because of the broad bandwidth it is difficult to measure the Doppler shift of the drone to measure its speed and direction. This presents a problem for classical sensors as they are not sensitive enough to pick up signals from drones from more than a couple of km and do not have sufficient SNR in noisy environments (such as airports) to determine the position and heading of the craft.

The ion-trap quantum sensor can offer a solution with the target specifications and improvement over state-of-the-art classical system. The system will potentially offer very narrow bandwidth (Hz-μHz) detection and high sensitivity maximising the potential SNR of the system, which will lead to longer range detectors. We can also use a special technique to measure the exact peak frequency of the signal down to sub-millihertz (see section 5.3), which would allow us to measure the Doppler shift of the drone and with an array of detectors, within a few seconds you could calculate the exact trajectory of the drone and its speed. Trapped-ions are inherently sensitive to very particular frequencies in the MHz range, which it can be tuned to by changing the static magnetic field at the ion. Although the ion is very sensitive, it is only collecting magnetic field at a single point in space, so is inherently less sensitive than a simple antenna, which is detecting magnetic fields over an area roughly on the order of the size of the wavelength of the radiation (for drones on the order of 10 - 20 m). So the solution we propose is to combine the sensitivity and narrow bandwidth of the ion with the large pickup area of an antenna. We can do this by attaching the antenna to a feedthrough into the vacuum system where we have the ion trapped and then to a small coil wrapped around the trapping area. This has the effect of collecting magnetic field over a large area and concentrating it at the ion, amplifying the signal (for more details see section 5).

This technique could of course be duplicated by other quantum sensors such as N-V centres or SQUID's, but trapped-ions have certain advantages that would make them better for this particular application. This includes a narrower bandwidth and a far higher sensitivities at RF frequencies (see section 1.1), typically used by drones. For a comprehensive comparison see table 5, which assumes that we are sensing a drone which is emitting 100mW at 27MHz:

These numbers were found using the following calculations:

Using equation 110 from section 5.4 can be applied to find the maximum detectable range of the system by firstly calculating the SNR and set it to 1 to indicate the minimum detectable signal:

$$SNR_{ion} = \frac{B_{ion}}{B_{sens} + B_{noise}} = 1 \tag{114}$$

Where B_{sens} is the minimum detectable signal of the ion and B_{noise} is the electrical noise given by:

$$B_{noise} = \frac{4\mu_0 f}{c}\sqrt{\frac{\pi P_{noise}}{3Z_0}} \tag{115}$$

Where P_{noise} is given by equation 112; r is the radius of the input coil around the ion; R is the resistance of the antennas and B_{ext} is the minimum detectable magnetic field of the ion-coil system. So this gives us:

$$1 = \frac{cB_{ext}}{8rf(B_{sens} + B_{noise})}\sqrt{\frac{3Z_0}{\pi R}}$$

$$B_{ext} = \frac{8rf(B_{sens} + B_{noise})}{c}\sqrt{\frac{\pi R}{3Z_0}} \tag{116}$$

	State of the art	Future need	Trapped ions	SQUID's
Bandwidth (Hz)	10000	1	1	100000
B-field sensitivity at antenna (fT)	12.3	<1	0.769	1740
B-field sensitivity at sensor (pT)	N/A	N/A	10	$\sim$1000
Maximum range (km)	4	>10	30	0.56
Image acquisition time	instant	variable	seconds	seconds

Table 5: Table of comparisons of our sensor for a drone emitting 27MHz radiation at 100 mW (with and without using the ion-coil technique) against the current cutting edge technology and the best quantum sensor available at the time of writing. This includes the achievable bandwidth of the sensors; The sensitivity of the detectors compared against the ion trap sensor with an antenna; sensitivity of the bare ion and the SQUID without an antenna being used; The maximum range for these detectors to detect drone and the amount of time it would take to get a result.

Using our own internal report made in collaboration with the company QinetiQ [9] we conducted the magnetic field strength signal attenuation of a 100 mW drone is given by:

$$B_{ext} = \frac{k}{D^2} \tag{117}$$

Where B is the magnetic field strength, D is the distance from the sensor to the drone and k is a scaling constant which indicates the loss of signal the further the receiver is from the emitter. This constant k is calculated using the Free Space Path Loss formula (FSPL) [33] given by:

$$FSPL = 20\log_{10}(d) + 20\log_{10}(f) + 20\log_{10}\left(\frac{4\pi}{c}\right) - G_t - G_r \tag{118}$$

Where d is the distance between the emitter and receiver, f is the frequency of the radiation detected, c is speed of light, G_t and G_r, transmitter and receiver antenna gains respectively, which are calculated in the QinetiQ study [9] (Available on request). This leads us to the following k constants

$$27MHz : k = 11.25^{-7}Tm^2$$
$$35MHz : k = 6.69^{-7}Tm^2$$

I used these frequencies as these were the frequencies provided to us by QinetiQ, who know that these particular frequencies would be of interest to the drone detection community. From this we can calculate the minimum detectable distance of the drone:

$$D = \sqrt{\frac{k}{B_{ext}}} \tag{119}$$

To calculate the amount of noise in the system we can use an expected noise spectrum for a built-up area [10] to estimate the noise temperature for a busy city centre such as you might expect in a major airport or a prison in a large city to be:

$$27MHz : T_{noise} = 23.4 \times 10^5 K$$

$$35MHz : T_{noise} = 9.0 \times 10^5 K \tag{120}$$

This leads us to a maximum range of:

$$27MHz : D = 40.2km$$

$$35MHz : D = 29.5km \tag{121}$$

Now we can examine how this compares to a conventional system.

Conventional sensing

Using equation 113 and assuming that the minimum detectable signal will have an SNR of one then we can find the minimum detectable incident magnetic field flux density:

$$SNR_{con} = \frac{3Z_0}{k_B T \Delta f}\left(\frac{B_{min}\lambda}{8\mu_0}\right)^2 = 1$$

$$B_{min} = \frac{8\mu_0}{\lambda}\sqrt{\frac{k_B T \Delta f}{3Z_0}} \tag{122}$$

Where T is the total Noise temperature of the system. Using the noise spectrum [10] and equation 120 we can estimate the range of a typical conventional drone detection scheme with a bandwidth of 10 kHz. We can then use equation 117 and equation 119 to give a range of:

$$27MHz : D = 6.4km$$

$$35MHz : D = 5.5km$$

This means there is a predicted six-fold increase in range for the ion-trap magnetometer over conventional techniques.

There are some limitations to using this technique instead of a conventional detector. It could be that a very noisy environment could couple to a state in the ion causing instability and reducing sensitivity. Also the narrow bandwidth could make it difficult to find a drone unless the frequency being emitted is known beforehand.

7.3 NQR measurement

There is a growing market for the detection of explosives and narcotics with more technologies being brought to the market constantly. These technologies are usually limited to trace chemical detection, which means detecting molecules of explosive in the air. So if the explosive is sealed in a container then it will not be detectable and these sensors generally have a very limited range [27]. What this industry wants is a way to detect explosives at a distance; to identify exactly what compound it is; how much there is; and to find all this information in a matter of seconds. Because current methods are so limited you do not see explosive detection at airports on the same scale as say X-ray scanners, possibly leaving open a huge possible market. Such a detector would have a multitude of different applications such as: an airport scanner; border control; police searches; mine detection in a warzone or anti-terrorist operations.

Current methods for explosive detection are rather rudimentary, using a combination of manual searching, sniffer dogs and chemical detection [27]. These methods have serious limitations, what the industry would really want is to have an x-ray scanner type device that luggage or people can be placed inside of to determine whether they contain explosives or narcotics. Fortunately there is a technique already established for detecting nitrogen based explosives and narcotics called: Nuclear Quadrupole Resonance (NQR). This technique works in a similar manner as NMR for medical scanners and involves sending pulses of resonant radiation to a sample, which induces an echo back that can be collected and identified. Unfortunately this method is limited by the fact that the signals attenuate with r^3 distance from the source and are short lived, so hard to detect especially at range [28]. This technique has generally only been demonstrated in a sealed laboratory environment with minimal noise and usually with large sample sizes with the sample inside a detection coil. They are principally limited by the sensitivity and bandwidth of the detector, so to overcome this problem it would require a detector which is sensitive enough to detect these very weak signals with a narrow bandwidth so that the noise is limited as much as possible. This device should be small enough to be taken out of the laboratory into the field to be utilised by the military or to protect civilian installations.

What our sensor can offer that the current competition cannot is its adjustable bandwidth so it can focus on particular resonant frequencies while remaining unaffected by the noise from the surrounding frequencies. It also has the ability to quickly tune itself to different resonant frequencies to check for different known nitrogen compounds. This works in a similar way to the conventional NQR method except instead of the signal being amplified and recorded it is instead connected to a small loop around the ion in the sensor, which measures the concentrated magnetic field from the coil. This method can also be employed by other quantum sensors, but the resonant NQR frequencies are generally in the MHz regime in which other quantum sensors are not sensitive as they are most sensitive in the low RF and DC regimes. The best other quantum sensor for this task would be the SQUID detector, but at these frequencies only has a sensitivity of a few nT as opposed to 10pT for trapped-ions (See section 1.1).

I will make a calculation for the improved sensitivity of the system for NQR as this would be an approximate value, because the device I have described assumes a far field radiation projection from a point source, but in this case NQR produces a near field magnetic field. This represents an approximation for when the distance D is much more than size of the object being sensed. Also it is not clear whether it is a good approximation at all as the amplification factor assumes that the effective area of the external antenna is very large for the RF regime and therefore far larger than the distance D. But to demonstrate how the range can be greatly increased here is the equation for how a TNT signal B is attenuated: [9] (reference available on request).

$$B = \frac{k}{D^3}$$

For TNT: $k = 4 \times 10^{-18} Tm^{-3}$

$$D = \sqrt[3]{\frac{k}{B}}$$

$$D = 70cm$$

So this shows even with an D cubed relationship in the near field we can still measure signals at an increased distance from a few millimetres before to 70cm. This could mean that we can calculate the exact amount of a substance in a given sample if we know its mass and the measurement was made in closer proximity.

The equation used to ascertain the value k is given by equation 118 and also gives an equation which uses Faraday's law to describe what voltage would be induced in a coil with a sample within it [11]:

$$S_L = \zeta \mu_0 2\pi\nu M(\nu) A_{tot} \sqrt{\frac{QR}{2\pi\nu L}} \tag{123}$$

Where ζ is the filling factor of the coil and the sample; $M(\nu)$ is the total magnetic moment of the sample per unit volume; A_{tot} is the total area of every turn of the coil; Q is the quality factor of the coil; R is the resistance of the system; ν is resonant frequency of the sample and L is the total inductance of the coil.

The quality factor of a coil is equal to:

$$Q = \frac{2\pi\nu L}{R} \tag{124}$$

Plugging in equation 124 into equation 123 the square root can cancel leaving:

$$S_L = \zeta\mu_0 2\pi\nu M(\nu) A_{tot} \tag{125}$$

Now the filling factor ζ is simply the ratio of the sample volume and the volume of the coil.

$$\zeta = \frac{V_{sample}}{V_{coil}}$$

Where V_{coil} can be written as:

$$V_{coil} = Ah$$

Where A is the area of a single turn in the coil and h is the height of the coil:

$$h = Nr_s$$

Where r_s is the spacing of the turns in the coil and N is the number of turns of the coil. Hence we can write:

$$\zeta = \frac{V_{sample}}{ANr_s} \tag{126}$$

Also we can write A_{tot} as:

$$A_{tot} = AN \tag{127}$$

So plugging in equation 127 and equation 126 into equation 125 gives us:

$$S_L = \mu_0 2\pi\nu M(\nu) AN \frac{V_{sample}}{ANr_s}$$

$$S_L = \mu_0 2\pi\nu M(\nu) \frac{V_{sample}}{r_s} \tag{128}$$

Now as $M(\nu)$ is the magnetic moment density of the sample it can be written as:

$$M(\nu) = \frac{M_{tot}(\nu)}{V_{sample}} \tag{129}$$

Where $M_{tot}(\nu)$ is the total magnetic moment of the sample.

Plugging equation 129 into equation 128 finally gives us:

$$S_L = \frac{2\pi\mu_0\nu M_{tot}(\nu)}{r_s} \tag{130}$$

Now M_{tot} is calculated to be [11]:

$$M_{tot}(\nu) = 0.43\frac{h^2\gamma_n\nu N_s}{3kT} \tag{131}$$

Where γ_n is the gyromagnetic ratio of nitrogen 14 atoms and N_s is the total number of resonant nitrogen atoms given by:

$$N_s = \frac{N_a W_f m}{A_W} \tag{132}$$

Where N_a is Avogadro's number; W_f is the fraction of molecules that contain resonant N^{14} atoms. m is the mass of the sample and A_W is the atomic mass of the sample in $gmol^{-1}$.

Now we need to convert that voltage signal into a magnetic field signal at the ion:

$$I = \frac{S_L}{R}$$

$$B = \frac{\mu_0 I}{2r}$$

$$B = \frac{\mu_0 S_L}{2rR} \tag{133}$$

To give an example for how sensitive our system is we can assume that we are trying to sense a 100 g sample of TNT, which has a resonance at 840 Hz and has three nitrogen molecules, which each have a unique resonance peak and also there is a left handed and a right handed version, so we would only be detecting 1 in every 6 nitrogen-14 atoms. But there are two versions of TNT then the overall weight factor is: 0.5.

If we plug in these numbers plus the numbers we have already used for detection then divide by our sensitivity to give us a signal to noise ratio of:

$$SNR = 259$$

This is far higher than with an conventional system, which would only have a SNR of around 1.6 [11].

This shows there is a clear advantage in using our technique over conventional NQR detection (see table 6) with not only higher SNR for a small sample but also a detection range of over half a metre, which would open up a whole new market for detection of explosives at range. This technique could be hampered by magnetic field noise in very noisy environments as NQR signals are relatively broad (≈500 Hz) which would necessitate tuning the ion to a broader bandwidth.

	State of the art	Future need	Trapped ions
Bandwidth (Hz)	10000	1	1
B-field sensitivity at antenna (fT)	12.3	<1	0.769
B-field sensitivity at sensor (pT)	N/A	N/A	10
SNR of a 100g sample of TNT	$\sim$1.6	$\sim$100	$\sim$200
Maximum range (cm)	$\sim$cm	$\sim$1m	$\sim$70cm
Image acquisition time	instant	variable	seconds

Table 6: Table of comparisons of our sensor for a TNT NQR signal at (with and without using the ion-coil technique) against the current cutting edge technology, comparing calculated SNR of a 100 g TNT inside a coil connected to the ion and the maximum range that one could detect a 1 kg brick of TNT

Magnetic anomaly estimates : (estimates valid only within order of magnitude)			
Object	**Size**	**Depth/distance**	**Anomaly**
Steel Pipeline	Dia: 15cm Thick: ∼1cm	1m	1400nT
		2m	500nT
		5m	75nT
	Dia: 30cm Thick: 1.5cm	1m	7000nT
		2m	1700nT
		5m	282nT
Iron block	0.5kg	1m	50nT
		2m	4nT
		5m	<1nT
	1kg	1m	50nT
		2m	4nT
		5m	<1nT
	100kg	5m	160nT
		10m	10nT
		20m	<1nT

Table 7: Table showing the required sensitivity to detect a ferromagnetic object at a given distance through water. Here a steel pipeline and an iron block are used with certain sizes and weights. These numbers were calculated in [9].

7.4 Steel Pipeline and Buried Ferromagnetic Objects

Many of the geophysical applications utilise a technique known as Magnetic Anomaly Detection (MAD) which is a passive method used to detect visually obscured ferromagnetic objects by revealing the anomalies in the ambient Earth magnetic field caused by the objects [29].

Table 7 shows magnetic anomaly signals caused by various ferromagnetic objects such as:

- Pipelines: Depending on diameter and wall thickness of the pipelines
- Iron blocks: depending on the mass of the objects

Once the anomaly map is worked out, using data analyses techniques and protocols, the size and depth of the buried ferromagnetic objects can be estimated as discussed in [29].

Looking at the numbers given in table 7, we can see that our sensor has the potential to detect or track buried ferromagnetic objects up to a 5 metre depth, as the sensitivity of our device for the DC fields lies in the $\sim nT$ range. Although most other quantum sensors provide far greater sensitivity in the DC range, they generally require large amounts of shielding or have heating /cooling requirements, which make it difficult for field use (see section 1.1). We have worked with Planet Ocean Ltd who have confirmed that if the power and size requirements can be met then the RF ion quantum sensor could be a very valuable device on their autonomous submarines. Although it might be possible to track a buried pipeline under the seabed by applying

Submarine signal detection: (estimates valid only within order of magnitude)				
Signal to be detected	Initial strength (supposed)	Attenuation in seawater at 100m in dB	At sea surface (100m depth)	Total signal strength at 100m (water)+400m (air) =500m
50Hz	1μT	24.5 dB	3.6nT	~22 fT
	1mT	24.5 dB	3.6μT	22 pT
400Hz	1μT	69 dB	0.12 pT	~0.78 aT
	1mT	69 dB	124 pT	0.78 fT
Static B-field	1μT	1/r3	1 pT	8 fT
	1mT	1/r3	1 nT	8 pT

Table 8: Table of data supplied by Qinetiq, which shows the attenuation of different RF and DC signals through water and air, with the required sensitivity of the sensor.

low amplitude a/c signal of frequency around few 100s of kHz and then detect the field around the pipeline. This would significantly increase the detection range as the sensor has an increased sensitivity at higher frequencies [30].

7.5 Submarine Detection

The detection of military submarines is of great interest to governments the world over, who have invested heavily in expanding their capabilities in this area. Unfortunately there is very little information available on a given submarines magnetic signature. The following are the possible magnetic field signatures caused by electrical power equipment used in submarines as indicated to us by QinetiQ.

- Static B-field caused by current carrying cables
- 50/60/400 Hz Ac field

The static B-field drop off is proportional to the cube of the distance and an e/m wave drops off exponentially with respect to frequency in seawater as seen in Table 8. Through discussions with QinetiQ it was determined that a total distance between the submarine and the sensor of 500m (including 100m under water) is desirable.

Given the sensitivity of the sensor for static and low frequency signals, it's almost impossible to detect any signal at the distance of 500 m (100 m seawater + 400 m air) as suggested by QinetiQ the attenuation of a 50 Hz and 400 Hz signal is $\sim$ 0.25 and 0.7 dB/m in seawater excluding reflection losses. In table 8, the field strength at the interested distances.

7.6 RADAR detection

We are currently investigating how our device could be applied for RADAR applications involving detecting aircraft. By connecting a patch antenna close to the ion to an external RADAR dish we will see an amplification factor for the minimum magnetic field detectable for the system on the order of what we have calculated for RF applications (see section 5.4). If this was realised then our sensor will have a greatly enhanced range and SNR capabilities compared to a conventional system. The bandwidth would also be the same as with the RF detection set-up. This will lead to far greater range and greater frequency accuracy, which would lead to highly accurate speed and heading measurements on aircraft, from measuring their Doppler shift. We are currently working on conducting the calculations and simulations for this application and expect to have results soon.

7.7 Absolute RF Frequency Measurement

In addition to the measurement of the absolute magnetic field component, absolute frequency measurements is also important for many applications such as calibration of other magnetometers/frequency sources. This task is of interest in, for example, chemical analysis, molecular structure determination, and microwave spectroscopy [24]. The sensing mechanism of our magnetometer is based on certain atomic transitions (see section 2), hence providing absolute field measurements with sub-millhertz accuracy.

Following the methods described in [24] our device could be able to resolve frequency components of the fields at micro-Hertz level. Existing RF frequency spectrum analysers have a resolution in the $\sim$Hz range. Our device is tuneable from DC to $\sim$100 MHz range or more if sensitivity constraints are relaxed. The highly tuneable, narrow-band frequency lock-in feature of the ion trap magnetometer can be utilised to look for specific frequency signals. For more details on this method read section 5.3.

8 Conclusion

When the sensing project was first created four and a half years ago with no experiment and no assembled components, we were given a set of objectives by our funders the 'Birmingham quantum hub for sensors and metrology'. These objectives included: build a demonstrator system capable of trapping, cooling and sensing both RF and microwaves using ytterbium ions; improve and optimise the system to demonstrate its superiority over both its classical and quantum contemporaries; as well as work on miniaturising the components of the demonstrator towards a packaged portable experiment for commercial exploitation. Over time after talking with our prospective end-users, we decided to concentrate on enhanced sensing techniques detailed in section 5.4. This is because they were more interested in the far-field applications that would benefit from these techniques, while not requiring a particularly small sensing platform. I believe we have been largely been successful in achieving these objectives, with the construction of the demonstrator, which has demonstrated $pT\sqrt{Hz}$ sensitivities for RF fields as well as microwaves for the first time in the world with trapped-ions. I have also been successful in finding techniques to enhance our sensor for future experiments as shown in section 5.

At the beginning of the project there was much work done to calculate how the Yb ion trap sensor would function and what sensitivities we wouuld expect in both the RF and microwave regimes. This work was mostly undertaken by former group members Andrea Rodriguez-Blanco and Dr. Altaf Nizamani. The IQT group already had extensive experience using trapped $^{171}Yb^{+}$ and microwave dressed states for high fidelity qubit gates towards the development of a scalable universal quantum computer [23]. Much of the theory for manipulation of the internal states of the $^{171}Yb^{+}$ for quantum sensing was based on the two-qubit gate work of theoreticians at IQT such as Joeseph Randall [63]. From this theoretical work we found that with this sensor we should expect very long coherence times compared to other quantum sensors on the order of ≈1 s and sensitivities of around $\approx pT\sqrt{Hz}$ for both RF and microwaves (see section 2). These sensitivities are exceptional compared to other quantum sensors as they typically can only produce sensitivities of around $\approx nT\sqrt{Hz}$ in the MHz and GHz regime [72]. When combined with the ion-coil technique detailed in section 5.4 this sensor can even compete with conventional RF antenna system due to its exceptional bandwidth of 1 Hz to even ≈ μHz.

From the start of my PhD I have been deeply involved in the construction of the demonstrator system. This work involved designing various subsystems, ordering parts for them, and finally assembling and testing them. The subsystems I constructed almost exclusively were the DC system and the entire control system hardware as well as all the ARTIQ Python software used to run the experiments. I was also heavily involved in other components of the experiment such as the laser system, which I have recently redesigned; assembling and optimising the state detection system; I also helped order, clean, assemble, bake and install the entire vacuum system as well as rigorously test the internal electronics. This work resulted in a system that was robust enough to trap within just days of beginning trapping attempts.

Once trapping was achieved we moved quickly to optimise the trap to limit micro-motion and maximise the trap depth. Within just a month of experiments we were able to analyse all the relevant transitions with in the $^2S_{1/2}$ manifold of the $^{171}Yb^{+}$, to set up the both microwave and RF dressed states. These dressing fields were instrumental in reducing the decoherence in our sensing measurements. This is evident in comparing the coherence time measurements of the microwave transition $|0\rangle \rightarrow |+1\rangle$ with $T_2 = 4.31(1)$ ms and the dressed microwave transition $|0\rangle \rightarrow |D'\rangle$ of 1153 ms. These coherence times were also important in determining the optimal time for the sensitivity experiments to carry on for, as described in section 2.4.2. Unfortunately we were not able to carry out sensitivity measurements close to $t = T_2/2$ as the trap in our system tends to heat the ion, so it ejected from the trap after around 100 ms of not being exposed to the cooling laser. Nevertheless we achieved sensitivity measurements of $102 \pm 11.0\ pT\sqrt{Hz}$ for microwaves and $126 \pm 26.2\ pT\sqrt{Hz}$.

It is desirable to compare these results against the literature, to see how they push the field of quantum metrology forward. The paper that we based much of our work on was by Baumgart et al. [3]. In this work they used trapped $^{171}Yb^{+}$ ions to achieve a maximum sensitivity of 4.6 $pT/\sqrt{Hz}$, when sensing 14 MHz RF. This sensitivity is over an order of magnitude less then what we achieved, which was probably due to a combination of factors. Firstly, in their work they used a blade trap, unlike the surface trap we used. These traps generally incur less decoherence to the ion compared to surface traps, due to the greater distance between the ions and the electrodes. We also had problems with the coherence time not being as high as we expected, as well as having the ions experience a greater than expected heating rate (more details in section 4). Although they demonstrated high RF sensitivity using microwave dressed states, they did not employ RF dressed states to demonstrate microwave sensitivity, as we did. As far as we can ascertain from the literature there is no other quantum sensor that has demonstrated sensitivities this low, with frequencies as high as 12.6 GHz. There have also been a number of attempts to stretch other quantum sensors into the low RF regime such as in the work of Lee et al. [73]. Where a potassium vapour cell was employed to detect low frequency RF signal emitted from an NQR substance, ammonium nitrate. They used a system similar to the one I suggested in section 7.3, where a coil was wrapped around a sample, which was connected to the vapour cell. This experiment yielded a sensitivity of 0.24 $fT/\sqrt{Hz}$ and an SNR of 9 for detecting a 22 g sample of ammonium nitrate. This is many orders of magnitude better than our results with a RF frequency, but this is using a coil amplification technique, which could also be employed by our system, as I have shown in section 5.4. There I showed that I would see an up to 10^4 increase in sensitivity, which would bring our sensor far closer to this sensitivity. Vapour cell magnetometers are also very bulky requiring heating elements as well as shielding, making them impractical for field use compared to our sensor. Superconducting quantum interference devices (SQUIDs) are generally seen as the most sensitive quantum sensor for DC magnetic field sensing. Even at RF frequencies they do retain significant sensitivity as shown by Bal et al. [74], who demonstrate RF sensing from 100 kHz - 10 MHz with a sensitivity of 3.3 $pT/\sqrt{Hz}$ at 10 MHz. Their sensitivity is significantly better than ours at roughly this frequency, but is in line with our expected sensitivity from section 2. It is very possible that we could achieve a sensitivity the same or better than this if we managed to isolate the sources of decoherence on our system and eliminate them. Our sensor should also provide sensitivity to far higher frequencies, of up to 150 MHz and even 12.6 GHz microwaves. Like the vapour cell, SQUIDs are also very sensitive to DC noise, making them ill suited to work outside of a laboratory environment.

Although mid-way through the project we took the decision to move away from the development of the portable system, to work more on the ion-coil technique, there was still substantial work done on this project. This included the design of a miniaturised low power atomic oven; multiple designs of a small passively pumped vacuum chamber; laser diodes for all three of the principal lasers for the experiment and an integrated complete control board in development by Enterpoint Ltd. Although this device has not come to fruition, there are many technologies we have developed that will be useful in the future when we move to commercialise the RF and microwave quantum sensor in future.

Even with these accomplishments there is still a lot of scope for improvement. As mentioned in the previous paragraph, the heating rate problem is seriously hindering the maximum sensitivity, which is still quite far from its theoretical limits. This could be remedied by trying to isolate the source of the heating, which could be floating electrodes on the chip or from some other source. A new chip such as the one detailed in section 5.2 could provide a lesser heating rate as well as provide a multi-sensing capability, which would increase our sensitivity by up to an order of magnitude. Future experiments would also be enhanced by the ion-coil technique detailed in section 5.4. This would open up new applications that our prospective end-users are interested in, such as drone detection for RF signals from the drone fed to the ion, or explosive/narcotic detection using NQR. I believe there is great scope for continuing RF and microwave sensing using trapped-ions into the future and could be incredibly disruptive in a number of fields.

References

[1] Lewis Coe.
Wireless Radio A Brief History
Book, McFarland & Company Inc, Publishers, North Carolina, and London

[2] K.S. Packard.
The Origin of Waveguides: A Case of Multiple Rediscovery
IEEE Transactions on Microwave Theory and Techniques (Volume: 32, Issue: 9, Sep 1984)

[3] I. Baumgart, J.-M. Cai, A. Retzker, M. B. Plenio, and Ch. Wunderlich.
Ultrasensitive magnetometer using a single atom
Department Physik, Naturwissenschaftlich-Technische Fakultat, Universitat Siegen, 57068 Siegen, Germany

[4] Paul W., Steinwedel H.
Ein neues Massenspektrometer ohne Magnetfeld
Zeitschrift für Naturforschung A, Volume 8, Issue 7, Pages 448–450

[5] David Francesco Murgia.
Microchip ion traps with high magnetic field gradients for microwave quantum logic
PhD thesis, Imperial College London, Centre for Doctoral Training in Controlled Quantum Dynamics, Department of Physics

[6] Johnson, J. B.
THERMAL AGITATION OF ELECTRICITY IN CONDUCTORS
`https://journals.aps.org/pr/pdf/10.1103/PhysRev.32.97`

[7] S.-K. Lee and M. V. Romalis.
Calculation of magnetic field noise from high-permeability magnetic shields and conducting objects with simple geometry
Journal of Applied Physics 103, 084904 (2008)

[8] McDonald, Kirk T.
Power Received by a Small Antenna
Princeton University,

http://puhep1.princeton.edu/~kirkmcd/examples/power.pdf

[9] Nizamani, Altaf.
Feasibility study of Ion Array Magnetometer
Internal University of Sussex report (available on request).

[10] Farson, Adam M.
Antenna and Receiver Noise Figure
http://www.ab4oj.com/icom/nf.html

[11] Miller, Joel B.
Nuclear Quadrupole Resonance Detection of Explosives
US Naval Research Laboratory internal report (available on request).

[12] Zhao Sheng Wang.
Microscopie à microsquid
NEEL institut
http://neel.cnrs.fr/spip.php?article914&lang=en

[13] B.D.Josephson.
Possible new effects in superconductive tunnelling
Physics Letters Volume 1, Issue 7, 1 July 1962, Pages 251-253
https://www.sciencedirect.com/science/article/pii/0031916362913690?via%3Dihub

[14] L. J. Friedman, A. K. M. Wennberg, S. N. Ytterboe, and H. M. Bozler.
Direct detection of low frequency NMR using a DC SQUID
Review of Scientific Instruments 57, 410 (1986)

[15] C. Affolderbach, M. Stähler, S. Knappe, R. Wynands.
An all-optical, high-sensitivity magnetic gradiometer
Institut für Angewandte Physik, Universität Bonn
https://link.springer.com/article/10.1007%2Fs00340-002-0959-8

[16] W. Clark Griffith, Svenja Knappe, and John Kitching1.
Femtotesla atomic magnetometry in a microfabricated vapor cell
Vol. 18, No. 26 / OPTICS EXPRESS 27167
https://www.researchgate.net/publication/49720023_Femtotesla_atomic_magnetometry_in_a_microfabricated_vapor_cell

[17] Savukov, I. M. et al.
Tunable Atomic Magnetometer for Detection of Radio-Frequency Magnetic Fields
Phys. Rev. Lett., Vol. 95, Issue.6, 2005

[18] Dmitry Budker and Derek F. Jackson.
Optical Magnetometery
Cambridge University press, New York, 2013.

[19] J.M.Taylor, P.Capellaro, L.Childress, L.Jiang, D.Budker, P.R.Hemmer, A.Yacoby, R.Walswortg and M.D.Lunkin.
High-Sensitivity diamond magnetometer with nanoscale resolution,
Nature Physics,4, 810-816(2008)

[20] L. M. Pham, N. Bar-Gill, C.Belthangady, D.Le Sage, P.Cappellaro, M.D.Lukin, A.Yacoby and R.L.Walsworth.
Enhanced solid-state multi-spin metrology using dynamical decoupling
Rev.B 86,045214 (2012)

[21] M. Bal, et al.
Ultrasensitive magnetic field detection using a single artificial atom
Nature Communications, Vol. 3, 2012

[22] M. Koschorreck et al.
High resolution magnetic vector-field imaging with cold atomic ensembles
Applied Physics Letters Vol. 98, 2011

[23] B. Lekitsch, S. Weidt, A.G. Fowler, K. Mølmer, S.J. Devitt, Ch. Wunderlich, and W.K. Hensinger.
Blueprint for a microwave trapped ion quantum computer
Science Advances 3, e1601540 (2017)

[24] Simon Schmitt, Tuvia Gefen, Felix M. Stürner.
Submillihertz magnetic spectroscopy performed with a nanoscale quantum sensor
Science Vol. 356, Issue 6340, pp. 832-837

[25] Alexander Stark, Nati Aharon, Thomas Unden, Daniel Louzon, Alexander Huck, Alex Retzker, Ulrik L. Andersen1 and Fedor Jelezko.
Narrow-bandwidth sensing of high-frequency fields with continuous dynamical decoupling
Nature communications DOI: 10.1038/s41467-017-01159-2

[26] Allen D. Elster, MD FACR.
Receiver Bandwidth
Questions and answers in MRI article

[27] Dr. John E. Parmeter.
Guide for the selection of Drug Detectors for Law Enforcement Applications

National Institute of Justice

[28] Butt, Naveed; Gudmundson, Erik; Jakobsson, Andreas.
An Overview of NQR Signal Detection Algorithms
Magnetic Resonance Detection of Explosives and Illicit Materials 10.1007/978-94-007-7265-6-2

[29] Sheldon Breiner.
Magnetic Search in the Marine Environment
Geometrics, Inc.
ftp://geom.geometrics.com/pub/mag/Literature/MarineSearch.pdf

[30] Correspondence with Qinetiq

[31] Vrba J, Robinson SE.
Signal Processing in Magnetoencephalography
Methods Volume 25, Issue 2, October 2001, Pages 249-271

[32] Gwyn Topham.
Gatwick drone disruption cost airport just £1.4m
Article, The Guardian, Tue 18 June 2019
https://www.theguardian.com/uk-news/2019/jun/18/gatwick-drone-disruption-cost-airport-just-14m

[33] Prof. Murat Torlak.
Path Loss presentation
EE4367 Telecom. Switching and Transmission
https://www.utdallas.edu/ torlak/courses/ee4367/lectures/lectureradio.pdf

[34] Johnson, J. B.
Thermal agitation of electricity conductors.
Phys. Rev. 32, pp. 97–109.

[35] D. F. Murgia.
Microchip ion traps with high magnetic field gradients for microwave quantum logic.
PhD thesis, University of Sussex, 2017.

[36] S. Weidt.
Towards microwave based ion trap quantum technology.
PhD thesis, University of Sussex, 2013.

[37] James D. Siverns.
Yb ion trap experimental set-up and two-dimensional ion trap surface array design towards analogue quantum simulations.

PhD thesis, University of Sussex, 2011.

[38] Ligo vacuum compatible materials list.
`dcc.ligo.org/E960050/public`

[39] Ethan Potter.
Development and Demonstration of a High Bandwidth, Ultra Sensitive Trapped Ion Magnetometer
PhD thesis, University of Sussex, 2018.

[40] Tomas Navickas.
Towards high-fidelity microwave driven multi-qubit gates on microfabricated surface ion traps PhD. thesis, University of Sussex, 2018.

[41] Malte Schmidt1, Marco Prevedelli, Antonio Giorgini, Guglielmo M. Tino, Achim Peters1.
A portable laser system for high precision atom interferometry experiments
Applied Physics B 102(1)

[42] A.T. Nguyen, L.B. Wang, M. M. Schauer, J. R. Torgerson.
Extended temperature tuning of an ultraviolet diode laser for trapping and cooling single Yb + ions
Review of Scientific Instruments 81, 053110 (2010); doi: 10.1063/1.3386580

[43] S.V. Chepurov, A.A. Lugovoy, S.N. Kuznetsov.
Laser system for Doppler cooling of ytterbium ion in an optical frequency standard
IOP Science DOI: 10.1070/QE2014v044n06ABEH015450

[44] Tom Whitmore.
Report on wavemeter
Internal report by IQT available on request

[45] James D. Whitea and Robert E. Scholtenb.
Compact diffraction grating laser wavemeter with sub-picometer accuracy and picowatt sensitivity using a webcam imaging sensor
REVIEW OF SCIENTIFIC INSTRUMENTS 83, 113104 (2012)

[46] P. D. Zavitsanos and G. A. Carlson.
Experimental study of the sublimation of graphite at high temperatures
The Journal of Chemical Physics, Volume 59, Issue 6, p.2966-2973

[47] Ronnie Parker, Harry Bostock, Altaf Nizamani, Winfried Hensinger.
Miniaturised Low Power Yb Atomic Oven for Portable Ion Trap Quantum Devices
University of Sussex Bsc honours dissertation

Available on request.

[48] A. Ashkin.
ACCELERATION AND TRAPPING OF PARTICLES BY RADIATION PRESSURE
Volume 24, number 4 PHYSICAL REVIEW LETTERS 26 January 1970

[49] H. G. Dehmelt.
Radiofrequency spectroscopy of stored ions I: storage.
Adv. At. Mol. Phys., 3(53), 1967.

[50] W. Paul, O. Osberghaus, and E. Fischer. Ein ionenkfig.
Forschungsberichte des Wirtschafts- und Verkehrsministeriums Nordrhein-Westfalen,
Book, published by VS Verlag für Sozialwissenschaften, 1958.

[51] Carl E. Wieman, David E. Pritchard, David J. Wineland.
Atom cooling, trapping, and quantum manipulation
Reviews of Modern Physics, Vol. 71, No. 2, Centenary 1999 0034-6861/99/71(2)/253(10)

[52] S. Earnshaw.
On the nature of the molecular forces which regulate the constitution of the luminiferous ether.
Trans. Camb. Phil. Soc., 7(97-112), 1842.

[53] M. D. Hughes, B. Lekitsch, J. A. Broersma, and W. K. Hensinger.
Microfabricated ion traps.
Cont. Phys., 52(505), 2011.

[54] D. J. Wineland, C. Monroe, W. M. Itano, D. Leibfried, B. E. King, and D. M.Meekhof.
Experimental issues in coherent quantum-state manipulation of trapped atomic ions.
J. Res. Nat. Inst. Stand. Tech., 103(259-328), 1998.

[55] J. J. McLoughlin, A. H. Nizamani, J. D. Siverns, R. C. Sterling, M. D. Hughes, B. Lekitsch, B. Stein, S. Weidt, and W. K. Hensinger.
Versatile ytterbium ion trap experiment for operation of scalable ion-trap chips with motional heating and transition-frequency measurements.
Phys. Rev. A, 83(013406), 2011.

[56] M. J. Madsen, W. K. Hensinger, D. Stick, J. A. Rabchuk, and C. Monroe.
Planar ion trap geometry for microfabrication.
Appl. Phys. B, 78(639-651), 2004.

[57] W. Paul.
Electromagnetic traps for charged and neutral particles.
Rev. Mod. Phys., 62(531-540), 1990.

[58] C. Donald.
Development of an ion trap quantum information processor.
PhD thesis, University of Oxford, 2000.

[59] M. Abramowitz and I. Stegun.
Handbook of Mathematical Functions.
Book, Dover Publications, New York, 1964.

[60] A. H. Nizamani, J. J. McLoughlin, and W. K. Hensinger.
Doppler-free yb spectroscopy with fluorescence spot technique.
Phys. Rev. A, 82(043408), 2010.

[61] P. T. H. Fisk, M. J. Sellars, M. A. Lawn, and C. Coles.
Accurate measurement of the 12.6 GHz-clock transition in trapped 171yb+ ions.
IEEE Trans. Ultrason. Ferroelectr. Freq. Control, 44(344-354), 1997.

[62] G. Breit and I. I. Rabi.
Measurement of nuclear spin.
Phys. Rev., 38(2082), 1931

[63] J. Randall.
High-Fidelity Entanglement of Trapped Ions using Long-Wavelength Radiation.
PhD thesis, Imperial College London, 2016.

[64] S. C. Webster, S. Weidt, K. Lake, J. J. McLoughlin and W. K. Hensinger.
Simple Manipulation of a Microwave Dressed-State Ion Qubit
PRL 111, 140501 (2013)

[65] M. P. Fewell, B. W. Shore, and K. Bergmann.
Coherent population transfer among three states: Full algebraic solutions and the relevance of non adiabatic proceses to transfer by delayed pulses.
Aust. J. Phys., 50(281-308), 1997.

[66] Łukasz Cywiński, Roman M. Lutchyn, Cody P. Nave, and S. Das Sarma.
How to enhance dephasing time in superconducting qubits
Phys. Rev. B 77, 174509 (2008)

[67] J. M. Taylor, P.Capellaro, L. Childress, L. Jiang, D. Budker, P. R. Hemmer, A. Yacoby, R. Walswortg, and M. D. Lunkin.
High-sensitivity diamond magnetometer with nanoscale resolution. Nature Physics, 4(810-816), 2008.

[68] W. M. Itano, J. C. Bergquist, J. J. Bollinger, J. M. Gilligan, D. J. Heinzen, F. L. Moore, M. G. Raizen, and D. J. Wineland.
Quantum projection noise: Population fluctuations in two-level systems.
Phys. Rev. A, 47(5), 1993.

[69] Harry Bostock.
Investigations Into Rotating Wall Regimes to Control Electron and Positron Plasma Density
University of Swansea, Masters Dissertation (Available on request)

[70] K. Lake.
Yb ion trap experimental set-up and two-dimensional ion trap surface array design towards analogue quantum simulations.
PhD thesis, University of Sussex, 2011.

[71] G. A. Alvarez, A. Ajoy, X. Peng, and D. Suter.
Performance comparison of dynamical decoupling sequences for a qubit in a rapidly fluctuating spin bath.
Phys. Rev. A, 82(042306), 2010.

[72] T. Joas, A. M. Waeber, G. Braunbeck & F. Reinhard.
Quantum sensing of weak radio-frequency signals by pulsed Mollow absorption spectroscopy
Nature Communicationsvolume 8, Article number: 964 (2017)

[73] S. -K. Lee, K. J. Sauer, S. J. Seltzer, O. Alem, M. V. Romalis.
Subfemtotesla radio-frequency atomic magnetometer for detection of nuclear quadrupole resonance
Applied physics letters 89, 214106 (2006)

[74] M. Bal, C. Deng, J.-L. Orgiazzi, F.R. Ong & A. Lupascu.
Ultrasensitive magnetic field detection using a single artificial atom
nature communications DOI: 10.1038/ncomms2332

A ARTIQ Python scripts

A.1 SPAM

```
from artiq.experiment import *

class Spam(HasEnvironment):
    '''Basic state prep and measurement routines'''
    def build(self):
        self.setattr_device("core")
        self.setattr_device("scheduler")
        self.setattr_device("PMT")
        self.setattr_device("aom369")
        self.setattr_device("eom369")
        self.setattr_device("clock_mw")
        self.setattr_device("plus_mw")
        self.setattr_device("minus_mw")
        #print('initialising Spam class')

    @kernel
    def dopplerOn(self):
        self.aom369.on()
        self.eom369.on()
        self.clock_mw.on()
        self.plus_mw.on()
        self.minus_mw.on()

    @kernel
    def dopplerOff(self):
        self.aom369.off()
        self.clock_mw.off()
        self.plus_mw.off()
        self.minus_mw.off()

    @kernel
    def doppler(self, cool_time=1*ms):
        with parallel:
            self.aom369.pulse(cool_time)
            self.clock_mw.pulse(cool_time)
            self.plus_mw.pulse(cool_time)
            self.minus_mw.pulse(cool_time)

    @kernel
    def prep(self, prep_time=200*us):
        timep = prep_time
        self.core.break_realtime()
        self.eom369.off()
        #print(prep_time)
        self.aom369.pulse(timep)
        self.eom369.on()

    @kernel
    def readout(self, readout_time=1*ms):
        with parallel:
            self.PMT.gate_rising(readout_time)
            self.aom369.pulse(readout_time)

        return self.PMT.count()
```

A.2 Analysis

```
import time
import random

import numpy as np
from scipy.optimize import curve_fit

from artiq.experiment import *




class Analysis(HasEnvironment):

    def build(self):
        self.setattr_device("scheduler")
        self.setattr_device("ccb")

    def gaussian(self, x, amp, cen, wid):
        return amp * np.exp(-(x-cen)**2 / wid)

    def rabi_flop(self, x, tpi):
        return np.sin((x*np.pi)/tpi - (np.pi/2))/2 + 0.5

    def analyse(self, xdata, ydata, model, p0):
        # Use get_dataset so that analyze can be run stand-alone.
        yfit = self.get_dataset(ydata)
        xfit = self.get_dataset(xdata)

        popt, pcov = curve_fit(model, xfit, yfit, p0)
        return popt

    def plot_fit(self, xdata, xname, ydata, yname, model, p0):
        xfit = self.get_dataset(xdata)
        xbegin = xfit[1]
        xend = xfit[-1]

        xarray = np.linspace(xbegin, xend, 1000)
        l = len(xarray)

        self.set_dataset("xplot", xarray, persist=True, save=False)
        self.set_dataset("yplot",np.array([model(x, *p0) for x in xarray]),
broadcast=True, save=False)


        self.ccb.issue("create_applet", "plot_fit", "plot_xyfit {}--x {}--fit
yplot --fitx xplot --xlabel {}--ylabel {}".format(ydata, xdata, xname, xdata))
```

A.3 Basic scan

```
from artiq.experiment import *
from spam import Spam
from Analysis_Harry import Analysis
import time
import numpy as np
class BasicScan(HasEnvironment):
    """base parameter scan class"""
    def build(self):
        self.setattr_device("core")
        self.setattr_device("scheduler")
        self.setattr_device("PMT")
        self.setattr_device("aom369")
        self.setattr_device("eom369")
        self.setattr_device("clock_mw")
        self.setattr_device("plus_mw")
        self.setattr_device("minus_mw")
        self.setattr_device("extra_mw")
        self.setattr_device("rf1")
        self.setattr_device("rf2")
        self.setattr_device("rf3")
        self.setattr_device("rf4")
        self.setattr_device("AD9959")
        self.cooling_freq = self.get_dataset("cooling.freq")
        self.cooling_amplitude = self.get_dataset("cooling.amplitude")
        self.detect_time = self.get_dataset("spam.detect_time")
        self.cool_time = self.get_dataset("spam.cool_time")
        self.prep_time = self.get_dataset("spam.prep_time")
        self.threshold = self.get_dataset("spam.threshold")
        self.setattr_argument("nruns", NumberValue(default=100, ndecimals=0,
step=1))
        self.spam = Spam(self)
        self.analysis = Analysis(self)
        self.scan_parameter = None

    def prepare_experiment(self, nsteps):
        self.AD9959.setChannel(1, self.cooling_freq, self.cooling_amplitude, 0)
        self.set_dataset("probability", np.full(nsteps, np.nan), broadcast=True,
persist=True)
        self.set_dataset("av_counts", np.full(nsteps, np.nan), broadcast=True,
persist=True)
        self.set_dataset("counts", np.full( (nsteps, self.nruns) , np.nan),
broadcast=True, persist=True)

    def prepare_scan_point(self, stepnum=0, stepped_parameter=0):
        pass

    @kernel
    def scan_experiment(self, stepnum=0, stepped_parameter=0.0):
        pass

    @kernel
    def scan_point(self, stepnum=0, stepped_parameter=0.0):
        counts = [0 for i in range(self.nruns)]     # allocate count array
        self.core.reset()
```

```
    # self.PMT.input()
    # self.PMT.gate_rising(self.detect_time)
     self.spam.dopplerOff()
     #delay(10*ms)
     bright = 0
     total_counts = 0
     for i in range(self.nruns):
         self.core.break_realtime()
         #delay(1*ms)
         self.spam.doppler(self.cool_time)
         self.spam.prep(self.prep_time)
         self.scan_experiment(stepnum, stepped_parameter)
         clicks = self.spam.readout()
         counts[i] = clicks
         if clicks >= self.threshold:
             bright += 1
         total_counts += clicks
         self.mutate_dataset("counts", stepnum, counts)
     self.core.break_realtime()
     self.spam.dopplerOn()
     #delay(1*ms)
     prob = bright/self.nruns
     av_counts = total_counts/self.nruns
     self.mutate_dataset("probability", stepnum, prob)
     self.mutate_dataset("av_counts", stepnum, av_counts)



def run(self):
    try:
        if self.scan_parameter:
            self.prepare_experiment(len(self.scan_parameter))
            #for _ in range(len(self.scan_parameter)):
            for j, parameter in enumerate(self.scan_parameter):
                self.prepare_scan_point(j, parameter)
                self.scan_point(j, float(parameter))
                self.scheduler.pause()
        else:
            print('No scanning parameter!')
    except TerminationRequested:
            print("Terminated experiment early")
```

A.4 Microwave dressed state experiments

```
from basicScan2 import *
class MwClockfreqScan(BasicScan, EnvExperiment):
    """Microwave clock Frequency scan v3.0"""
    def build(self):
        self.peak_freq_width = self.get_dataset("clock.width")
        self.peak_freq = self.get_dataset("clock.freq")
        self.pulse_time = self.get_dataset("clock.pi_time")
        self.setattr_argument("MW_frequency",
Scannable(default=RangeScan(self.peak_freq-30000, self.peak_freq+30000, 26),
ndecimals=8, unit='kHz'))
        self.setattr_argument("mw_amplitude", NumberValue(default = 0.3,
ndecimals=3, step=0.1, min = 0, max = 1), tooltip = 'amplitude (0-1)')
        super().build()
        self.scan_parameter = self.MW_frequency
    def prepare_experiment(self, nsteps):
        self.set_dataset("freq", np.full(nsteps, np.nan), broadcast=True,
persist=True)
        super().prepare_experiment(nsteps)
    def prepare_scan_point(self, stepnum=0, stepped_parameter=0):
        freq = stepped_parameter
        self.AD9959.setChannel(0, freq, self.mw_amplitude, 0)
        self.mutate_dataset("freq", stepnum, stepped_parameter)

    @kernel
    def scan_experiment(self, stepnum=0, stepped_parameter=0.0):
        self.extra_mw.pulse(self.pulse_time)
    def analyze(self):
        p0 = [1, self.peak_freq, self.peak_freq_width]
        para = self.analysis.analyse("freq", "probability",
self.analysis.gaussian, p0)
        print(para)

        [n_peakh,n_peakf,n_peakw] = para
        self.set_dataset("clock.width", n_peakw, persist=True, save=False)
        self.set_dataset("clock.freq", n_peakf, persist=True, save=False)
        print("your clock frequency is:{}kHz".format(n_peakf/1000))
        self.analysis.plot_fit("freq", "frequency /Hz", "probability",
"probability", self.analysis.gaussian, para)

class MwplusfreqScan(BasicScan, EnvExperiment):
    """Microwave plus Frequency scan v3.0"""
    def build(self):
        self.peak_freq_width = self.get_dataset("plus.width")
        self.peak_freq = self.get_dataset("plus.freq")
        self.pulse_time = self.get_dataset("plus.pi_time")
        self.setattr_argument("MW_frequency",
Scannable(default=RangeScan(self.peak_freq-30000, self.peak_freq+30000, 26),
ndecimals=8, unit='kHz'))
        self.setattr_argument("mw_amplitude", NumberValue(default = 0.3,
ndecimals=3, step=0.1, min = 0, max = 1), tooltip = 'amplitude (0-1)')
        super().build()
        self.scan_parameter = self.MW_frequency

    def prepare_experiment(self, nsteps):
```

```
        self.set_dataset("freq", np.full(nsteps, np.nan), broadcast=True,
persist=True)
        super().prepare_experiment(nsteps)

    def prepare_scan_point(self, stepnum=0, stepped_parameter=0):
        freq = stepped_parameter
        self.AD9959.setChannel(0, freq, self.mw_amplitude, 0)
        self.mutate_dataset("freq", stepnum, stepped_parameter)

    @kernel
    def scan_experiment(self, stepnum=0, stepped_parameter=0.0):
        self.extra_mw.pulse(self.pulse_time)

    def analyze(self):
        p0 = [1, self.peak_freq, self.peak_freq_width]
        para = self.analysis.analyse("freq", "probability",
self.analysis.gaussian, p0)
        [n_peakh,n_peakf,n_peakw] = para
        self.set_dataset("plus.width", n_peakw, persist=True, save=False)
        self.set_dataset("plus.freq", n_peakf, persist=True, save=False)
        print("your plus frequency is:{}kHz".format(n_peakf/1000))
        self.analysis.plot_fit("freq", "frequency /Hz", "probability",
"probability", self.analysis.gaussian, para)

class MwminusScan(BasicScan, EnvExperiment):
    """Microwave minus Frequency scan v3.0"""
    def build(self):
        self.peak_freq_width = self.get_dataset("minus.width")
        self.peak_freq = self.get_dataset("minus.freq")
        self.pulse_time = self.get_dataset("minus.pi_time")
        self.setattr_argument("MW_frequency",
Scannable(default=RangeScan(self.peak_freq-30000, self.peak_freq+30000, 26),
ndecimals=8, unit='kHz'))
        self.setattr_argument("mw_amplitude", NumberValue(default = 0.3,
ndecimals=3, step=0.1, min = 0, max = 1), tooltip = 'amplitude (0-1)')
        super().build()
        self.scan_parameter = self.MW_frequency

    def prepare_experiment(self, nsteps):
        self.set_dataset("freq", np.full(nsteps, np.nan), broadcast=True,
persist=True)
        super().prepare_experiment(nsteps)

    def prepare_scan_point(self, stepnum=0, stepped_parameter=0):
        freq = stepped_parameter
        self.AD9959.setChannel(0, freq, self.mw_amplitude, 0)
        self.mutate_dataset("freq", stepnum, stepped_parameter)

    @kernel
    def scan_experiment(self, stepnum=0, stepped_parameter=0.0):
        self.extra_mw.pulse(self.pulse_time)

    def analyze(self):
        p0 = [1, self.peak_freq, self.peak_freq_width]
```

```
        para = self.analysis.analyse("freq", "probability",
self.analysis.gaussian, p0)
        [n_peakh,n_peakf,n_peakw] = para
        self.set_dataset("minus.width", n_peakw, persist=True, save=False)
        self.set_dataset("minus.freq", n_peakf, persist=True, save=False)
        print("your minus frequency is:{}kHz".format(n_peakf/1000))
        self.analysis.plot_fit("freq", "frequency /Hz", "probability",
"probability", self.analysis.gaussian, para)

class MwClockTimeScan(BasicScan, EnvExperiment):
    """Microwave Clock Rabi Scan v3.0"""
    def build(self):
        self.mw_frequency = self.get_dataset("clock.freq")
        self.mw_amplitude = self.get_dataset("clock.amplitude")
        self.pi_time = self.get_dataset("clock.pi_time")
        self.setattr_argument("pulse_time", Scannable(default=RangeScan(0,
500e-6, 26), unit='us'))
        super().build()
        self.scan_parameter = self.pulse_time

    def prepare_experiment(self, nsteps):
        self.set_dataset("time", np.full(nsteps, np.nan), broadcast=True,
persist=True)
        super().prepare_experiment(nsteps)

    def prepare_scan_point(self, stepnum=0, stepped_parameter=0):
        self.AD9959.setChannel(0, self.mw_frequency, self.mw_amplitude, 0)
        self.mutate_dataset("time", stepnum, stepped_parameter)

    @kernel
    def scan_experiment(self, stepnum=0, stepped_parameter=0.0):
        pulse_time = stepped_parameter
        self.extra_mw.pulse(pulse_time)

    def analyze(self):
        para = self.analysis.analyse("time", "probability",
self.analysis.rabi_flop, self.pi_time)
        self.set_dataset("clock.pi_time", para, persist=True, save=False)
        print("your clock pi time is:{}us".format(para*1000000))
        self.analysis.plot_fit("time", "time /s", "probability", "probability",
self.analysis.rabi_flop, para)

class MwplusTimeScan(BasicScan, EnvExperiment):
    """Microwave plus Rabi Scan v3.0"""
    def build(self):
        self.mw_frequency = self.get_dataset("plus.freq")
        self.mw_amplitude = self.get_dataset("plus.amplitude")
        self.plus_pi_time = self.get_dataset("plus.pi_time")
        self.setattr_argument("pulse_time", Scannable(default=RangeScan(0,
500e-6, 26), unit='us'))
        super().build()
        self.scan_parameter = self.pulse_time

    def prepare_experiment(self, nsteps):
```

```
        self.set_dataset("time", np.full(nsteps, np.nan), broadcast=True,
persist=True)
        super().prepare_experiment(nsteps)

    def prepare_scan_point(self, stepnum=0, stepped_parameter=0):
        self.AD9959.setChannel(0, self.mw_frequency, self.mw_amplitude, 0)
        self.mutate_dataset("time", stepnum, stepped_parameter)

    @kernel
    def scan_experiment(self, stepnum=0, stepped_parameter=0.0):
        pulse_time = stepped_parameter
        self.extra_mw.pulse(pulse_time)

    def analyze(self):
        para = self.analysis.analyse("time", "probability",
self.analysis.rabi_flop, self.plus_pi_time)
        self.set_dataset("plus.pi_time", para, persist=True, save=False)
        print("your plus pi time is:{}us".format(para*1000000))
        self.analysis.plot_fit("time", "time /s", "probability", "probability",
self.analysis.rabi_flop, para)

class MwminusTimeScan(BasicScan, EnvExperiment):
    """Microwave minus Rabi Scan v3.0"""
    def build(self):
        self.mw_frequency = self.get_dataset("minus.freq")
        self.mw_amplitude = self.get_dataset("minus.amplitude")
        self.plus_pi_time = self.get_dataset("minus.pi_time")
        self.setattr_argument("pulse_time", Scannable(default=RangeScan(0,
500e-6, 26), unit='us'))
        super().build()
        self.scan_parameter = self.pulse_time

    def prepare_experiment(self, nsteps):
        self.set_dataset("time", np.full(nsteps, np.nan), broadcast=True,
persist=True)
        super().prepare_experiment(nsteps)

    def prepare_scan_point(self, stepnum=0, stepped_parameter=0):
        self.AD9959.setChannel(0, self.mw_frequency, self.mw_amplitude, 0)
        self.mutate_dataset("time", stepnum, stepped_parameter)

    @kernel
    def scan_experiment(self, stepnum=0, stepped_parameter=0.0):
        pulse_time = stepped_parameter
        self.extra_mw.pulse(pulse_time)

    def analyze(self):
        para = self.analysis.analyse("time", "probability",
self.analysis.rabi_flop, self.plus_pi_time)
        self.set_dataset("plus.pi_time", para, persist=True, save=False)
        print("your plus pi time is:{}us".format(para*1000000))
        self.analysis.plot_fit("time", "time /s", "probability", "probability",
self.analysis.rabi_flop, para)
```

```
class RamseyPhaseScan(BasicScan, EnvExperiment):
    """Microwave Ramsey experiment v3.0"""
    def build(self):
        self.setattr_argument("pi_2_pulse_freq", NumberValue(default=102837e3,
ndecimals=3, step=1e-3, unit='kHz'))
        self.setattr_argument("pi_2_time", NumberValue(default=100e-6,
ndecimals=3, step=1, unit='us'))
        self.setattr_argument("clock_freq", NumberValue(default=102837e3,
ndecimals=3, step=1e-3, unit='kHz'))
        self.setattr_argument("clock_amplitude", NumberValue(default = 0.3,
ndecimals=3, step=0.1, min = 0, max = 1), tooltip = 'amplitude (0-1)')
        self.setattr_argument("rf_amplitude", NumberValue(default = 0.3,
ndecimals=3, step=0.1, min = 0, max = 1), tooltip = 'amplitude (0-1)')
        self.setattr_argument("pulse_start_phase_degrees", NumberValue(default =
0, ndecimals=5, step=1, min = 0, max = 360), tooltip = 'start phase (0-359)')
        self.setattr_argument("pulse_phase_step_degrees", NumberValue(default =
10, ndecimals=5, step=1, min = 0, max = 180), tooltip = 'phase step (1-180)')
        self.setattr_argument("delay_time", NumberValue(default=0e-6,
ndecimals=3, step=1, unit='us'))
        self.setattr_argument("phase", Scannable(default=RangeScan(0, 360, 10)))

        super().build()
        self.scan_parameter = self.phase

    def prepare_experiment(self, nsteps):
        self.set_dataset("phase", np.full(nsteps, np.nan), broadcast=True,
persist=True)
        super().prepare_experiment(nsteps)

    def prepare_scan_point(self, stepnum=0, stepped_parameter=0):
        #phase = self.pulse_start_phase_degrees +
stepnum*self.pulse_phase_step_degrees
        phase = stepped_parameter

        self.AD9959.setChannel(1, self.clock_freq, self.clock_amplitude, 0)
        self.AD9959.setChannel(2, self.pi_2_pulse_freq, self.rf_amplitude, 0)
        self.AD9959.setChannel(3, self.pi_2_pulse_freq, self.rf_amplitude,
phase)

        self.mutate_dataset("phase", stepnum, phase)

    @kernel
    def scan_experiment(self, stepnum=0, stepped_parameter = 0.0):
        # Ramsey experiment
        self.plus_mw.pulse(self.pi_2_time)
        delay(self.delay_time)
        self.minus_mw.pulse(self.pi_2_time)
```

A.5 RF dressed state experiments

```
from basicScan import *
class DressedRffreqScan(BasicScan, EnvExperiment):
    """Dressed RF Frequency scan"""
    def build(self):
        self.setattr_argument("clock_amplitude", NumberValue(default = 0.3,
ndecimals=3, step=0.1, min = 0, max = 1), tooltip = 'amplitude (0-1)')
        self.setattr_argument("clock_freq", NumberValue(default=102819.69e3,
ndecimals=8, step=1e-3, unit='kHz'))
        self.setattr_argument("rf_freq", Scannable(default=RangeScan(102837e3,
103837e3, 26), ndecimals=8, unit='MHz'))
        self.setattr_argument("rf_amplitude", NumberValue(default = 0.3,
ndecimals=3, step=0.1, min = 0, max = 1), tooltip = 'amplitude (0-1)')
        self.setattr_argument("pulse_time", NumberValue(default=20e-6,
ndecimals=3, step=1, unit='us'))
        self.setattr_argument("clock_pi_time", NumberValue(default=20e-6,
ndecimals=3, step=1, unit='us'))

        super().build()
        self.scan_parameter = self.rf_freq

    def prepare_experiment(self, nsteps):
        self.set_dataset("freq", np.full(nsteps, np.nan), broadcast=True,
persist=True)
        super().prepare_experiment(nsteps)

    def prepare_scan_point(self, stepnum=0, stepped_parameter=0):
        rf_freq = stepped_parameter
        self.AD9959.setChannel(1, self.clock_freq, self.clock_amplitude, 0)
        self.AD9959.setChannel(4, rf_freq, self.rf_amplitude, 0)

        self.mutate_dataset("freq", stepnum, stepped_parameter)

    @kernel
    def scan_experiment(self, stepnum=0, stepped_parameter=0.0):

        self.clock_mw.pulse(self.clock_pi_time)
        self.rf1.pulse(self.pulse_time)
        self.clock_mw.pulse(self.clock_pi_time)

class RftimeScan(BasicScan, EnvExperiment):
    """Dressed RF time scan"""
    def build(self):
        self.setattr_argument("rf_amplitude", NumberValue(default = 0.3,
ndecimals=3, step=0.1, min = 0, max = 1), tooltip = 'amplitude (0-1)')
        self.setattr_argument("clock_amplitude", NumberValue(default = 0.3,
ndecimals=3, step=0.1, min = 0, max = 1), tooltip = 'amplitude (0-1)')
        self.setattr_argument("clock_freq", NumberValue(default=102819.69e3,
ndecimals=8, step=1e-3, unit='kHz'))
        self.setattr_argument("rf_freq", NumberValue(default=102819.69e3,
ndecimals=8, step=1e-3, unit='kHz'))
        self.setattr_argument("clock_pi_time", NumberValue(default=87.35e-6,
ndecimals=4, step=1, unit='us'))
        self.setattr_argument("pulse_time", Scannable(default=RangeScan(0,
500e-6, 26), unit='us'))
```

```
        super().build()
        self.scan_parameter = self.pulse_time

    def prepare_experiment(self, nsteps):
        self.set_dataset("time", np.full(nsteps, np.nan), broadcast=True,
persist=True)
        super().prepare_experiment(nsteps)

    def prepare_scan_point(self, stepnum=0, stepped_parameter=0):
        self.AD9959.setChannel(1, self.clock_freq, self.clock_amplitude, 0)
        self.AD9959.setChannel(4, self.rf_freq, self.rf_amplitude, 0)

        self.mutate_dataset("time", stepnum, stepped_parameter)

    @kernel
    def scan_experiment(self, stepnum=0, stepped_parameter=0.0):
        time = stepped_parameter
        self.clock_mw.pulse(self.clock_pi_time)
        self.rf1.pulse(time)
        self.clock_mw.pulse(self.clock_pi_time)

class DressedRf_MWfreqScan(BasicScan, EnvExperiment):
    """Dressed RF Microwave Frequency scan"""
    def build(self):
        self.setattr_argument("clock_amplitude", NumberValue(default = 0.3,
ndecimals=3, step=0.1, min = 0, max = 1), tooltip = 'amplitude (0-1)')
        self.setattr_argument("clock_freq", NumberValue(default=102819.69e3,
ndecimals=8, step=1e-3, unit='kHz'))
        self.setattr_argument("mw_amplitude", NumberValue(default = 0.3,
ndecimals=3, step=0.1, min = 0, max = 1), tooltip = 'amplitude (0-1)')
        self.setattr_argument("MW_frequency",
Scannable(default=RangeScan(102837e3, 103837e3, 26), ndecimals=8, unit='MHz'))
        self.setattr_argument("rf_plus_freq", NumberValue(default=102819.69e3,
ndecimals=8, step=1e-3, unit='kHz'))
        self.setattr_argument("rf_plus_amplitude", NumberValue(default = 0.3,
ndecimals=3, step=0.1, min = 0, max = 1), tooltip = 'amplitude (0-1)')
        self.setattr_argument("rf_minus_freq", NumberValue(default=102819.69e3,
ndecimals=8, step=1e-3, unit='kHz'))
        self.setattr_argument("rf_minus_amplitude", NumberValue(default = 0.3,
ndecimals=3, step=0.1, min = 0, max = 1), tooltip = 'amplitude (0-1)')
        self.setattr_argument("pulse_time", NumberValue(default=20e-6,
ndecimals=3, step=1, unit='us'))

        super().build()
        self.scan_parameter = self.MW_frequency

    def prepare_experiment(self, nsteps):
        self.set_dataset("freq", np.full(nsteps, np.nan), broadcast=True,
persist=True)
        super().prepare_experiment(nsteps)

    def prepare_scan_point(self, stepnum=0, stepped_parameter=0):
        MW_frequency = stepped_parameter
```

```
        self.AD9959.setChannel(1, self.clock_freq, self.clock_amplitude, 0)
        self.AD9959.setChannel(2, MW_frequency, self.mw_amplitude, 0)
        self.AD9959.setChannel(4, self.rf_plus_freq, self.rf_plus_amplitude, 0)
        self.AD9959.setChannel(5, self.rf_minus_freq, self.rf_minus_amplitude,
0)

        self.mutate_dataset("freq", stepnum, stepped_parameter)

    @kernel
    def scan_experiment(self, stepnum=0, stepped_parameter=0.0):
        with parallel:
            self.rf1.pulse(self.pulse_time)
            self.rf2.pulse(self.pulse_time)
            self.plus_mw.pulse(self.pulse_time)

class DressedRf_MWrabiScan(BasicScan, EnvExperiment):
    """Dressed RF Microwave rabi scan"""
    def build(self):
        self.setattr_argument("clock_amplitude", NumberValue(default = 0.3,
ndecimals=6, step=0.1, min = 0, max = 1), tooltip = 'amplitude (0-1)')
        self.setattr_argument("clock_freq", NumberValue(default=102819.69e3,
ndecimals=8, step=1e-3, unit='kHz'))
        self.setattr_argument("mw_amplitude", NumberValue(default = 0.3,
ndecimals=6, step=0.1, min = 0, max = 1), tooltip = 'amplitude (0-1)')
        self.setattr_argument("MW_frequency", NumberValue(default=102819.69e3,
ndecimals=8, step=1e-3, unit='kHz'))
        self.setattr_argument("rf_plus_freq", NumberValue(default=102819.69e3,
ndecimals=8, step=1e-3, unit='kHz'))
        self.setattr_argument("rf_plus_amplitude", NumberValue(default = 0.3,
ndecimals=6, step=0.1, min = 0, max = 1), tooltip = 'amplitude (0-1)')
        self.setattr_argument("rf_minus_freq", NumberValue(default=102819.69e3,
ndecimals=8, step=1e-3, unit='kHz'))
        self.setattr_argument("rf_minus_amplitude", NumberValue(default = 0.3,
ndecimals=6, step=0.1, min = 0, max = 1), tooltip = 'amplitude (0-1)')
        self.setattr_argument("pulse_time", Scannable(default=RangeScan(0,
500e-6, 26), unit='us'))

        super().build()
        self.scan_parameter = self.pulse_time

    def prepare_experiment(self, nsteps):
        self.set_dataset("time", np.full(nsteps, np.nan), broadcast=True,
persist=True)
        super().prepare_experiment(nsteps)

    def prepare_scan_point(self, stepnum=0, stepped_parameter=0):
        self.AD9959.setChannel(1, self.clock_freq, self.clock_amplitude, 0)
        self.AD9959.setChannel(2, self.MW_frequency, self.mw_amplitude, 0)
        self.AD9959.setChannel(4, self.rf_plus_freq, self.rf_plus_amplitude, 0)
        self.AD9959.setChannel(5, self.rf_minus_freq, self.rf_minus_amplitude,
0)

        self.mutate_dataset("time", stepnum, stepped_parameter)
```

```
    @kernel
    def scan_experiment(self, stepnum=0, stepped_parameter=0.0):
        time = stepped_parameter
        with parallel:
            self.rf1.pulse(time)
            self.rf2.pulse(time)
            self.plus_mw.pulse(time)

class DressedRFT1Scan(BasicScan, EnvExperiment):
    """Dressed RF T1 scan"""
    def build(self):
        self.setattr_argument("clock_amplitude", NumberValue(default = 0.3,
ndecimals=3, step=0.1, min = 0, max = 1), tooltip = 'amplitude (0-1)')
        self.setattr_argument("clock_freq", NumberValue(default=102819.69e3,
ndecimals=8, step=1e-3, unit='kHz'))
        self.setattr_argument("rf_plus_amplitude", NumberValue(default = 0.3,
ndecimals=3, step=0.1, min = 0, max = 1), tooltip = 'amplitude (0-1)')
        self.setattr_argument("rf_plus_freq", NumberValue(default=109758.78e3,
ndecimals=8, step=1e-3, unit='kHz'))
        self.setattr_argument("rf_minus_amplitude", NumberValue(default = 0.3,
ndecimals=3, step=0.1, min = 0, max = 1), tooltip = 'amplitude (0-1)')
        self.setattr_argument("rf_minus_freq", NumberValue(default=95858.22e3,
ndecimals=8, step=1e-3, unit='kHz'))
        self.setattr_argument("MW_frequency", NumberValue(default=102819.69e3,
ndecimals=8, step=1e-3, unit='kHz'))
        self.setattr_argument("mw_amplitude", NumberValue(default = 0.3,
ndecimals=3, step=0.1, min = 0, max = 1), tooltip = 'amplitude (0-1)')
        self.setattr_argument("mw_pi_time", NumberValue(default=87.35e-6,
ndecimals=4, step=1, unit='us'))
        self.setattr_argument("delay_time", Scannable(default=RangeScan(0,
500e-6, 26), unit='us'))

        super().build()
        self.scan_parameter = self.delay_time

    def prepare_experiment(self, nsteps):
        self.set_dataset("time", np.full(nsteps, np.nan), broadcast=True,
persist=True)
        super().prepare_experiment(nsteps)

    def prepare_scan_point(self, stepnum=0, stepped_parameter=0):
        self.AD9959.setChannel(1, self.clock_freq, self.clock_amplitude, 0)
        self.AD9959.setChannel(4, self.rf_plus_freq, self.rf_plus_amplitude, 0)
        self.AD9959.setChannel(5, self.rf_minus_freq, self.rf_minus_amplitude,
0)
        self.AD9959.setChannel(2, self.MW_frequency, self.mw_amplitude, 0)
        self.mutate_dataset("time", stepnum, stepped_parameter)

    @kernel
    def scan_experiment(self, stepnum=0, stepped_parameter=0.0):
        time = stepped_parameter
        with parallel:
            self.rf1.on()
            self.rf2.on()
```

```
        self.plus_mw.pulse(self.mw_pi_time)
        delay(time)
        self.plus_mw.pulse(self.mw_pi_time)
        with parallel:
            self.rf1.off()
            self.rf2.off()

class DressedRFT2Scan(BasicScan, EnvExperiment):
    """Dressed RF T2 scan"""
    def build(self):
        self.setattr_argument("clock_amplitude", NumberValue(default = 0.3,
ndecimals=6, step=0.1, min = 0, max = 1), tooltip = 'amplitude (0-1)')
        self.setattr_argument("clock_freq", NumberValue(default=102819.69e3,
ndecimals=8, step=1e-3, unit='kHz'))
        self.setattr_argument("rf_plus_amplitude", NumberValue(default = 0.3,
ndecimals=6, step=0.1, min = 0, max = 1), tooltip = 'amplitude (0-1)')
        self.setattr_argument("rf_plus_freq", NumberValue(default=109758.78e3,
ndecimals=8, step=1e-3, unit='kHz'))
        self.setattr_argument("rf_minus_amplitude", NumberValue(default = 0.3,
ndecimals=6, step=0.1, min = 0, max = 1), tooltip = 'amplitude (0-1)')
        self.setattr_argument("rf_minus_freq", NumberValue(default=95858.22e3,
ndecimals=8, step=1e-3, unit='kHz'))
        self.setattr_argument("MW_frequency", NumberValue(default=102819.69e3,
ndecimals=8, step=1e-3, unit='kHz'))
        self.setattr_argument("mw_amplitude", NumberValue(default = 0.3,
ndecimals=3, step=0.1, min = 0, max = 1), tooltip = 'amplitude (0-1)')
        self.setattr_argument("mw_pi_time", NumberValue(default=87.35e-6,
ndecimals=4, step=1, unit='us'))
        self.setattr_argument("delay_time", NumberValue(default=20e-6,
ndecimals=3, step=1, unit='us'))
        self.setattr_argument("phase", Scannable(default=RangeScan(0, 360, 10)))
        self.setattr_argument("Add_spin_echo", BooleanValue())

        super().build()
        self.scan_parameter = self.phase

    def prepare_experiment(self, nsteps):
        self.set_dataset("phase", np.full(nsteps, np.nan), broadcast=True,
persist=True)
        super().prepare_experiment(nsteps)

    def prepare_scan_point(self, stepnum=0, stepped_parameter=0):
        phase = stepped_parameter
        self.AD9959.setChannel(1, self.clock_freq, self.clock_amplitude, 0)
        self.AD9959.setChannel(2, self.MW_frequency, self.mw_amplitude, 0)
        self.AD9959.setChannel(3, self.MW_frequency, self.mw_amplitude, phase)
        self.AD9959.setChannel(4, self.rf_plus_freq, self.rf_plus_amplitude, 0)
        self.AD9959.setChannel(5, self.rf_minus_freq, self.rf_minus_amplitude,
0)
        self.mutate_dataset("phase", stepnum, stepped_parameter)

    @kernel
    def scan_experiment(self, stepnum=0, stepped_parameter=0.0):
        if self.Add_spin_echo == True:
```

```
        with parallel:
            self.rf1.on()
            self.rf2.on()
        self.plus_mw.pulse(self.mw_pi_time/2)
        delay(self.delay_time/2)
        self.plus_mw.pulse(self.mw_pi_time)
        delay(self.delay_time/2)
        self.minus_mw.pulse(self.mw_pi_time/2)
        with parallel:
            self.rf1.off()
            self.rf2.off()

    else:
        with parallel:
            self.rf1.on()
            self.rf2.on()
        self.plus_mw.pulse(self.mw_pi_time/2)
        delay(self.delay_time)
        self.minus_mw.pulse(self.mw_pi_time/2)
        with parallel:
            self.rf1.off()
            self.rf2.off()
```